UCLouvain

École polytechnique de Louvain

Characterization of CIGS/Oxide interface passivation for $Cu(In,Ga)Se_2$ solar cell applications

Effect of oxide passivation layers, surface cleaning and post-deposition annealing

Author: **Romain Scaffidi**
Supervisor: **Denis Flandre**
Readers: **Dilara Gokcen Buldu, Denis Flandre, Laurent Francis**
Academic year 2019–2020
Master [120] in Electrical Engineering

Acknowledgements

First of all, I would like to sincerely thank my supervisor Denis Flandre for his guidance and availability at all moments. It has been an honour and a pleasure to be under his supervision for these past years and his always constructive remarks have just made me a better engineer. My sincere thanks also go to Sébastien Faniel and Jackson Lontchi Jioleo for their help on respectively the processing and the analysis of titanium dioxide samples. I am also grateful to Laurent Francis for accepting to be examiner of my work.

Second, I am also very grateful to Dilara Gokcen Buldu, my daily supervisor during this whole project whose guidance, support and kindness was one of the keys to the success of this experience. Thanks to her, the past six months have been the most exciting experience of my entire life during which I discovered and learnt new things every single day, whether it concerns the field of CIGS or the R&D sector in general. On the whole, I want to express my dearest gratitude to every collaborator met inside imec's and EnergyVille's infrastructures without whom all of this would not have been possible. In particular, I am beholden to Guy Brammertz and Thierry Kohl for their help in my investigations of numerical simulations and CV analysis. I am sincerely grateful to Tim Oris for his help on the processing of my samples and to Gizem Birant for her proposition of collaboration about HfO_2 back passivation. I owe special thanks to Bart Vermang and Marc Meuris for their kindness and constant availability, and to all the other members of the team, Jessica de Wild, Abdullah Bin Shams, Yevhenii Rybalchenko and Iryna Kandybka for making EnergyVille such a pleasant place to work.

Finally, I am forever beholden to my family and close friends. I want to thank my two parents for their eternal support and for giving me the opportunity to undertake such a meaningful project to me. I want to thank my two brothers Baptiste and Thomas for always boosting my ambitions and self-confidence as well as pushing my curiosity to the highest.

Abstract

In this thesis, we characterize the passivation effects of three different dielectric materials (Al_2O_3, HfO_2 and TiO_2) at the interface with $Cu(In,Ga)Se_2$ so as to determine their eligibility for the production of front passivated CIGS solar cells. Using simulations and experiments on Metal-Insulator-Semiconductor study structures, the effectiveness of these oxide passivation layers is both qualitatively and quantitatively described along with the influence of diverse parameters, mainly surface pre-cleaning and post-deposition annealing. In particular, we show that Al_2O_3 and HfO_2 both exhibit effective chemical passivation with densities of interface traps D_{it} of the order of $10^{11} cm^{-2} eV^{-1}$, on average slightly lower for Al_2O_3, and further reduced by annealing treatments at 300°C in N_2 environment. On the contrary, we observe negative densities of fixed charges Q_f of the order of $10^{12} cm^{-2}$ in both materials, again moderately lower for Al_2O_3, which result in misdirected field-effect potentially limiting the overall improvements induced by passivation effects. The negative values found for Q_f can be reduced by activating positive charges through similar annealing treatments as for chemical passivation. We highlight the suspected presence of other phenomena such as series resistance, secondary phases and complex defects whose behaviours are affected by CIGS surface pre-cleaning along with chemical passivation. The superposition of Al_2O_3 and HfO_2 in a multi-layer passivation stack is investigated so as to solve the issue of processing compatibility in complete solar cells. For that innovative design, we show effective chemical passivation ($D_{it} \sim 10^{11} cm^{-2} eV^{-1}$) and negative Q_f similarly to both individual materials. The application of Ammonia pre-cleaning and 300°C Nitrogen annealing on those samples lead to our optimal design for front interface passivation. Eventually, we discuss the need for further investigations and adapted analysis techniques taking into account the peculiar properties of TiO_2 as compared to Al_2O_3 and HfO_2. Our preliminary qualitative analysis suggests potential passivation effects of titania at the interface with CIGS.

Lists of acronyms

Acronym	Signification
ALD	Atomic Layer Deposition
AS	Ammonium Sulfide - $(NH_4)_2S$
CB	Conduction Band
CBD	Chemical Bath Deposition
CGI	Copper to Gallium and Indium ratio (Cu/(Ga+In))
CIGS	Copper Indium Gallium Diselenide
CM	Conductance method
C-V/CV	Capacitance-Voltage
GGI	Gallium to Gallium and Indium ratio (Ga/(Ga+In))
G-V/GV	Conductance-Voltage
HLF	High-Low Frequency technique
I-V/IV	Current-Voltage
MIS	Metal-Insulator-Semiconductor
PDA	Post-deposition Annealing
PL	Photoluminescence
PV	Photovoltaic
SC	Semiconductor
SLG	Soda-Lime Glass
VB	Valence Band
XRF	X-Ray Fluorescence

Contents

Chapter 1

Introduction

1.1 Context

The need for changing our means of producing energy has never been as urgent as it is right now. Throughout the world, the consequences of climate change due to human activity are affecting populations and ecosystems. If no measures are rapidly taken to reduce our consumption of fossil fuels, the situation will deteriorate further and faster, leaving an extremely uncertain future to humanity. Next to cutting down the yearly amount of energy used by our society, the expansion of renewable energies is another way to reduce the greenhouse gases emissions that recently increased worryingly fast (figure 1.1).

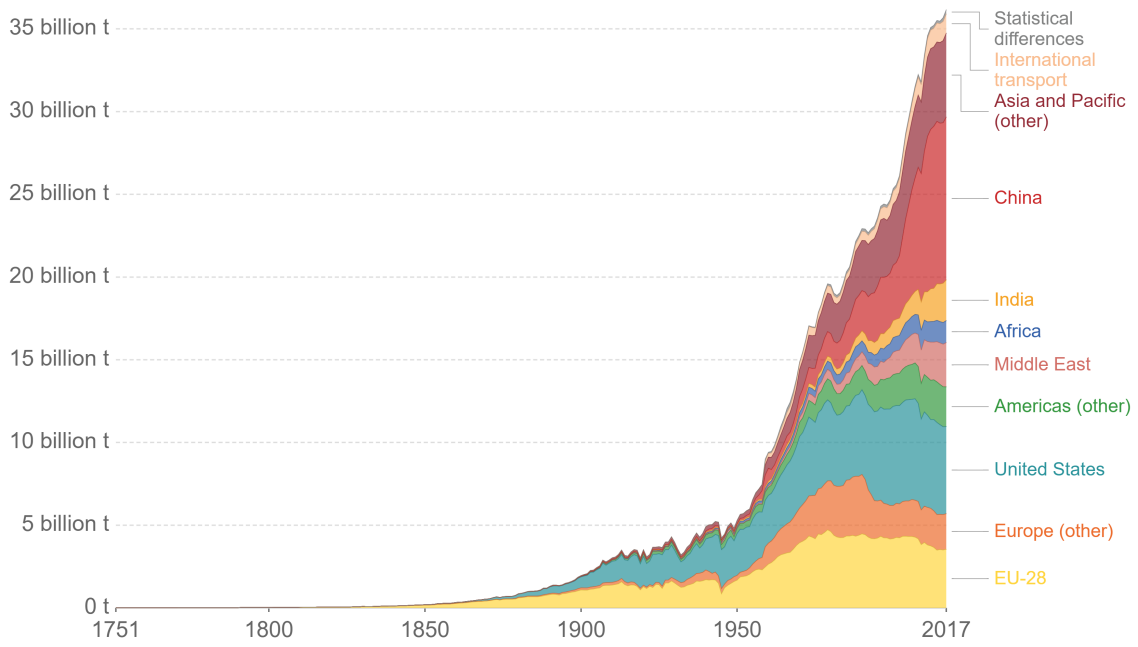

Figure 1.1: Annual total CO_2 emissions by world region, from [1].

One famous and promising technology capable of solving such a challenge is solar power, i.e. extracting the energy radiated by the Sun to create electricity. The potential is huge: every hour, the Sun provides an amount of energy to the Earth that is nearly sufficient to fulfill the worldwide energy consumption over a complete year [2]. One could then naively think that it would be enough to cover the whole Earth with solar panels to solve the climate crisis.

Despite obvious practical problems in terms of economical feasibility and energy storage, this vision omits certain technical challenges intrinsically related to the technology itself, namely its physical efficiency limitations. Indeed, photovoltaic (PV) panels convert the solar energy to electricity with a certain yield. This one is right now not high enough to sustain the global energy demand only with solar power. To tackle this issue, technological breakthroughs and advances in PV systems are highly required whether it is about their laboratory performances or their commercial competitivity compared to fossil fuels. Trying to solve this efficiency issue is precisely the focus of this work, in the case of one particular PV technology: CIGS solar cells.

The name of this technology relates to its main component, $CuIn_xGa_{1-x}Se_2$, a semiconductor material with great light absorption properties, thus well suited to PV applications. When combined with other functional layers, one obtains a complete solar structure which benefits from a much smaller thickness of the active layer compared to conventional Silicon modules. Along with other PV technologies such as Perovskites, CIGS cells are part of the "thin-film" generation of solar cells. Their lower thickness enables them, among other things, to be produced on lightweight flexible substrates, for which they are widely believed to be the future of the "building-integrated PV " sector (figure 1.2). In theory, they also have the advantage of a less material-consuming and costly production compared to Silicon.

Figure 1.2: Application of building-integrated CIGS PV panels from [3].

Still, the PV market gives place to harsh competition between the different technologies and in practice efficiency is one if not the most important parameter settling the market shares. Concerning this very aspect, Silicon PV remains by far the most dominant of all with more than 90% of market share around the globe [4]. For alternative PV technologies to catch up with Silicon, further research work is needed to tackle their efficiency limitations.

1.2 Topic overview

The problem studied here is a major bottleneck in the field of CIGS PV research, i.e. the performance losses due to interfacial recombination, an inevitable physical mechanism which is detailed further in this report. Indeed, one great difference between Silicon and CIGS cells is their configuration. On the one hand, Silicon cells have a thick layer of high-purity crystalline Silicon surrounded by thin additional layers usually based on Silicon as well. On the other hand, CIGS cells rely on an intricate hetero-junction structure including multiple interfaces and connecting different materials with various crystalline lattices (see figure 1.3). These interfaces induce undesirable effects reducing the global efficiency, mainly by cancelling the generation of charge carriers when absorbing light.

To cope with that, common practice is to perform "interface passivation", i.e. to insert metal oxide layers at both of CIGS surfaces, denoted on figure 1.3 as "back" and "front" interfaces. This design enables to mitigate the electrical losses inevitably appearing at the two interfaces between the CIGS and the two adjacent layers made of Cadmium Sulfide and Molybdenum. Since research has been mainly focusing on the passivation of the back interface lately [5–13], we found it innovative and important to study the front interface passivation. Still, the two topics being strongly related to each other, references in both fields will be used throughout this report.

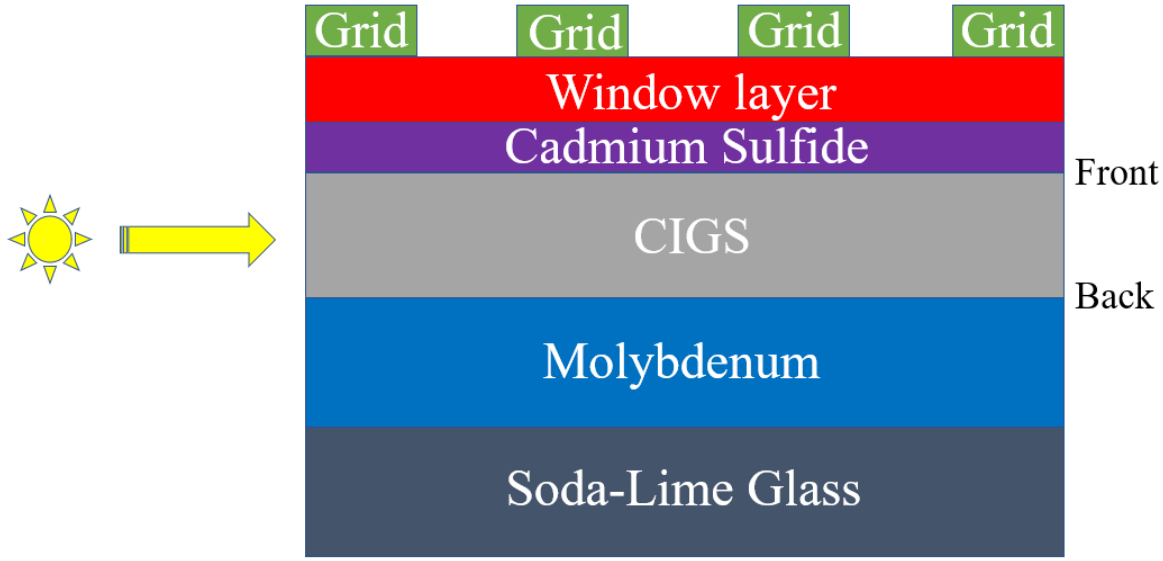

Figure 1.3: Schematic representation of an illuminated standard CIGS solar cell (arbitrary scale) and the terminology related to both interfaces of the CIGS layer.

1.3 Objectives

The purpose of this work is to characterize the interface between CIGS and different dielectric materials so as to quantify the potential passivation effects for solar cell applications. In order to determine the best design with regards to passivation effects, the influence of multiple parameters is investigated: CIGS processing, composition and pre-cleaning; oxide layer material, thickness and ALD temperature; post-deposition annealing. This translates into several sub-objectives:

- Investigating 3 different metal oxide materials to be used as passivation layers in CIGS solar cells: Al_2O_3, HfO_2, TiO_2
- Processing high quality Metal-Insulator-Semiconductor (MIS) study structures to enable an accurate characterization of the electrical behaviour and passivation effects of the CIGS/Oxide interface
- Performing multiple types of measurements on these MIS samples (Capacitance-Voltage at room and low temperatures, Current-Voltage, Photoluminescence, ...) in order to extract important electrical figures-of-merit (R_{sh}, R_s, D_{it}, Q_f, ...)
- Investigating the influence of multiple experimental parameters and procedures (processing, composition, surface cleaning, post-deposition thermal annealing) so as to assess and compare their specific effectiveness in terms of interface passivation while attempting to highlight the optimal design
- Implementing numerical simulation models for MIS structures (SCAPS [14] and MATLAB®) that provide results to which our experimental observations can be confronted

1.4 Structure of the report

In the following, an introduction about the relevant theoretical background is presented in the second chapter, from the basic CIGS solar cell to the complete front-passivated design and the methods to characterize passivation effects using MIS structures. After that, the experimental methodology implemented throughout this work is detailed in the third chapter. This includes the complete description of the samples, the measurement setups and parameters, and the extra experimental process steps investigated (surface cleaning, PDA, ...). The fourth and next chapter describes the effect of the introduction of a passivation layer made of different materials at the CIGS/CdS interface: Al_2O_3, HfO_2, a superposition of Al_2O_3 and HfO_2 referred to as multi-layer, and finally TiO_2. This is done through the analysis and interpretation of mainly Capacitance-Voltage (C-V) and Photoluminescence (PL) measurements performed on MIS samples. The influence on samples quality and passivation effects of not only the different materials but also the other parameters mentioned above is discussed. In that same chapter, numerical simulations models of MIS capacitors (SCAPS [14] and MATLAB®) are introduced and their main results are confronted to the experimental results obtained. The last chapter concludes the report and opens up the discussion about future research.

Chapter 2

Theoretical Background

2.1 Overview

This chapter intends to give a thorough introduction to most of the theoretical concepts and phenomena encountered throughout our study. First, the study case of a simple p-n junction is developed in section 2.2 so as to contextualize the rest of the discussion and introduce the basic theory related to semiconductors and solar cells. Second, the important efficiency limitations targeted by our study and reported in the CIGS PV technology are described and mathematically formalized in section 2.3. Third, section 2.4 presents the main solution proposed in this work to solve the performance issues just mentioned. Commonly referred to as "interface passivation", this design is qualitatively detailed and its effectiveness explained and demonstrated in the same section. Based on the previous discussion and relevant literature references, a short selection of interesting materials to investigate is established in section 2.5. Moreover, specific figures-of-merit, criteria and parameters are highlighted in order to give a general direction to our investigations. In section 2.6, all of the previously discussed points are gathered to result in our theoretical state-of-the-art solar cell design whose specifications and performances give the key guidelines of this work. Section 2.7 closes this chapter by describing the typical characterization structures used in our study as well as the relevant measurements and analysis techniques.

2.2 Basic CIGS PV technology

2.2.1 CIGS/CdS hetero p-n junction

When two semiconductors, one doped with acceptors (p-type) and one doped with donors (n-type), are put in contact, a p-n junction is formed. This well-known structure has the ability of generating electrical current under illumination, i.e. precisely the function of a PV cell. Although the design of realistic and efficient solar cells is actually much more complex than the simple realization of a p-n junction, let us first consider and describe the simple PV cell configuration illustrated on figure 2.1. This vertical structure globally consists of an hetero p-n junction sandwiched in between two ohmic contacts. The junction is composed of a thick p-type absorber layer made of CIGS and a thin n-type buffer layer made of Cadmium Sulfide (CdS), similarly to real CIGS solar cells.

One of the most important properties in the theory of p-n junctions is the coexistence of two transport phenomena, i.e. diffusion and drift, inside and close to the contact zone

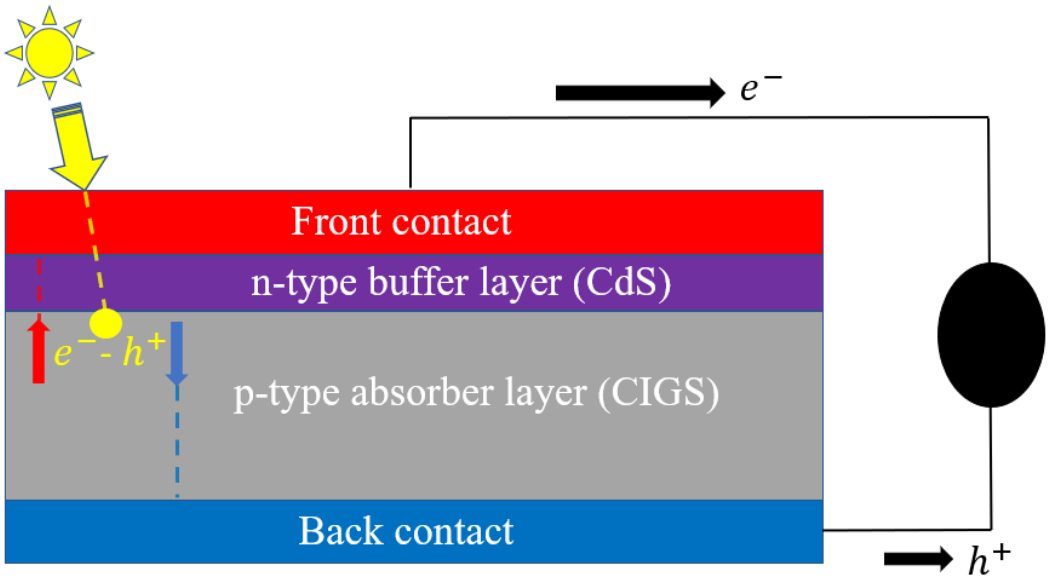

Figure 2.1: Basic configuration of an illuminated PV cell including a p-n junction, two metallic contacts and an external circuit. Photogenerated electrons and holes are respectively noted e^- and h^+.

between the p and n sides. Indeed, the important gradient in charge carriers concentrations at the p-n interface induces diffusion phenomena that repel majority carriers away from the contact (electrons migrating to the p side and inversely for holes). As a result, both sides of the p-n interface become depleted of their majority carriers and fixed charges of opposite signs appear on each side (figure 2.2). Inside this "depletion zone", an important electrical field (blue arrow) appears due to the high density of charges distributed on a small distance compared to the whole thickness of the CIGS layer. The drift force induced by this electrical field acts in opposition to the carriers diffusion in such a way that an equilibrium between the two phenomena is eventually reached and maintains itself as long as no external forces or disturbances intervene. The scope of that electrical field outside of the depletion zone, i.e. the distance from the edges of the depletion zone within which charges feel the influence of the field, is limited to the diffusion length of the carriers. Beyond that distance, the carriers concentrations mostly stay constant and nearly no charges or electrical field are present. The electrical activity of the p-n junction is then mainly concentrated in the vicinity of the contact between its two sides. Let us now consider the effect of illumination and discuss the actual conversion of light to electrical current.

2.2.2 Photogeneration of carriers

Based on the photovoltaic effect, we know that "electron-hole (e-h) pairs" can be created inside the p-type absorber layer from figure 2.1 when it is illuminated. Indeed, since the bandgap of the CIGS is direct, it is possible for the electrons present in the valence band (VB) to be directly promoted to the conduction band (CB) after absorbing a sufficient amount of energy without any kinetic contribution. This is precisely the case when incident photons with an energy at least equal to the bandgap of the CIGS are absorbed by electrons from the VB. Consequently to the promotion of electrons to the CB, holes appear in the VB as a counterpart and e-h pairs are created. The same applies for the n-type buffer

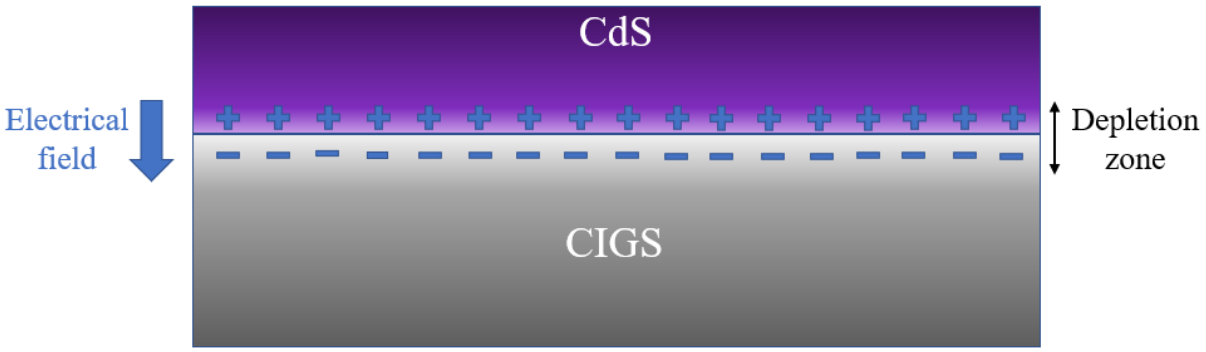

Figure 2.2: Schematic representation of the built-in electrical field present in the depletion zone at the CIGS/CdS interface (diffusion phenomena are not shown).

layer made of CdS except that: first, its higher bandgap than CIGS corresponds to the absorption of another part of the light spectrum; second, its lower thickness and optical absorption coefficient result in a small contribution to the total photogeneration of carriers.

Given the fact that the CB of a semiconductor is empty at room temperature contrarily to metals, the electrons can move freely inside it and likewise for the holes in the VB. These particles are thus designated as "free charge carriers". Generally speaking, given the high absorption coefficient of CIGS and the negligible optical contribution of the CdS layer, it is reasonable to consider that most of the light is absorbed as soon as it reaches the top surface of the CIGS, meaning that the photogenerated e-h pairs are mainly located just below the CIGS/CdS interface. If one manages to separate the e-h pairs in such a way that electrons migrate together towards one end of the solar cell while the holes migrate towards the other end, an electrical current appears in the structure since the front and back contacts are connected to each other by an external circuit (figure 2.1). For that conversion of solar power towards electricity to actually appear, the e-h pairs should be kept dissociated during a sufficiently long time for them to attain the external circuit and supply the load in energy, which is precisely the problem treated hereafter.

2.2.3 Charge collection and e-h pairs dissociation

The natural way through which e-h pairs are maintained in the dissociated state is the built-in electrical field present in the depletion zone of the p-n junction. Indeed, based on the previous discussion, we know that not only most of the photogenerated carriers are concentrated near the CIGS/CdS interface (within their diffusion length) but also that the strong drift force present at that very interface has a sufficient scope to interact with them. As depicted on figure 2.3, the effect of that intrinsic electrical field is to separate the photo-excited e-h pairs by driving the electrons (minority carriers) upwards to the front contact and the holes (majority carriers) downwards to the back contact. However, the mechanism with which the photogenerated carriers are successfully converted into electricity presents two major limitations regarding its efficiency.

On the one hand, the vertical drift force is not sufficiently strong to successively dissociate all of the photogenerated e-h pairs and drive the separated holes and electrons in the right direction. On the other hand, the migration path of these charge carriers through

the CIGS/CdS interface and the rest of the structure is full of "obstacles" hindering their circulation. Consequently, a certain amount of free carriers do not contribute to the charge flow which naturally translates into electrical losses. Before reviewing the solutions to this two-fold efficiency limitation, let us first focus on the physical and mathematical formalization of that problem of carriers migration.

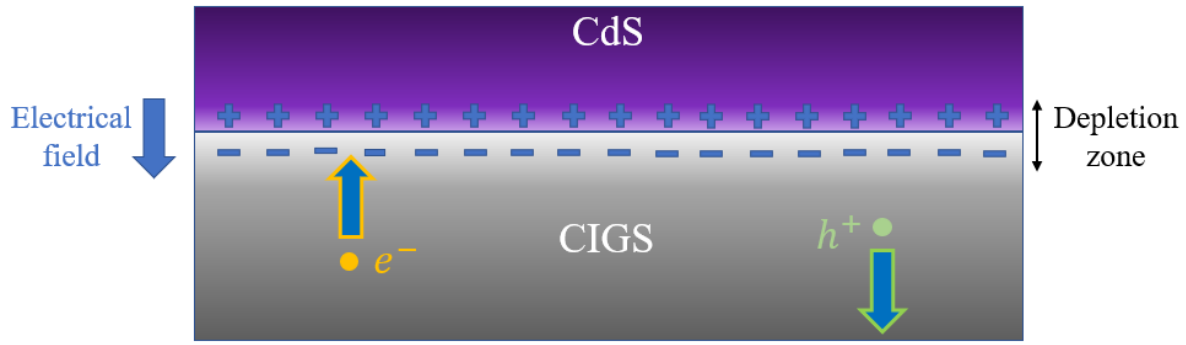

Figure 2.3: Schematic representation of the e-h pairs dissociation carried out by the built-in electrical field present in the depletion zone at the CIGS/CdS interface. The photogenerated carriers are represented by dots (orange for electrons, green for holes) and their respective directions of circulation are represented by arrows.

2.3 Recombination mechanisms

2.3.1 Definition and losses

As mentioned before, the condition for generating an electrical current in the solar cell is to keep the photogenerated e-h pairs in the dissociated state until reaching the external circuit. Besides that, the semiconductors theory tells us that without any means to keep them separated, the generated free carriers would naturally disappear past a certain amount of time, called carrier lifetime, spent in the semiconductor material. This occurs when the excited carriers, i.e electrons in the CB, fall back in their initial energy level, i.e. the VB, by losing the energy previously absorbed from light. The mechanism describing this cancellation of e-h pairs is called recombination and it is characterized by a certain rate or speed at which the pairs vanish in the material per unit of time. In the view of a power system, the annihilation of free carriers translates into electrical losses and is then to be avoided as much as possible. Therefore, the objective of our study is precisely to investigate a specific solution to limit the losses related to the mechanism of recombination in CIGS solar cells so as to to enhance their global efficiency.

2.3.2 Types of recombination and surface recombination

Recombination is a natural phenomenon that cannot be completely extinguished and which declines in two forms (figure 2.4). On the one hand, there is the "radiative recombination" mechanism, which characterizes the physical process by which excited carriers lose their energy by emitting light past a certain amount of time given the tendency of any corps to minimize its energy. This type of recombination, inevitable and intrinsic because not involving any external entities, is not the focus of this study.

On the other hand, the "non-radiative recombination" mechanism characterizes the cancellation of e-h pairs which involves defects present in the semiconductor crystalline lattice. This mechanism is very common since every crystalline material presents a certain volumic density of undesired particles related to various species such as vacancies, interstitials, dangling bonds, etc, ... Each of these impurities has a specific type (acceptor, donor or even neutral in some cases) and a corresponding bound energy level, similarly to the doping elements intentionally put in n-doped or p-doped semiconductors. Therefore, free electrons (holes) entering the vicinity of acceptor(donor)-type defects are susceptible to "recombine" with them, resulting not only in the generation of negatively (positively) fixed charges but also in recombination-related electrical losses. The energy initially gained through the absorption of photons is used to promote these external impurities, also called recombination centers and traps, to higher energy and charge state instead of contributing to the generation of photocurrents.

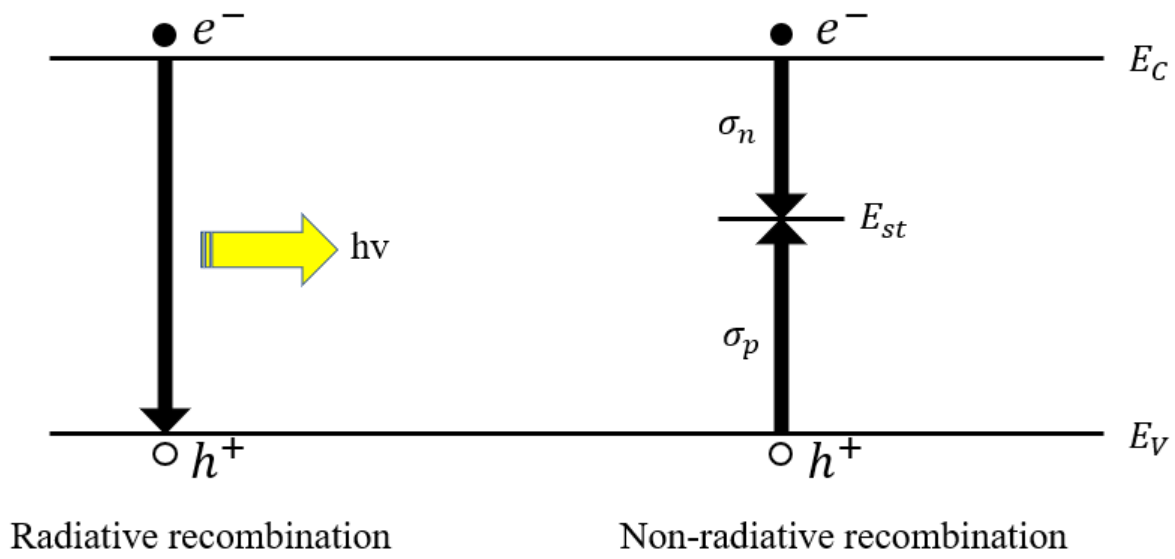

Figure 2.4: Schematic representation of the two recombination mechanisms considered in this work (E_C is the minimum energy of the conduction band and E_V is the maximum energy of the valence band). Left: radiative recombination by direct band-to-band transition and emission of light. Right: non-radiative recombination assisted by band-to-defect transition (σ_p and σ_n are the trap capture cross sections of respectively the holes and electrons in the semiconductor, E_{st} is the energy level associated to the recombinative defect).

One important thing to remark is that these impurities are essentially concentrated in sensitive crystalline areas presenting broken symmetries, vacancies and dangling bonds such as the contact surfaces between layers. Therefore, it is precisely on the defects located at these interfaces, i.e. the CIGS/CdS interface in our case, that the action of mitigating recombination mechanisms should be focused. As more thoroughly described below, the solution to this problem is two-fold: controlling the density of these recombination centers at the interfaces while monitoring the behaviour of the free e-h pairs in their surroundings. Let us see how this translates in terms of physical quantities (right of figure 2.4): the non-

radiative recombination rate S at the surface of a semiconductor crystal due to interfacial trap states with energy level E_{st} obeys the Shockley-Read-Hall (SRH) statistics [15]:

$$S = \frac{(p_s n_s - n_i^2) N_{it} v_{th}}{\left(\frac{n_s + n_i exp(\frac{E_{st}-E_i}{kT})}{\sigma_p}\right) + \left(\frac{p_s + n_i exp(\frac{E_i - E_{st}}{kT})}{\sigma_n}\right)} \tag{2.1}$$

where p_s and n_s are the concentrations of respectively holes and electrons at the concerned interface in cm^{-3}; N_{it} is the density of interface recombination traps in cm^{-2} and E_{st} is the associated energy level in eV; v_{th} is the thermal velocity of carriers in cm/s; n_i is the intrinsic concentration of carriers in the semiconductor in cm^{-3}; σ_p and σ_n are the trap capture cross sections of respectively the holes and electrons in the semiconductor in cm^2; E_i and kT are respectively the midgap energy of the semiconductor and the thermal energy, both in eV. One important observation from this equation is that the activity of recombination centers increases as their energy levels E_{st} get closer to the midgap energy E_i of the semiconductor [15]. Therefore, interface defects are more detrimental when located deeper in the interface band gap than close the band edges. The next section reviews two solutions to reduce the surface recombination rate S.

2.4 Interface passivation

The passivation of interfaces consists in attenuating the activity of recombination mechanisms at those very interfaces. Therefore, the objective here is to somehow decrease the value of S from equation 2.1 at the CIGS/CdS interface. This can be achieved either through reducing N_{it} at the numerator, which is called "chemical passivation", or by acting on the carriers concentrations n_s and p_s, which is called "field-effect passivation", since the other quantities in equation 2.1 are either constant parameters or difficult to control. The two components of interface passivation are separately detailed below even if, in practice, both of them are applied simultaneously with a single bivalent design: the thin oxide passivation layer. An important remark is that for this section, we consider that physical contact between the p and n sides is still ensured even after the insertion of the oxide layer, typically via the realization of holes through the thickness of the oxide (more details in section 2.6.2). This allows the previously described drift and diffusion phenomena to keep occurring. This section also specifies the particular requirements for a front interface oxide passivation layer so as to introduce the selection of suitable oxide materials presented in section 2.5.

2.4.1 Chemical passivation

The first option to limit interface recombination in equation 2.1 would naively be to reduce N_{it} at the numerator, since reducing the density of recombination traps at a certain interface naturally translates into lower recombination rates at that very interface. This practice is commonly referred to as "chemical passivation" because it concerns interface trap states that are usually induced by dangling chemical bonds present at the contact surface. In our specific case, the objective is then to improve the "quality" of the CIGS/CdS interface or in other terms to ensure higher interfacial matching so as to reduce crystalline defects density at that interface. This can be achieved by inserting, at the problematic interface, a thin oxide layer resulting in a CIGS/Oxide/CdS configuration with lower interface trap

densities compared to the unpassivated CIGS/CdS interface. The different techniques to extract the value of N_{it} for a certain oxide layer are presented and described in section 2.7.3.2.

The new value of N_{it} after the addition of the oxide layer, which quantifies the effectiveness of the chemical passivation, depends on several parameters such as the interfacial matching between the oxide material and the semiconductors and the oxide deposition conditions. Consequently, our first criterion of eligibility for suitable dielectric materials is a density of interface traps N_{it} that is sufficiently low to reduce recombination losses in CIGS solar cells. In the literature related to standard crystalline Silicon and CIGS cells, there are some examples of typical dielectric materials used for passivation [16–20]: SiO_2, SiN, Al_2O_3, Ga_2O_3 and HfO_2.

2.4.2 Field-effect passivation

Next to decreasing the density of recombination centers at the interface, the second option considered here is to prevent charge carriers (n_s and p_s in equation 2.1) from approaching interfaces where recombination is likely to occur. As the final objective is to create a strong and unilateral electrical current through the whole structure, it is necessary that most carriers of the same charge are driven in the same direction, i.e. the electrons going upwards and the holes going downwards as explained in section 2.2.3. Actually, this is already taken care of by the electrical field present in the depletion zone of the CIGS/CdS interface but not sufficiently. Therefore, a certain amount of photogenerated holes present in the CIGS layer can circulate in the wrong direction, i.e. upwards, and recombine at the front interface (p_s in equation 2.1). Naturally, the same applies for electrons migrating downwards to the back interface (n_s in equation 2.1) as well as the small amount of free carriers photo-generated in the CdS layer for absorption spectrum enlargement. However, as the target of our study remains the passivation of the front interface, the reasoning developed in this section focuses on the former issue related to the recombination of holes at the CIGS/CdS interface.

In order to limit the concentration of holes p_s present at the front interface, the initial downward electrical field created by the p-n junction (blue arrow on figure 2.3) should be strengthened so that holes are further repelled from that interface. This can be done for instance by an additional charge distribution creating a supplementary electrical field that is aligned with the initial one. Actually, the oxide layer previously suggested for "chemical passivation" is conveniently also capable of solving this very issue. Indeed, some of the bulk defects intrinsically present in the dielectric materials are actually native fixed charges behaving differently from the interface traps discussed above [21]. If the sign of their charge is adequate, i.e. positive as shown on figure 2.5, these defects create an electrical field which is aligned with the built-in field from the depletion zone. The result is an improvement of the dissociation of e-h pairs and thus a higher electrical efficiency. In [21], it is said that the charged impurities present in the oxide are categorized as being either fixed charges Q_f, mobile ionic charges Q_m or oxide trapped charges Q_{ot}. However, it is usually admitted in the literature [13, 18, 19, 22] that only the fixed charges Q_f have a significant impact in CIGS field-effect passivation. Therefore, only this type of charges is considered in the rest of this report.

The defects naturally present in any oxide layer are usually distinguished by the the different physical flaws to which they correspond such as oxygen vacancies, aluminum

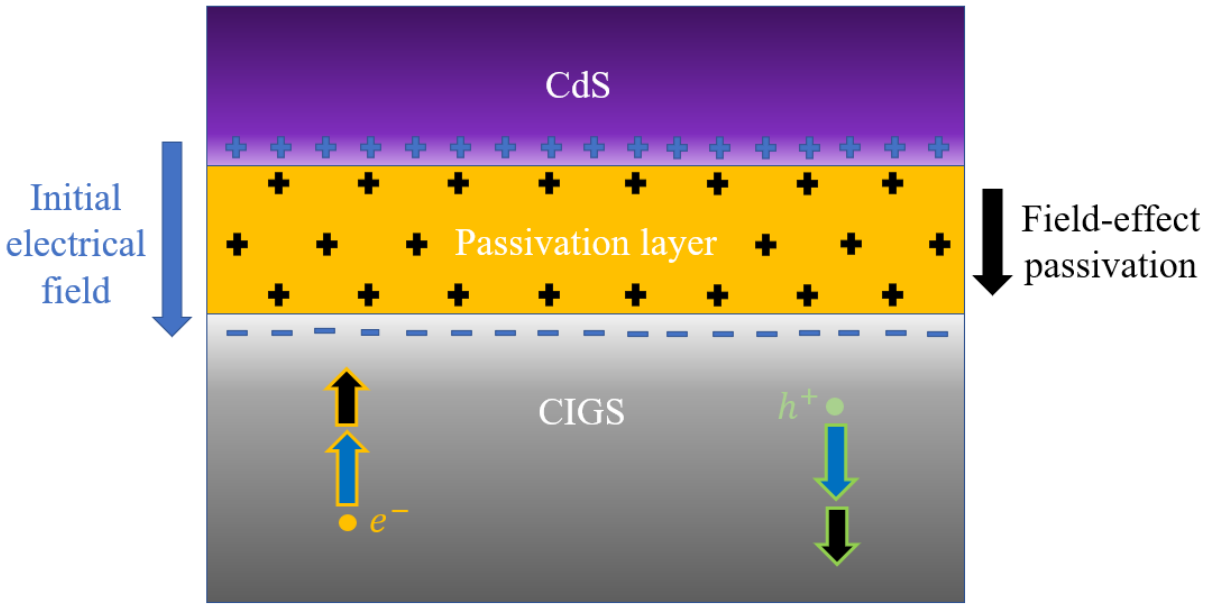

Figure 2.5: Schematic representation of the field-effect due to the fixed charges distribution in the passivation layer. The additional electrical field (in black) adds to the built-in electrical field from the depletion zone (in blue) which enhances the dissociation of photogenerated carriers.

interstitials or dangling bonds for the example of Al_2O_3 [23]. To a certain type of defects, the oxygen vacancy for example, corresponds a specific type (acceptor, donor or neutral), a specific volumic density in cm^{-3}, and specific energy levels spread across the band gap of the dielectric material, each of them with a corresponding charge state whose occupation depends on the Fermi level at the interface. For instance, it is calculated in [23] that the defects corresponding to Aluminum vacancies are of the acceptor type with 3 different energy level and charge states: the "0/-" state located 1.4eV above the VB, the "-/2-" state located 1.7eV above the VB and the "2-/3-" state located 2.6eV above the VB (the particular case of Al_2O_3 is thoroughly treated in section 4.2 with the help of numerical simulations). Naturally, we have also that the individual charge density $\rho_{f,i}$ linked to a certain type of defects i, Al vacancies for instance, is simply equal to the charge of every defect of this type multiplied by their density.

Therefore, it is possible to generalize our reasoning so as to express the total equivalent density of charges which is precisely the one charge distribution illustrated on figure 2.5. Indeed, our objective here is to study the total resulting field-effect passivation of the oxide layer rather than the individual contribution of each type of defects. Thus, the extensive knowledge of the individual energy positions and densities corresponding to every type of defects is not necessary. On the contrary, in the view of quantifying field-effect passivation and given the high complexity and variability of each type of defects, we can limit our study to the total fixed charges density ρ_f that is equal to the sum of the individual fixed charge densities $\rho_{f,i}$ corresponding to each type of defects. By extracting the value of ρ_f which is precisely one of the objectives of this work (section 2.7.3.1), it is possible to obtain the direction and the magnitude of the field-effect created by the inserted oxide layer. In the case of a Semiconductor/Oxide interface, the value and sign of ρ_f depends not only on the nature of the defects (acceptor, donor or neutral) and their charge valency

(single, double or multivalent) but also on the position of their energy level compared to the Fermi level of the semiconductor [23]. Other parameters related to the oxide deposition and possible post-annealing treatment as well as the CIGS crystalline orientation influence the value of ρ_f [13, 21]. On the contrary, the sign and magnitude of ρ_f are "not greatly affected by the oxide thickness or by the type or concentration of impurities" in the CIGS [21].

It is common practice in the characterization of field-effect passivation to assimilate the volumic fixed charges density ρ_f to a surface density Q_f instead, using two hypotheses. First, let x be the variable of vertical position along the oxide thickness such that $x = 0$ is the top surface of the oxide in contact with the front grid whereas $x = d$ is the CIGS/Oxide interface (d is the oxide thickness). Second, let $\rho_f(x)$ be the distribution along the oxide thickness of the volumic fixed charges density: single, uniform, linear, gaussian, etc, ... As detailed in [21], the total charge contained in $\rho_f(x)$ can be expressed as the total charge contained in a charge sheet with charge density Q_f and located at the CIGS/Oxide interface using the following formula:

$$Q_f = \frac{1}{d}\int_0^d x\rho(x)dx \ [cm^{-2}] \tag{2.2}$$

As mentioned in [21], equation 2.2 gives more importance to charged defects that are physically closer to the Semiconductor/Oxide interface given the inverse dependence of Coulomb interactions with distance. In the rest of this work, the characterization of field-effect passivation then resides in quantifying the Q_f resulting from the complex combination of the fixed charge densities induced by the various defects present in the oxide layer. In particular, it appears that the sign of Q_f is of great importance since it determines the direction of the resulting electrical field. In our case, it is visible on figure 2.5 that for the additional field (black arrow) to be aligned with the initial one (blue arrow), the sign of the fixed charges sheet Q_f located at the CIGS/Oxide interface should be positive (black positive sign symbols). This very point is the second criterion used to select well-adapted dielectric materials in the next section.

2.5 Selection of oxide materials for passivation

Al_2O_3-Alumina This metallic oxide is used as standard back passivation layer in the "passivated emitter and rear cells" (PERC) Silicon technology [16, 17] but also for back passivation of CIGS cells [5–13]. In most of these references, it is demonstrated that the good surface passivation properties of Alumina induce substantial improvements regarding the electrical aspect of energy conversion. These are due to low density of interface traps N_{it} and high negative density of fixed charges Q_f. However, as explained above, positive Q_f rather than negative is more appropriate regarding field-effect passivation of the front interface. This is one of the reasons justifying our investigation of alternative dielectric materials such as HfO_2 and TiO_2.
Nevertheless, it remains possible to improve and tune the passivation behaviour of alumina passivation layers for instance with post-deposition annealing as described in [13]. Using SCAPS simulation on alumina passivation layer, it is demonstrated in this reference that Q_f becomes negative after annealing, whereas it remains positive without annealing. Chemical passivation is naturally active before post-annealing but the density of interface traps N_{it} becomes lower after the high-temperature treatment which is an improvement. In the case of front interface passivation, there is a trade-off appearing between the improvement and

degradation of respectively chemical and field-effect passivation after post-annealing due to lower N_{it} and sign inversion of Q_f. This leaves place for optimization and resonates with the previously defined objectives (section 1.3) about post-annealing investigation.

HfO_2-Hafnia As it is the case for alumina, hafnia has been investigated for back and/or front interface passivation in both PERC Silicon [24, 25] and CIGS cells [10, 19, 20]. However, the efficiency of hafnia layers for CIGS chemical passivation and more precisely the resulting N_{it} and Q_f are not as referenced as for alumina, which further motivates our study. It is shown in [24, 25] that the properties of hafnia as passivation layer for Silicon solar cells depend on processing, cleaning and post-deposition conditions. In particular, the fixed charges density Q_f can either be positive or negative depending on these parameters which explains the use of hafnia for respectively front and back interface passivation. Our objective here is to contribute to the investigations on the usage of hafnia for the passivation of the CIGS/CdS interface by providing reliable data about its passivation properties (N_{it} and Q_f) and the parameters influencing them (post-annealing, surface cleaning, ...).

TiO_2-Titania Titanium dioxide is widely used as an electron-selective layer for thin-film PV technologies such as dye-sensitized and Perovskites [26], but also thin-film Silicon solar cells [27]. Titanium dioxide has already been experimented as rear passivation layer in CIGS cells [28]. Given that its utilization as front passivation layer for CIGS cells is nearly not documented, it is both interesting and innovative to investigate this material. Moreover, the electronic selectivity of TiO_2 could greatly contribute to the passivation effect at the CIGS/CdS interface since it should theoretically repel the holes and thus mitigate recombination. For that to happen, the VB edge offset should be high and the CB edge offset low so that holes are blocked but electrons are let through. Thus, specific considerations about the narrower bandgap of titania but also its possible n-type electronic conductivity [29] compared to alumina and hafnia should be taken into account [30].

2.6 State-of-the-art front-passivated CIGS solar cell

The whole discussion presented above eventually leads to our target design of a front-passivated CIGS solar cell, depicted on figure 2.6. Before describing the different layers, some complementary information and remarks require to be mentioned. First of all, $CuIn_xGa_{1-x}Se_2$ or CIGS is a quaternary p-type semiconductor compound with chalcopyrite crystalline structure [31]. Its direct band-gap, tunable between 1 and 1.7eV (mostly visible light) by varying the elemental composition, and its high optical absorption coefficient make it well suited to PV applications [26, 31]. As mentioned above, the typical n-type buffer layer used in the CIGS technology is Cadmium Sulfide, separated from the CIGS by the now familiar oxide passivation layer, which constitutes the only significant variation between figures 1.3 and 2.6.

All the samples analyzed in this report actually consist in MIS structures (section 2.7) whose dimensions and structure, presented in chapter 3, are thus deeply different from the design on figure 2.6. The purpose of this study is to suggest efficiency improvements of the targeted theoretical solar cell design through the analysis of measurements realized on MIS structures, a keystone in the investigation of surface passivation effects.

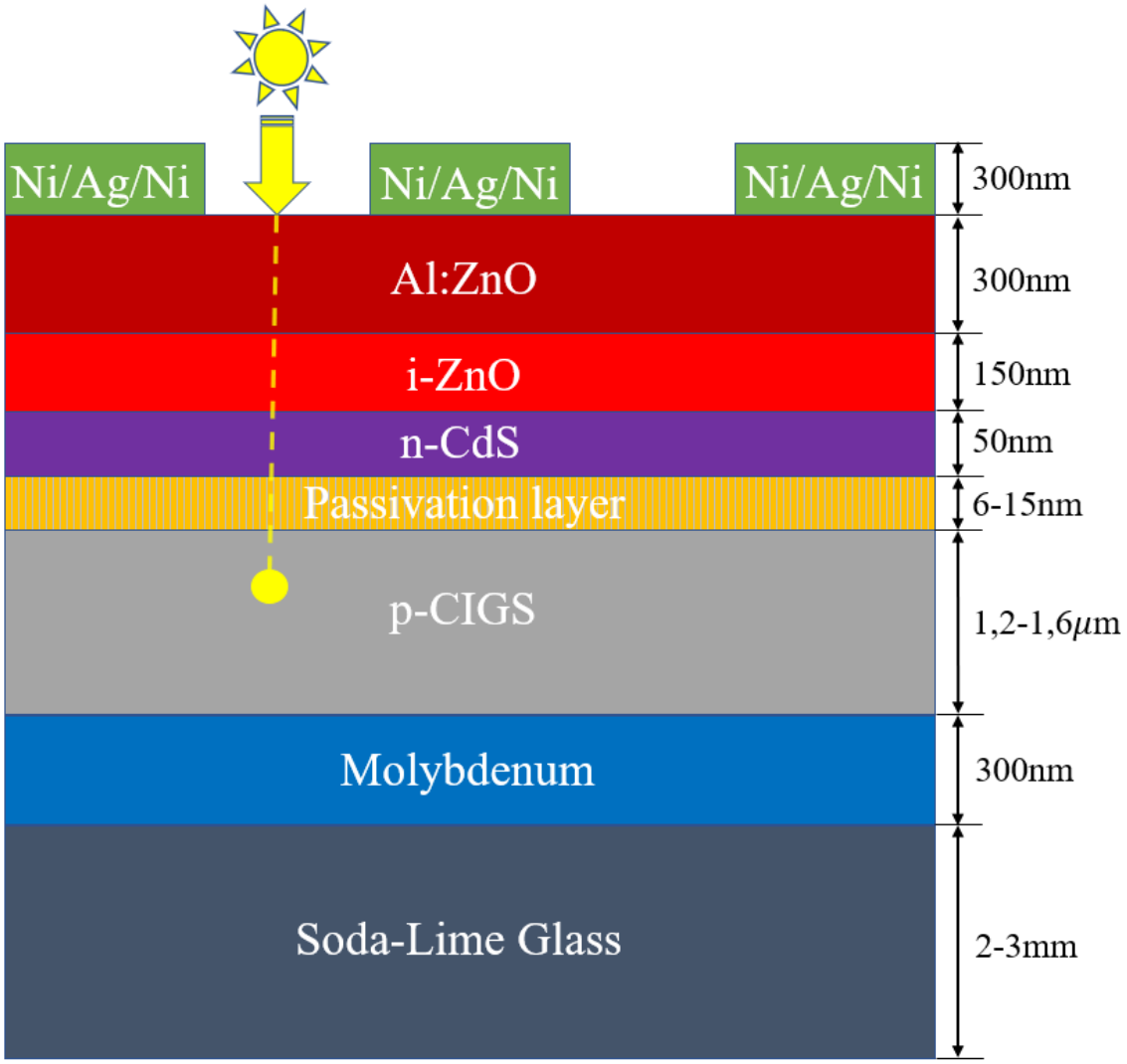

Figure 2.6: Theoretical state-of-the-art CIGS solar cell targeted in this work. The front passivation layer presents nano-openings (gray vertical lines) to allow contacting between the CIGS and CdS layer. The layer thicknesses are typical expected values (not to scale for a matter of clarity). The external circuit is omitted and not considered in this work.

2.6.1 Unpassivated design

Let us briefly review, from top to bottom, the standard layers presented on figure 2.6 without firstly considering the front passivation layer. The references used in this section are [26, 31]. It is worth mentioning that external connections of the solar cell to the eventual load are neither shown or considered in this section. At the very top of figure 2.6, the 300nm-thick Ni/Ag/Ni front grid ensures ohmic contact between the solar cell and the implicit external circuit. Below the top contact lies the sputtered Zinc Oxide window layer, divided in two sub-layers of Al-doped ZnO (Al:ZnO) and undoped ZnO (i-ZnO). The Al-doped ZnO layer guarantees good contacting and charge collection between the underlying CdS and the top grid while the intrinsic ZnO protects the former from processing damages. Also called Transparent Conducting Oxide (TCO), the window layer should let most of the incident light travel towards the p-n junction while allowing electrons to flow in the inverse direction, i.e. upwards to be collected at the front metal grid.

The central part of the cell is the hetero p-n junction made of 3-stage co-evaporated CIGS and CdS processed by Chemical Bath Deposition (CBD). We know from section 2.2.2 that even though the main absorber is the CIGS layer, CdS is also semiconductor and can therefore create e-h pairs after absorbing light. The specific part of the light spectrum absorbed by each material obviously depends on their band gap, which is typically $1.15eV$ (visible light and near infrared) for standard CIGS and $2.4eV$ (visible light) for CdS. Underneath, the 300nm-thick sputtered Molybdenum back contact simultaneously reflects the unabsorbed light back to the CIGS and takes care of holes collection towards the external circuit. The whole cell is typically deposited on a really thick Soda-Lime Glass substrate which has certified efficiency assets due to Sodium diffusion during deposition process.

2.6.2 Passivation layer

Each oxide layer studied in this report is deposited using thermal Atomic Layer Deposition (ALD) and made of either Al_2O_3, HfO_2, a superposition of Al_2O_3 and HfO_2, or TiO_2. Concerning alumina and hafnia, their wide bandgap (above 6eV [30, 32]) makes them nearly transparent to light whereas the narrower bandgap and lower CB offset of TiO_2 [30] might raise some questions about parasitic light absorption and conduction (see section 4.8). For the MIS samples, the oxide thicknesses processed (20nm to 100nm) are higher than for the hypothetical complete solar cells (6-15nm) to guarantee well-behaved MIS capacitors with the lowest leakage currents possible. Indeed, no charge should ideally flow through the MIS structure with such oxide thicknesses (section 4.3.4 of [21]). However, in practice, parasitic transport phenomena inevitably appear and may degrade the accuracy with which our samples are characterized. This is verified and discussed in Chapters 3 and 4, namely using I-V measurements.

In the case of complete solar cells, current has to flow through the whole structure so as to produce power. Since metal oxides basically are dielectric materials with extremely poor electrical conductivity properties, it makes sense to wonder how charge carrier transport through the passivation layer is taken care of on figure 2.6. The solution adopted for our final design is the "point nano-openings" approach. This strategy has become more and more popular in the Silicon technology and started being investigated for CIGS cells as well [5, 9, 11, 20, 28, 33]. It consists in scribing a pattern of transverse holes through the thickness of the passivation oxide so as to let the carriers through (gray lines through the oxide thickness on figure 2.6). Therefore, in the rest of this report, carrier transport issues in solar cells are thus considered as solved by the nano-openings design. Although the actual realization of nano-openings through the oxide layer is not treated in this study since our samples consist in MIS structures, reflections about the compatibility of the different materials with potential nano-openings are made in chapter 4.

2.7 Characterization of CIGS/Oxide interface

2.7.1 MIS structure

The MIS structure (figure 2.7), also called MIS capacitor, is the very basis to characterize the behaviour of semiconductor surfaces [21], mainly by performing Capacitance-Voltage (C-V) measurements. Our objective here is to study the surface passivation effects due to the addition of a certain oxide layer, either Al_2O_3, HfO_2 or TiO_2 (no openings considered in this case), at the interface with a p-type semiconductor, i.e. CIGS. Therefore, the MIS configuration and the C-V measurements are the two basic analysis tools used throughout this work, with one exception. Indeed, the optical characterization experiment called Photoluminescence (PL) measurement, realized on a simple CIGS/Oxide structure in our case (no grid compared to the MIS structure), is very helpful to qualitatively evaluate passivation effects, as introduced below in section 2.7.4.

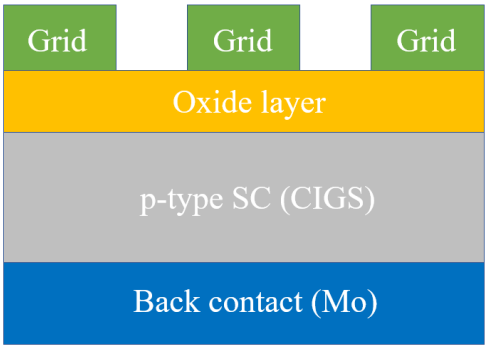

Figure 2.7: Typical MIS structure with p-type SC (arbitrary scale).

Nevertheless, the analysis of C-V measurements performed on MIS structures remains the most important part of our study. In particular, the two key parameters presented above, namely the density of interface levels (D_{it} in $cm^{-2}eV^{-1}$) as well as the surface density of fixed charges (Q_f in cm^{-2}), can both be extracted from C-V measurements realized on MIS structures as it is discussed in the rest of this section. The density of interface levels D_{it} in $cm^{-2}eV^{-1}$ is related to the density of interface traps N_{it} in cm^{-2} by the characteristic energy E_{char} in eV such that $D_{it} = N_{it}/E_{char}$. E_{char} is the width of the energy distribution of the interface levels around the central energy level E_{st} as in equation 2.1. In the following, the typical C-V curves and behaviour of an ideal p-type MIS structure without any defects are firstly presented in section 2.7.2. After that, section 2.7.3 discusses the expected influence of non-zero defects densities D_{it} and Q_f as well as different methods to use for extracting their actual values. The utilization of PL measurements in the characterization of passivation effects is then described in section 2.7.4.

2.7.2 Ideal Capacitance-Voltage (C-V) measurements

2.7.2.1 Overview

The main type of measurement to perform on MIS capacitors consists in measuring the capacitance and conductance for varying voltage bias and frequency (left of figure 2.8). The voltage signal is composed of a varying DC bias V relative to the ground (black triangle) on which an AC small-signal of fixed-amplitude and variable frequency f (or angular frequency ω) is superimposed. As it is the case in the rest of this report, these measurements are usually designated as C-V measurements even though the conductance is also measured and the frequency is varying. In our case, the exact quantity being measured is the parallel admittance which decomposes into a capacitive component C_p and a conductive component G_p (right of figure 2.8). These experiments are essential to quantify passivation effects since the extraction of the two important passivation figures of

merit, i.e. D_{it} and Q_f, greatly relies on the evolution curves of C_p and G_p with voltage and/or frequency. In the rest of this report, the 2D graphs depicting the evolution of either C_p or G_p with regards to voltage and frequency at the same time are designated as "2D maps". Before considering the impact of D_{it} and Q_f, let us first focus on the ideal case where no substantial amounts of defects are present either in the bulk of the oxide or at the interface with the semiconductor, i.e. D_{it} and Q_f are negligible.

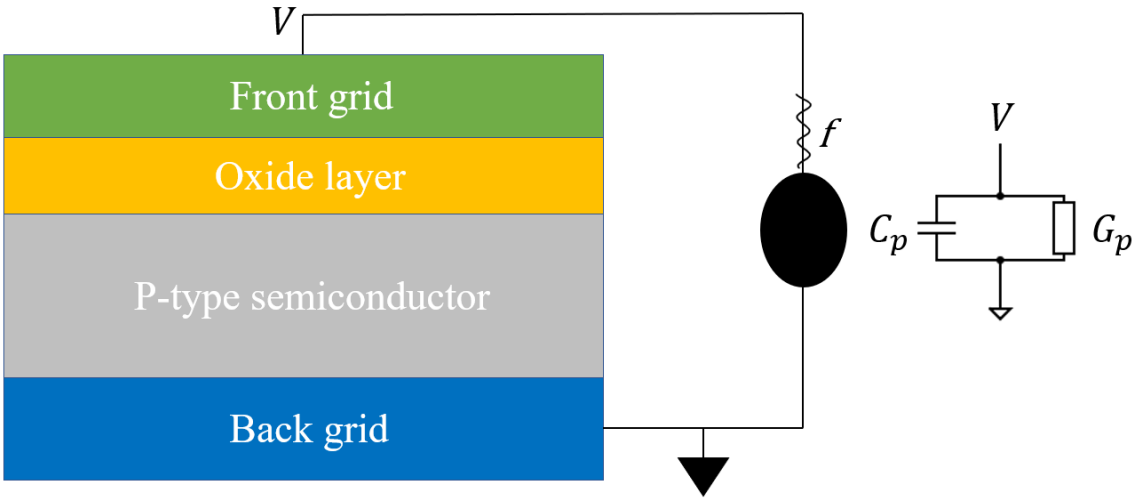

Figure 2.8: Typical configuration and equivalent circuit of C-V measurements performed on p-type MIS capacitor. Parallel conductance G_p and capacitance C_p are measured at varying DC bias V with a superimposed AC small-signal of frequency f.

2.7.2.2 Voltage regimes

Most of this section is greatly inspired from section 4.2 in [21]. As we know from the band bending theory [21], the difference of Fermi level E_F between a metal and a semiconductor separated by an oxide, i.e. inside a MIS capacitor, is theoretically equal to the voltage V applied to the whole structure. Thus, if no voltage is applied ($V = 0$), the MIS structure is at equilibrium and the Fermi levels of the metal grid and the semiconductor are aligned (figure 2.9). This situation is called "flat-band" and the corresponding voltage, different from zero in realistic structures, is called "flat-band voltage" and noted V_{fb}. During C-V measurements, while the applied bias is varying from negative towards positive bias, the evolution of the total measured capacitance indicates how the different charged elements present in the MIS capacitor react to the varying DC voltage carrying an AC small-signal. Without any charge transport through the oxide, E_F does not follow band bending and stays constant even when voltage is applied [21].

In particular, the band bending theory states that by varying the DC voltage applied to the structure, the alignment of the Fermi levels changes likewise [21]. For instance, if the sign of the DC bias inverts, the direction of band bending (either upwards or downwards) inverts accordingly, depending on the type of semiconductor. CIGS being of the p-type, only this type of semiconductors is treated in the following. On figure 2.9, E_g is the semiconductor bandgap, E_i is the midgap energy, χ and χ_i are the electron affinities of respectively the semiconductor and the dielectric, and ϕ_m is the work-function of the grid metal.

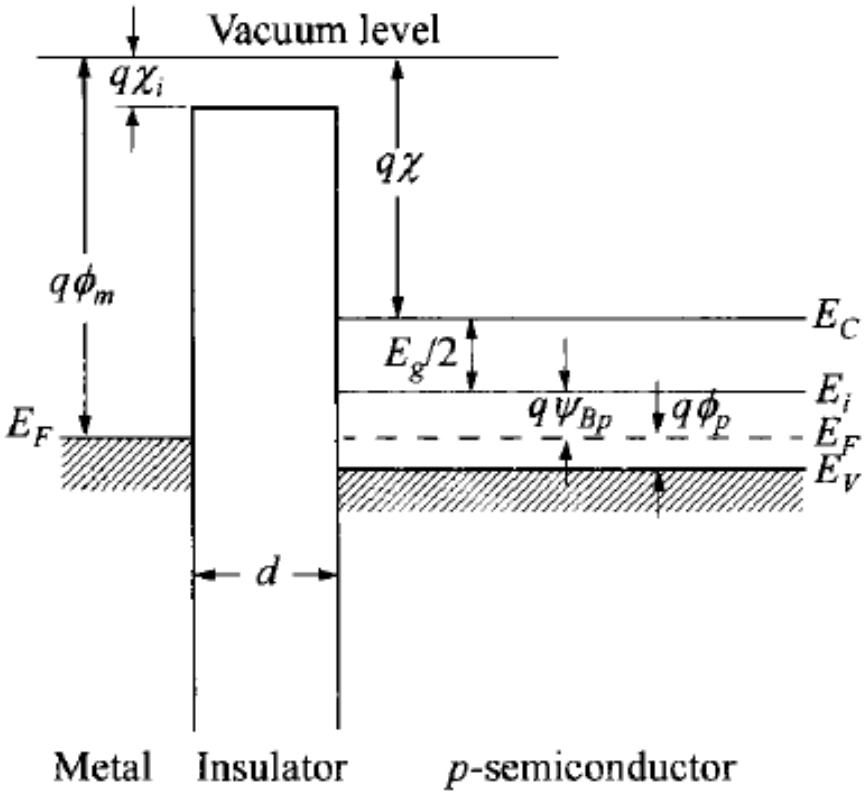

Figure 2.9: Energy bands diagram at equilibrium ($V = 0$), also called "flat-band" situation, for a p-type semiconductor at the interface with an oxide layer of thickness d. Taken from [21].

If the applied voltage is negative, then the energy bands of the semiconductor bend upwards as the Fermi level of the semiconductor attempts to align with the one of the metal grid (top left of figure 2.10). In terms of charge distribution, applying a negative bias at the grid has the effect of attracting more holes at the bottom interface of the oxide (bottom left of figure 2.10). As the SC is of the p-type, holes are majority carriers and thus an "accumulation" layer is formed below the oxide. The measured capacitance in the so-called "accumulation" bias regime only consists in the geometrical capacitance of the dielectric layer (left part of the curve from figure 2.11). Indeed, electrons being stacked at the top oxide surface and the accumulation holes being stacked at the bottom surface, we have $C_p = C_{ox} = \frac{\epsilon_{ox}}{t_{ox}}$ in F/m^2 where C_{ox} is the oxide capacitance (named C_i on figure 2.11), ϵ_{ox} and t_{ox} respectively are the dielectric constant and thickness of the oxide.

As the bias increases above 0V but remains close to the flat-band situation, the band bending direction inverts and holes are repelled from the bottom surface of the oxide by the positive charges stacked at the top surface of the oxide (left of figure 2.10). Consequently, the concentration of electrons starts to become comparable to the concentration of holes in the region below the semiconductor/oxide interface, then becoming progressively "depleted" in holes as for the p-n junction in section 2.2. This bias regime is then logically referred to as "depletion regime" (middle of figures 2.10 and 2.11) The total capacitance, now composed of C_{ox} connected in series to the smaller depletion capacitance C_D related to the carrier-depleted region below the oxide, decreases as on figure 2.11.

If the bias keeps on progressing towards positive values, the concentration of electrons stacked below the oxide starts to surpass the concentration of holes which thus become minority carriers. The so-called "weak inversion regime" on figure 2.11 sees the depleted region getting thicker and eventually the total capacitance diminishing. Higher gate voltages bring the structure into the "strong inversion regime" (right part of figures 2.10 and 2.11) in which the previously depleted region becomes n-type semiconductive due to the dense layer of electrons stacked below the semiconductor/oxide interface. At low frequency, this leads to C_D disappearing from the equivalent circuit and the total capacitance returning to its maximum value C_{ox}. At higher AC frequencies, some electrons of the inversion layer are not able to follow the fast variations of the voltage small-signal and therefore contribute to a further increase of the depletion capacitance C_D. Subsequently, the total capacitance on figure 2.11 evolves to lower and lower values than C_i as the frequency increases. In each of the bias regime mentioned, the parallel conductance remains low since the charge transport through the oxide layer is considered negligible as already discussed above. Let us now investigate, based on section 4.3 from [21], the more realistic situation in which defects are influencing the voltage-frequency behaviour of the equivalent parallel capacitance and conductance.

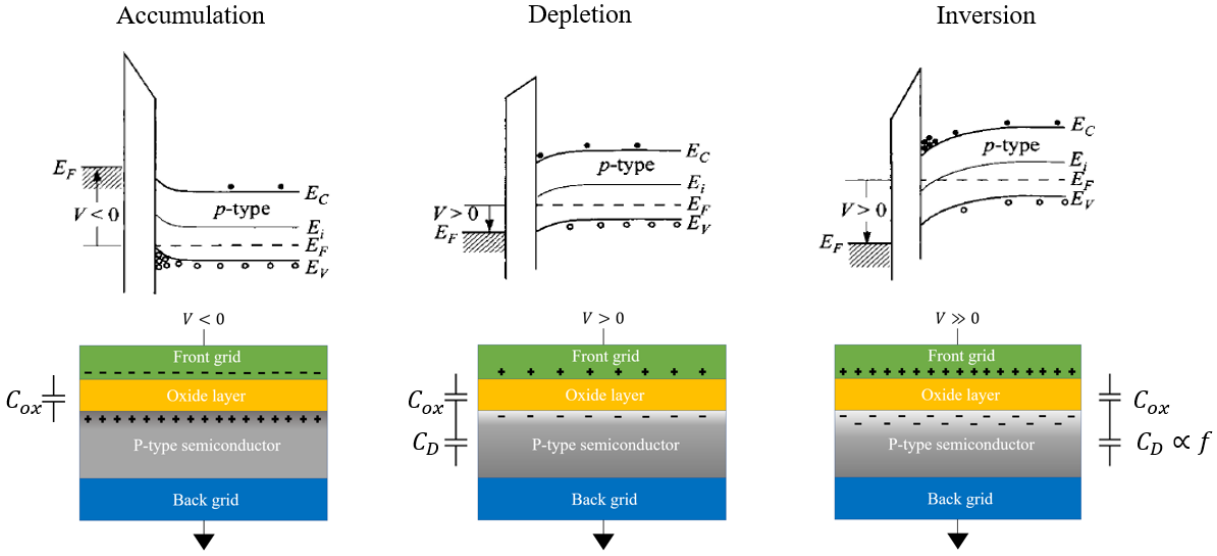

Figure 2.10: Band-bending diagram with the different bias regimes (from left to right): accumulation, depletion and strong inversion. The MIS structure is considered ideal without any defects apart from the p-type dopants. C_{ox} and C_D are respectively the oxide capacitance and the depletion capacitance. Upper figure taken from [21].

2.7.3 Influence of defects

Most of this section is greatly inspired from section 4.3 in [21]. The actual measurements obtained on realistic samples present several differences compared to the theoretical curves just presented, namely because of the defects present at the Semiconductor/Oxide interface and inside the bulk of the oxide. In particular, as introduced above in this chapter, the objective of this study is to focus on the recombination rate reduction due to the insertion of an oxide passivation layer. The physical explanation for this improvement is two-fold: on the one hand, suitable dielectric layers exhibit lower density of interface traps D_{it} than

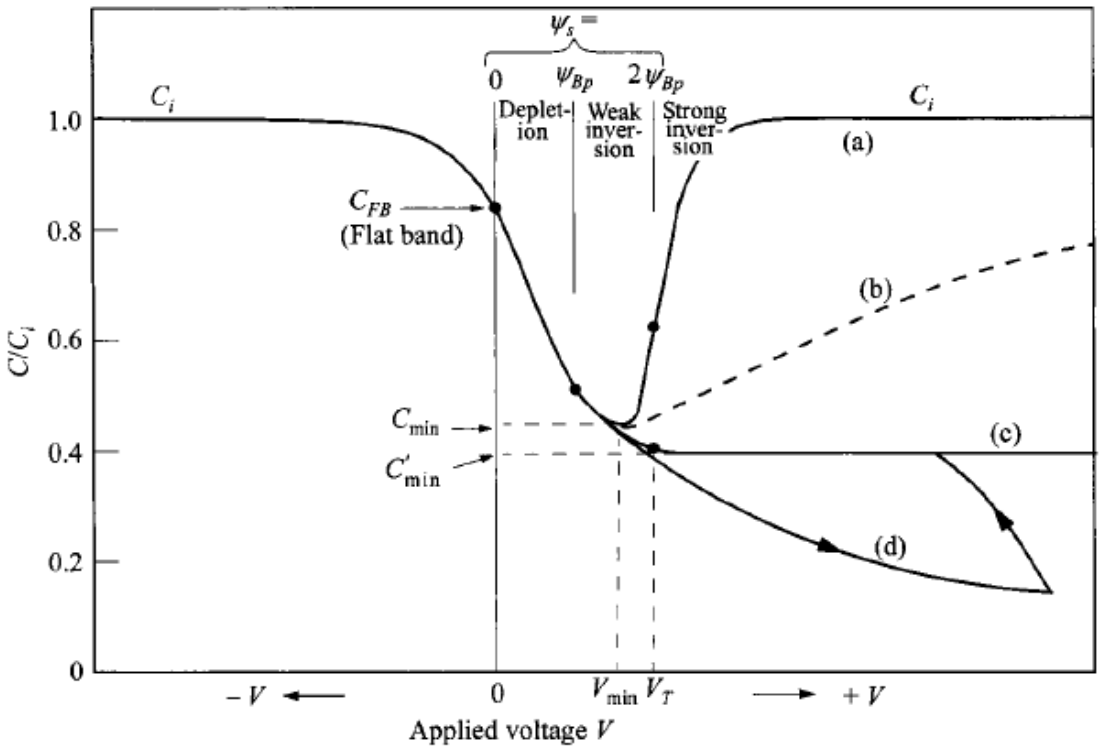

Figure 2.11: Ideal normalized C-V curves of a p-type Silicon MIS capacitor. (a) Low frequency. (b) Intermediate frequency. (c) High frequency. (d) High frequency with fast sweep (deep depletion). Taken from [21].

the initial CIGS/CdS interface; on the other hand, the density of fixed charged defects Q_f present in the bulk of the oxide induce an electrical field-effect which, if the equivalent charge has the right sign, repels undesired carriers from the concerned recombinative interface. In our case, it has been demonstrated in section 2.4 that the sign of this surface charge sheet Q_f should be positive so as to push back the holes away from the CIGS/CdS interface. Based on the physical explanations provided in [15, 21, 34], this section successively presents and discusses not only the theoretical influence of these two type of defects on the ideal C-V measurements presented above, but also several extraction techniques designed to quantify the value of the two key parameters Q_f and D_{it}.

2.7.3.1 Density of fixed charges - Q_f

As discussed above in section 2.4, the volumic density of fixed charged defects present in the bulk of a dielectric layer can be assimilated to a charge sheet present at the bottom surface of the oxide layer using equation 2.2. It appears then necessary to be able to quantify the magnitude and sign of this surface charge density Q_f so as to assess the strength and direction of the resulting field-effect for a specific sample. To do so, the strategy presented in [21] takes advantage of the consequence that this charge sheet has on the C-V curves of the concerned sample. Indeed, at a given work function for the metal grid, the electrostatic potential related to Q_f results in a horizontal voltage shift of the C-V curves compared to the ideal case with no defects and $V_{fb} = 0V$. It can be seen on figure 2.12 from [21] that this shift is leftwards in the case of positive charges, and rightwards for negative charges.

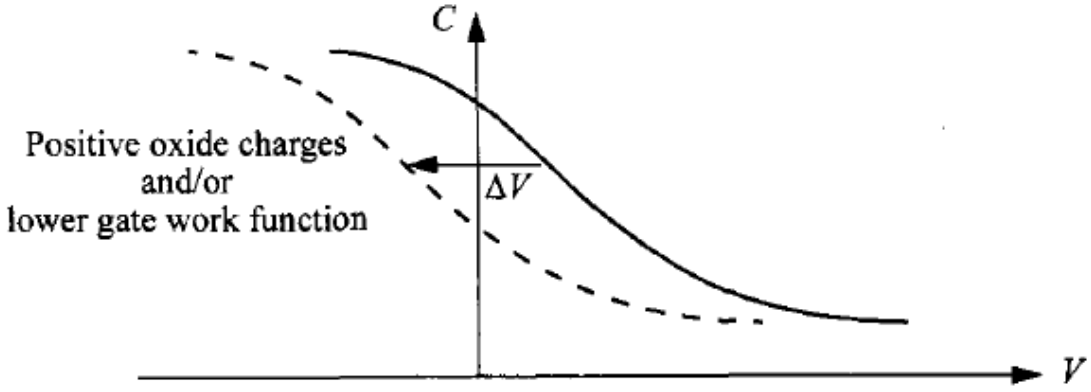

Figure 2.12: Voltage shift of the C-V curves for a p-type semiconductor, due to positive fixed charges at fixed gate work function, taken from [21]. The voltage shift ΔV_f is in the inverse direction, i.e. rightwards, for negative fixed charges.

An intuitive explanation for that can be found in [21] too: "Positive charge is equivalent to an added positive gate bias for the semiconductor so it requires a more negative gate bias to achieve the same original semiconductor band bending". Using Gauss' law as in [21], the voltage shift ΔV_f due to fixed charges in the bulk of the oxide can be related to the surface density Q_f of these charges:

$$\Delta V_f = \frac{-q * Q_f}{C_{ox}} \ [V] \tag{2.3}$$

in which C_{ox} is the geometrical oxide capacitance in F/cm^2 and q is the elementary charge such that $-q * Q_f$ is the amount of charges per unit area in C/cm^2. Since the voltage offset due to the oxide bulk fixed charges is purely horizontal, its value ΔV_f should then be equal to the new value of the flat-band voltage V_{fb} if it is considered that no other effect has induced an additional shift in bias. However, as mentioned in [21], the difference between the work function of the metal grid and the Fermi level of the semiconductor, denoted ϕ_{ms} and expressed in eV, is rarely equal to 0. The resulting built-in potential also creates a shift in voltage, denoted $V_{ms} = \phi_{ms}/q$ and expressed in V, which should then be taken into account in the expression of V_{fb}. Moreover, the charge state of the interface defects also play a role in the intrinsic potential present in the structure. Nevertheless, it is not taken into account in our study given the difficulty of assessing the exact energy level and charge state of the different interface traps. Eventually, we obtain the expression of the new value of the flat-band voltage V_{fb} due not only to the effect of fixed charges in the oxide but also to the built-in potential difference V_{ms} present in the MIS structure [21]:

$$V_{fb} = \Delta V_f + \frac{\phi_{ms}}{q} = \frac{-q * Q_f}{C_{ox}} + V_{ms} \ [V] \tag{2.4}$$

in which $\phi_{ms} = \phi_m - (\chi_{SC} + \frac{E_g}{2} + \frac{kT}{q} ln(\frac{N_a}{n_i}))$ with ϕ_m the work-function of the metal grid, χ_{SC} and E_g respectively the electronic affinity and band gap of the p-type semiconductor, N_A the density of shallow acceptor dopants and n_i the intrinsic density of carriers in the semiconductor, and kT/q the thermal energy. This equation can be rewritten in order to

express Q_f, i.e. our unknown, in terms of constants (ϕ_{ms}, C_{ox}, ...) and V_{fb}:

$$Q_f = C_{ox}\Big(\frac{V_{ms} - V_{fb}}{q}\Big)\ [cm^{-2}] \tag{2.5}$$

in which V_{fb} can be deduced from C-V measurements by identifying the bias point at which the net charge in the MIS capacitor is zero, located in the transition zone between the accumulation and the depletion regime. In [35], the simplest suggested solution is to first draw the evolution of $(\frac{C_{ox}}{C_m})^2 - 1$ with voltage. After that, the idea is to identify a linear part on that curve and extrapolate the intersection of the implicit tangent with the horizontal axis. The value of the V_{fb} is then precisely the bias position of that intersection (real example in chapter 4). Eventually, it becomes possible to compute the magnitude and sign of Q_f, which is precisely the objective of this section. However, the actual value of some of the parameters mentioned in this section are usually comprised within relatively large numerical ranges rather than undoubtedly equal to an accurate figure. This is discussed in details below in section 4.3.3.

2.7.3.2 Density of interface traps - D_{it}

Since the physical mechanisms behind chemical and field-effect passivations are quite different, the extraction techniques used to estimate D_{it} greatly differ from the one related to Q_f. Estimating the density of interface traps relies not only on the evolution of parallel capacitance C_p with voltage such as for Q_f but also on the parallel conductance G_p and the frequency dependence of both C_p and G_p. Indeed, trap states at the semiconductor/oxide interface behave differently than oxide bulk defects in terms of bias and frequency dependence because they are able, among others, to quickly "exchange charges" with the semiconductor [21]. Therefore, the occupation state of these interface states depends on the Fermi level at the interface and consequently of the applied voltage through energy band bending. The model presented in [21] is commonly used to study the behaviour of interface states through an equivalent interface traps distribution D_{it} with a neutral energy level E_0 determining the charge state of the traps by their relative energy position compared to the interface Fermi level. As explained in [21], if one varies the applied bias, the band bending is modified accordingly and the charge state of the interface traps fluctuates, eventually changing the value of the total capacitance. In particular, some of the charges normally used to reach a certain bend bending are charge-feeding the interface traps instead, which reduces the actual band bending obtained for a certain applied bias, causing an horizontal stretch out [21] of the C-V curves (figure 2.14).

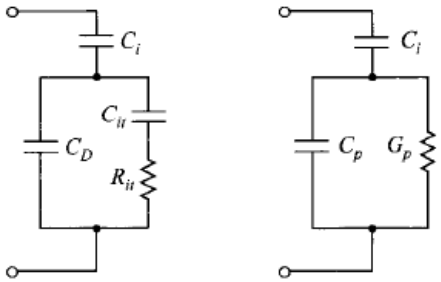

Figure 2.13: Left: Equivalent circuit with the interface traps circuit elements. Right: Equivalent circuit with frequency dependent parallel capacitance and conductance. Taken from [21].

Since interface traps have an influence on the total capacitance, it is possible as in [21] to represent their effect through supplementary equivalent circuit elements, i.e. a capacitance C_{it} and the associated series resistance R_{it} both "functions of energy" [21], in the basic dielectric-depletion capacitance equivalent circuit of figure 2.13. C_i is the geometrical capacitance of the dielectric layer (referred to as C_{ox} above) and C_D remains

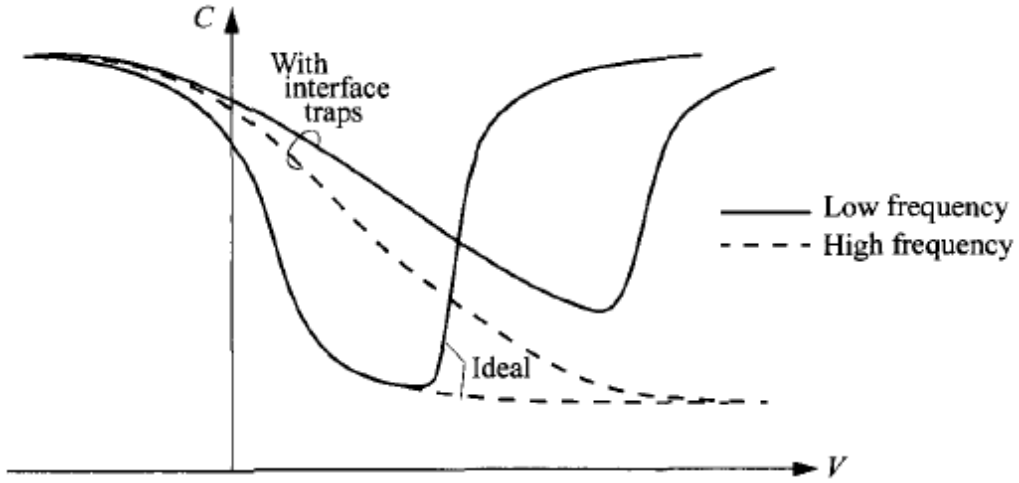

Figure 2.14: Influence of interface defects on the C-V curves for a p-type semiconductor at high and low frequency, taken from [21].

the depletion capacitance. The two equivalent circuits from figure 2.13 suggest that the data obtained by measuring the parallel conductance and capacitance at different voltages and frequencies enables to estimate the density of interface traps D_{it} through the circuit elements C_{it} and R_{it}. Moreover, it appears clear that the frequency response of these interface states is governed by the time constant $\tau_{it} = C_{it}R_{it}$ of the series RC network to which they are assimilated [21]. In order to simplify the matching between equivalent circuit and measured parallel elements as in [21], the equivalent circuit on the left-hand side of figure 2.13 can be translated into the circuit on the right of figure 2.13. In particular, there is one mathematical relation given in [21] which links G_p to R_{it} and C_{it}. It is one of the key elements to extract D_{it} from C_p and G_p measurements at various bias and frequencies:

$$\frac{G_p}{\omega} = \frac{C_{it}\omega\tau_{it}}{1+\omega^2\tau_{it}^2} \; [F/cm^2] \tag{2.6}$$

in which ω is the angular frequency of the AC excitation in rad/s and $\tau_{it} = C_{it}R_{it}$ is the "interface-trap lifetime" [21]. The two next sections discuss two different analysis procedures designed for the extraction of D_{it}, one based on the conductance data and the other one based on the capacitance data. At this point, two remarks are made in [21] about the density of interface traps: first, D_{it} is actually the density of interface levels that takes into account the energy distribution of trap states along the interface; second, the extraction techniques in the two next paragraphs allow to estimate D_{it} but not to determine the type of the corresponding interface defects.

Conductance method This method is based on the fact that, at a certain fixed bias, the curve drawn by the evolution of G_p/ω from equation 2.6 with respect to ω should reach a peak at a frequency $\omega_0 = 1/\tau_{it}$ and the height of this peak is equal to $C_{it}/2$ [21]. Therefore, measuring the parallel conductance G_p over a typical range of frequencies, i.e. usually between 1kHz and 1MHz, allows for an estimation of the density of interface traps D_{it} as it is described in details in [34]. Although many supplementary corrections and hypotheses can be considered for reaching an extremely accurate extraction, it is common practice in the field to use a simplified and straightforward expression of D_{it} that is derived

from the development in [34]:

$$D_{it} = \frac{\left(\frac{G_p}{A\omega}\right)_{max}}{f_D(\sigma_s) * q} \; [cm^{-2}eV^{-1}] \tag{2.7}$$

in which $f_D(\sigma_s)$ is the dimensionless correction factor related to the width σ_s of the conductance peak due to band bending [34], $\left(\frac{G_p}{A\omega}\right)_{max}$ is the height of the peak observed at $\omega_0 = 1/\tau_{it}$ on the G_p/ω vs. ω curve, normalized by the device area A and expressed in F/cm^2, and q is the elementary charge. Generally speaking, the conductance peaks related to interface traps appear in the depletion and weak inversion voltage regimes [34], as further discussed in chapter 4.

High-Low Frequency Capacitance method Contrarily to the conductance method, this extraction technique rather relies on the value of the parallel capacitance C_p. Although theoretically less accurate than the previous method according to [34], the High-Low Frequency (HLF) technique reveals useful in our case for multiple reasons. First, it is the simplest of the three capacitance-based extraction techniques presented in [34] because it does not require any computation of theoretical C-V curves. Second, it relies on the capacitance data which, in our case, are more reliable due to a specific issue described in section 3.3. Third, it serves as a point of comparison with the conductance method in chapter 4.

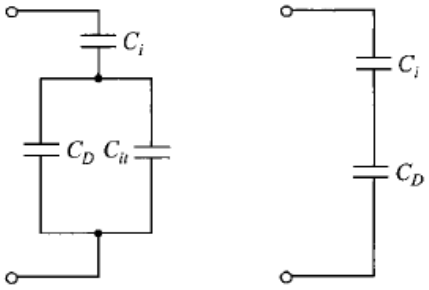

Figure 2.15: Equivalent circuit with R_{it} omitted. Left: Low frequency limit. Right: High frequency limit. Taken from [21].

The HLF method itself consists in comparing the value of the measured parallel capacitance C_p at high and low frequency so as to isolate C_{it} in the equivalent circuit as on figure 2.15: at low frequency, the capacitive part of the interface trap impedance dominates and R_{it} can be neglected; at high frequency, the $R_{it} - C_{it}$ network is not present anymore because interface traps are not able to follow such fast voltage variations [21]. Since the only difference between the two circuits of figure 2.15 is C_{it}, it is possible to express C_{it} and thus also D_{it} in terms of the capacitance measured at high and low frequency, i.e. C_{HF} and C_{LF}, and of the difference between these two values $\Delta C = C_{LF} - C_{HF}$ as demonstrated in [21]:

$$D_{it} = \frac{\Delta C}{q^2}\Big(1 - \frac{C_{HF} + \Delta C}{C_i}\Big)^{-1}\Big(1 - \frac{C_{HF}}{C_i}\Big)^{-1} \; [cm^{-2}eV^{-1}] \tag{2.8}$$

This expression enables, based only on two C-V curves at two different frequencies, to estimate D_{it} over the whole range of voltages at which C_p is measured.

Bandgap scanning The two methods presented above provide a value of D_{it} that depends on the applied bias, which makes sense given that interface states are usually spread all over the interface bandgap [21]. In particular, it is experimentally demonstrated in [21] that the time constant τ_{it} related to interface traps depends exponentially on the energy through the surface potential, an image of the applied bias and corresponding band bending. Therefore, it is possible, by varying the applied voltage, to "scan" the interface states present in the bandgap. In particular, the energy term present in the exponential

of τ_{it} is related to the energy difference between the band edge and the energy of the concerned interface trap. In other terms, depending on the bias that is applied to the MIS capacitor, either deeper of shallower interface states are scanned. This is illustrated on figure 2.16 from [21] which represents the logarithmic evolution of τ_{it} in function of the surface potential and thus the applied voltage.

This actually highlights the interest of using the MIS structure to characterize interface defects. Compared to the complete solar cell structure in which the Fermi level is imposed by the p-n junction equilibrium, the p-type MIS capacitor enables a thorough scanning of the interface states in a wider energy range around the Fermi level. However, with a p-type semiconductor, it is in practice only possible to scan the lower half of the bandgap where the Fermi level is located [21] since realistic voltage and frequency ranges do not allow to scan bandgap regions that are too far away from E_F. The solution for characterizing the other half of the CIGS bandgap would then be to do the same analysis on the n-type counterpart of CIGS (figure 2.16) but it seems complicated to do in practice.

The graph on figure 2.16 shows that, for the case of a Si-SiO_2 MIS structure, the lifetime of interface states is higher at midgap than at the VB edge. The same trend is expected for our samples with CIGS and the concerned dielectric materials. It is also important to mention that the effects of the built-in potentials V_{ms} and V_f respectively related to Fermi level difference between grid and semiconductor and to the density of fixed charges are not taken into account in this development. These intrinsic potentials should only cause a horizontal shift of the curve from figure 2.16 and thus not change its slope. At constant surface potential and thus constant bias, the log-linear temperature dependence of the interface-trap time constant might be utilized to estimate the energy level of the corresponding trap state, as mentioned in chapter 4.

2.7.4 Photoluminescence measurements

Although PL measurements only allow a qualitative characterization of passivation effects, they constitute a simple and relatively straightforward solution to compare the influence of several parameters investigated in this study such as the oxide material and its thickness, the CIGS surface cleaning and the post-deposition annealing. This in turn makes it a well suited and complementary characterization technique to combine with the quantitative but more complex IV/CV analysis described above. Contrarily to all the electrical characterization techniques previously presented in this report, optical-based PL analysis relies on light emission measurements. Therefore, they do not require any physical contact through metallic electrodes and are realized on a slightly modified version of the structure from figure 2.7, i.e. no metal grid is deposited over the oxide layer to avoid undesired reflection effects (see section 3.5).

The objective with steady-state and time-resolved PL measurements usually is to qualitatively assert passivation effects related to the addition of an oxide layer in contact with the studied semiconductor (CIGS). Consequently, PL measurements should also be taken before the deposition of the oxide layer on top of the CIGS, i.e. on the upper surface of the bare CIGS layer, so as to have a point of comparison in the assessing of passivation effects (figure 2.17). In our case, the first step is the steady-state PL measurement: the surface of the sample is exposed to a laser beam of controllable wavelength (green line on figure

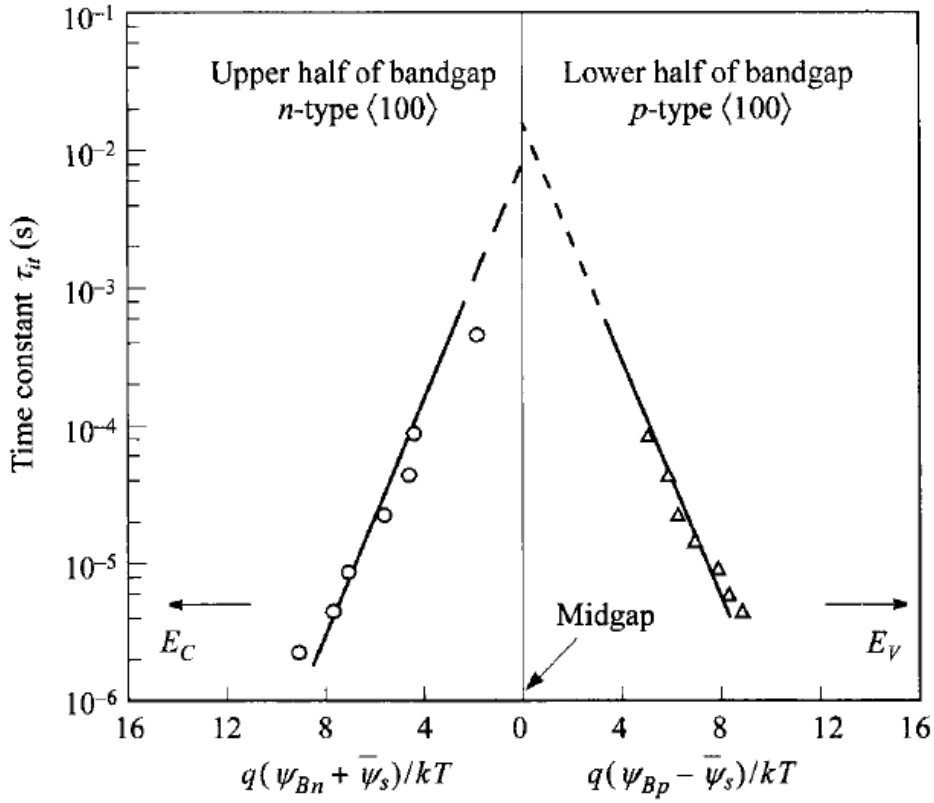

Figure 2.16: Energy dependence of the interface-trap lifetime τ_{it} at room temperature, for a Si-SiO_2 MIS capacitor. Taken from [21].

2.17). Meanwhile, the tool detects the intensity of the light (called PL intensity) that is emitted back by the sample through different radiative energy transitions as summarized in [36]. This process is repeated over a whole range of wavelengths to obtain the evolution of the PL intensity as a function of the incident wavelength, called PL spectrum.

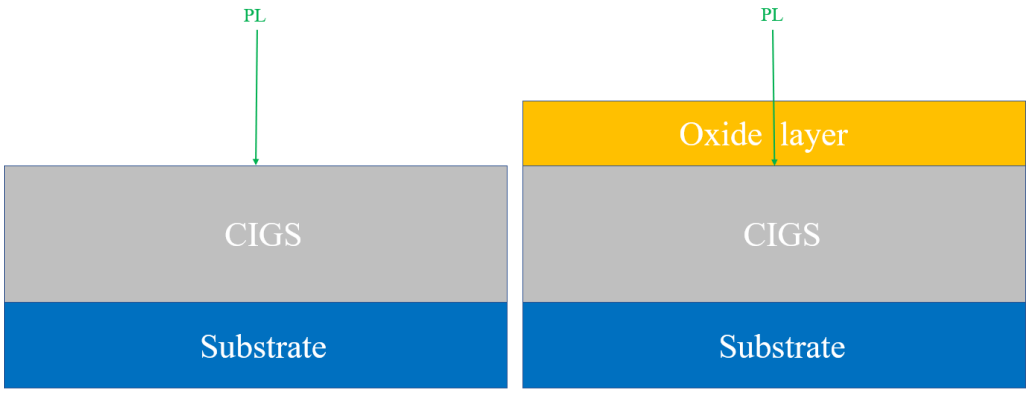

Figure 2.17: Study structures for PL measurements. Left: PL measurements on bare CIGS layer. Right: PL measurements on CIGS/Oxide structure to assess passivation effects.

In the ideal case, the PL spectrum should consist in a single peak located around the wavelength corresponding to the semiconductor bandgap, and should be as high and narrow as possible [36, 37]. However, the presence of defects in real samples expands the

field of possible energy transitions which in turn can modify the PL spectrum (broadening of the single peak, multiplication of peaks, ...) [36, 37]. Nonetheless, whichever the shape of the PL spectrum before the oxide deposition (left of figure 2.17), a global increase in PL intensity after the oxide deposition (right of figure 2.17) tends to indicates active passivation effects [12, 38], eventually leading to higher solar cell performances.

Once the steady-state PL spectrum is obtained and the central wavelengths of the different peaks are identified, the analysis of time-resolved PL (TRPL) measurements allow to estimate the carrier lifetime corresponding to each one of these energy transitions (figure 2.18). With the knowledge of both the wavelength-energy position of the PL peaks on the spectrum and the corresponding carrier lifetimes, it becomes possible to identify the type of material features to which the energy transitions correspond (band-to-band, band-to-defect, etc, ...) as in [36]. It proves then interesting to compare the change in carrier lifetime before and after the oxide deposition, especially for the wavelength that corresponds to the bandgap of the studied material, i.e. CIGS in our case. If the time constant associated to the band-to-band peak increases after the oxide deposition, effective passivation is suggested by a reduction of the recombination mechanisms.

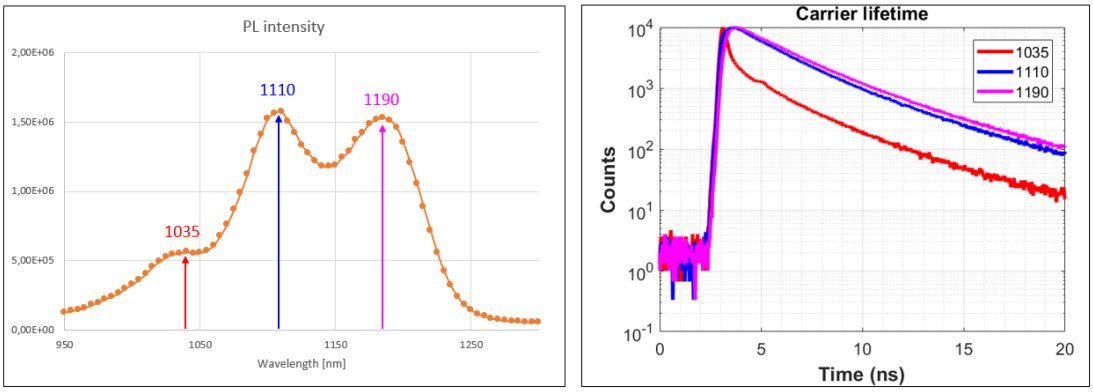

Figure 2.18: Example of PL and TRPL measurements for a CIGS/Al_2O_3/HfO_2 MIS sample studied in this work. Left: PL spectrum exhibiting three different peaks at wavelengths of 1035nm (1.20eV), 1110nm (1.13eV) and 1190nm (1.04eV). Right: TRPL measurements showing a clear lifetime difference between the peak at 1035nm and the two other peaks at 1110nm and 1190nm.

Concerning the complete analysis of the PL results in chapter 4, the objective is two-fold: on the one hand, qualitatively confirming the effectiveness of the oxide layers in terms of passivation; on the other hand, preliminary investigating the influence of different parameters (oxide material and thickness, CIGS processing technique and surface cleaning) on the PL data so as to highlight specific trends to be confirmed using IV and CV measurements afterwards. As explained further in section 3.7, the effect of annealing is not studied through PL measurements in this work.

Chapter 3

Experimental methodology

3.1 Overview of samples structure and processing

The general layout of our samples is depicted on figure 3.1 with the specific variations and designations for each set of samples presented in the next section. The front grid typically consists in a $200nm$-thick square lattice made of thermally evaporated Silver with a contact area of $0.01cm^2$ per device. The ALD oxide layers can be either made of Al_2O_3, HfO_2, TiO_2 or a superposition of Al_2O_3 and HfO_2, with typical total thicknesses between $20nm$ and $100nm$ (ALD recipes and details below).

The CIGS layers used for this project are produced either by sputtering or 3-stage co-evaporation with typical thickness between $1.2\mu m$ and $1.8\mu m$. Their top surface is cleaned with Ammonia or Ammonium sulfide prior to the oxide deposition (see section 3.6). It is also important to note that the roughness of the CIGS top surface is globally higher for sputtered CIGS than for co-evaporated CIGS as demonstrated in [39]. Therefore, the effect of surface cleaning is expected to be more significant for sputtered CIGS than for supposedly smoother co-evaporated CIGS. In the case of co-evaporated CIGS, the diffusion of Na atoms to the CIGS during its processing is ensured by an underlying NaF-based Sodium precursor layer (omitted on figure 3.1) making contact with the $300nm$-thick DC sputtered Molybdenum back electrode. For samples with sputtered CIGS, there is no Sodium precursor layer between the Mo contact and the absorber layer. Instead, the Sodium atoms directly diffuse from the $2-3mm$-thick soda-lime glass (SLG) substrate towards the CIGS during its processing.

Concerning the composition of co-evaporated CIGS, the presence of a notch-type Gallium grading results in the coexistence of one minimum and one maximum bandgap (important for analyzing PL measurements). Besides that, each sample has a total geometrical area of $2.5cm \times 2.5cm$, with the particularity for samples with co-evaporated CIGS to initially belong to a larger $10cm \times 10cm$ cut of 16 samples resulting from a single co-evaporation process. Since the top surface CIGS composition is available through XRF 2D maps for these $10cm \times 10cm$ cuts (CGI, GGI, ...), it is possible to qualitatively discuss the influence of CIGS composition as an explanation for certain differences observed between samples. These considerations are also used in chapter 4 to regroup samples by similar composition (Cu-rich and Cu-poor samples, ...). In general, the CGI and GGI ratios for the co-evaporated CIGS layers studied in this work are respectively comprised within the $[0.7; 0.93]$ and $[0.27 : 0.34]$ ranges.

ALD tools and recipes

- Al_2O_3 - 300°C Thermal ALD Savannah: TMA used as precursor and H_2O used as a reactant for a rate of 0.13nm/cycle.
- HfO_2 - 250°C Thermal ALD Savannah: TEMAH used as precursor and H_2O used as a reactant for a rate of 0.15nm/cycle.
- TiO_2 - 150°C/250°C/275°C Thermal ALD Cambridge Fidji.

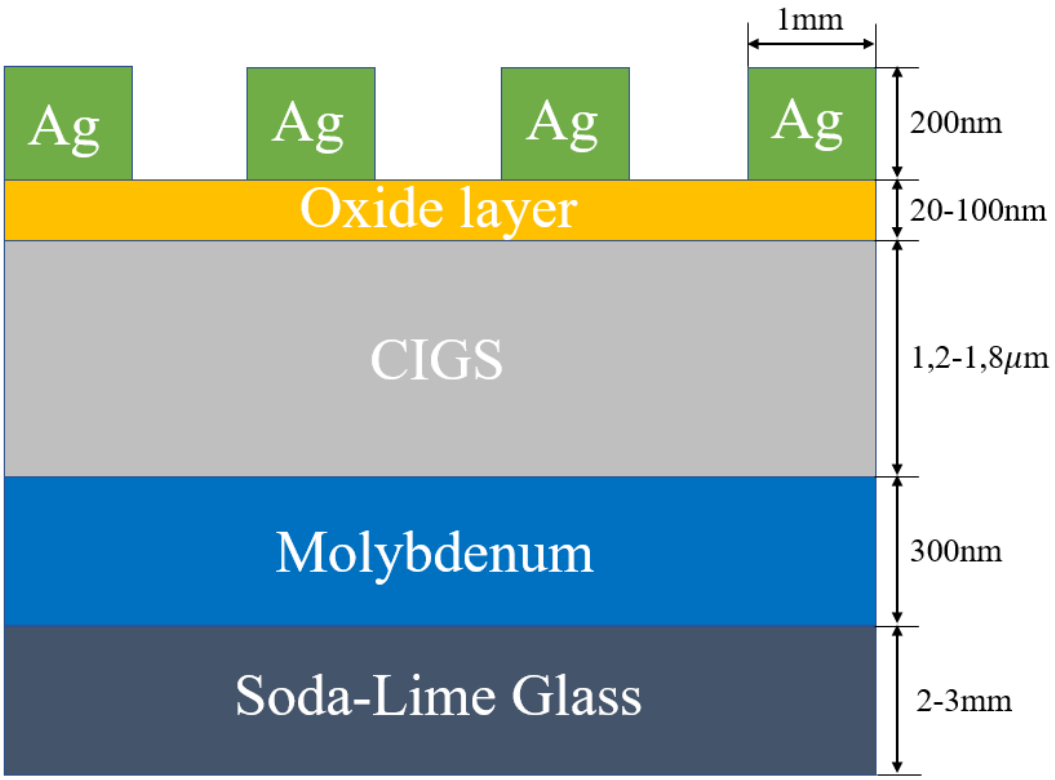

Figure 3.1: Schematic representation of the study MIS structures processed for this work (approximate scale). The Sodium precursor layer present for co-evaporated CIGS layers is not represented.

3.2 Specific description of the samples

3.2.1 Aluminum oxide - Al_2O_3

3.2.1.1 First set - 3-stage CIGS and 20nm Al_2O_3 on thin glass - AL1

Layer	Thickness	Deposition	Cleaning
Ag	200nm	Thermal	X
Al_2O_3	20nm	ALD (300°C)	X
CIGS	1.2μm	3-stage co-evaporation	Ammonia
NaF	6nm	Evaporation	X
Mo	300nm	DC sputtering	X
SLG	1mm	X	X

Table 3.1: Description of the processing and dimensions of the first set of MIS samples with Aluminum oxide, designated AL1 in the rest of this report. The cleaning column indicates the surface cleaning procedure applied on the CIGS top surface before depositing the oxide layer, more thoroughly described in section 3.6.

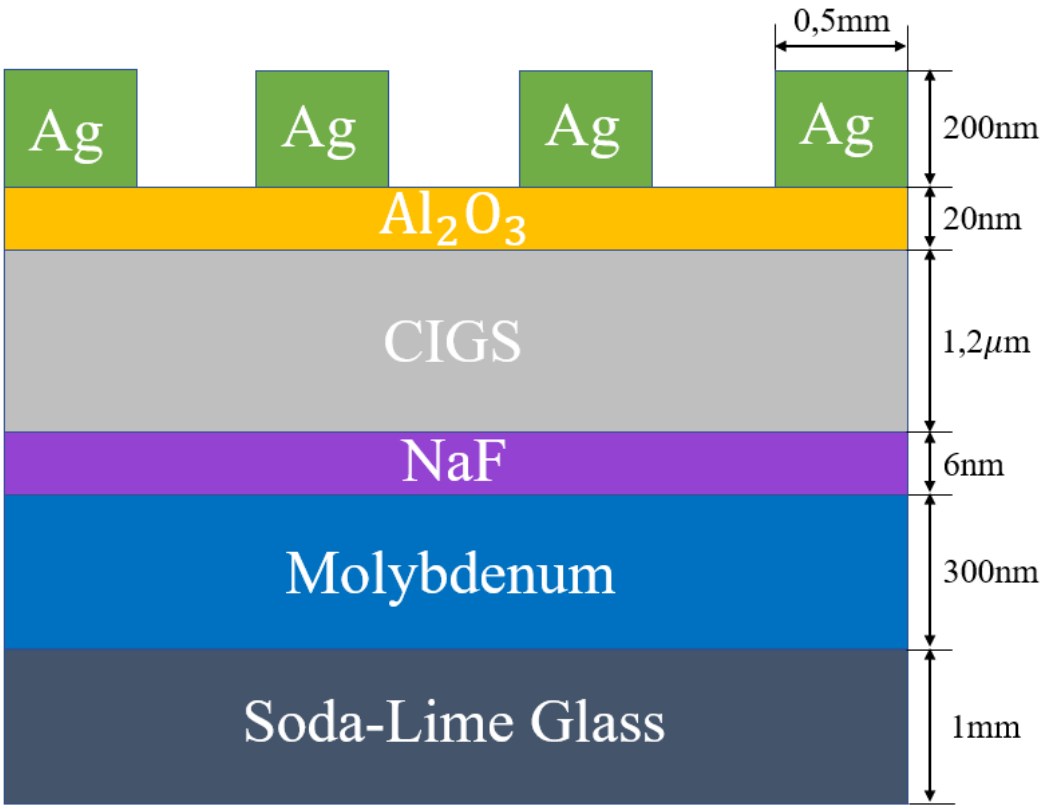

Figure 3.2: Schematic representation of the first set of Al_2O_3 samples (approximate scale) described in table 3.1.

3.2.1.2 Second set - 3-stage CIGS and 20nm Al_2O_3 on thick glass - AL2-17

Layer	Thickness	Deposition	Cleaning
Ag	200nm	Thermal	X
Al_2O_3	20nm	ALD (300°C)	X
CIGS	1.6μm	3-stage co-evaporation	Ammonia
NaF	10nm	Evaporation	X
Mo	300nm	DC sputtering	X
SLG	2-3mm	X	X

Table 3.2: Description of the processing and dimensions of the second set of MIS samples with Aluminum oxide, designated AL2 to AL17 in the rest of this report (16 samples). The surface cleaning procedure applied on the CIGS top surface before depositing the oxide layer utilizes $NH_3 \cdot H_2O$ (Ammonia) as more thoroughly described in section 3.6.

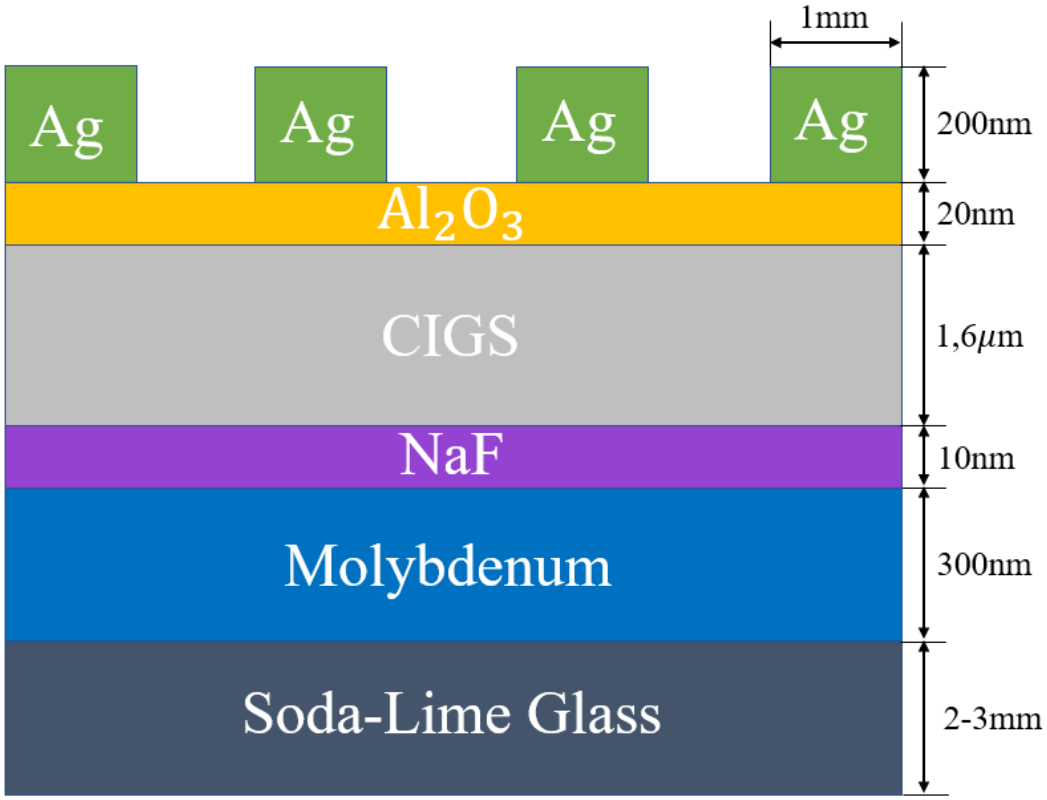

Figure 3.3: Schematic representation of the second set of Al_2O_3 samples (approximate scale) described in table 3.2.

3.2.1.3 Third set - Sputtered CIGS and 30nm Al_2O_3 on thick glass - AL18-21

Layer	Thickness	Deposition	Cleaning
Ag	200nm	Thermal	X
Al_2O_3	30nm	ALD (300°C)	X
CIGS	1.6μm	Sputtering	Ammonia/AS
Mo	300nm	DC sputtering	X
SLG	2-3mm	X	X

Table 3.3: Description of the processing and dimensions of the third set of MIS samples with Aluminum oxide, designated AL18 to AL21 in the rest of this report (4 samples). The surface cleaning procedure applied on the CIGS top surface before depositing the oxide layer utilizes either Ammonia for AL18 and 19 or $(NH_4)_2S$ (Ammonium sulfide - AS) for AL20 and 21, with complete cleaning procedure described in section 3.6.

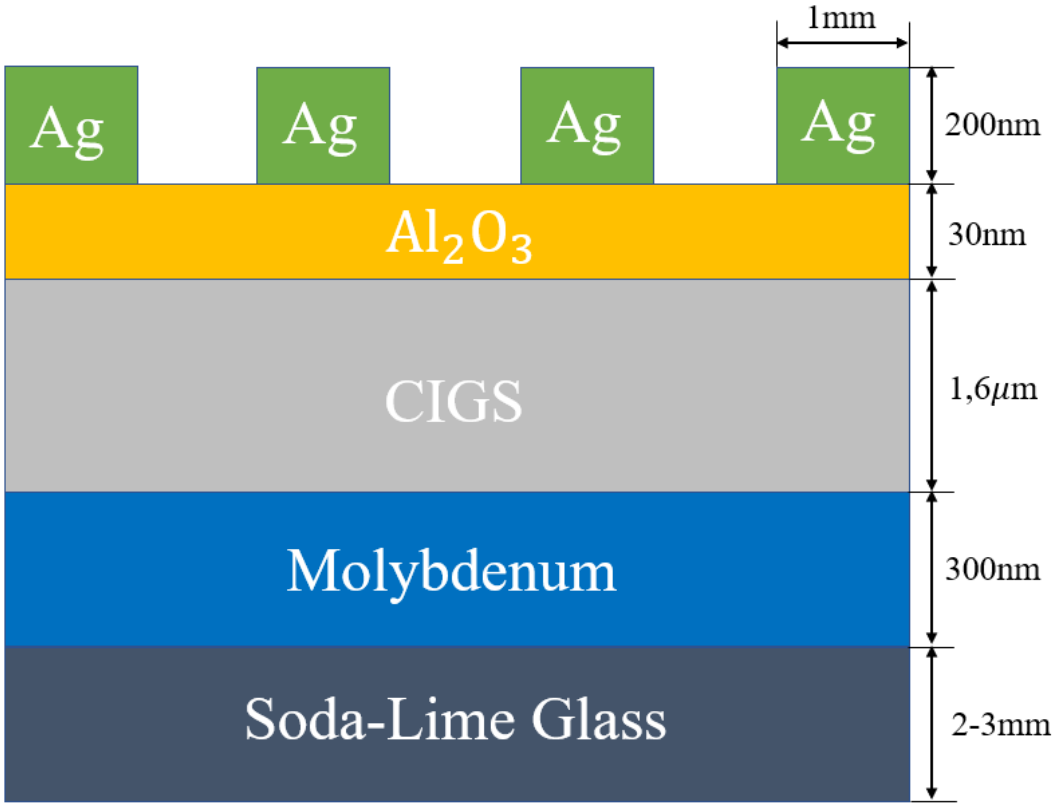

Figure 3.4: Schematic representation of the third set of Al_2O_3 samples (approximate scale) described in table 3.3.

3.2.2 Hafnium oxide - HfO_2

3.2.2.1 First set - 3-stage CIGS and 30nm HfO_2 on thick glass - HF1-8

Layer	Thickness	Deposition	Cleaning
Ag	200nm	Thermal	X
HfO_2	30nm	ALD (250°C)	X
CIGS	1.8μm	3-stage co-evaporation	Ammonia/AS
NaF	10nm	Evaporation	X
Mo	300nm	DC sputtering	X
SLG	2-3mm	X	X

Table 3.4: Description of the processing and dimensions of the first set of MIS samples with Hafnium oxide, designated HF1-8 in the rest of this report (8 samples). The surface cleaning procedure applied on the CIGS top surface before depositing the oxide layer utilizes either Ammonia (HF1-4) or AS (HF5-8) as more thoroughly described in section 3.6.

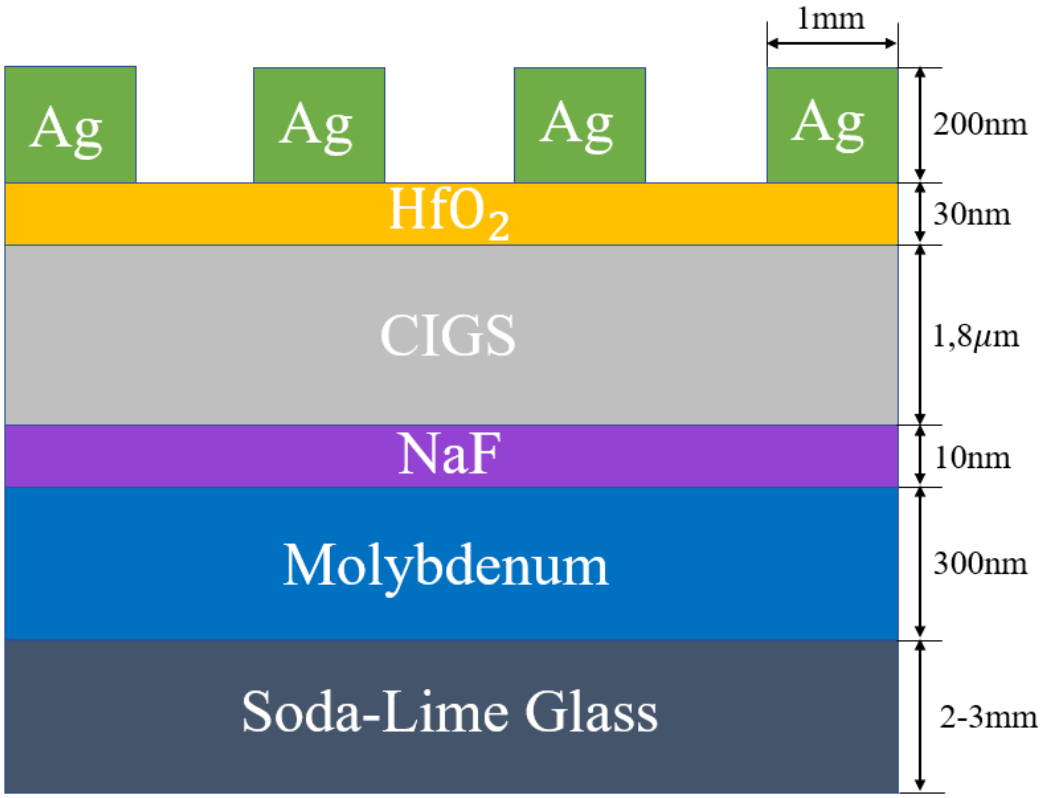

Figure 3.5: Schematic representation of the first set of HfO_2 samples (approximate scale) described in table 3.4.

3.2.2.2 Second set - Sputtered CIGS and 30nm HfO_2 on thick glass - HF9-12

Layer	Thickness	Deposition	Cleaning
Ag	200nm	Thermal	X
HfO_2	30nm	ALD (250°C)	X
CIGS	$1.6\mu m$	Sputtering	Ammonia/AS
Mo	300nm	DC sputtering	X
SLG	2-3mm	X	X

Table 3.5: Description of the processing and dimensions of the second set of MIS samples with Hafnium oxide, designated HF9 to HF16 in the rest of this report (4 samples). The surface cleaning procedure applied on the CIGS top surface before depositing the oxide layer utilizes either Ammonia for HF9 and 10 or AS for HF11 and 12, with complete cleaning procedure described in section 3.6.

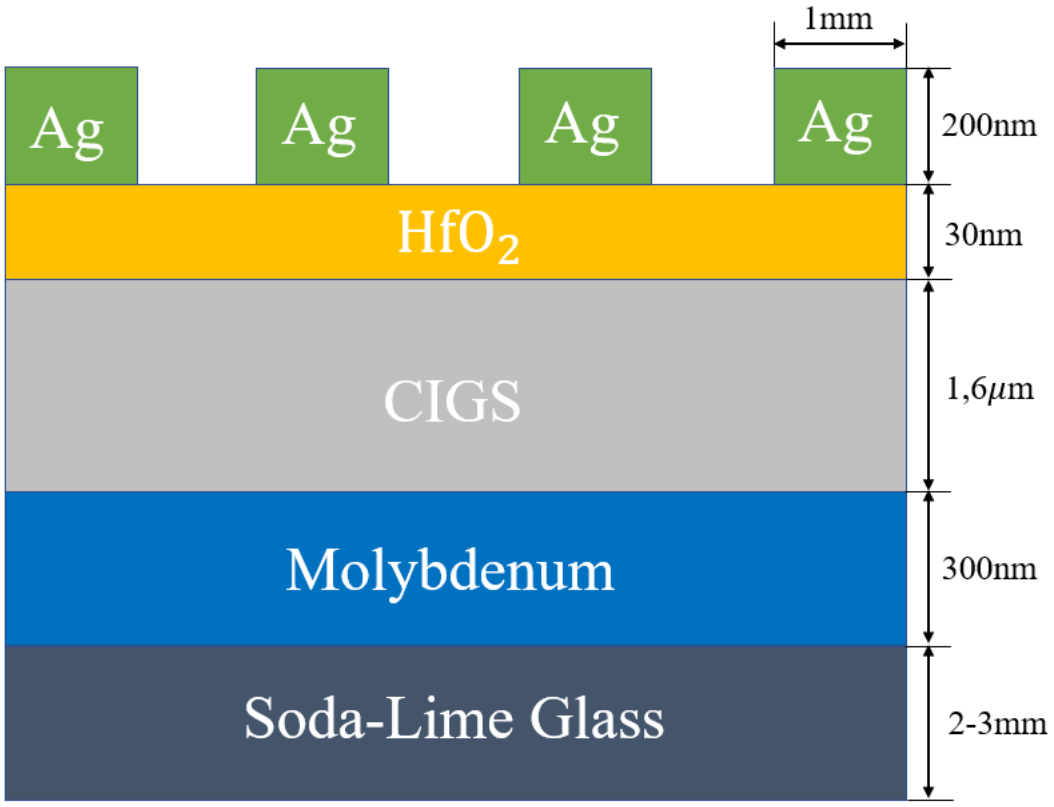

Figure 3.6: Schematic representation of the second set of HfO_2 samples (approximate scale) described in table 3.5.

3.2.3 Multi-layer Al_2O_3/HfO_2

3.2.3.1 3-stage CIGS and 30nm Al_2O_3/20nm HfO_2 on thick glass - ALHF1-8

Layer	Thickness	Deposition	Cleaning
Ag	200nm	Thermal	X
HfO_2	20nm	ALD (250°C)	X
Al_2O_3	30nm	ALD (300°C)	X
CIGS	1.8μm	3-stage co-evaporation	Ammonia/AS
NaF	10nm	Evaporation	X
Mo	300nm	DC sputtering	X
SLG	2-3mm	X	X

Table 3.6: Description of the processing and dimensions of the set of MIS samples with combination of Aluminum and Hafnium oxide, designated ALHF1-8 in the rest of this report (8 samples). The surface cleaning procedure applied on the CIGS top surface before depositing the oxide layer utilizes either Ammonia (ALHF1-4) or AS (ALHF5-8) as more thoroughly described in section 3.6.

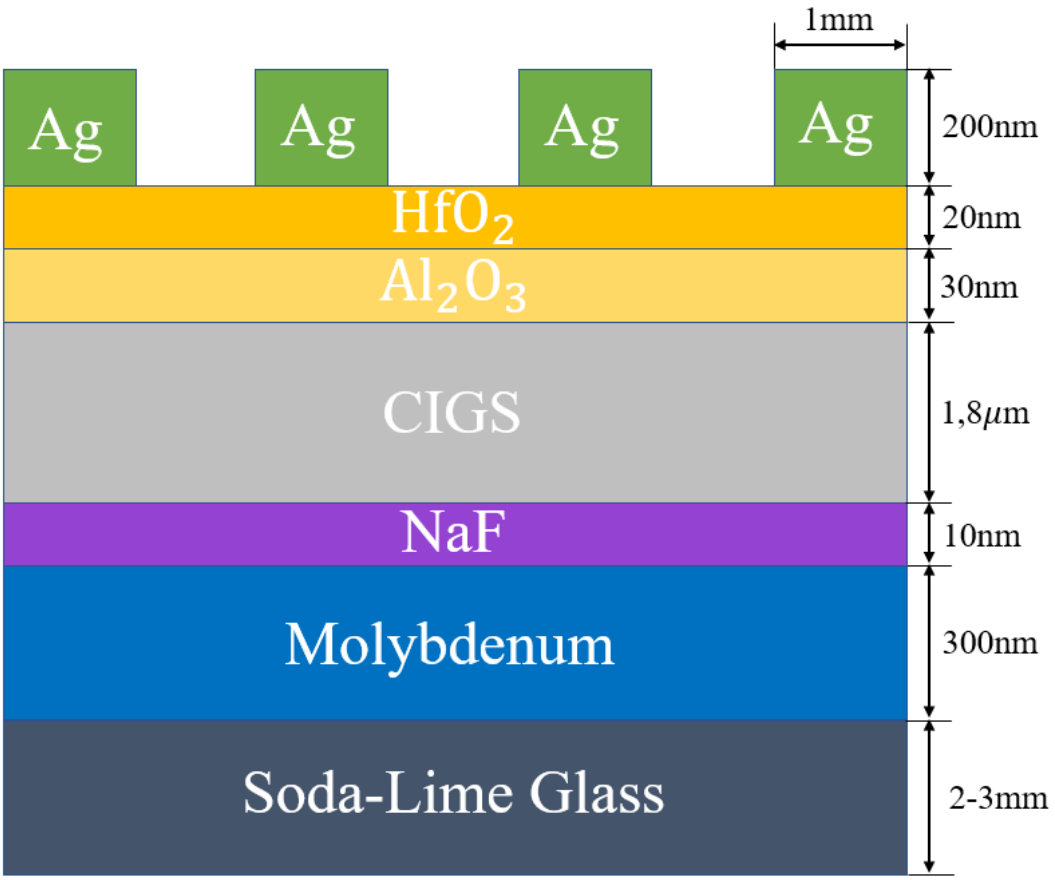

Figure 3.7: Schematic representation of the set of multi-layer samples (approximate scale) described in table 3.6.

3.2.4 Titanium oxide - TiO_2

3.2.4.1 First set - 3-stage CIGS and 50-75-100nm TiO_2 on thick glass - Ti1-15

Layer	Thickness	Deposition	Cleaning
Ag	200nm	Thermal	X
TiO_2	50-75-100nm	ALD (150/250°C)	X
CIGS	1.6μm	3-stage co-evaporation	Ammonia/AS
NaF	10nm	Evaporation	X
Mo	300nm	DC sputtering	X
SLG	2-3mm	X	X

Table 3.7: Description of the processing and dimensions of the first set of MIS samples with Titanium dioxide, designated Ti1-15 in the rest of this report (15 samples). The surface cleaning procedure applied on the CIGS top surface before depositing the oxide layer utilizes either Ammonia or AS as more thoroughly described in section 3.6. The TiO_2 layer for half of the samples (Ti1-7) is deposited with 150°C ALD (Ti1-5 are cleaned with Ammonia and have respectively 50nm TiO_2 for Ti1, 75nm TiO_2 for Ti2-4 and 100nm for Ti5; Ti6 and Ti7 are cleaned with AS and have respectively 75 and 100nm TiO_2). The ALD deposition for the other half (Ti8-15) is at 250°C (Ti8-12 are cleaned with Ammonia and have respectively 50nm TiO_2 for Ti8, 75nm TiO_2 for Ti9 and 100nm TiO_2 for Ti10-12; Ti13-15 are cleaned with AS and have respectively 75nm TiO_2 for Ti13 and 100nm TiO_2 for Ti14-15).

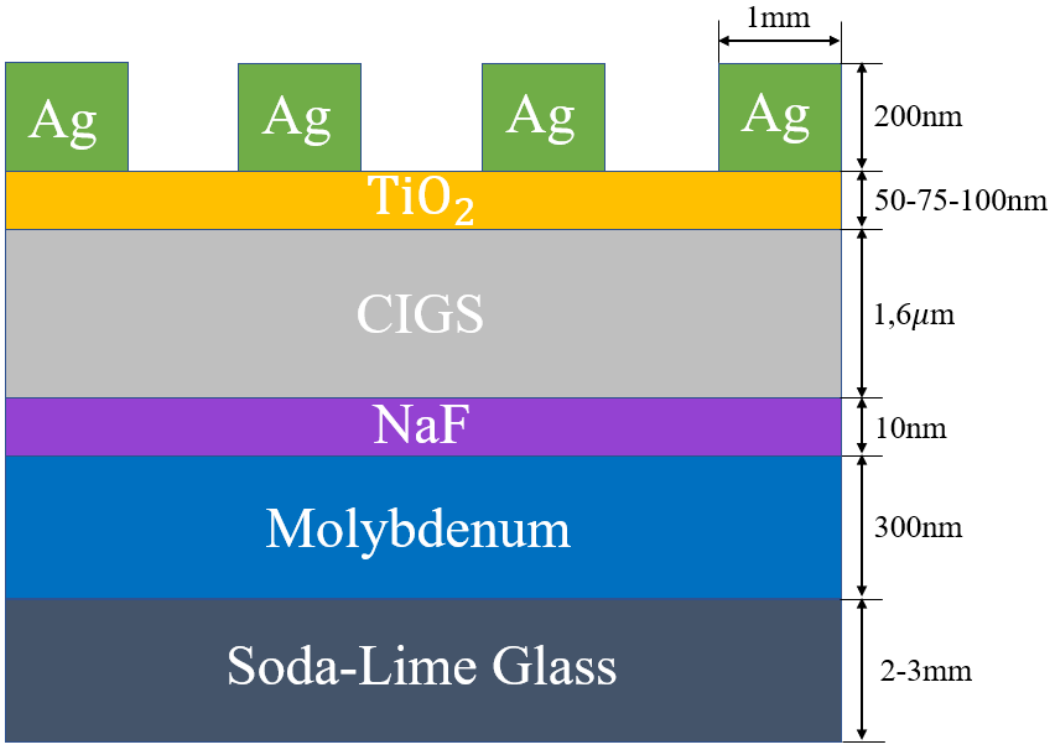

Figure 3.8: Schematic representation of the first set of TiO_2 samples (approximate scale) described in table 3.7.

3.2.4.2 Second set - Sputtered CIGS and 100nm TiO_2 on thick glass - Ti16-19

Layer	Thickness	Deposition	Cleaning
Ag	200nm	Thermal	X
TiO_2	100nm	ALD (150/250°C)	X
CIGS	1.6μm	Sputtering	Ammonia/AS
Mo	300nm	DC sputtering	X
SLG	2-3mm	X	X

Table 3.8: Description of the processing and dimensions of the second set of MIS samples with Titanium dioxide, designated Ti16 to Ti19 in the rest of this report (4 samples). The surface cleaning procedure applied on the CIGS top surface before depositing the oxide layer utilizes either Ammonia (Ti16 for ALD-150°C and Ti17 for ALD-250°C) or AS (Ti18 for ALD-150°C and Ti19 for ALD-250°C) as more thoroughly described in section 3.6.

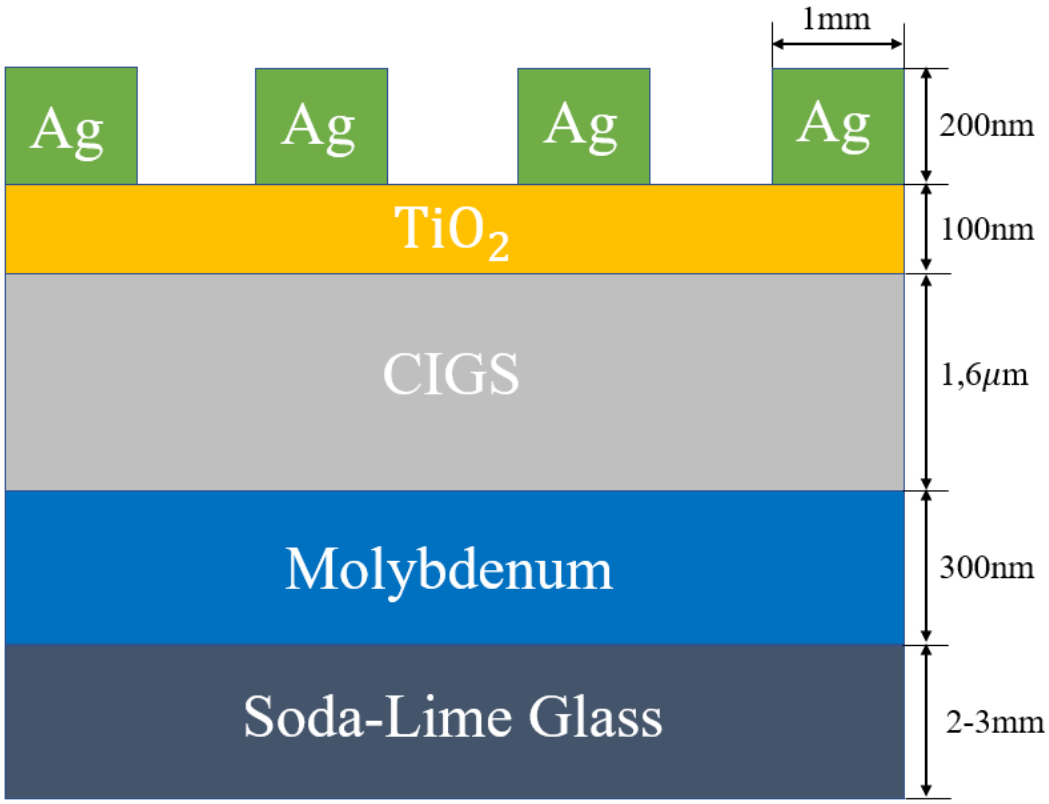

Figure 3.9: Schematic representation of the second set of TiO_2 samples (approximate scale) described in table 3.8.

3.3 Capacitance-Voltage measurements

3.3.1 Tool setup

C-V measurements are performed on the Agilent E4980A Precison LCR meter. The largest ranges of frequencies and voltage utilized for this work are respectively $[100\text{Hz}, 1\text{MHz}]$ and $[-1.5V, 2V]$. For any C-V measurement, there are at least 41 data points for both the voltage and frequency, respectively in linear and logarithmic sweep. Since our objective is to characterize the electrical behaviour of MIS structures, the optical aspect is not considered nor studied. Therefore, black clothes are always put below and on top of the sample being measured so as to prevent any parasitic illumination and reflections. The amplitude of the AC small-signal is always equal to $50mV$.

3.3.2 Probes configuration and contacts

As it is presented in the next chapter, series resistance effects have been observed at high frequencies. In order to mitigate the parasitic degradation of series resistance on the C-V measurements, the 4 probes configuration is always preferred to the 2 probes configuration except in the case of low-temperature C-V measurements for which the setup does not allow 4 probes connection (see below in section 3.3.4). In either case, the high potential/current needles are put in contact with the Silver front grid and the low potential/low current needle(s) are put in contact with the Molybdenum back electrode so as to obtain the same configuration as in chapter 2. Since the back contact is initially not apparent at the surface of our samples, the superior layers (oxide, CIGS and NaF) are first manually scratched before soldering an Indium layer on top of the then-apparent Molybdenum so as to protect it from air oxidation (figure 3.10).

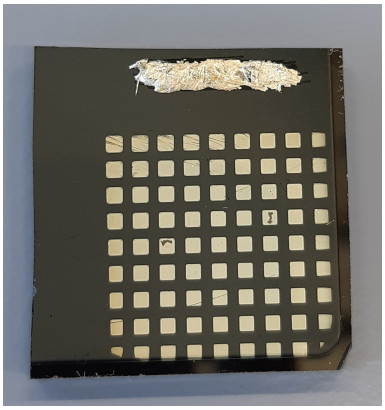

Figure 3.10: Picture of a typical MIS sample used in this work showing the front and back contacts.

3.3.3 Measurement sequence and accuracy

In our case, the two outputs of the Capacitance-Voltage measurements are the parallel conductance (G_p) and capacitance (C_p). The tool measures G_p and C_p at a fixed frequency (from lowest to highest) and for the whole range of bias in increasing order, i.e. from the negative towards the positive voltages. Once the voltage sweep is completed at the given frequency, the frequency increases to the next step and the bias sweep starts again as C_p and G_p are being measured. Since the conductance data suffers from a lower precision than the capacitance data due to a tool issue, the derivative of the capacitance with respect to frequency $-f\frac{dC_p}{df}$ has been substituted to the conductance $\frac{G_p}{\omega}$ necessary to characterize chemical passivation.

3.3.4 Temperature-dependent C-V

In order to obtain further insight about the behaviour of defects and series resistance, CV measurements at lower temperatures are investigated in this study. In order to perform such measurements, modifications of the CV setup presented just above are required.

First, only the 2 probes configuration could be used as the needles used in the 4 probes setup are too brittle to be used at low temperature. Second, the sample was placed inside the "Temperature monitoring" setup. This one consists of a copper plate on which the sample is attached. This plate is standing elevated on four insulating feet and placed in a thermally insulated box which is open at the top. The copper plate is connected to a temperature sensor and soldered to a voltage source-powered resistor. This basic handcrafted setup has a simple working principle: the voltage source powers the resistor so that it heats up the plate until it reaches the temperature setpoint.

To reach low temperatures, liquid nitrogen is poured into the insulated box until it gets in contact with the bottom of the copper plate. Once the desired temperature setpoint (lowest temperature around $-180°C$ with liquid nitrogen) is indicated by the temperature sensor, the C-V measurement starts as described above. At this point, several remarks have be to be emphasized concerning the reliability and accuracy of those measurements. Firstly, there is a non-negligible error on the actual sample temperature during those measurements. This comes not only from the fact that the temperature sensor measures the temperature of the copper plate and not of the sample itself, but also because the setup is not completely closed from the outside and therefore cannot stabilize at very low temperatures. Nevertheless, as the temperature is going up, the temperature drift decreases and the temperature control becomes stable around $-120°C$. Secondly, the setup cannot indefinitely keep the temperature at the specified setpoint. Consequently, one has to act fast while taking these measurements. This in turn translated into modifications of the measurements range and precision for certain samples and very low temperatures, which are mentioned further where relevant.

3.4 Current-Voltage measurements

I-V measurements are performed on the Keithley 2401 Sourcemeter. Although theoretically there should not be any current circulating in our MIS samples (see section 2.6.2), I-V measurements can quickly indicate major leakage problems inside them and are therefore realized as a preliminary sanity check before C-V measurements. The probes and contacts configuration are perfectly similar to the one for C-V measurements except that the high and low potential/current needles are inverted so that negative currents are observed for negative voltages and likewise for positive voltages. The tool linearly sweeps voltage in the $[-1V, 1V]$ range and measures the current through the structure, with a voltage step of $13.3mV$ for a total of 150 points per measurement. Similarly to the C-V measurements, two black clothes are put below and on top of the samples to isolate them from ambient light.

3.5 Photoluminescence measurements

Steady-state and time-resolved PL measurements are performed on the Picoquant FluoTime 300 with an excitation wavelength of 532nm, integration time of 250ps and repetition rate of 3MHz. The wavelength range used in this study is $[950nm, 1400nm]$ with an expected PL peak around $1080nm$ corresponding to the bandgap of CIGS, i.e. 1.15eV. The wavelength step is $5nm$ and the hold time between successive steps is 0.5 sec. Since the PL spectra of our samples regularly present multiple peaks, the carrier lifetime is

measured for each one of those so as to distinguish the related energy transition (band to band, band to defect, etc, ... as presented in section 2.7.4). The presence of more than one peak on the PL spectrum of CIGS generally indicates the coexistence of multiple phases with different bandgaps such as CIS and CIGS typically. Therefore, PL measurements are performed on at least two different points on the surface of each sample so as to not only reduce variability due to local sample composition for comparisons between samples, but also to observe its influence on the observed PL data for a given sample. As mentioned in chapter 2, the PL measurements are taken on the different samples before the deposition of the Silver front grid so as to avoid reflections from the metallic contacts.

3.6 Surface cleaning methods

As mentioned above, the effect of CIGS surface cleaning is one of the parameters investigated in this study. In particular, the objective is to compare the effect of Ammonia and Ammonium Sulfide cleaning [40] on the two interface passivation figures-of-merit studied here, i.e. Q_f and D_{it}. These chemicals are commonly used in surface cleaning of III/V devices. To do so, samples with the exact same configuration have been processed with the only difference being the surface cleaning treatment applied on the CIGS top surface before the ALD deposition of the oxide layer. Since the Ammonia cleaning procedure is made by default, several sets of samples only have this type of cleaning performed as detailed above in section 3.2. Thus, it is not possible to make the comparison with AS cleaning for these very samples. In practice, the cleaning procedures with $NH_3 \cdot H_2O$ (Ammonia) or $(NH_4)_2S$ (AS) are slightly different as described below:

- **$NH_3 \cdot H_2O$ (Ammonia) cleaning**
  1. 6 minutes dipping into 30% $NH_3 \cdot H_2O$ solution
  2. 3 minutes rincing into deionized water
  3. 3 minutes rincing into deionized water
- **$(NH_4)_2S$ (AS) cleaning for 3-stage co-evaporation CIGS**
  1. 5 minutes dipping into $(NH_4)_2S$ (AS) solution with 6.5-7% Sulfur concentration
  2. 2 minutes rinsing into deionized water
  3. 2 minutes rinsing into deionized water
- **$(NH_4)_2S$ (AS) cleaning for sputtered CIGS**
  1. 15 minutes dipping into $(NH_4)_2S$ (AS) solution with 6.5-7% Sulfur concentration
  2. 2 minutes rinsing into deionized water
  3. 2 minutes rinsing into deionized water

3.7 Annealing

Post-deposition thermal annealing is another process whose influence on passivation effects is investigated in this study. The most important parameters about annealing processes usually are their duration, temperature and gas environment. In this work, we performed

annealing processes with a duration of 30 minutes for the high-temperature plateau at either 300 or 400°C, and under constant N_2 flow. Similar procedures are used in relevant literature references [13, 24, 25, 41]. The annealing itself is performed inside the ATV PEO601 fast ramping furnace. Given the already mentioned variability of CIGS composition between samples and to increase the reliability of our results about annealing, we decided to perform the post-annealing on samples that already have the front grid and Indium soldering deposited at the top surface and for which as deposited IV/CV data is already available. The presence of the front contacts in turn explains why PL measurements are not performed on the annealed samples. In general, we tried as much as possible to perform C-V measurements in the same region of the sample before and after the annealing so as to limit the changes in CIGS composition and ensure reliable comparisons between as deposited and annealed data.

The annealing sequence is as follows:

1. **Initialization** $\longrightarrow$ 2 minutes of hold time under N_2 flow
2. **Heating up** $\longrightarrow$ 10 or 15 minutes of heating up to respectively reach 300°C or 400°C under N_2 flow
3. **Annealing** $\longrightarrow$ 30 minutes of thermal annealing at 300°C or 400°C under N_2 flow
4. **Cooling down** $\longrightarrow$ 20 or 25 minutes of cooling down to respectively reach 300°C or 400°C under N_2 flow

Several samples are subjected to two separate and successive annealing processes, typically a first annealing at 300°C and a second annealing at 400°C with both the same duration and separated by a rest period of typically one day at least. The objective is to investigate the possible cumulative effects of successive annealing treatments.

Chapter 4

Results

4.1 Overview

This chapter presents the main results obtained throughout the study of front interface passivation of CIGS solar cells, starting with numerical simulations of alumina-based MIS capacitors in section 4.2. After that, section 4.3 presents once and for all the analysis methodology implemented for this work with an example on a particular sample. This chapter is articulated in the same way as section 3.2. This means that the experimental results and their analysis are successively presented for each different dielectric material: Al_2O_3, HfO_2, Al_2O_3/HfO_2 combination and TiO_2, with a distinction between the three former configurations (sections 4.4-4.6) summarized in section 4.7 and the latter, qualitatively discussed at the very end of this chapter (section 4.8). The different samples are designated by their respective names as presented in section 3.2. The application of the analysis methodology to our experimental data leads to both qualitative observations and quantitative results which can be confronted to the numerical outcomes of the simulation models detailed just below.

Besides that, the respective influence of the main parameters investigated (oxide thickness, CIGS processing and composition, surface cleaning and thermal annealing) is discussed in parallel with the advantages of the different dielectric materials. With the objective of characterizing passivation effects and extracting the important figures-of-merit D_{it} and Q_f, only the most interesting results are shown in this chapter whereas complementary data are available for the reader in Appendix A. For alumina and/or hafnia-based configurations, there is a general discussion in section 4.7 which tends to highlight the most promising design regarding the different aspects investigated whereas titania is treated individually in section 4.8.

4.2 Numerical simulations

This section attempts to confront the qualitative theoretical concepts presented above in chapter 2 to the quantitative CV results obtained either via the SCAPS software [14] or with MATLAB®. Although the simulations presented below only treats the case of $CIGS/Al_2O_3$ MIS capacitors, we believe that highly similar results should be observed with HfO_2 as well. Given its rather different properties compared to the other materials, TiO_2 is treated separately at the end of this chapter with no corresponding simulations. The objective is to obtain a simulation model that correctly integrates the effect of

the two passivation figures-of-merit D_{it} and Q_f in the case of Al_2O_3 but transposable to HfO_2 and Al_2O_3/HfO_2 stacks as well. Even though similar results already exist in the literature for the case of alumina [7, 13], we believe that our MIS capacitor simulations result in a better reference point to which our experimental results can be compared.

The efficiency improvements of solar cells related to interface passivation are no longer to be confirmed [5–12, 16–20, 24, 25, 33]. The purpose of this work is to reach an optimized oxide passivation layer that results in a low value of D_{it} of the order of $10^{11} cm^{-2} eV^{-1}$ and a strong field-effect passivation associated to a positive value of Q_f of the order of $10^{12} cm^{-2}$. Therefore, similar values of D_{it} and Q_f are used throughout this whole section so as to study their impact on the CV behaviour of typical CIGS/Al_2O_3 MIS capacitors using two different softwares and their respective model: first, the SCAPS model is inspired from [7, 22, 42] and provides the general direction being aimed at in our study regarding D_{it} and Q_f; second, the MATLAB® simulations use the model from [43] and give an insight into supplementary effects that are not considered nor investigated with SCAPS.

The complete set of values and parameter used in both models is provided in table A.1 from Appendix B and for the example of Al_2O_3, except for the work-functions of the back and front electrodes whose values are presented just below. There is also a particular focus on the parameters used to introduce defects of 3 different types in the various layers of the models (table A.2). The defects parameters are constantly tuned in the following in order to study their impact on the CV measurements whereas the general parameters from table A.1 are rather fixed. Eventually, complementary results of simulations are also provided in Appendix B.

4.2.1 SCAPS

The most important parameters to consider in the SCAPS model concern the bulk defects in the CIGS and the Al_2O_3 layer as well as the interface defects. More particularly, their density (in cm^{-3} for bulk and in $cm^{-2} eV^{-1}$ for interface), their type (acceptor, donor or neutral), their valency (single, double or multivalent) and their energy distribution (central energy level, characteristic energy, type of distribution). Apart from their thickness, other parameters are also important with regards to the simulations of both the CIGS and Al_2O_3 layers, namely fixed parameters related to their intrinsic properties: dielectric permittivity, electronic affinity and bandgap.

The SCAPS model is relatively straightforward: the Al_2O_3/CIGS structure is sandwiched in between two metallic contacts. The thicknesses of respectively the oxide and CIGS layers are set to $20nm$ and $1.6\mu m$. The work-function of the back electrode is set to $5.5eV$ so as to have a flat-band situation at the back electrode/CIGS interface when no bias is applied. The work-function of the front contact is set to $5.3eV$ for two reasons: on the one hand, it guarantees that the built-in potential difference with the CIGS Fermi level is not too high at the front contact, i.e. $\phi_{ms} = 5.3 - 5.49 = -0.19eV$.; on the other hand, it ensures a wider range of numerical convergence ($[-0.9V; 0.9V]$) in terms of band alignment compared to other values. All other parameters are available in Appendix B. The ideal 10kHz CV curve obtained with that model is shown on figure 4.1, for D_{it} and Q_f both set to zero and the example of Al_2O_3.

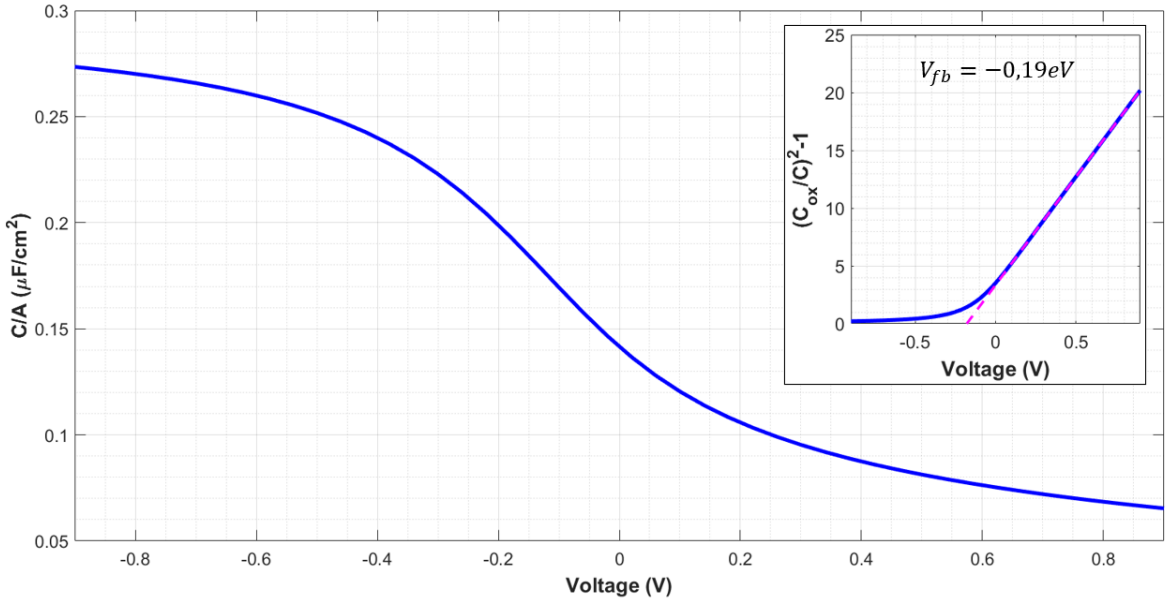

Figure 4.1: Ideal 10kHz CV curve obtained with the alumina-based MIS capacitor SCAPS model for D_{it} and Q_f both set to zero. The value in accumulation is slightly below the geometrical oxide capacitance $C_{ox} = 0.3\mu F/cm^2$. Inset: Flat-band voltage extraction providing $V_{fb} = V_{ms} = -0.19V$, from [35] as detailed in the text.

Surface density of fixed oxide charges - Q_f First of all, one can see that the flat-band voltage without the presence of any defect is well equal to the difference ϕ_{ms} between the grid work-function and the CIGS Fermi level as shown on the inset of figure 4.1. The method used to extract V_{fb} is the one already detailed above in section 2.7.3.1 and taken from [35]. Second, the expected trend to observe on the simulations is a horizontal shift of the CV curves consequently to an increase of bulk defects density in the Al_2O_3 layer. In particular, if the resultant density of fixed charges in the dielectric is positive (resp. negative), the CV curves should be shifted leftwards (resp. rightwards) compared to the ideal situation without any fixed charges in which $V_{fb} = -0.19V$. Moreover, the magnitude of that shift should be directly proportional to the equivalent surface density of charges Q_f inserted in the oxide simulation model. Even though the bulk defect densities are expressed in cm^{-3} in SCAPS, the equivalent surface density of fixed charges Q_f can still be obtained by using the volume-surface conversion formula from equation 2.2. Several hypotheses are made at this point: first, the energy and spatial distribution of the defects densities are considered the simplest possible. In other terms, the different charge states of the defects have a single level of energy and a constant volumic density over the whole oxide thickness; second, this uniform density gradient greatly simplifies the volume-surface conversion from equation 2.2:

$$Q_f = \frac{d}{2} * \rho_f = 10^{-6} * \rho_f \ [cm^{-2}] \tag{4.1}$$

in which $d = 20nm$ is the thickness of the Al_2O_3 layer with a total density of fixed charges ρ_f; third, ρ_f from equation 4.1 results from the combination of all the individual volumic densities of the different defects. As mentioned in section 2.4.2, there are multiple type of native defects present in every dielectric material and thus Al_2O_3 as well. Each one of these defect types has a specific density which, on the one hand, is difficult to estimate for a particular sample and on the other hand, is likely to vary from one sample to another.

Although our investigation is limited to the extraction of the total resultant Q_f, the knowledge of the energy position and distribution of the different native defects in Al_2O_3 is helpful to reach a more complete simulation model. The detailed characterization of the different defects present in Al_2O_3 is investigated in [23], i.e. the reference case used in this section. Even though not investigated in this study, the transfer of our model to the case of HfO_2 using [44] is expected to give similar results to the ones shown here. As mentioned above, the study of TiO_2-based MIS simulations is not presented here and requires supplementary considerations that are briefly expressed in section 4.8.

Let us now discuss the effect of non-zero bulk defects densities inside the alumina layer. It is demonstrated in [23] that 6 different types of defects are intrinsically present in the alpha phase of Al_2O_3: vacancies, interstitials and dangling bonds for both Oxygen and Aluminum atoms. It is said in that same reference that even though the ALD deposition of Al_2O_3 layers result in an amorphous phase rather than $\alpha - Al_2O_3$, the results obtained in [23] can still be extrapolated to ALD amorphous alumina as in our case. On figure 4.2, the 10kHz CV curve obtained by setting all 6 individual defect densities to $2 * 10^{17} cm^{-3}$ is represented. A leftward shift of $0.2V$ is observed in comparison to the ideal case from figure 4.1. According to equation 2.5, this corresponds to a surface density of charges:

$$Q_f = C_{ox}\Big(\frac{V_{ms} - V_{fb}}{q}\Big) = 0.3 * 10^{-6}\Big(\frac{0.2}{q}\Big) = +3.8 * 10^{11}\ [cm^{-2}] \tag{4.2}$$

This example confirms the shifting effect of bulk defects with equal densities in the aluminum oxide, resulting in a higher negative flat-band voltage and thus positive equivalent fixed charges density. In practice, the exact densities of defects are not known for each sample and it is also not likely that all the types of defects have the same individual densities as simulated here. Still, the objective being here to quantify the total Q_f rather than each individual defect density, the reasoning developed here is limited to the simple case The positive sign of Q_f can be explained by inspecting the charge state of the different defects. Among all of the 6 native defect types present in Al_2O_3 and reported in [23], it appeared in our simulations that one of them, i.e. the oxygen interstitial, has no significant influence on the total charge density and is therefore no longer taken into account.

Besides that, the occupation probability of the other defects as computed by SCAPS indicates that they each occupy a specific charge state: 2-/3- for Al vacancy, 0/- for O dangling bond, +/0 for Al dangling bond, 2+/+ for O vacancy and 3+/2+ for Al interstitial. Summing up all of these charge states results in an equivalent 2+/+ charge state with volumic density $2 * 10^{17} cm^{-3}$, corresponding to a value of Q_f within the $[2 - 4] * 10^{11} cm^{-2}]$ range and rather close to the previous estimation of Q_f hereabove. It is mentioned in [23] that the vacancies and interstitials related to Aluminum do act as fixed charges and not interface states. The dangling bonds of Al and O and the vacancies of O seem to act also as fixed charges given the results obtained with SCAPS but might as well contribute to interface or border traps densities [23].

Even though one of our objectives is precisely to obtain a positive density of fixed charges so as to passivate the front interface of CIGS solar cells, one cannot conclude from these first results that alumina is undoubtedly well suited to front interface passivation. Indeed, on figure 4.3 it is visible that by varying the density of acceptor-type Al vacancies alone for instance, the CV curves are greatly shifted to the right which in turn would result in

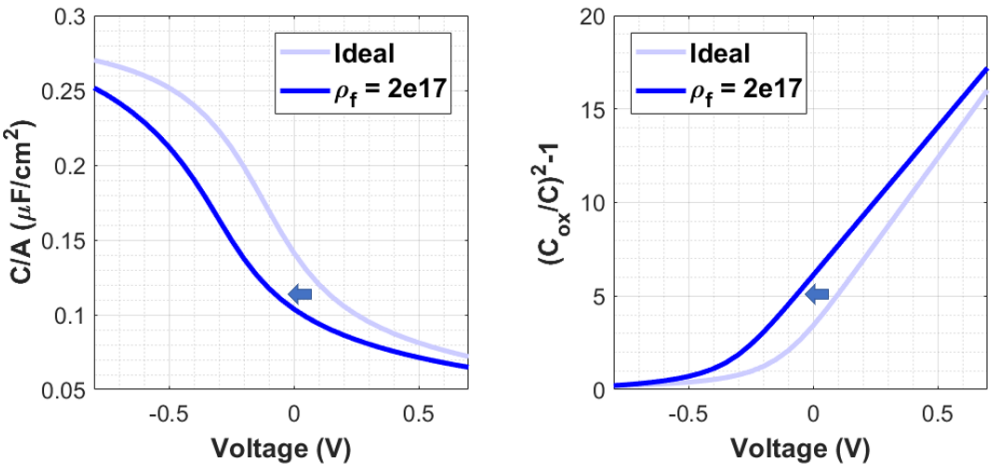

Figure 4.2: Comparison of the simulated 10kHz CV curves obtained on the CIGS/Al_2O_3 MIS model, with and without $\rho_f = 2 * 10^{17} cm^{-3}$ set for each defect type (D_{it} set to zero). There is an obvious leftward shift of $0.2V$ resulting in a new flat-band voltage of $-0.39V$.

negative values of Q_f. The invert trend can be seen on figure A.10 from Appendix B for the donor-type vacancies of Oxygen. Therefore, the actual value of Q_f for a particular sample results from the sum of the different defect densities and is thus subject to major variations depending on the material and composition of the oxide layer, the possible annealing treatments and the processing conditions [23, 44]. The reciprocal of this reasoning states that, by looking at the value of Q_f for a specific MIS sample, some information can be extracted about the dominant defects in the oxide layer of that very sample.

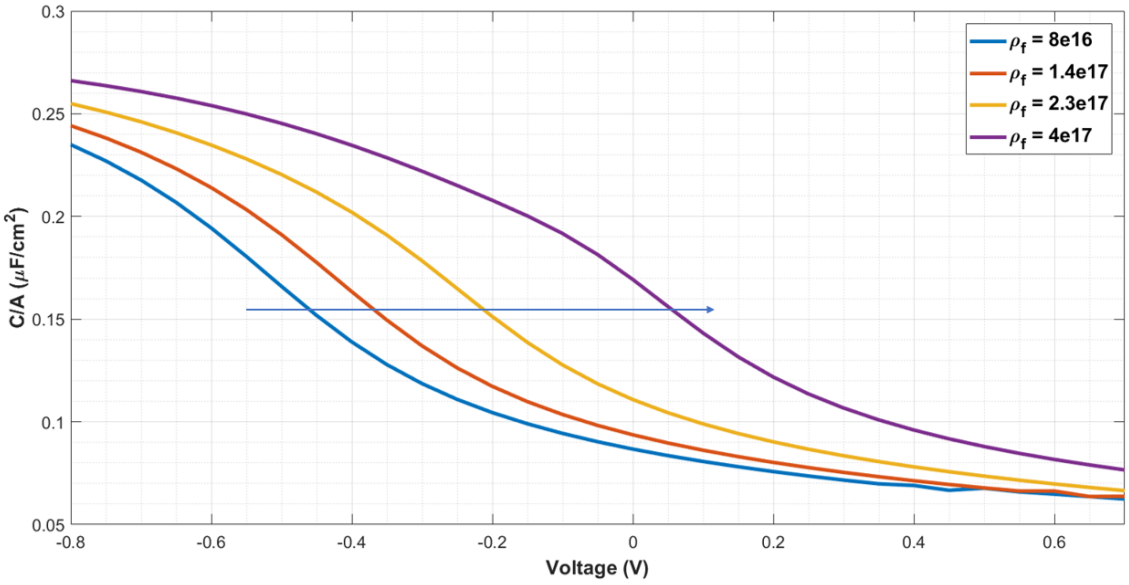

Figure 4.3: Influence of the volumic density of Aluminum vacancies on the 10kHz CV curves (D_{it} set to zero) for an alumina-based MIS capacitor. The voltage shift is rightwards because the vacancies of Aluminum are of the acceptor type.

The same trends are likely to be observed in the case of passivation layers made of hafnia [44] and titania [29] with several differences concerning the respective energy level and

charge state of the native defects. Generally speaking, the interest on the solar cell aspect remains to quantify the resultant Q_f rather than characterize the exact defects densities for each sample. Moreover, it is said in [23, 44] that post-deposition annealing treatments can alter the densities of certain defects in all three oxides and for example activate positive fixed charges in the case of HfO_2. This reveals very interesting in our case since it is precisely one of our criteria for effective front interface passivation. To conclude, the main outcome of this section is the validation of our CIGS/Al_2O_3 MIS capacitor model with regards to field-effect passivation. This provides a point of comparison for the analysis of experimental data presented in sections 4.3 to 4.6 in both the cases of alumina and hafnia. Apart from approving our extraction of V_{fb} and Q_f, this section also provides more insight into the behaviour of the native defects present in alumina.

Density of interface levels - D_{it} The density of levels D_{it} at the Al_2O_3/CIGS interface is the second important variable. The stretch-out of the CV curves related to interface states recombination should evolve in accordance to the magnitude and characteristics of the distribution of traps along the interface. Moreover, as explained in chapter 2, the effect of such defects should be observed on the G_p/ω vs. ω curve as a peak whose frequency position, height and width determine the distribution and value of D_{it}. Since the behaviour of interface traps depends not only on the frequency but also on the voltage, it is interesting to represent the CV and GV data as a function of both quantities at the same time on 2D plots. This way, a clear and straightforward representation of the evolution of the G_p/ω vs. ω curves at different bias is obtained.

Nonetheless, it is mentioned in section 3.3 above that, given the fact that the experimental data obtained for G_p is less reliable than C_p in practice here, the capacitance derivative $-fdC/df$ is usually substituted to G_p/ω. The equivalence between the two expressions is of course firstly verified in the following with simulations. The same comparison for our real experiments is then shown once in section 4.3, leading to the exclusive usage of $-fdC/df$ instead of G_p/ω in the rest of this report. The 2D plot of fdC/df in function of both voltage and frequency is here designated as "2D map". The effect of non-zero interface states density is shown on figures 4.4-4.6 on separate voltage and frequency dependence, in the case of no fixed oxide charges in the alumina layer ($Q_f = 0$ and $V_{fb} = V_{ms} = -0.19eV$). The 10kHz CV curves on figure 4.4 exhibit a peak mainly located in the depletion regime whose magnitude and width both increase with D_{it}. The simulated CV response of the MIS capacitor to the interface states is relatively different from the theoretical curves from chapter 2. The comparison with experimental data is presented in the following sections.

Figure 4.5 illustrates the same variation of D_{it} but observed on the G_p/ω vs. ω curves, for a fixed bias of $0.3V$ (depletion regime where the CV peaks appear). The conductance peaks move up along the frequency axis and their height increase as D_{it} is increasing too. At the lowest values of D_{it} (inset of figure 4.5), there seems to be two different peaks. The peak at highest frequency becomes dominant when D_{it} reaches higher values. The good equivalence between G_p/ω and $-fdC/df$ is visible by comparing figures 4.5 and 4.6, the main difference being that the peaks are narrower when using the capacitance derivative. It is now possible to assess the accuracy of the two D_{it} extraction techniques presented in chapter 2: the conductance method and the HLF capacitance method. The former estimates D_{it} based on the height and width of the conductance peak observed on the

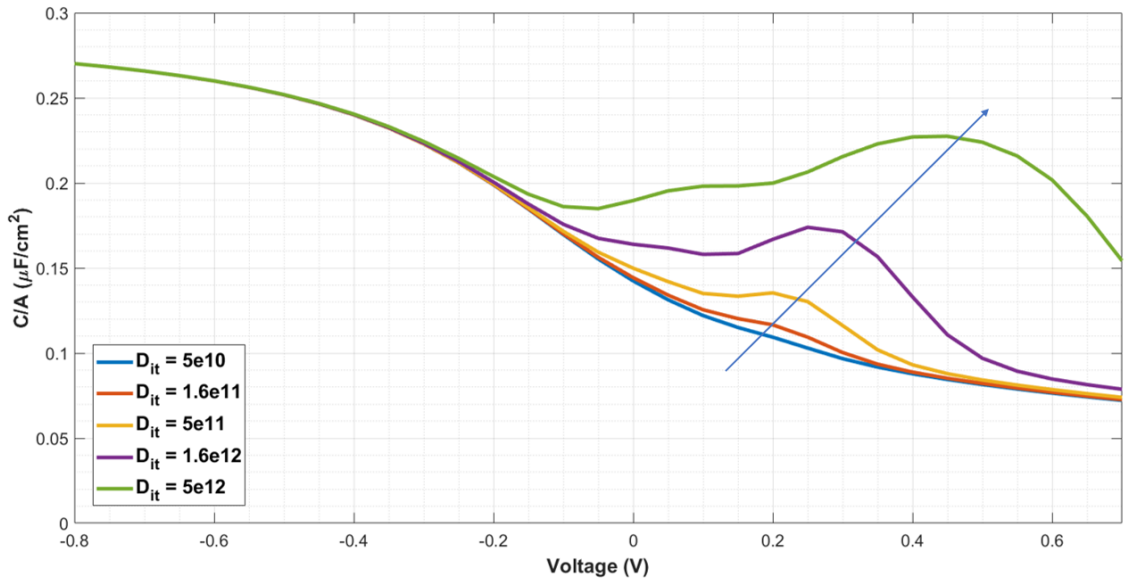

Figure 4.4: Influence of the density of interface traps D_{it} on the simulated CV curves at 10kHz (Q_f set to zero) for an alumina-based MIS capacitor. The acceptor-type defects are introduced at the CIGS/Al_2O_3 interface, with a central energy level located $0.35eV$ above the interface VB edge and a $0.1eV$-wide Gaussian distribution.

$G_p/A\omega$ vs. ω curve at a bias in the depletion or weak inversion regimes, i.e. $0.3V$ in this case. Although the width of the peak is lower when using $-fdC/df$ instead of $G_p/A\omega$, the resulting difference in the estimations of D_{it} should not be significant. Indeed, the correction factor $f_D(\sigma_s)$ in equation 2.7 related to the peak width is not as determinant of D_{it} as the peak height. Furthermore, that factor $f_D(\sigma_s)$ is usually considered constant and equal to 0.4 in practice [6, 7, 18], leading to:

$$D_{it} = \frac{2.5 * \left(\frac{G_p}{A\omega}\right)_{max}}{q} \simeq \frac{2.5 * \left(\frac{-fdC}{df}\right)_{max}}{q} \; [cm^{-2}eV^{-1}] \tag{4.3}$$

The height of the conductance peak for the curves with $D_{it} = 5 * 10^{11}cm^{-2}eV^{-1}$ is around $0.08\mu F/cm^2$, leading to an estimation of $D_{it}^* = 1.3{*}10^{11}cm^{-2}eV^{-1}$ (* denotes the estimated value). This result indicates the difficulty to obtain highly accurate estimations of D_{it}, which is especially the case when the actual value of D_{it} is out of the $10^{10} - 10^{12}cm^{-2}eV^{-1}$ range [34]. This motivates the usage of another extraction technique (HLF method) so as to compare the obtained results.

It is worth mentioning that the objective of our characterization of chemical passivation remains to confirm a value of D_{it} that is of the order of $10^{11}cm^{-2}eV^{-1}$ rather than provide the exact density of interface levels. The HLF method relies on the comparison of two CV curves at high and low frequency, i.e. at respectively 1MHz and 1kHz. The resulting estimated values of D_{it} in function of applied bias are shown on figure 4.7, with an estimated value of $D_{it}^* = 4.7 * 10^{11}cm^{-2}eV^{-1}$ at $0.2V$ compared to the real value of $5 * 10^{11}cm^{-2}eV^{-1}$. Although the HLF method seems more accurate than the conductance method in this case, the coincidence of other effects (series resistance and border traps) on the experimental data makes the HLF technique less reliable than expected in practice

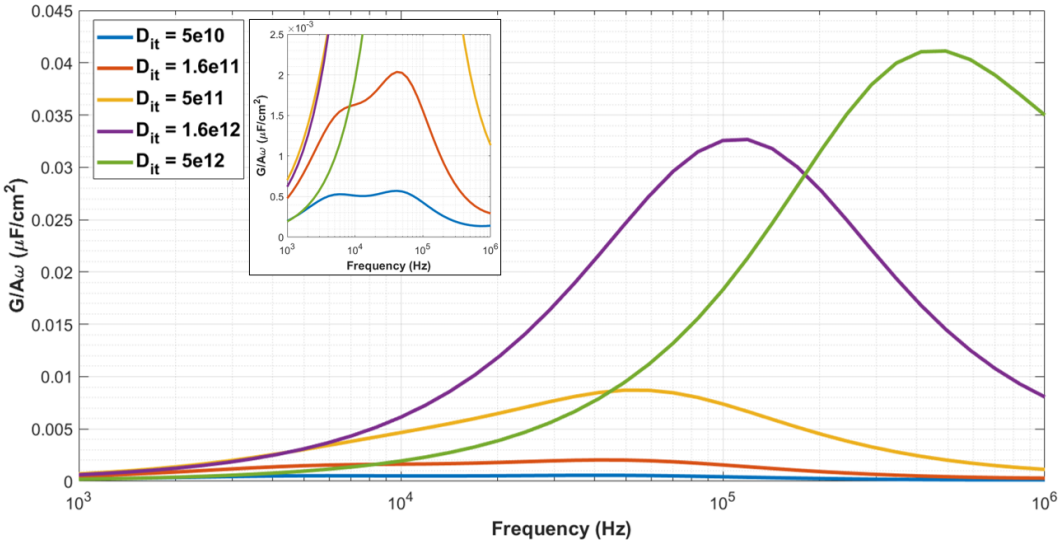

Figure 4.5: Influence of the density of interface traps D_{it} on the simulated $G_p/A\omega$ vs. ω curves at $0.3V$ (Q_f set to zero).The acceptor-type defects are introduced at the CIGS/Al_2O_3 interface, with a central energy level located $0.35eV$ above the VB edge and a $0.1eV$-wide Gaussian distribution. Inset: Zoom on the curves with the lowest D_{it}.

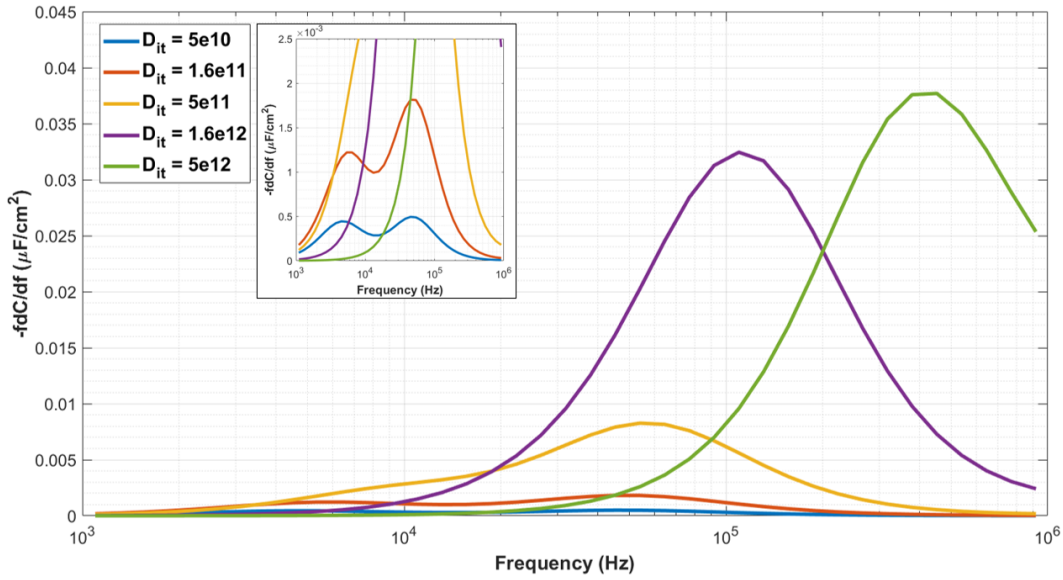

Figure 4.6: Influence of the density of interface traps D_{it} on the simulated $-fdC/df$ vs. f curves at $0.3V$ (Q_f set to zero). The acceptor-type defects are introduced at the CIGS/Al_2O_3 interface, with a central energy level located $0.35eV$ above the VB edge and a $0.1eV$-wide Gaussian distribution. Inset: Zoom on the curves with the lowest D_{it}.

(section 4.3). In particular, the theoretical perfect superimposition of the simulated CV curves on figure 4.7 explains the high accuracy with which D_{it} is estimated. As investigated in the rest of this chapter, this is not necessarily the case for our realistic samples.

It is discussed hereabove that representing the evolution of G_p/ω or equivalently $-fdC/df$ in function of voltage and frequency at the same time on "2D maps" can provide a general overview of the CV behaviour of a particular sample. This requires to use sufficient amounts of both voltage and frequency points in the chosen ranges so that the resolution

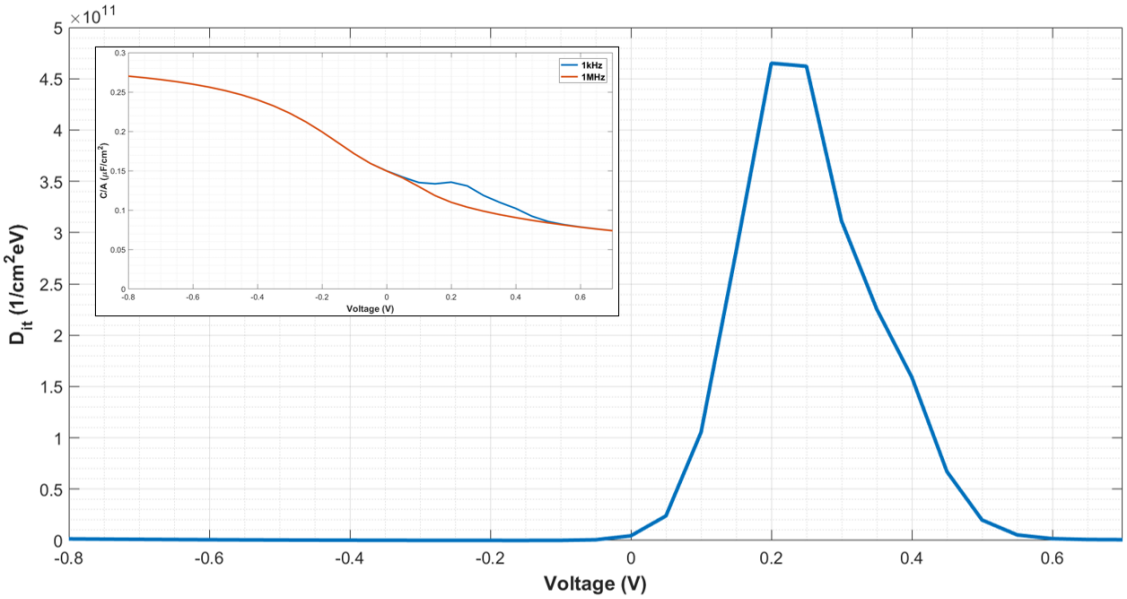

Figure 4.7: Extraction of the value of D_{it} with the HLF method in function of the applied bias, using two simulated CV curves at 1kHz and 1MHz shown in the inset (Q_f set to zero). The actual value of D_{it} is $D_{it} = 5 * 10^{11}$, for acceptor-type defects introduced at the CIGS/Al_2O_3 interface, with a central energy level located $0.35eV$ above the interface VB edge and a $0.1eV$-wide Gaussian distribution. The estimated value is $D_{it}^{*} = 4.7 * 10^{11} cm^{-2} eV^{-1}$ at $0.2V$.

of the map is adequate. An example of CV curves and corresponding simulated 2D map is shown on figure 4.8 with both interface and oxide bulk defects introduced. Their energy distributions are the same as above in this section.

The interface-trap peaks appearing in the depletion regime of the CV curves are identified as a diagonal trail on the 2D map (figure 4.8 right). Since low values of D_{it} might result in CV data exhibiting only slight modifications compared to the ideal case (e.g. the CV curve for $D_{it} = 1.6 * 10^{11} cm^{-2} eV^{-1}$ on figure 4.4), it may be useful to identify the 2D response corresponding to a certain energy position of interface defects (shallow or deep levels below midgap energy). Indeed, as the interface-trap time constant τ_{it} introduced in section 2.7.3.2 depends on the energy distribution of the concerned defects (section 2.7.3.2), the corresponding 2D response also depends on that parameter.

Therefore, the knowledge of the 2D signatures associated to the different general types of interface states in the lower half of the bandgap allows a graphical analysis of the features present in a given sample. Spotting the same response as figure 4.8 on the measured 2D map of a given sample then suggests that similar interface states are likely to be present with a non-negligible density in that very sample, i.e. acceptor-type interface defects at $0.35eV$ above the VB edge. The precise shape and location of that interface response mainly depend on the density of interface states and their energy position. In particular, higher (resp. lower) central energies translate into a downward (resp. an upward) shift of the diagonal 2D response as shown on figure A.11 in Appendix B.

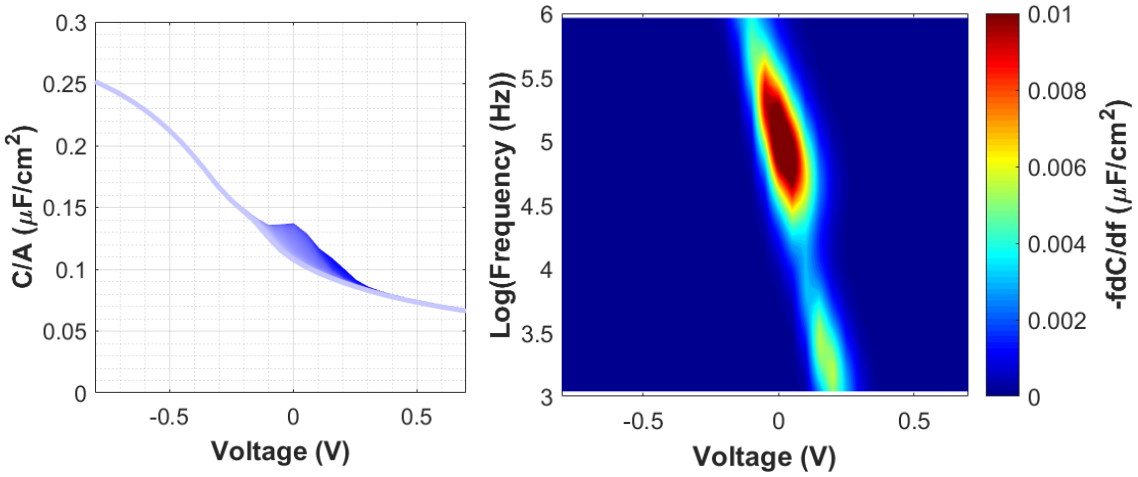

Figure 4.8: SCAPS simulations of the combined effect of interface traps ($D_{it} = 5 * 10^{11} cm^{-2} eV^{-1}$) and oxide fixed charges ($\rho_f = 2 * 10^{17} cm^{-3}$ for each bulk defect in the oxide) on the CV results of an alumina-based MIS capacitor. Left: capacitance per unit area vs. voltage, at frequencies from 1kHz (dark blue) to 1MHz (light blue). Right: voltage-frequency evolution of the capacitance derivative $-fdC/df$.

4.2.2 MATLAB

The MATLAB model for alumina-based MIS capacitor, taken from [43], presents several differences and similarities with SCAPS: on the one hand, it does not allow to insert bulk oxide defects in the same way as SCAPS whereas it is possible to introduce border traps in the oxide layer instead (utilized further in this chapter); on the other hand, both the SCAPS and MATLAB models enable to simulate multiple interface defects with arbitrary energetic distributions and both provide similar results. More details about this model are presented in Appendix B and in [43].

Figure 4.9 illustrates the 2D signature of acceptor-type interface traps with a density of $D_{it} = 5 * 10^{11} cm^{-2} eV^{-1}$ and located at $0.35eV$ above the VB edge, to be compared with the 2D map obtained via SCAPS on figure 4.8 (MATLAB results for other interface traps distribution also in Appendix B). Apart from a slight voltage shift between the two simulations due to the presence of oxide bulk defects in SCAPS and not MATLAB, the CV response and 2D signature have relatively similar features: diagonal shape on the 2D map and slight peaks shifting with frequency on the CV curves. The comparison with experimental data presented in the next section attempts to determine which one of the two simulations models gives the more reliable results, while considering additional effects such as multiple interface states, series resistance and border traps.

4.3 CV analysis methodology

This section illustrates how all the different concepts presented up to here about CV measurements apply in the case of real MIS samples from the AL series. The purpose is to show not only the similarities but also the differences between, on one side, the theoretical expectations and simulated results, and on the other side, the observations made on the

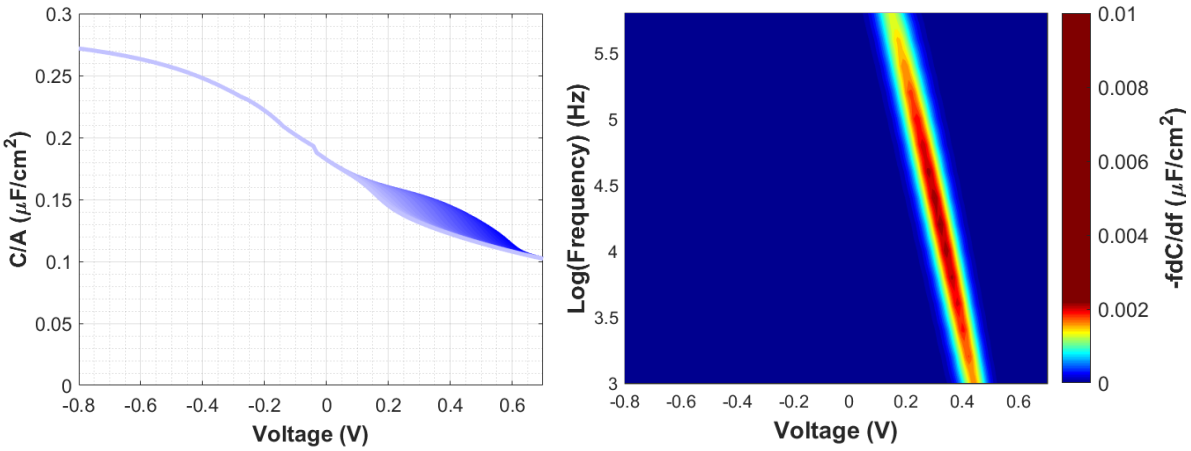

Figure 4.9: MATLAB simulations of the effect of interface traps ($D_{it} = 5 * 10^{11} cm^{-2} eV^{-1}$) on the CV results of an alumina-based MIS capacitor. Left: capacitance per unit area vs. voltage, at frequencies from 1kHz (dark blue) to 1MHz (light blue). Right: voltage-frequency evolution of the capacitance derivative $-fdC/df$.

experimental data. In particular, two supplementary effects mentioned above, i.e. series resistance and border traps density, have a non-negligible influence on the behaviour of the samples studied in this report. Their impact as well as their physical origin are discussed below with the help of further SCAPS and MATLAB simulations. The end of this section consists in extracting the two important figures-of-merit D_{it} and Q_f from the CV measurements obtained and presenting the accuracy range related to the variability of parameters used in the Q_f extraction.

4.3.1 Preliminary observations

First of all, general observations are expressed about the raw data obtained by realizing the $C_p - V - f$ and $G_p - V - f$ measurements on the AL1 sample (figure 4.10), i.e. a typical MIS structure with a $1.6\mu m$-thick CIGS layer and a $20nm$-thick Al_2O_3 layer. On the left of figure 4.10, the capacitance measured at low frequency (dark blue) presents the two expected accumulation and depletion plateaus at respectively high negative and positive bias, separated by a relatively steep transition zone around 0V. In the accumulation regime, the value of C_p is as expected slightly below the theoretical oxide capacitance $C_{ox} = \frac{\epsilon_0 \epsilon_{ox}}{t_{ox}} = 0.3 \mu F/cm^2$ with $\epsilon_{ox} = 6.7$ the relative dielectric permittivity of Al_2O_3 [32], $\epsilon_0 = 8.85 * 10^{-12} F/m$ the vacuum dielectric permittivity and $t_{ox} = 20nm$ the oxide thickness of the AL1 sample. As the bias increases until reaching the depletion regime, the capacitance quickly drops by a factor 10 in the surroundings of the flat-band voltage V_{fb} (accurate extraction in section 4.3.3 below).

Apart from that, two phenomena can be observed on figure 4.10: first, there is a downward dispersion of the measured capacitance at high frequency from the accumulation regime until the beginning of depletion, i.e. from $-1.5V$ until $0.3V$ approximately. The corresponding 2D signature is the relatively large "island" located on the top left corner of the map. The origin of this effect is discussed just below; second, the 2D map also presents a diagonal frequency response located in the depletion regime, i.e. roughly between $0V$ and

$1V$, and present at most frequencies (highlighted in white on the 2D map). It translates into a slight modification of the slope of the CV curves in the vicinity of the "elbow" present at the inset of the depletion-to-accumulation transition, i.e. around 0.25V. As demonstrated above with simulations, this diagonal signature is very likely related to interface-trap conductance peaks from which an estimation of D_{it} is obtained at the end of this section.

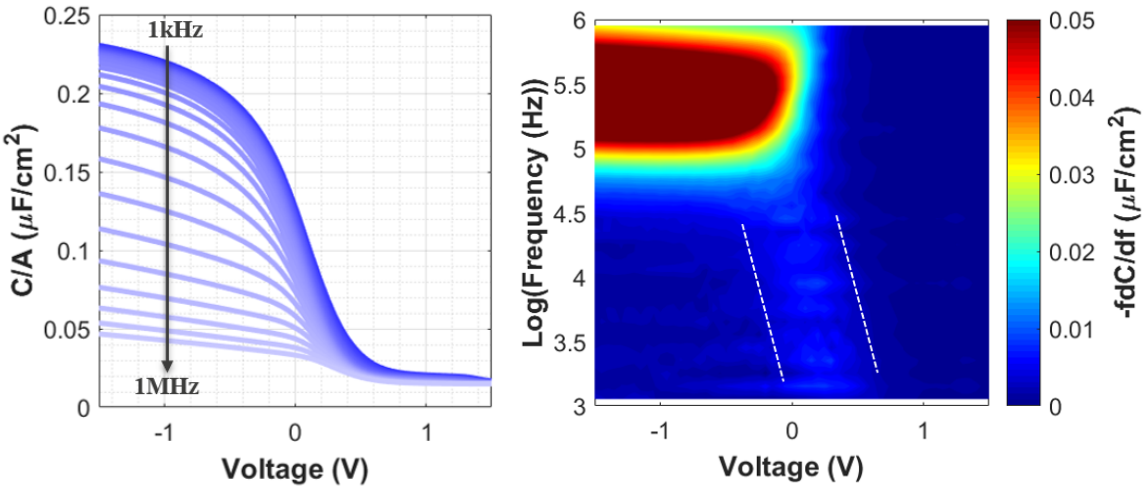

Figure 4.10: Raw measurements obtained on the AL1 sample. Left: Measured capacitance per unit area vs. voltage, at frequencies from 1kHz (light blue) to 1MHz (dark blue). Right: Voltage-frequency 2D map of the capacitance derivative $-fdC/df$ with the 2D signature of interface states highlighted by two dotted white lines.

4.3.2 Series resistance

The CV response observed at high frequency and mostly for negative bias on figure 4.10 is typically related to the effect of a parasitic series resistance, designated R_s here, as mentioned in [45]. The capacitance drop occurring at high frequency translates into the large 2D signature present on the voltage-frequency map. The physical origin of this series resistance effect is, in our opinion, two-fold.

Border traps First, based on the results obtained for III/V MOS structures in [43, 46, 47], it is admitted in [13] that the co-existence of a "border traps" density [48] in the Al_2O_3 layer next to the usual interface traps density induces non-negligible series resistance effects through tunneling in the conduction and valence band. The simulated CV degradation corresponding to a $5*10^{19}cm^{-3}$ density of border traps present at the VB edge is shown on figure 4.11. The central energy level of the border traps energy distribution is set at the VB maximum with a characteristic energy of 0.1eV. The spatial distribution of these border traps is concentrated near the Oxide/CIGS interface with a relatively narrow extension, i.e. 2nm, through the oxide thickness. The slight CV frequency dispersion (highlighted in red) and spread out low-magnitude 2D signature indicate a border traps response that is moderately affecting every frequency. This CV feature is rather similar to the trend observed for the experimental CV curves at the lowest frequencies on figure 4.10. However,

the presence of border traps cannot explain the much larger CV frequency dispersion affecting the highest frequencies, contrarily to the phenomenon discussed hereafter.

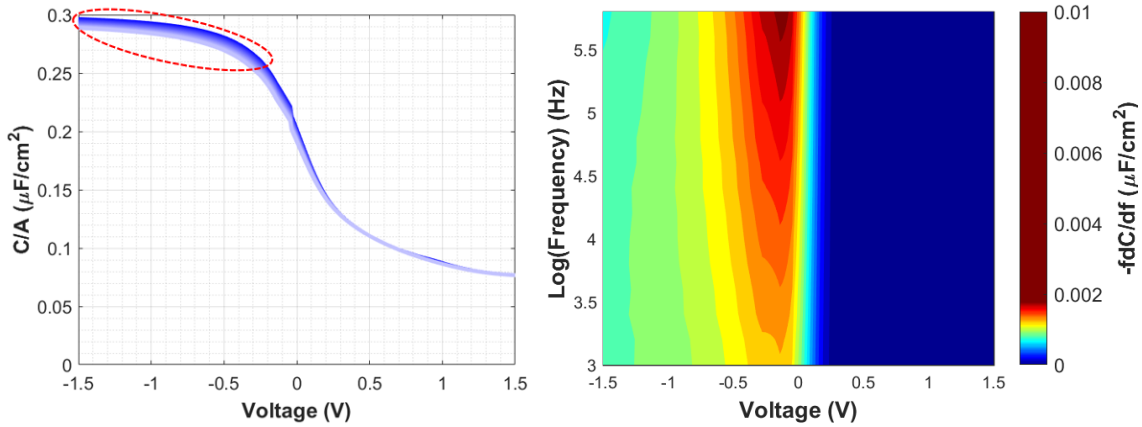

Figure 4.11: MATLAB simulations of the effect of border traps located at the VB edge and physically concentrated next to the Oxide/CIGS interface. Left: Capacitance per unit area vs. voltage, at frequencies from 1kHz (dark blue) to 1MHz (light blue). Right: Voltage-frequency 2D map of the capacitance derivative $-fdC/df$ with a lower scale than figure 4.10 for the sake of clarity.

$MoSe_2$ potential barrier Indeed, an interfacial layer made of $MoSe_2$ usually grows between the Mo/NaF and CIGS layers consequently to the selenization step of CIGS co-evaporation [49, 50], resulting in a Mo/NaF/$MoSe_2$/CIGS back contact interface. Contrarily to effective TiN or MoN_x barrier layers [49], the NaF Sodium precursor layer is relatively thinner (6nm) and, even though the Sodium content of the CIGS impacts the formation of $MoSe_2$ [49, 50], not supposed to completely block the growth of $MoSe_2$. Therefore, it is reasonable to think that the somewhat uncontrolled growth of that interfacial $MoSe_2$ layer may bring its thickness out of the optimal range. This could in turn create a resistive potential barrier at the back interface [49], represented as a fixed resistance R_s in series with the whole equivalent circuit. Since the deposition of the Silver front grid is considered as reliable and providing quasi-ohmic contacts, the oxide (border traps) and the back interface ($MoSe_2$ and NaF precursor layer) are the most likely places from which this series resistance could originate.

The results of the MATLAB simulation with an extra resistance $R_s = 1\Omega.cm^2$ connected in series are shown on figure 4.12. The resemblance between the experimental data (figure 4.10) and simulated results (figure 4.12) tends to demonstrate that the high frequency response observed on our measurements is well related to series resistance. Actually, the comparison of the simulated CV curves for the individual effect of border traps and fixed series resistance to the experimental results suggests that both effects may simultaneously occur in that very sample. This is further highlighted by the simulations of both constant R_s and border traps density on figure 4.13. Eventually, besides the diagonal response probably related to interface states, it appears from the simulated results that the AL1 sample is also affected by a potential barrier-related series resistance at the back interface and a non-negligible density of border traps near the VB edge.

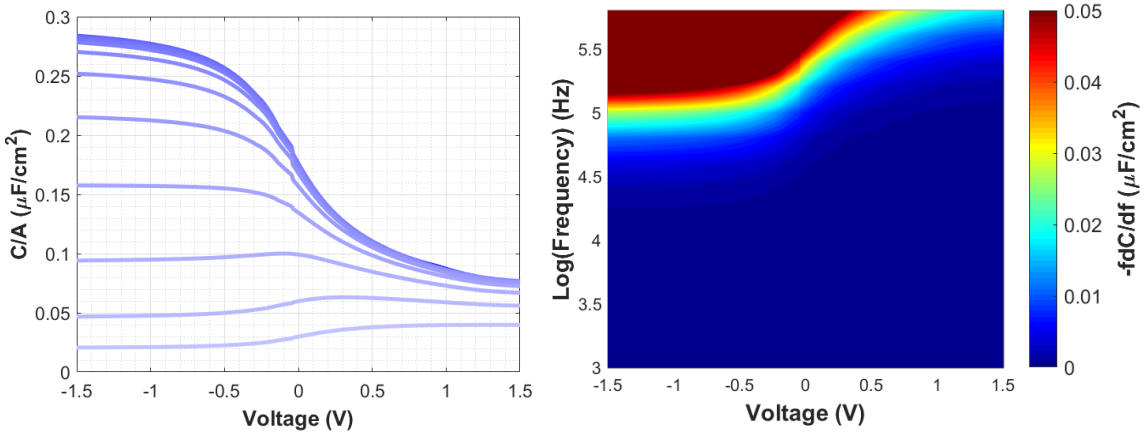

Figure 4.12: MATLAB simulations of the effect of fixed series resistance $R_s = 1\Omega.cm^2$. Left: Capacitance per unit area vs. voltage, at frequencies from 1kHz (dark blue) to 1MHz (light blue). Right: Voltage-frequency 2D map of the capacitance derivative $-fdC/df$.

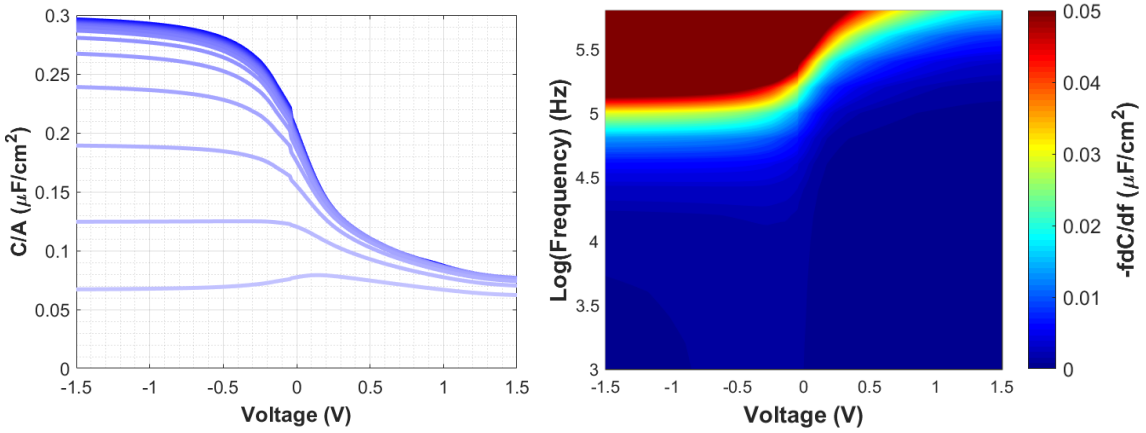

Figure 4.13: MATLAB simulations of the combined effect of fixed series resistance $R_s = 1\Omega.cm^2$ and border traps density of $5 * 10^{19} cm^{-3}$ at the VB edge. Left: Capacitance per unit area vs. voltage, at frequencies from 1kHz (dark blue) to 1MHz (light blue). Right: Voltage-frequency 2D map of the capacitance derivative $-fdC/df$.

Determination of $MoSe_2$ potential barrier One way to demonstrate the effective presence of a resistive potential barrier at the back interface would be to show its log-linear temperature dependency. Moreover, this would also allow to extract its height as in [51]. If one finds a height of the potential barrier that corresponds to the energy bands alignment between the $MoSe_2$ and CIGS, it is likely to be the origin of the series resistance response observed on the measurements. In [51] they report a very thin $MoSe_2$ layer below the CIGS which in turn induces a rather low potential barrier of $5.6meV$. Let us check the results in our case using temperature-dependent CV measurements on one sample concerned by the effect of series R, i.e. the AL4 sample, which is highly similar to the AL1 sample.

It is visible on figure 4.14 that, as the value of the series resistance is increasing, the corresponding 2D island is moving downward on the capacitance derivative map. This

illustrates the fact that the capacitive impedance Z_{C_p} becomes comparable to R_s at lower frequency when the value of R_s is higher. Therefore, the lower the series resistance 2D responses appears on the 2D map, the higher the value of R_s. Since the series resistance related to a potential barrier is a decreasing function of the temperature [51], our experimental 2D maps at lower temperature should exhibit a downward shift of the R_s response.

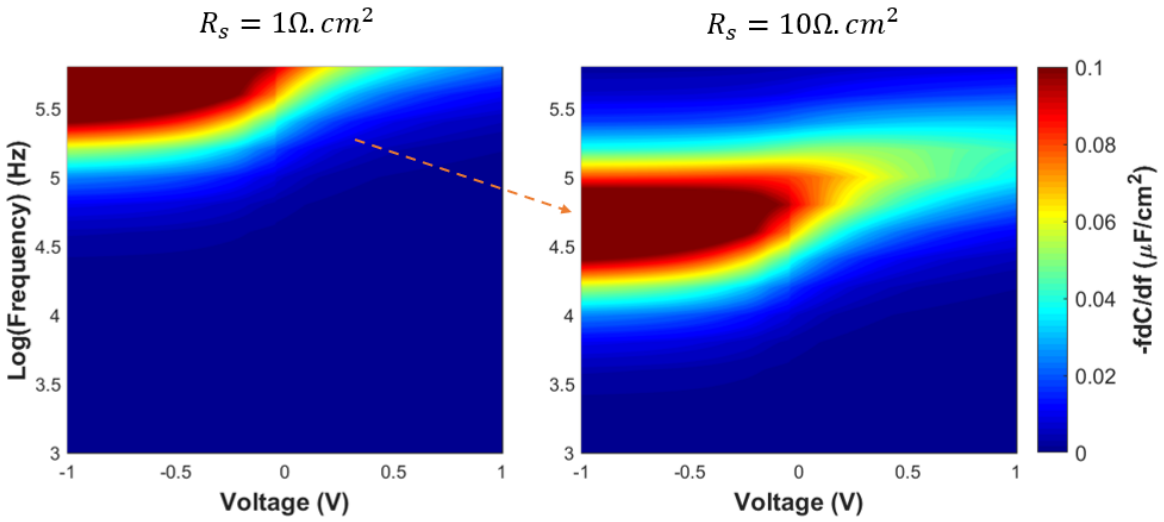

Figure 4.14: MATLAB simulations of the increase of series resistance from $1\Omega.cm^2$ to $10\Omega.cm^2$. The 2D response is shifted downwards because the dominance of the capacitive impedance occurs at lower frequency when R_s is increased.

This is precisely the trend observed in our measurements on figure 4.15. In particular, it is expressed in [51] that, at temperatures lower than 300K, the total series resistance is related to the temperature T and to the potential barrier height ΔE through this equation:

$$R_s = \frac{k}{qA^*T} \exp\left(\frac{\Delta E}{kT/q}\right) \tag{4.4}$$

in which A^* is the effective Richardson constant. Therefore, by plotting the evolution of $\ln(R_sT)$ in function of the inverse thermal energy $1/kT$, one should obtain an increasing linear curve whose slope is precisely ΔE. However, on the one hand, the extraction of R_s based on IV measurements is not straightforward for MIS capacitors, and on the other hand, the realization of both IV and CV measurements at each temperature point was complex to achieve with the primary low-temperature setup described in section 3.3.4. A graphical alternative is to use MATLAB simulations so as to roughly estimate the value of R_s for each temperature.

Indeed, by matching the position of the simulated 2D response of a given series resistance to the experimental obtained at a certain temperature, it is possible to obtain an estimation of the actual value of R_s at that temperature, for example by comparing figures 4.14 and 4.15. This procedure is then applied, with a trial-and-error approach, to the experimental data at every relevant temperature and the estimated values of R_s are reported. Eventually, the $\ln(R_sT)$ vs. $1/kT$ plot is shown on figure 4.16, exhibiting a potential barrier height of 182.3meV, much higher than what is reported in [51]. This may be explained by differences in the processing recipes and back interface composition (barrier layer, precursor layer, ...)

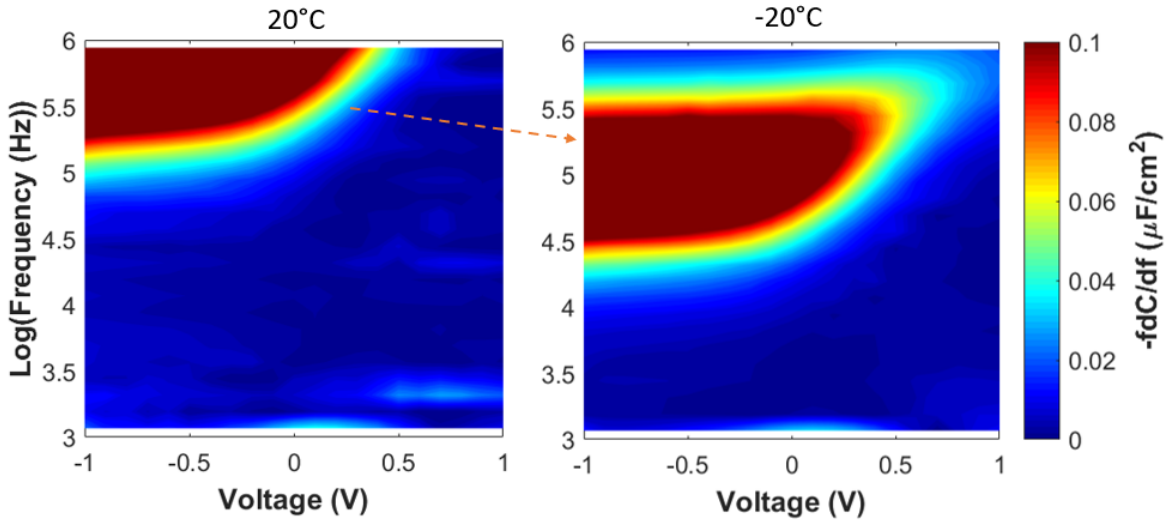

Figure 4.15: Experimental CV data showing the increase of series resistance at lower temperature, from 20°C to -20°C. The 2D response is shifted downwards because the dominance of the capacitive impedance occurs at lower frequency when R_s is increased.

as compared to the samples from [51]. In our case, it seems that the uncontrolled growth of $MoSe_2$ at the back interface leads to a relatively high and resistive potential barrier, which may in turn be detrimental for complete solar cells given the importance of low series resistance with regards to efficiency.

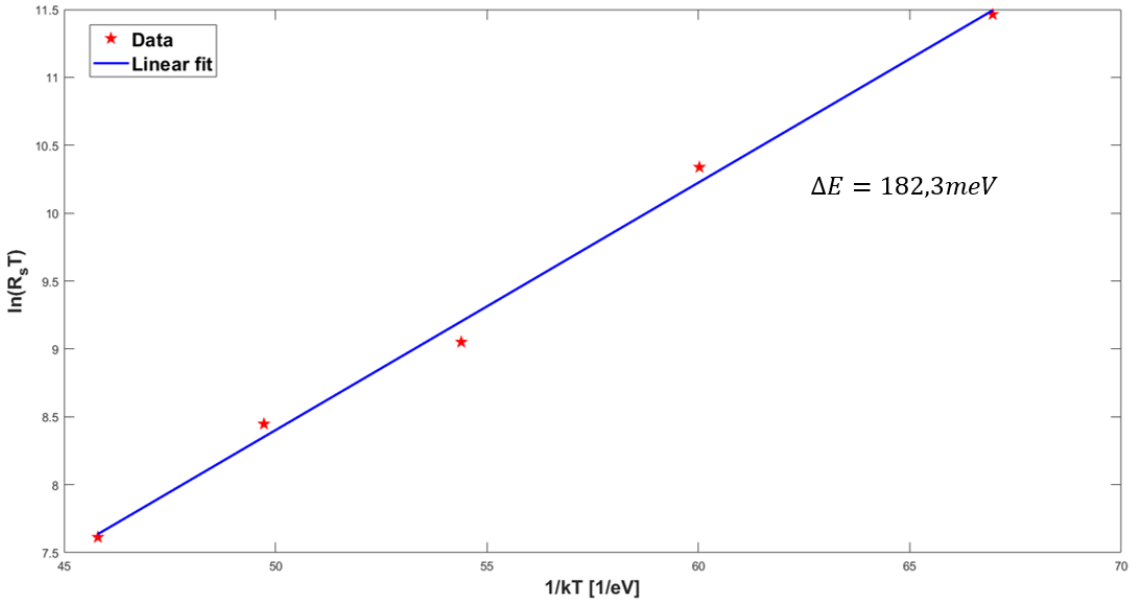

Figure 4.16: Determination of the height of the $MoSe_2$ resistive potential barrier at the back interface of the AL9 sample, estimated to be $\Delta E = 182.3meV$ by linear interpolation through the values of R_s estimated using MATLAB simulations.

Impedance of equivalent circuit Now that the origin and the effective presence of series resistance have been discussed and confronted to simulations, we can check if the trends observed on our measurements are in accordance with a simple reasoning about

frequency dependence of capacitive impedance. First of all, we know from section 2.11 and 3.3 that the C-V measurement tool, i.e. the LCR meter, attempts to discriminate and measure two quantities: C_p and G_p as presented on figure 4.17a. One hypothesis that we make here is that our samples are non-leaky, i.e. their shunt resistance R_{sh} (also designated as R_p) is very high, and thus the right branch of the circuit is close to an open-circuit. This assumption, whose veracity is discussed below with I-V measurements, has two implications: first, the circuit on figure 4.17a simplifies to a single capacitor C_p whose value can then be accurately determined by the measurement tool; second, the measured parallel conductance $G_p = \frac{1}{R_{sh}}$ remains comparatively low since R_{sh} is considered high.

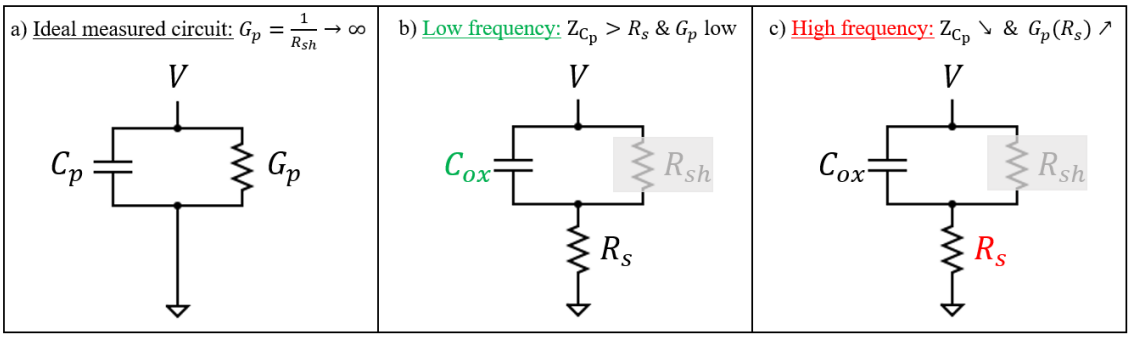

Figure 4.17: Equivalent circuit measured in accumulation by the LCR meter and effect of series resistance.

Both these suppositions are in accordance with the low-frequency measurements of C_p and G_p ("100Hz" case on figure 4.18). However, we believe that in practice there is another element being measured by the tool, which is precisely the series resistance R_s, and that justifies the observed high-frequency response. Wee limit our reasoning to the accumulation regime, i.e. at-1.5V, where the measured capacitance should ideally be equal to the oxide capacitance C_{ox}. Let the frequency-dependent impedance related to C_p be expressed as $Z_{C_p}(j\omega) = \frac{1}{j\omega C_p}$ where j is the imaginary unit and ω is the angular frequency. If we keep considering the shunt resistance as an open circuit, the equivalent circuit in accumulation is now composed of $C_p = C_{ox}$ in series with R_s (figure 4.17b and c), which means that the measured parallel admittance Y_p composed of C_p and G_p is now influenced by R_s.

At low frequency, for example 1kHz, we have that $|Z_{C_p}| = \frac{1}{2\pi * 10^3 * C_{ox}} \simeq 550\Omega.cm^2$ is in series with a much smaller R_s, typically of the order of $1\Omega.cm^2$ as seen above in the simulations. As the capacitive impedance remains dominant in that frequency range (figure 4.17b), the effect of R_s is not apparent at low frequency on figure 4.10 and 4.18. C_p is accurately measured by the tool and the low-frequency C-V curves have the expected shape and magnitude without any frequency dispersion (no island on the 2D map). The value of the measured conductance G_p is of the order of several μS which well corresponds to a high shunt resistance of several $M\Omega.cm^2$.

As the frequency keeps on increasing beyond 100kHz, the magnitude of Z_{C_p} decreases below $5\Omega.cm^2$ and becomes comparable to R_s. The consequence of that is the increase of the conductive part of the total admittance at the expense of the parallel capacitance. If the frequency keeps increasing, R_s becomes more and more prominent and C_p drops greatly

which creates the downwards broadening of the C-V curves at high frequency ("1MHz" case of figure 4.18). On this very figure, one can see at 1MHz that C_p has decreased by roughly a factor 5 compared to 100Hz and that G_p is nearly equal to $0.3 S/cm^2$ which is high for an ideally non-conductive MIS structure.

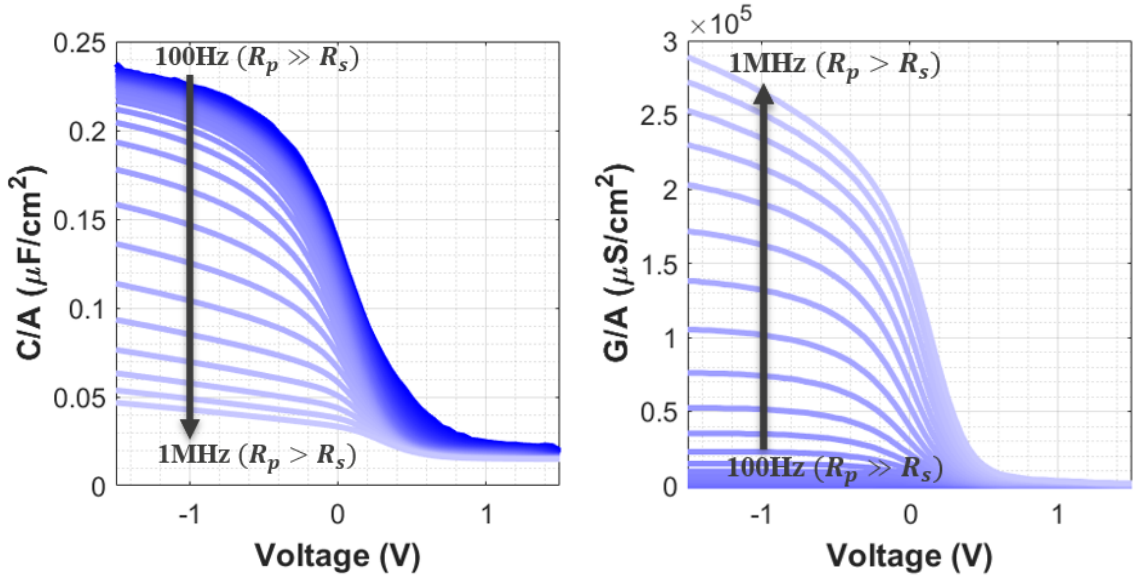

Figure 4.18: High-frequency broadening of the C-V and G-V curves obtained on the AL1 sample (R_p and R_s are respectively the shunt and series resistance). Left: measured capacitance per unit area vs. voltage, at frequencies from 100Hz (dark blue) to 1MHz (light blue). Right: measured conductance per unit area vs. voltage, at frequencies from 100Hz (dark blue) to 1MHz (light blue).

Shunt resistance Let us now verify that our previous assumption about the relative values of series and shunt resistance is correct. For ideal MIS structures, the current through the oxide should be zero at anytime, which then results in an infinite shunt resistance. In practice, R_p is not infinite and small currents can still circulate through the dielectric. The IV measurements realized on the AL4 sample, highly similar to the AL1 sample, are shown on figure 4.19. These results do not indicate particularly high leakage currents, with a current density lower than $0.2 mA/cm^2$ and a shunt resistance R_p (taken equal to dV/dJ in the surroundings of $0V$) which is around $0.2 M\Omega.cm^2$, much higher than the series resistance discussed hereabove.

"Two-frequency" correction Since the extraction of Q_f and D_{it} greatly relies on the CV data, it may be interesting to investigate a solution to correct this effect of series resistance so as to refine our measurements but also to have another estimation of R_s than through simulations. It is explained in [45] that if the value of R_p is known, it becomes possible to isolate the real capacitance value C_0 from the measured value C_m that is degraded by different parasitic elements at high frequency. In order to do that, the solution proposed in [45] is to use the measured G_p and C_p at two different frequencies, i.e. "two-frequency C-V correction", so as to eliminate the contribution of different parasitic elements such as series resistance. By using the G_p and C_p measured at two different

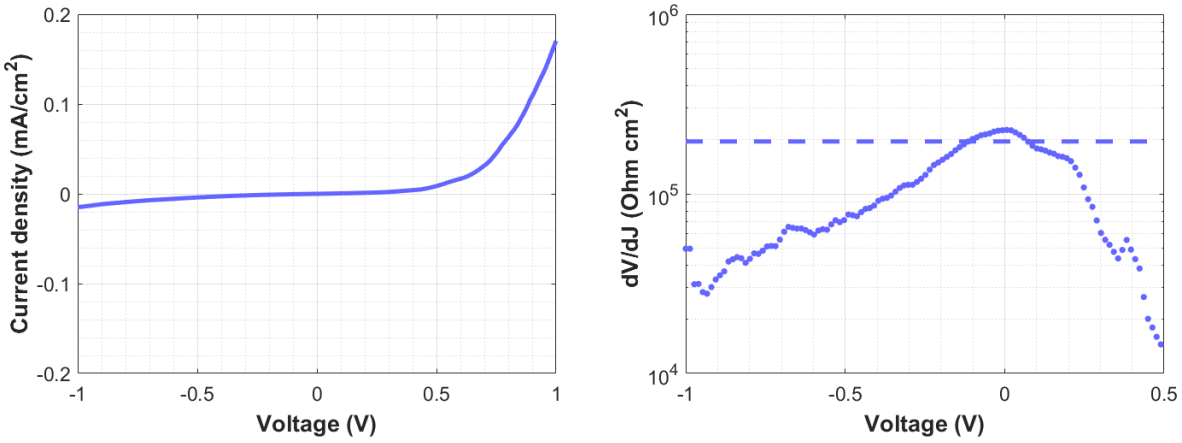

Figure 4.19: IV measurements obtained on the AL4 sample. Left: Measured current density vs. voltage in dark environment. Right: Derivative of the voltage with respect to the current density (dV/dJ) vs. voltage, extraction of the shunt resistance $R_p = R_{sh} = 0.2M\Omega.cm^2$.

frequencies, the capacitance C_0 corrected for the effect of parasitics is obtained:

$$C_0 = \frac{(\omega_2^2 - \omega_1^2)(G_{p1}^2 + \omega_1^2 C_{p1}^2)(G_{p2}^2 + \omega_2^2 C_{p2}^2)}{\omega_1^2\omega_2^2\Big(C_{p1}(G_{p2}^2 + \omega_2^2 C_{p2}^2) - C_{p2}(G_{p1}^2 + \omega_1^2 C_{p1}^2)\Big)} \tag{4.5}$$

in which ω is the angular frequency, G_p and C_p are the measured parallel conductance and capacitance, and index 1 and 2 refer to the two frequencies used for the correction. Given the width of the step between two adjacent frequencies on our 2D maps, the method presented in [45] is rather used here to estimate the value of R_s for a given sample as well as, in some cases, providing a corrected high frequency capacitance curve (typically using 1kHz-1MHz correction) to compute D_{it} with the HLF technique.

Indeed, not only it is still possible to identify the interface-trap response on the non-corrected 2D map, but also the values of D_{it} obtained with the HLF method can generally be extracted in such a voltage range that is not greatly affected by series resistance. These considerations are discussed in the following. By inspecting the 2D map on figure 4.10, one can identify the frequency at which the series resistance effect becomes significant to be around 100kHz. The CV curves resulting from the correction with similar frequency pairs to [45] are shown on figure 4.20, with an estimated mean value of R_s around $1.8\Omega.cm^2$ in accumulation, i.e. at -1.5V. This value of series resistance is in agreement with the previous MATLAB simulations and its validity is also verified with SCAPS simulations in the next paragraph.

SCAPS simulation We can also compare our observations and MATLAB simulations about the series resistance effect with SCAPS simulations (figure 4.21), in which the other parameters such as D_{it}, Q_f and the density of border traps are not considered. The input values of series and shunt resistance used in our SCAPS simulations are the ones extracted and presented above in this section, i.e. respectively $R_s = 1.8\Omega.cm^2$ and $R_{sh} = 0.2M\Omega.cm^2$. On the whole, the simulated curves on figure 4.21 show frequency responses that are similar to the ones observed on the measurements (figure 4.10).

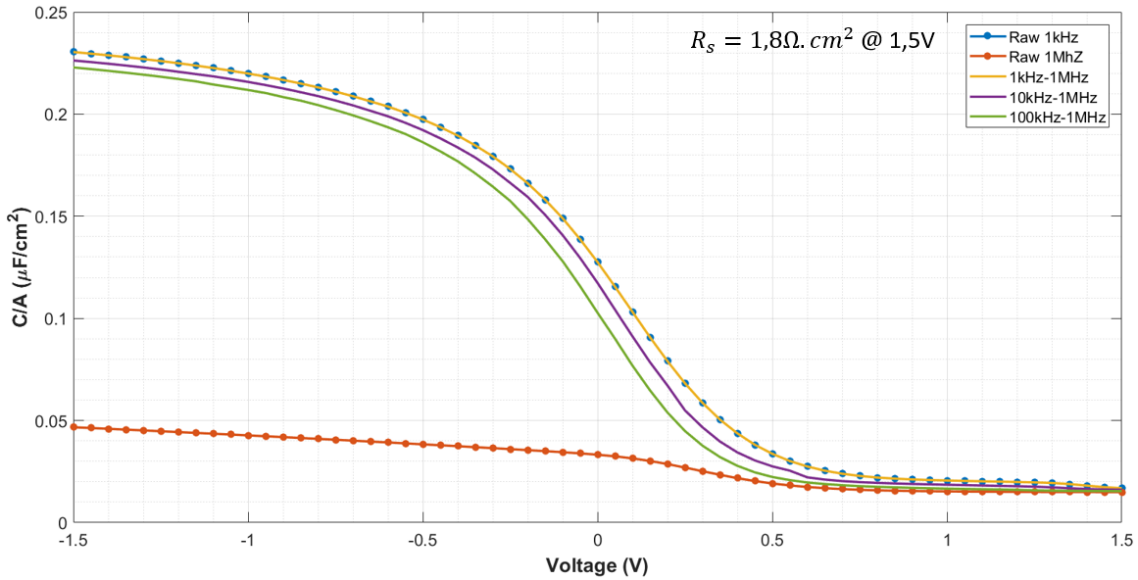

Figure 4.20: Comparison of raw (lines with circles) and two-frequency corrected (simple lines) CV curves for the AL1 sample. The best correction is obtained with the highest frequency gap, i.e. 1kHz-1MHz. The resulting estimation of R_s varies between 1.5Ω.cm^2 and 2.1Ω.cm^2 depending on the frequency chosen for the computation of parasitic circuit elements.

However, our SCAPS model for the effect of series resistance is not flawless since it considers a constant value of R_s for every combination of parameters, which might not be the case in practice for our actual samples. Moreover, the physical origin of R_s is ambiguous with the concurrency of border traps and resistive potential barrier potentially leading to voltage and frequency-dependent values of R_s.

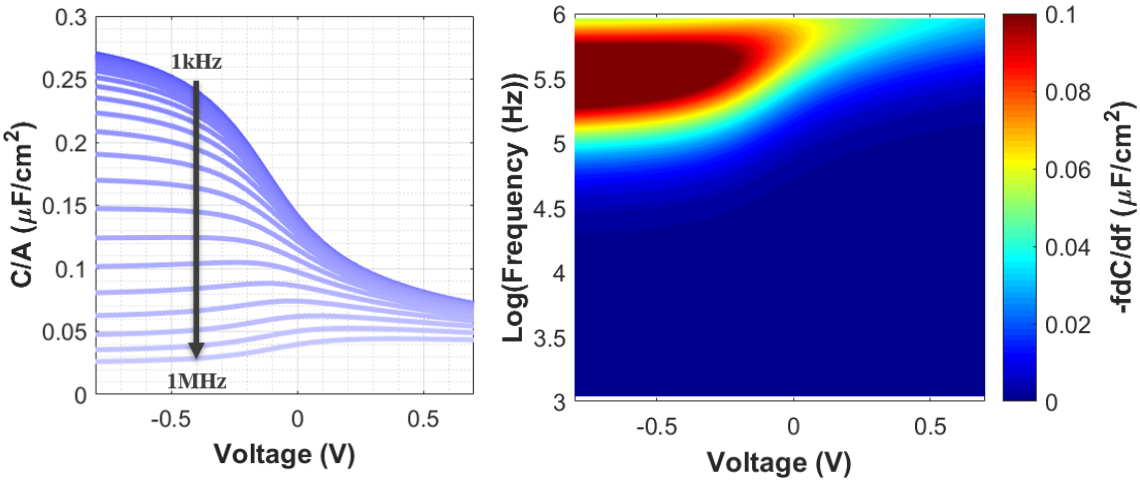

Figure 4.21: SCAPS simulations of the frequency dispersion due to series resistance effect ($R_s = 1.8\Omega.cm^2$ and $R_{sh} = 0.2M\Omega.cm^2$). Left: Capacitance-voltage curves at frequencies from 1kHz to 1MHz. Right: Voltage-Frequency 2D map of $-fdC/df$.

4.3.3 Field-effect passivation

The second step of our methodology is to extract V_{fb} and then Q_f in order to characterize and quantify the field-effect passivation in the AL1 sample. As a reminder from section 2.4.2, with the appropriate sign (positive in our case), the effective density of fixed charges Q_f present at the bottom surface of the oxide repels the holes and limit recombination mechanisms. In that very section it is presented that the flat-band voltage V_{fb} is the only unknown quantity in the mathematical expression of Q_f:

$$Q_f = C_{ox} * \frac{V_{ms} - V_{fb}}{q} \ [cm^{-2}] \tag{4.6}$$

in which $C_{ox} = 0.28\mu F/cm^{-2}$ is the oxide capacitance per unit area ($A = 2.5 * 10^{-3} cm^2$ is the device area for the AL1 sample), q is the elementary charge, and V_{ms} the intrinsic potential difference between the metal grid and the absorber layer.

Influence of parameters As already emphasized above in this report, the sign of Q_f is of great importance regarding the effectiveness of field-effect passivation. Since this one depends on the sign of the difference $V_{ms} - V_{fb}$ in equation 4.6, it seems rather important to consider the numerical variability of the different parameters involved in the expression of $V_{ms} - V_{fb}$ as also discussed in [18]. Since V_{fb} is experimentally estimated and rather constant for a particular sample, it is especially from V_{ms} that the variability originates. As a reminder, the built-in voltage V_{ms} is expressed as:

$$V_{ms} = \frac{\phi_m - (\chi_{CIGS} + \frac{E_g}{2} + kTln(\frac{N_a}{n_i}))}{q} \tag{4.7}$$

where ϕ_m is the work-function of the metal grid, χ_{CIGS} and E_g are respectively the electronic affinity and the bandgap of the CIGS layer, and N_a is the density of shallow acceptors dopants in the CIGS. The influence of this latter parameter N_a is negligible compared to the others, and its value is typically $5 * 10^{16} cm^{-3}$.

The three other parameters mainly depend on the composition and crystalline orientation of the corresponding material. In this study, the front electrode is made of Silver whose work function varies between 4.26 and 4.73eV according to [52]. The values of χ_{CIGS} and E_g depend on the elemental composition of the CIGS and especially the Gallium content [53, 54]. In particular, it is shown in [54] that GGI ratios in the [25%;35%] range lead to mean values of 1.18eV and 4.36eV for respectively the bandgap and electronic affinity of CIGS. Since this composition is similar to all the samples investigated in this study according to XRF maps, the values of 1.18eV and 4.36eV are used for E_g and χ_{CIGS} in the following. Finally, the estimated value of Q_f mainly depends on the value of the grid work function ϕ_m and is either presented as such in the rest of this report or computed for the mean value of ϕ_m.

Density of fixed charges The value of the flat-band voltage V_{fb} is equal to 0.24V for the AL1 sample, as shown on figure 4.22. The resulting value of Q_f for the AL1 sample can be found by plugging $V_{fb} = 0.24V$ and all the other parameters into equation 4.6. Considering the two possible extreme values of ϕ_m the obtained value of Q_F is comprised between $-1.7 * 10^{12} cm^{-2}$ and $-2.6 * 10^{12} cm^{-2}$, which is negative and falls into the expected order of magnitude for an ALD-alumina passivation layer as in [13, 19, 22]. This tends to

confirm our expectations that, for the case of Al_2O_3, field-effect passivation is effective and strong but not in the desired direction to limit recombination at the front interface. This precisely motivates our further investigations about annealing, surface cleaning and other dielectric materials in order to obtain the desired positive Q_f.

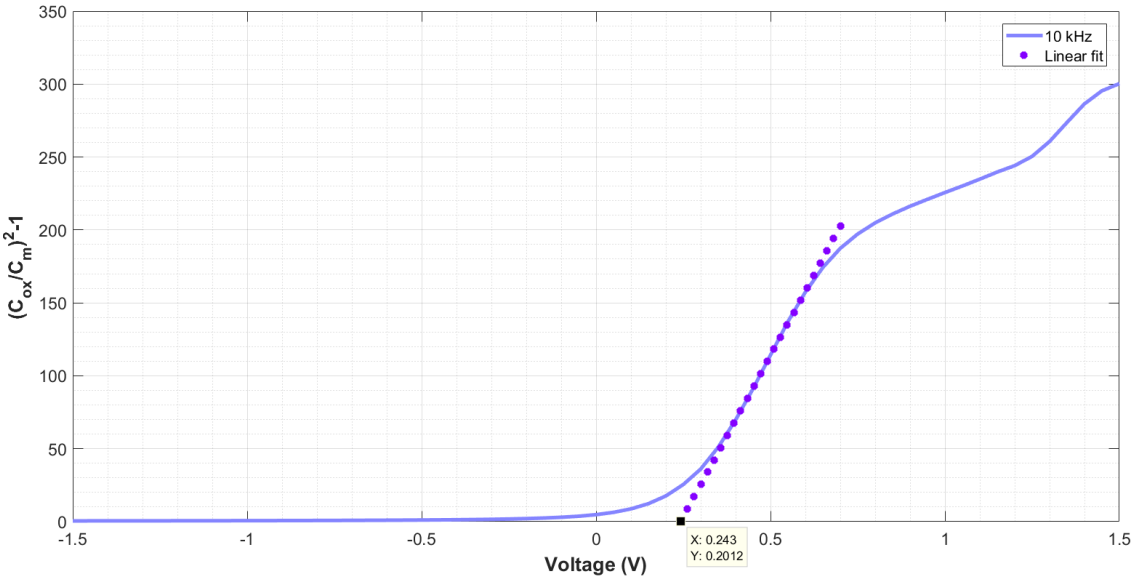

Figure 4.22: Graphical extraction of the flat-band voltage $V_{fb} = 0.24V$ at the frequency of 10kHz, with the method from [35] and detailed in section 2.7.3.1.

4.3.4 Chemical passivation

The final step is to characterize chemical passivation by estimating the density of trap states ah the CIGS/Oxide interface. As discussed above in chapter 2, the surface recombination rate at a given interface is directly proportional to the density of interface traps N_{it} present at that very interface. Thus, in order to assess an effective chemical passivation of the CIGS/CdS interface by a reduction of D_{it}, we need the two extraction techniques previously presented in section 2.7.3.2. As described hereunder, the application of these analysis methods on real samples exhibit additional challenges and differences compared to the theoretical case from section 2.7.3.2. This in turn makes the extraction of D_{it} much more complex than for Q_f in our case. In the following, we investigate both the conductance method and the HLF technique introduced in section 2.7.3.2. The objective is to compare not only the final values of D_{it} provided by these methods but also their respective simplicity and effectiveness depending on the quality of both the samples and the corresponding C-V measurements.

Density of interface traps The conductance method requires to study the evolution of $-fdC/df$ in function of frequency at a fixed bias in the depletion or weak inversion regime. The exact choice of that bias is made in such a way that it coincides with the position of the 2D signature related to interface traps as illustrated on the left of figure 4.23. The diagonal 2D signature appearing clearly on the 2D map and the matching with simulated interface-trap 2D responses tend to confirm the presence of interface states in the AL1 sample. Therefore, if the density of interface traps is not too low, one should be able to identify capacitance derivative peaks on the frequency-cut of the map shown on the right of figure 4.23.

For voltages in the [0.05V;0.35V] range highlighted in white on the 2D map, slight conductance peaks appear at low frequency next to the huge series resistance-related peaks at high frequency. At this point, it is important to consider the fact that the real interface-related conductance peaks might be also located at high frequency and thus hidden by the huge R_s response. This would make the extraction of D_{it} impossible for the AL1 sample. On the contrary, if the peaks highlighted by the orange line on figure 4.23 are well related to the response of interface states, then the mean height of those low-magnitude maxima is around $6.5nF/cm^2$ resulting in $D_{it} = 1 * 10^{11} cm^{-2} eV^{-1}$ using equation 2.7. Such a density of interface traps falls into the expected $10^{11} cm^{-2} eV^{-1}$ order of magnitude for effective chemical passivation, when compared to other references [5, 7, 10, 13, 18, 19].

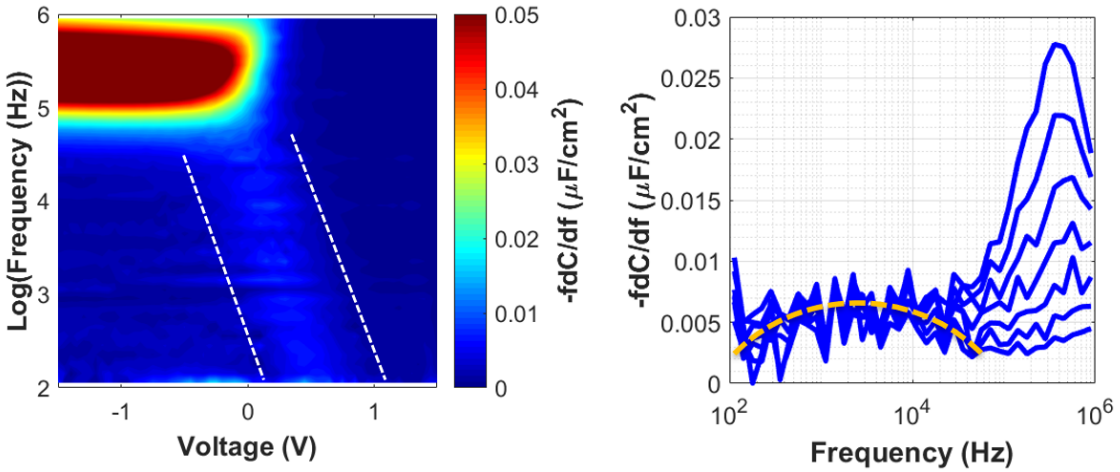

Figure 4.23: 2D map identification of the conductance peaks related to interface traps in the $[0V; 0.5V]$ range. Left: Voltage-frequency map of the capacitance derivative. The location of the peak is highlighted with the orange dotted line. Right: Vertical cut of the 2D map (along frequency axis) in the selected voltage range.

The HLF method should provide, by comparing high and low frequency CV curves, a value of D_{it} that is in the same order of magnitude as the conductance method. The frequency dispersion of CV curves due to border traps and resistive potential barrier may reduce the accuracy of the extraction. The evolution of the HLF-computed density of interface levels in function of the applied bias is shown on figure 4.24 for the same range of bias selected for the conductance method, i.e. from 0.05V to 0.35V. When applied on the raw data, the HLF method tends to overestimate D_{it} in comparison to the conductance method, with a rather high voltage dependence and mean value of $D_{it} = 8.2 * 10^{11} cm^{-2} eV^{-1}$. On the contrary, the HLF estimation of D_{it} based on the 1kHz-1MHz CV corrected curve leads to a much less bias dependent value of D_{it} around $1.7 * 10^{11} cm^{-2} eV^{-1}$, which is quite close to the result obtained with the conductance method.

Finally, even though the range of voltages chosen for the HLF method does not seem greatly impacted by the effect of series resistance, the two-frequency CV correction tends to bring the estimation closer to the one of the conductance method. Without R_s correction, the voltage dependence of D_{it} extracted by the HLF method is quite significant, dropping by roughly a factor 3 between 0.05V and 0.35V. The values of D_{it} obtained with the HLF

method are likely to be less accurate than those obtained with the conductance method. Moreover, even though applying the HLF method on samples not exhibiting the interface 2D signature is still possible, the obtained non-zero values of D_{it} are not likely to be as reliable as in the case of a clear trap states response. This is the reason why the samples for which it is the case in the rest of this report are rather used to estimate D_{it} in a relatively wide range of values.

Eventually, the final values of D_{it} extracted on the AL1 sample are relatively low, around $1 * 10^{11} cm^{-2} eV^{-1}$, which is further supported by the rather low magnitude of the corresponding 2D signature. Combined with the apparent weak degradation of the CV curves, the effect of interface states in the case of the AL1 sample seems less dominant than the effect of series resistance. This tends to indicate an effective interface chemical passivation which, as already discussed, should lead to performance improvements of Al_2O_3 front-passivated solar cells. This hypothesis is further verified below with other samples.

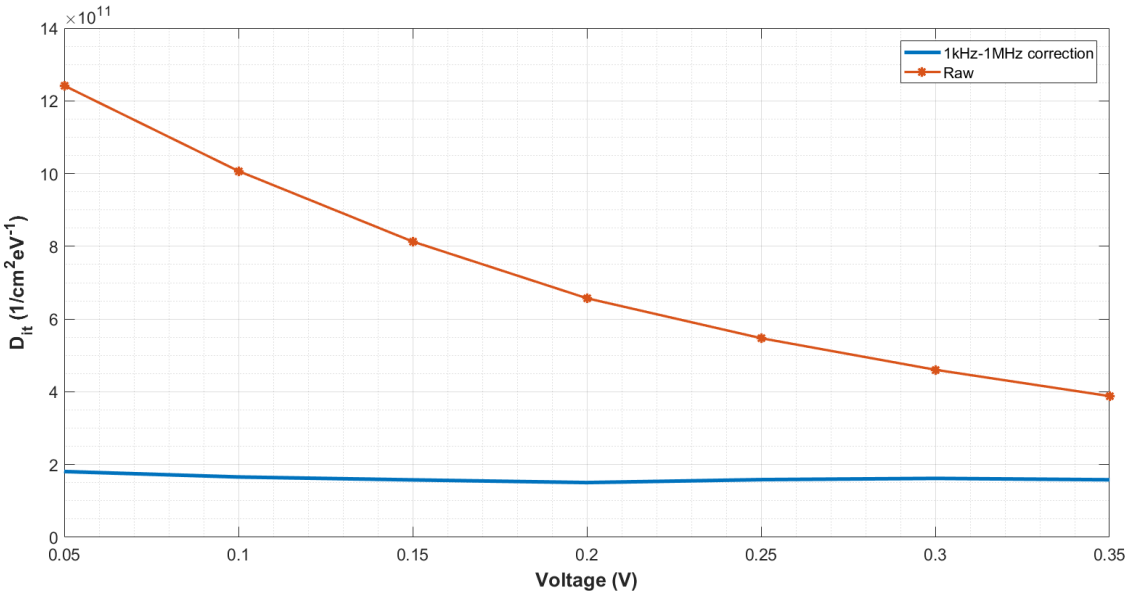

Figure 4.24: Comparison of the HLF extraction of D_{it} applied on both the R_s-corrected and raw data, in the same [0.05V;0.35V] restricted bias range as the conductance method.

4.4 Aluminum oxide - Al_2O_3

Similarly to the samples description in section 3.2.1, this section considers 3 different groups/series of MIS structures: the first group only includes AL1 which is already discussed above; the second series includes AL2-17 (20nm Al_2O_3 on 3-stage co-evaporated CIGS); the third group includes AL18-21 (30nm Al_2O_3 deposited on sputtered CIGS). The different parameters investigated are the CIGS deposition (co-evaporation and sputtering), the CIGS surface cleaning treatment (AS or Ammonia) and the post-deposition annealing (only with IV/CV data).

In the rest of this whole chapter, PL measurements realized on bare CIGS are denoted as "bare" or "AD" (as-deposited) in opposition to the complete MIS structure designated either as "Oxide" or by their respective cleaning procedure ("AS" or "Ammo"/"Ammonia") with the "oxide" term omitted. For IV/CV measurements, since the oxide layer is always present and the surface pre-cleaning already applied, only the terminology "AD" is used so as to compare with annealed samples referred to as "A1" for single annealing, and "A2" or "DA" for double annealing. The results obtained for alumina, hafnia and their combination are summarized and discussed in section 4.7.

4.4.1 PL measurements

Figure 4.25 shows the huge increase in PL intensity, i.e. up to 10 times higher, after the ALD deposition of 20nm Al_2O_3 compared to the as-deposited (AD) CIGS for the samples of the second group. This indicates the presence of strong surface passivation effects as reported in other references for alumina [12, 38]. Besides that, the PL spectra exhibit 2 to 3 peaks mostly located at 3 different energy transitions: the first peak probably corresponds to band-to-band transition across the bandgap of CIGS equal to 1.15eV [36], the second and third peaks at 1.05eV and 0.95eV may either be related to relatively shallow defects in the CIGS bulk [36] or interference effects [55].

Figure 4.26 magnifies the PL results of AL10-13 samples so that the shape of the bare absorber spectrum can be distinguished. For those samples, the successive cleaning with Ammonia and the oxide deposition seem to alter the relative height of the different peaks in such a way that the maximum value of the second peak (shallow defect) is closer to the one of the first peak (CIGS bandgap). Similar trends are observed on other samples but remain negligible compared to the general enhancement in PL intensity due to surface passivation effects of the oxide layer.

The multiple peaks observed on the PL spectra of the second series of samples may also be explained by their notch-type Gallium grading which results in the simultaneous presence of a maximum and minimum bandgap. On the contrary, the samples of the third group with sputtered CIGS exhibit a single peak on their PL spectra as on figure 4.27. Besides that, the degradation of PL measurements realized on CIGS due to interference effects has been reported in [55]. Therefore, the PL analysis made in this report is limited to preliminary suggesting the effectiveness of surface passivation by showing increase in PL intensity and carrier lifetime related to the band-to-band transition when possible.

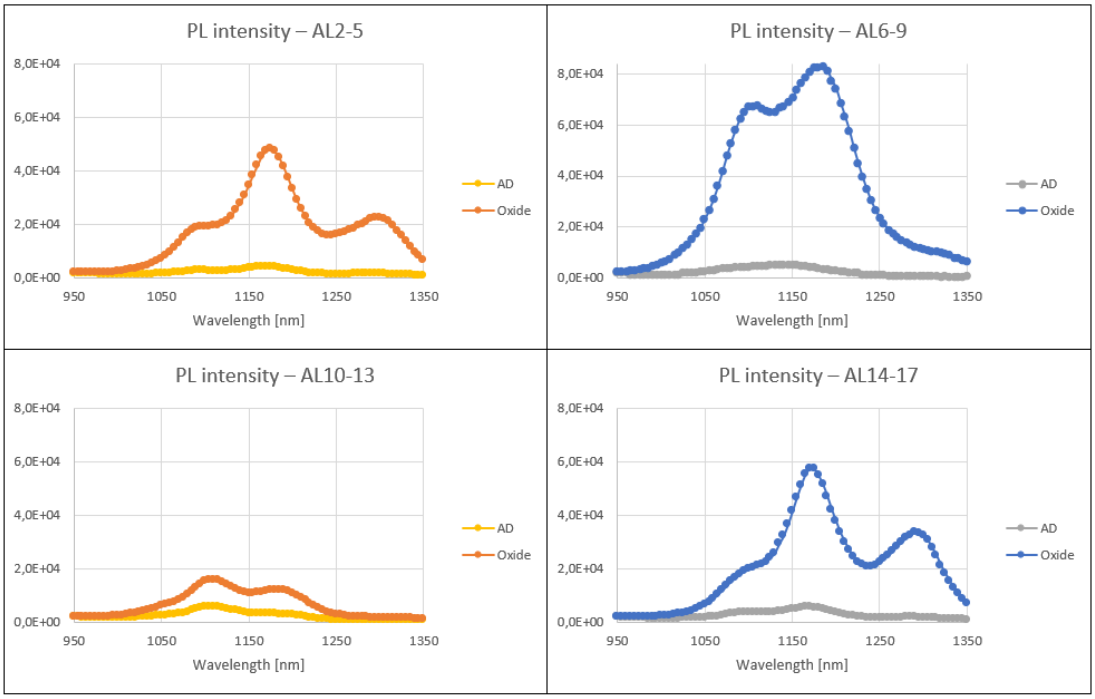

Figure 4.25: Comparison of average PL intensity before (AD) and after the deposition of of 20nm Al_2O_3 on 3-stage co-evaporated CIGS pre-cleaned with Ammonia. The AL samples are grouped by original substrate cut and thus similar CIGS composition.

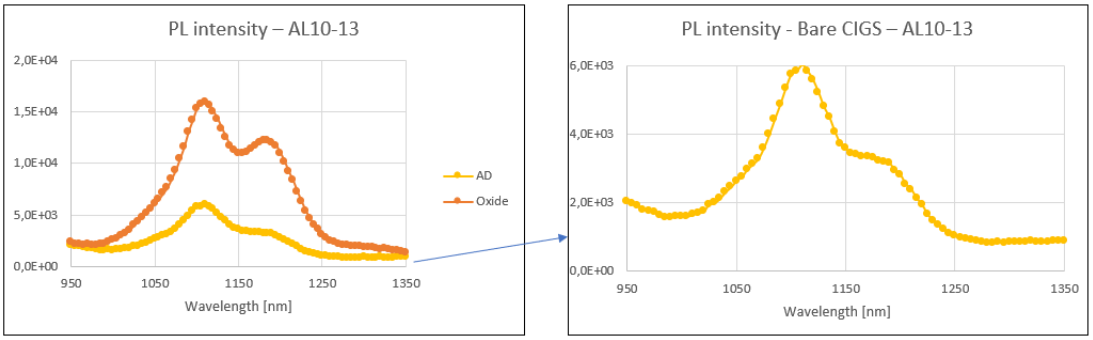

Figure 4.26: Zoom on the PL results for the AL10-13 samples. The relative height of the different PL peaks slightly varies after Ammonia cleaning and oxide deposition.

Effect of surface cleaning The comparison of AS and Ammonia cleaning is shown on figure 4.27 for the samples of the third group (sputtered CIGS). Supposedly due to the different elemental composition and the absence of notch-type Gallium grading of sputtered CIGS as compared to co-evaporated, the PL spectra have a single peak at an energy slightly below the bandgap of CIGS, i.e. 1.07eV. There are clear improvements in both PL intensity (1.5 to 2 times higher) and minority carrier lifetimes when the top surface of the CIGS layer is pre-cleaned with AS (blue curves) as compared to Ammonia (red curves). With a double exponential fitting applied on the TRPL decay curves (at the band-to-band transition of 1160nm), one finds a minority carrier lifetime, i.e. the larger time constant out of the two considered in [40], that is 1.5 to 2.5 times higher in the case of AS cleaning compared to Ammonia, which tends to indicate more effective defect passivation with the former cleaning treatment.

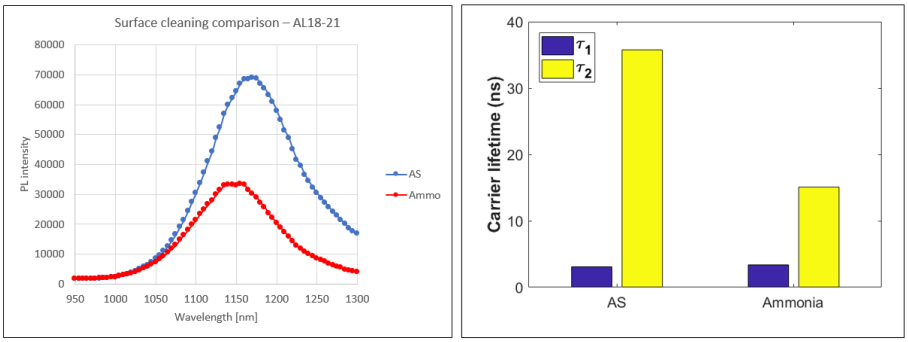

Figure 4.27: Comparison of average PL intensity after oxide deposition in function of the surface pre-cleaning, for the AL18-21 samples. Left: Average PL spectra exhibiting a single peak around 1160nm (1.07eV) showing higher intensity for AS cleaning compared to Ammonia. Right: Average carrier lifetime at 1160nm from TRPL measurements with τ_1 and τ_2 the two time constants of the double exponential fitting [40].

The same trend about AS cleaning-related improvements is observed in [56, 57]. While the previous section confirms the effective passivation of the CIGS top surface, the results shown here indicate that the best cleaning procedure to apply on sputtered CIGS seems to be the one using AS. It is shown in [40] that AS cleaning is able to remove undesired Cu_xSe secondary phases from the top surface of CIGS without degrading the absorber and more efficiently than Ammonia treatment. Moreover, the potential smoothing of the rough surface associated to sputtered CIGS may also explain the AS cleaning-related improvements observed on figure 4.27 for AL18-21.

It is also visible on figure 4.28 that Ammonia cleaning applied alone on bare 3-stage co-evaporated CIGS does not provide a significant improvement in the PL intensity compared to the increase that is induced by the passivation layer deposition over the CIGS (figure 4.25). The minority carrier lifetime is not greatly affected either by the Ammonia cleaning. This supports the already mentioned above hypothesis about co-evaporated CIGS being less affected by surface treatment than sputtered CIGS due to the different surface composition [39]. To conclude, AS cleaning seems to be more advantageous than Ammonia cleaning for especially sputtered CIGS surface treatment before depositing an Al_2O_3-based passivation layer.

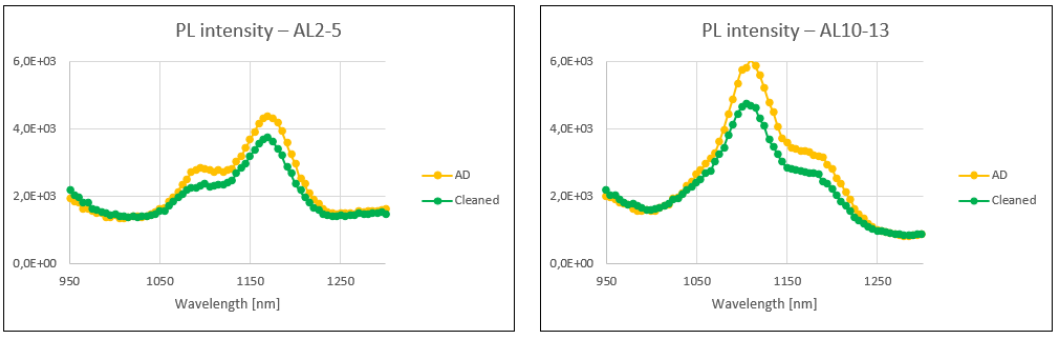

Figure 4.28: Comparison of average PL intensity of bare 3-stage co-evaporated CIGS absorber before (AD) and after Ammonia surface cleaning (cleaned), for the AL2-5/10-13 samples. The relative heights and positions of the different peaks is unchanged and the decrease in PL intensity after cleaning is not significant.

4.4.2 IV/CV measurements

4.4.2.1 Leakage

In this section, the IV/CV data available for the second series of samples are limited to AL2-9. Before digging into the characterization of interface passivation, it seems rather important to guarantee the validity of the CV results analyzed below by checking the amount of DC current circulating through the oxide of our MIS samples. In particular, we consider that a specific sample is not particularly leaky if the maximum current density flowing through it does not exceed $0.01 A/cm^2$ [45], roughly corresponding to a shunt resistance R_{sh} that is superior to $1k\Omega.cm^2$ so as to remain highly dominant compared to the typical series resistance observed in our samples, i.e. around $1\Omega.cm^2$.

The mean IV results and corresponding values of R_{sh} are presented on figure 4.29 in function of the processing and cleaning techniques used for the CIGS layer. Globally, the IV curves remain inferior to the upper limit of $0.01 A/cm^2$ considered here. The samples with a co-evaporated CIGS layer exhibit a higher shunt resistance than the sputtered ones, thus resulting in lower leakage currents. Among the samples with sputtered CIGS, the AS cleaning results in lower shunt than with Ammonia which is rather surprising since AS is supposed to prevent the formation of leaky Cu_xSe secondary phases [40].

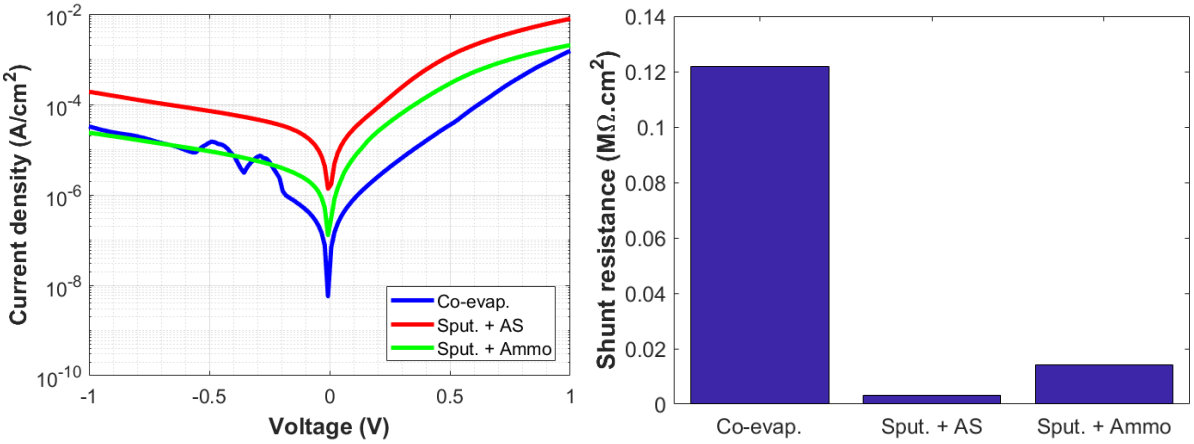

Figure 4.29: Summary of the average IV measurements obtained on the alumina-based MIS samples, in function of the CIGS processing (co-evaporation for the first and second series of samples (AL1-9) and sputtering for the third series (AL18-21)). Left: Average measured current density vs. voltage in dark environment. Right: Average shunt resistance extracted through the derivative of the voltage with respect to the current density (dV/dJ) around zero bias.

Besides that, PDA treatments might also affect the strength of leakage currents through our sample by changing not only the sheet resistance of the CIGS layer but also the series resistance [58]. The comparison of IV results and estimated R_{sh} for the second series of samples before and after annealing is presented on figure 4.30. Three different N_2 annealing procedures are applied: single 30-minute long annealing at 300°C (A1-300°C); single 30-minute long annealing at 400°C (A1-400°C); two 30-minute long successive annealing processes at 300°C first and then at 400°C, separated by a resting period and

noted DA for "double annealing" (see section 3.7). The results of the double annealing on figure 4.30 correspond to the second 400°C annealing treatment applied on the samples already annealed once at 300°C beforehand and labelled "A1-300°C" on the same graph.

It appears that the single 300°C annealing reduces the leakage by enhancing the shunt resistance. The same trend is generally observed for the other series of alumina-based samples (see Appendix A). Applying a second 400°C PDA on those already annealed samples seems to cancel the leakage reduction related to the first 300°C high-temperature treatment, resulting in similar results to the as-deposited situation. Directly performing the first annealing at 400°C leads to a rather large decrease in shunt resistance and increase in the IV slope for positive bias, bringing the maximum current density above the considered threshold. Generally speaking, the single 300°C annealing leads to the best results in terms of parasitic leakage currents through the MIS structures. However, it may not be as straightforward to extend these considerations about MIS samples to complete solar cells since the transport of carriers is actually desired and taken care of by nano-openings in that very case (section 2.6.2).

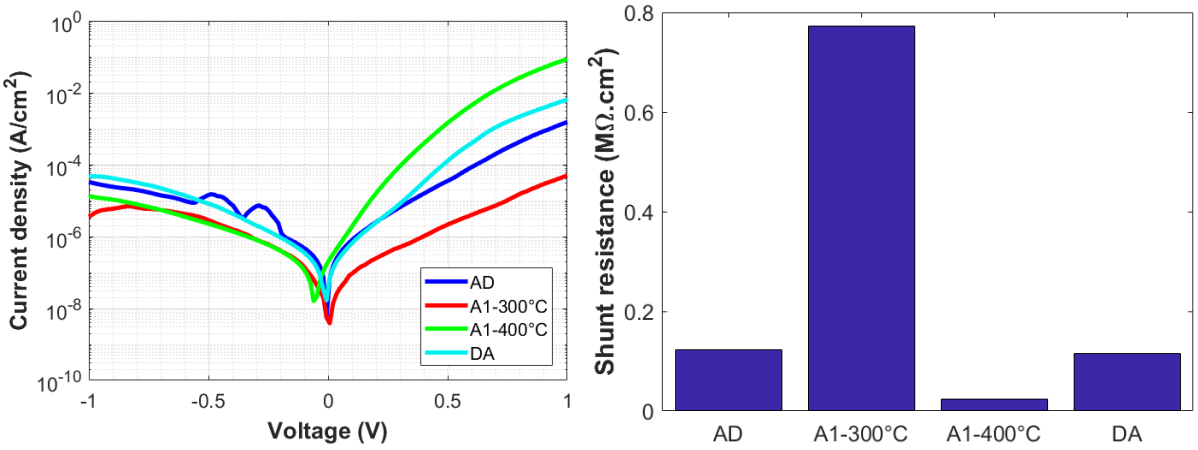

Figure 4.30: Influence of different annealing treatments on the IV curves and shunt resistance, for the AL2-9 samples (co-evaporated CIGS). Left: Measured average current density vs. voltage in dark environment. Right: Average shunt resistance extracted through the derivative of the voltage with respect to the current density (dV/dJ) around zero bias. Labels detailed in the text.

4.4.2.2 Series Resistance

The specific values of R_s for all the samples studied here are rather erratic and do not follow particular trends with regards to CIGS processing and surface cleaning. The post-deposition annealing processes do not influence the magnitude of R_s in a significant fashion either. The range of values observed for R_s in all the set of alumina-based MIS samples is $[0.05; 1.81]\Omega.cm^2$ for both annealed and non-annealed samples. As discussed above, this series resistance probably originates from two concurrent phenomena: back interface potential barrier and border traps density. By applying the same procedure as in section 4.3.2, the graph on figure 4.31 is obtained. The corresponding potential barrier is only $13meV$ lower than for the AL1 sample which tends to confirm that both samples suffer from the same problem of back interface series resistance.

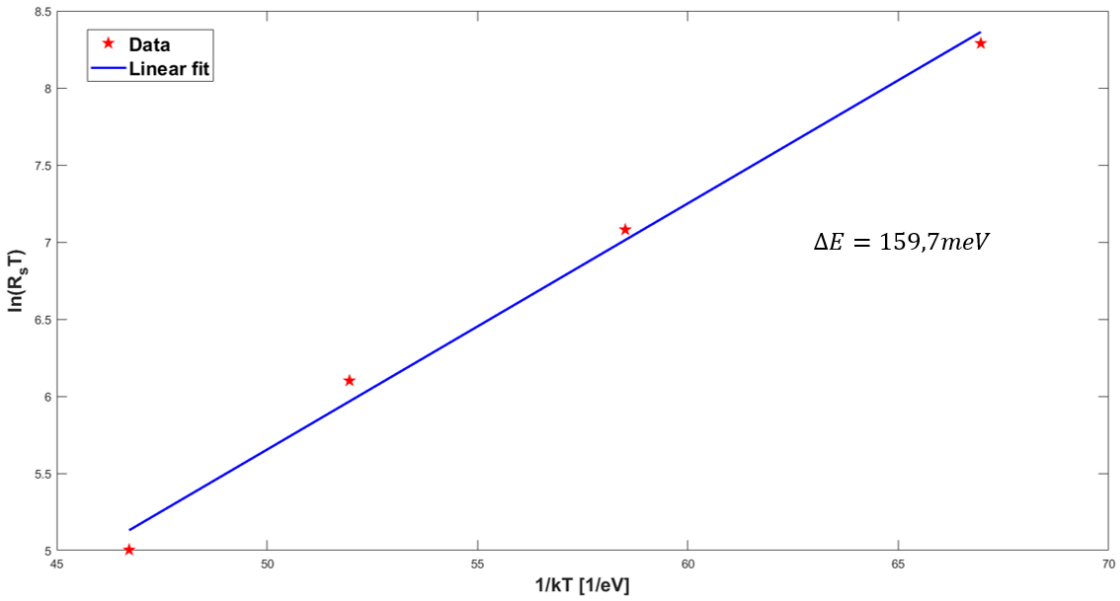

Figure 4.31: Determination of the height of the $MoSe_2$ resistive potential barrier at the back interface of the AL20 sample, estimated to be $\Delta E = 159.7meV$ by linear interpolation through the values of R_s estimated using MATLAB simulations.

4.4.2.3 Field-effect passivation

As mentioned above, the first results obtained on the AL1 sample (group 1) indicate that, even though the fixed charges are activated in the as-deposited Al_2O_3 layer with a surface density around $-2 * 10^{12}cm^{-2}$, the sign of Q_f is not positive as expected. On the contrary, it appears that the resulting charge density present in the oxide is negative, leading to a potential repulsion of the electrons from the CIGS/CdS interface. By applying the same procedure as in section 4.3.3 to the two other groups of alumina-based samples, the following range of values for Q_f is obtained: $[-1.24; -6] * 10^{12}cm^{-2}$ which includes the previous result for AL1. Since the sign and magnitude of Q_f mainly depend on the oxide layer itself, there is no dependence observed between the processing and cleaning of CIGS and the field-effect passivation.

We believe that hysteresis phenomena as well as samples processing and composition may be responsible for the sign difference of Q_f compared to the as-deposited positive Q_f reported in literature [7, 12, 18]. Still, negative values of Q_f are also observed for alumina layers in [19]. Given the considered rather low variability of ϕ_{ms}, it seems that the intrinsic distribution of fixed charges in our alumina layers is different from the observations in [7, 12, 18]. Since it is shown in these very references that post-deposition annealing (PDA) treatment is potentially able to influence the value and the sign of Q_f by activating fixed charges in the Al_2O_3 layer, similar processes are applied to our samples in order to possible invert the sign of Q_f as targeted here.

Annealing As a reminder, section 3.7 describes in details the different annealing processes used in this work. Figure 4.32 left shows an example of the effect of a 300°C N_2 annealing process on normalized CV curves for the AL20 sample (sputtered CIGS), exhibiting a leftward shift of around 0.4V. Figure 4.32 right shows the effect of a first 400°C annealing in Nitrogen applied on the AL5 sample (co-evaporated CIGS) with a

similar horizontal shift as for AL20. On figure 4.33, the same trend is also observed for a first annealing at 300°C in the case of the AL19 sample (sputtered CIGS), whereas the effect of the second annealing at 400°C on V_{fb} is not highly significant compared to the first high-temperature treatment.

For both sputtered and co-evaporated CIGS, the direction of the voltage shift is in the other direction than in [7, 12, 18], which is actually beneficial in our case since Q_f is closer to positive values. The new set of values for Q_f after the annealing treatments at either 300°C or 400°C is comprised between $-0.5 * 10^{12} cm^{-2}$ and $-1.94 * 10^{11} cm^{-2}$. Even though the sign of Q_f is not inverted, the magnitude reduction of the negative Q_f may still mitigate the potentially detrimental negative field-effect for front interface passivation.

Our conclusion is three-fold: first, thermal annealing does have an influence on the fixed charges distribution in the alumina layer and the resulting voltage shift brings Q_f closer to positive values which is precisely our target in this study; second, there is no significant difference observed between annealing temperatures of 300°C and 400°C with regards to field-effect passivation; third, applying two successive annealing treatments on the same sample does not seem to replicate the improvement related to the first.

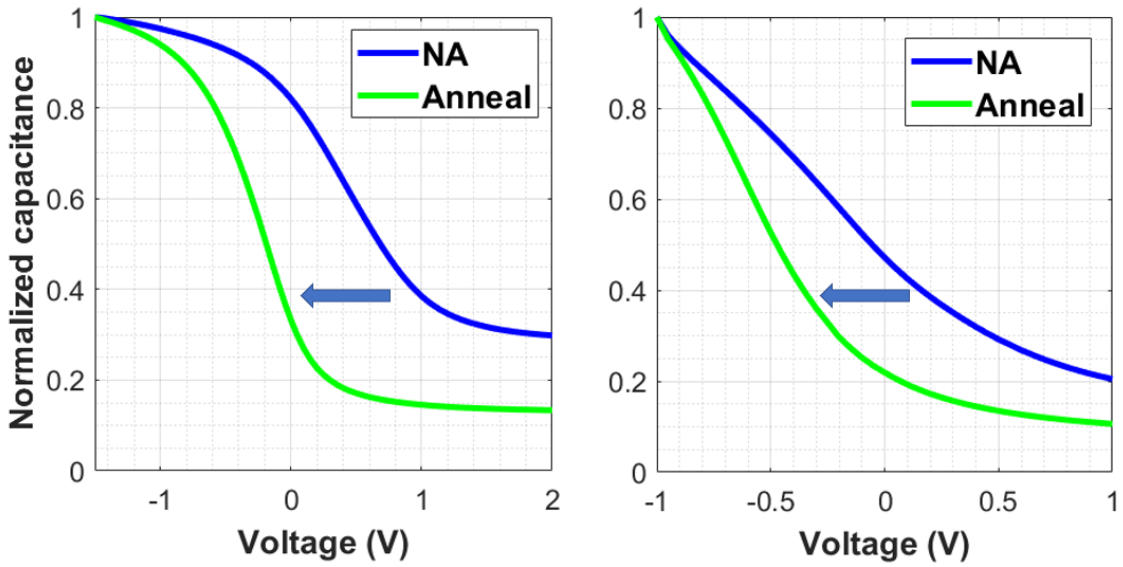

Figure 4.32: Horizontal shifting effect of post-deposition N_2 annealing (NA refers to non-annealed as deposited sample). Left: 20mins annealing at 300°C on the AL20 sample, with a leftward shift bringing Q_f close to positive values. Right: 20mins annealing at 400°C on the AL5 sample, with roughly the same horizontal shift.

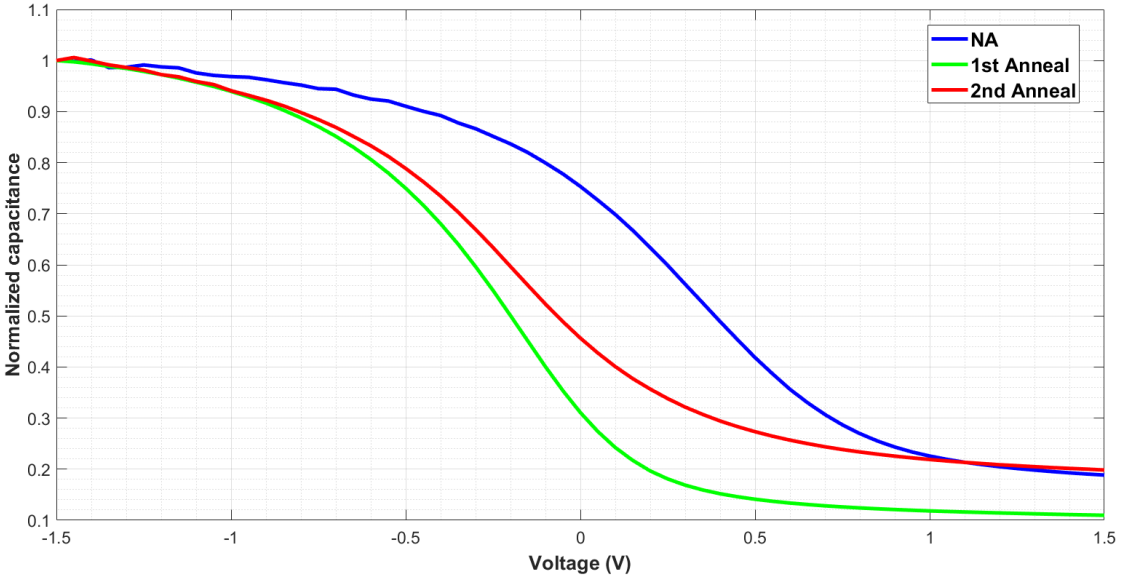

Figure 4.33: Effect of two successive post-deposition N_2 annealing treatments on the AL19 sample, the first annealing at 300°C and the second at 400°C. The shift related to the first annealing is not duplicated by the second high-temperature treatment.

4.4.2.4 Chemical passivation

In this section, the hypothesis of effective chemical passivation for alumina layers is verified by estimating, if possible, the values of D_{it} for all the samples in this set. However, it appears challenging to extract the density of interface traps for the samples with co-evaporated CIGS and pre-cleaned with Ammonia (AL2-9), given the complex identification of interface trap signature on their 2D maps.

Non-apparent interface signature - Co-evaporated CIGS Indeed, figure 4.34 presents the measured CV curves and 2D map for the AL9 sample on which it is relatively hard to identify the typical signature related to interface traps, similarly to all the other samples of that group (AL2-8). It is then quite difficult to apply the conductance method on those samples exhibiting no clear conductance peaks. Even though the HLF capacitance technique can still be applied, the obtained estimations of D_{it} are not likely to be reliable since the signature of interface traps is also difficult to distinguish on the CV measurements (left of figure 4.34). Therefore, the HLF-extracted values of D_{it} presented in table 4.1 for the AL2-9 samples are expressed with a questionable accuracy and in a wide interval corresponding to the whole measured voltage range given the complexity to localize the response of interface states along the bias axis.

The 2D maps of the co-evaporated samples (AL2-9) only exhibit the series resistance response at high frequency without any evidence of interface states. Two different hypotheses could explain this observation: first, the interface states are localized in a region of the bandgap that cannot be analyzed within the feasible voltage and frequency ranges; second, D_{it} may be so low that the corresponding interface response is not distinguishable from the background noise or more prominent effects such as series resistance, as mentioned above in section 4.3.4 for the case of AL1.

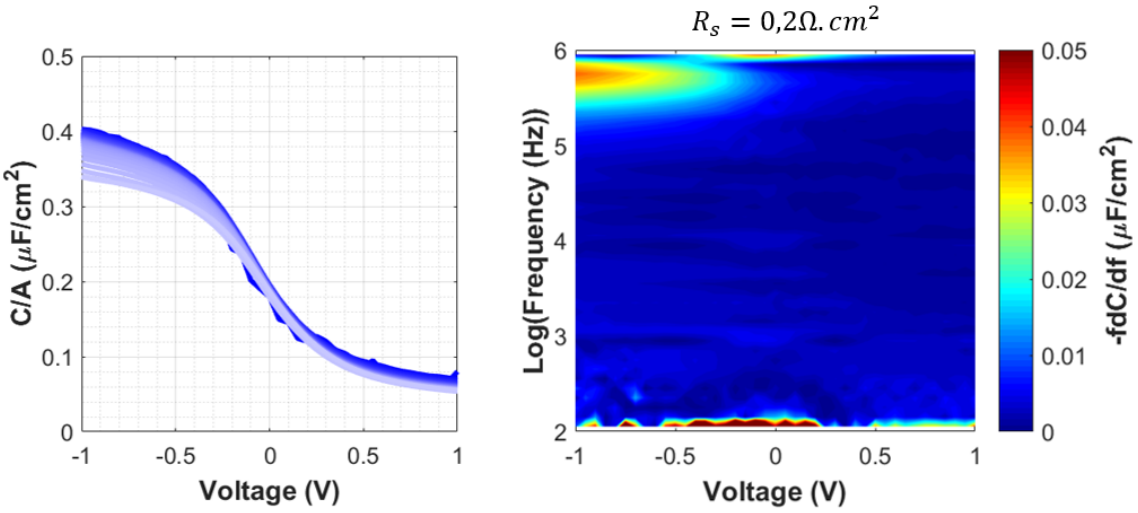

Figure 4.34: Example of measured CV curves and 2D map showing no interface-trap signature (AL9 sample). Left: Measured CV curves from 100Hz (dark blue) to 1MHz (light blue). Right: 2D map exhibiting the high-frequency response of series resistance ($0.2\Omega.cm^2$ as estimated by the two-frequency correction).

Since the effect of interface traps is observed within typical bias and frequency ranges for the AL1 sample, the latter hypothesis is the most plausible. Indeed, it is mentioned in [34] that the accuracy of D_{it}-extraction decreases when the actual value to be extracted is out of the $10^{10} - 10^{12} cm^{-2} eV^{-1}$ range. Since the response associated to values of D_{it} higher than $10^{12} cm^{-2} eV^{-1}$ should appear clearly on the 2D map (figure 4.8), this suggests that the high effectiveness of chemical passivation on the AL2-9 samples results in an Oxide/CIGS interface of high quality and low values of D_{it}.

Apparent interface signature - Sputtered CIGS Contrarily to the alumina-based samples with co-evaporated CIGS, the group of samples with sputtered CIGS exhibit the 2D signature associated to interface traps as depicted on figure 4.35. This relatively important difference with the previous series is likely to be related to the CIGS surface modification between co-evaporation and sputtering [39]. Yet, it does not result in significant differences regarding the estimated values of D_{it} in table 4.1. Still, since the conductance peaks are located at higher frequency on figure 4.35 than on figure 4.23, it seems that the interface states are shallower in the case of sputtered CIGS layer than with co-evaporation (see figure A.11 in Appendix B for the influence of interface states energy level). The resulting values of D_{it} are reported in table 4.1 below.

Surface cleaning It is also interesting to investigate the effect of the two different surface cleaning procedures on the effectiveness of chemical passivation. Indeed, the PL measurements from section 4.4.1 tend to indicate that, for sputtered CIGS with higher surface roughness [39], AS cleaning enhances the passivation effects related to the oxide layer as compared to Ammonia cleaning. Since field-effect passivation mainly depends on the bulk of the oxide layer whereas chemical passivation quantifies the matching at the CIGS/Oxide interface, there should be a dependence between the value of D_{it} and the cleaning of the surface on which that very parameter is estimated. The results from table

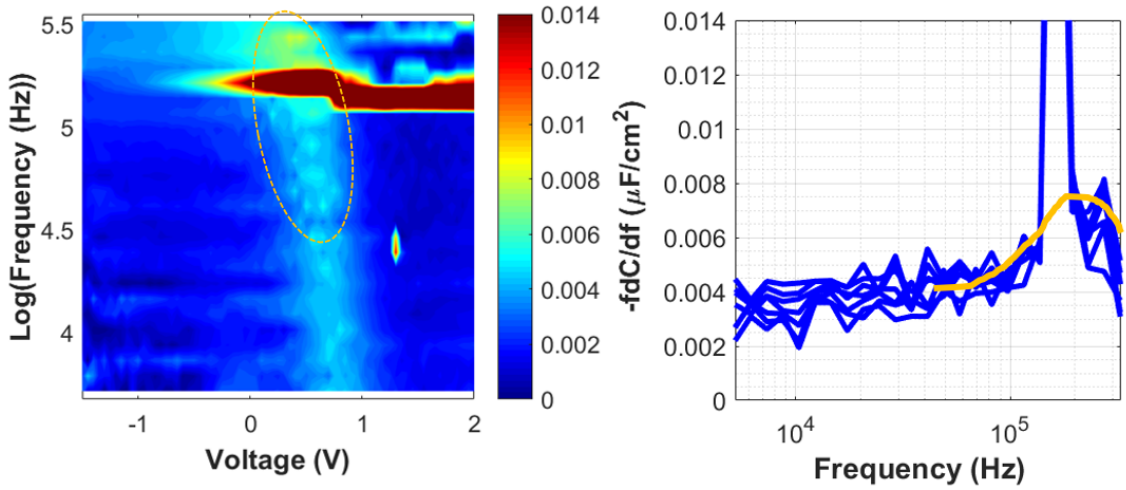

Figure 4.35: Left: Measured 2D map showing the expected interface-trap signature with a conductance peak height of approximately $7.5nF/cm^2$ (AL20 sample). The responses of series resistance ($0.05\Omega.cm^2$ from correction) and border traps are visible at higher frequency but omitted here for the sake of clarity. Right: Vertical cut of the 2D map (along frequency axis) in the selected voltage range with the conductance peaks highlighted with a solid orange line.

4.1 confirm the moderate improvements due to AS treatment applied on sputtered CIGS as compared to Ammonia cleaning, with a slightly lower mean value of D_{it} and thus more effective chemical passivation in the former case.

Annealing Eventually, the dependence of D_{it} with regards to single and double annealing treatments is investigated as for field-effect passivation. The resulting estimations of the density of interface states are shown in table 4.1, only for the samples with sputtered CIGS (third series) since they exhibit clear interface-trap responses. It appears that the single PDA treatment at 300°C results in lower values of D_{it} for both the Ammonia and AS-cleaned samples of that series, as also reported in [7, 41]. The second annealing at higher temperature (400°C) tends to cancel this improvement and leads to higher density of interface traps than the as-deposited samples. A similar trend is for instance observed for a first annealing at 500°C in [24].

4.4.3 Summary

There are several important conclusions to be drawn from this analysis of alumina-based MIS samples and the influence of the different parameters investigated: CIGS deposition technique, surface cleaning procedure and post-deposition annealing. First, the PL measurements exhibit an increase in intensity following the deposition of 20 and 30nm aluminum oxide on top of either co-evaporated or sputtered CIGS, suggesting an effective passivation effect. The corresponding increase in minority carrier lifetime is a proof of effective defect passivation, which is enhanced in the case of AS surface cleaning applied on sputtered CIGS.

Second, the IV measurements indicate no excessive leakage currents in our samples, with a stronger shunt in the case of co-evaporated CIGS but no improvements after AS cleaning on sputtered CIGS. One single annealing at 300°C seems to reduce leakage

Samples	$D_{it}[cm^{-2}eV^{-1}]$ (HLF)	$D_{it}[cm^{-2}eV^{-1}]$ (CM)
Co-evap. CIGS - Ammo		
AL1	$5 * 10^{11}$	$1 * 10^{11}$
AL2-9	$(0.5 - 12) * 10^{11}$	X
Sput. CIGS - Ammonia		
AD	$2.2 * 10^{11}$	$2.3 * 10^{11}$
A1 (300°C)	$0.23 * 10^{11}$	$0.6 * 10^{11}$
A2 (400°C)	$7.6 * 10^{11}$	$1.9 * 10^{11}$
Sput. CIGS - AS		
AD	$1.3 * 10^{11}$	$1.1 * 10^{11}$
A1 (300°C)	$0.9 * 10^{11}$	$0.5 * 10^{11}$

Table 4.1: Estimated average values of D_{it} for the different series of alumina-based MIS samples (CM is conductance method). The first and second series respectively include the AL1 and AL2-9 samples whose CIGS layer is processed by 3-stage co-evaporation. The third series includes the AL18-21 samples with sputtered CIGS and two different cleaning treatments. AD refers to as-deposited samples and A1 and A2 respectively correspond to first annealing at 300°C and second annealing at 400°C. "X" indicates impossible or not reliable extraction of D_{it}.

currents whereas single or second annealing processes at 400°C tend to degrade shunt. The effect of series resistance is observed on all samples with values of R_s within the $[0.05; 1.81]\Omega.cm^2$ range and associated potential barrier height between 160meV (AL20) and 180meV (AL9).

Third, the values of Q_f are comprised in the $[-1.24; -6] * 10^{12}cm^{-2}$ range for all the samples of this series before annealing, leading to misdirected field-effect passivation of the front interface. There is no apparent influence of the CIGS processing and cleaning on this parameter. Post-deposition annealing treatments induce the desired leftwards shifts of the CV curves but not sufficiently for the sign of Q_f to be inverted, i.e. Q_f belongs to the $[-0.5; -1.94] * 10^{12}cm^{-2}$ interval after annealing.

Finally, chemical passivation is likely to be effective on these samples with values of D_{it} comprised between $[0.5; 2.3] * 10^{11}cm^{-2}eV^{-1}$, supported by the nearly invisible degradation of CV data due to interface traps observed on the co-evaporated CIGS samples. Both AS surface cleaning and PDA seem to slightly enhance chemical passivation by further reducing the density of trap states at the CIGS/Al_2O_3 interface in the case of sputtered CIGS.

All of these results are summarized in table 4.4, along with the outcomes of the two next series of samples, i.e. the HfO_2 and Al_2O_3/HfO_2 configurations. The next section presents a similar analysis in the case of hafnia-based MIS samples, with mostly the same aspects discussed and the potential new observations highlighted. The main objective is to observe positive values of Q_f and thus effective field-effect passivation as well as investigating the impact of post-deposition annealing on that parameter. Chemical passivation is expected to be similarly active as for alumina.

4.5 Hafnium oxide - HfO_2

In this section, two distinct series of samples are considered (section 3.2.2): the first series includes HF1-8 (30nm HfO_2 on 3-stage co-evaporated CIGS) and the second series includes HF9-12 (30nm HfO_2 deposited on sputtered CIGS).

4.5.1 PL measurements

Similarly to the second series of Al_2O_3-based samples, there is a significant PL intensity up-scaling observed after the deposition of 30nm HfO_2 on top of both the Ammonia and AS-cleaned co-evaporated CIGS (figure 4.36). The maximum PL intensity is increased by roughly a factor 4 to 8, indicating effective passivation effects of the CIGS top surface related to the hafnia layer. Presumably for the same reason as AL2-17, there appears to be more than a single peak on the PL spectra of HF1-8: one major energy transition around 1060nm (1.15eV) corresponding to the CIGS bandgap, another clear peak between 1100nm (1.13eV) and 1150nm (1.08eV) related to either shallow defect transition or secondary bandgap (notch-type Gallium grading).

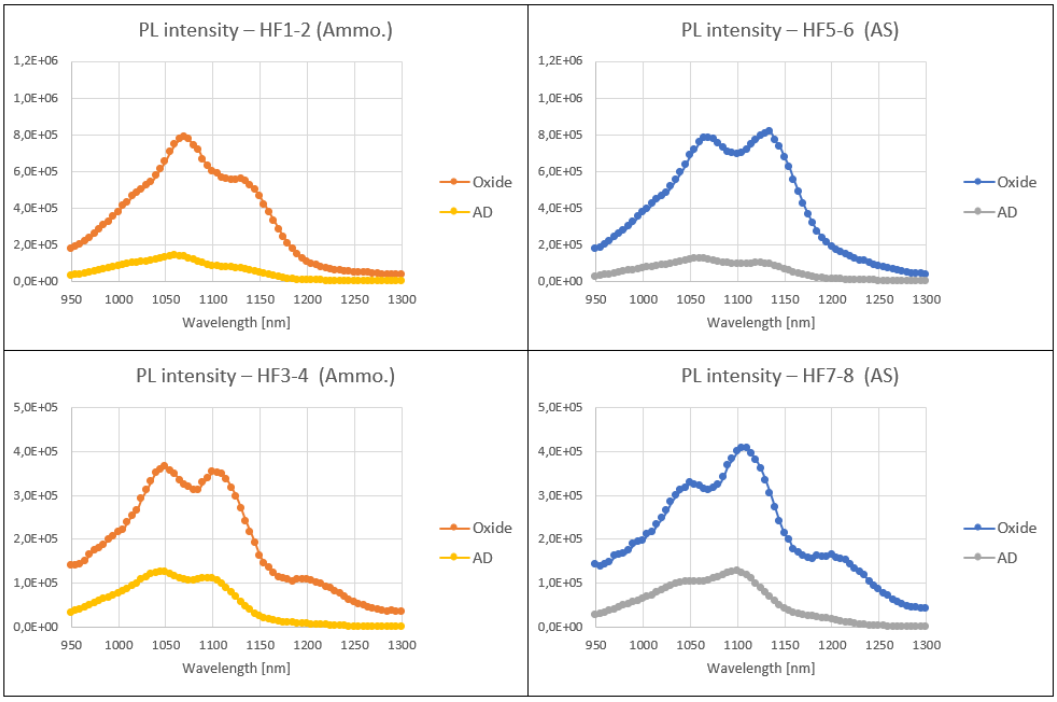

Figure 4.36: Comparison of average PL intensity before (AD) and after deposition of 30nm HfO_2 on 3-stage co-evaporated CIGS pre-cleaned with either AS or Ammonia. The HF1-2 and HF5-6 samples have similar CIGS composition with higher Cu content than the HF3-4 and HF7-8 samples. AD refers to as-deposited CIGS.

The samples HF1-2 and HF5-6 have similar CIGS composition with higher Cu content (Cu-rich, mean CGI=0.91) compared to the HF3-4 and HF7-8 samples with a lower content of Copper (Cu-poor, mean CGI=0.86). This Copper composition difference is may explain the presence of a third peak at higher wavelength for the HF3-4-7-8 samples only. Indeed, this peak is associated to a lower energy transition (1.03eV) than the bandgap and its presence is dependent on the Copper content. It could then presumably correspond to

a Cu-related bulk shallow defect as reported in [36, 37]. The effectiveness of passivation effects is also supported by the increase in average minority carrier lifetime following the pre-cleaning and oxide deposition shown on figure 4.37.

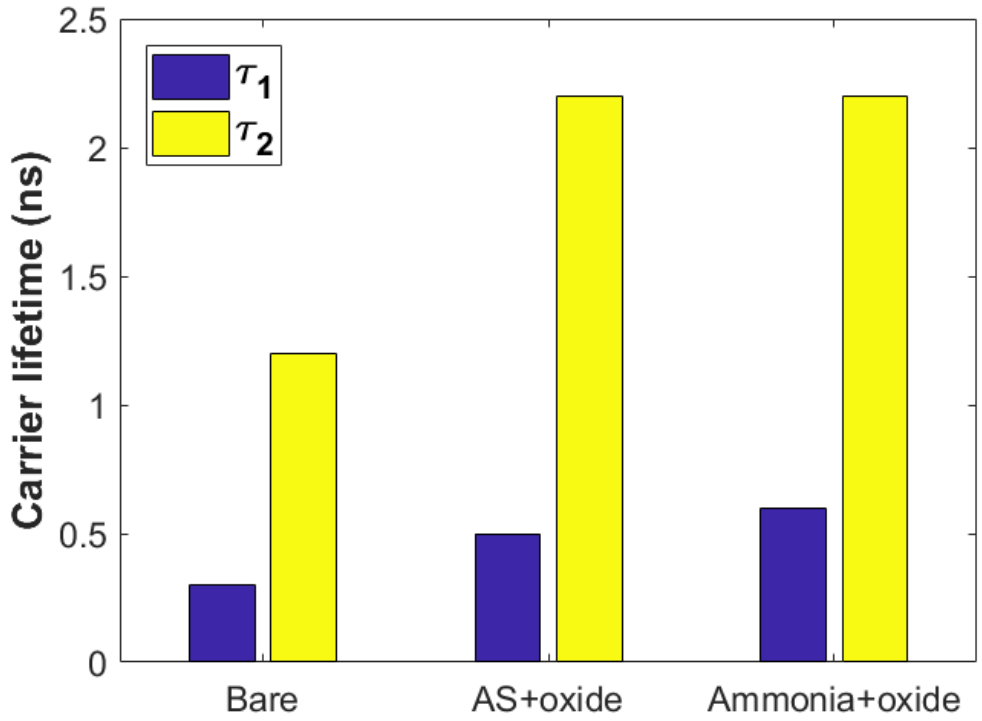

Figure 4.37: Average carrier lifetime at 1060nm (band-to-band) obtained from TRPL measurements on the HF1-2-5-6 samples, with τ_1 and τ_2 respectively the short and long time constants of the double exponential fitting [40]. Comparison between bare CIGS and 30nm HfO_2 deposited after AS or Ammonia pre-cleaning. Both surface treatment lead to similar improvements compared to the bare CIGS results.

Surface cleaning The trend observed about surface cleaning for alumina-based samples with sputtered CIGS (AS better than Ammonia) seems to be inverted in the case of hafnia as shown on the left figure 4.38 for the HF9-12 samples. Indeed, the PL intensity as well as the minority carrier lifetime of sputtered CIGS/hafnia structures are respectively 3 and 2 times higher with Ammonia cleaning than with AS treatment. Surface cleaning tends to have a significant impact on the PL results obtained for samples with sputtered CIGS, presumably because of the high roughness of the CIGS top surface [39]. It also appears that, contrarily to alumina-based samples, Ammonia treatment leads to better PL performances in the case of sputtered CIGS/HfO_2 stacks.

Presumably due to their lower surface roughness [39], co-evaporated CIGS samples show no striking difference between the two surface cleaning with regards to PL intensity (figure 4.36) for both Cu-rich (HF1-2-5-6) and Cu-poor(HF3-4-7-8) samples. Furthermore, the increase in carrier lifetime observed after the cleaning and oxide deposition is relatively similar for AS and Ammonia cleaned co-evaporated CIGS as illustrated on figure 4.37, with the same trends being also observed for the other samples of the first group (HF3-4-7-8) in Appendix A. This suggests that surface cleaning is less determinant in the case of co-evaporated CIGS.

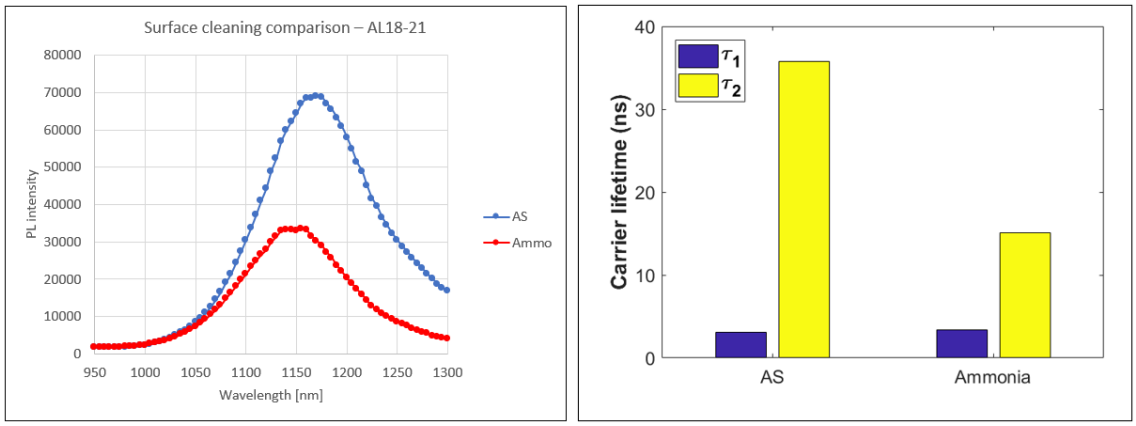

Figure 4.38: Comparison of average PL intensity after oxide deposition in function of the surface pre-cleaning, for the HF9-12 samples. Left: Average PL spectra exhibiting a single peak around 1175nm (1.06eV) with PL intensity roughly 2.5 times higher for Ammonia cleaning compared to AS. Right: Average carrier lifetime at 1175nm from TRPL measurements with τ_1 and τ_2 respectively the short and long time constants of the double exponential fitting [40].

4.5.2 IV/CV measurements

4.5.2.1 Leakage

The parasitic currents observed on figure 4.39 are on average 10 to 100 times higher than for alumina-based samples, especially in the negative bias region. Still, the leakage threshold of $0.01A/cm^2$ is hardly surpassed except for the high positive voltages. The best configuration in terms of leakage currents seems to be co-evaporated CIGS cleaned with Ammonia (HF1-4), approximately two orders of magnitude below the three other combinations sharing similar parasitic currents. Once again, the AS cleaning does not provide the expected reduction of leakage by removing undesired Cu_xSe phases.

On the contrary, it seems to reduce the shunt resistance in the case of both sputtered and co-evaporated CIGS compared to Ammonia treatment (AD on figure 4.40). Generally speaking, the shunt resistance is much lower for sputtered CIGS ($6.5k\Omega.cm^2$ in the best scenario) than for 3-stage co-evaporated CIGS (just below $500k\Omega.cm^2$ in the best scenario). Besides that, the first PDA at 300°C leads to a significant ramp up of R_{sh} in all cases except co-evaporated CIGS pre-treated with Ammonia, initially the best configuration in terms of leakage. In that situation, the co-evaporated CIGS pre-cleaned with AS becomes the best configuration regarding R_{sh}. If the first PDA is done at 400°C instead (left of figure 4.40), the enhancement in shunt is more moderate for co-evaporated CIGS. The application of a second annealing at 400°C on the sputtered CIGS samples (right of figure 4.40) partially cancels the improvements induced by the first PDA at 300°C. Although these considerations concern MIS samples, the outcomes may prove important for complete solar cells as well.

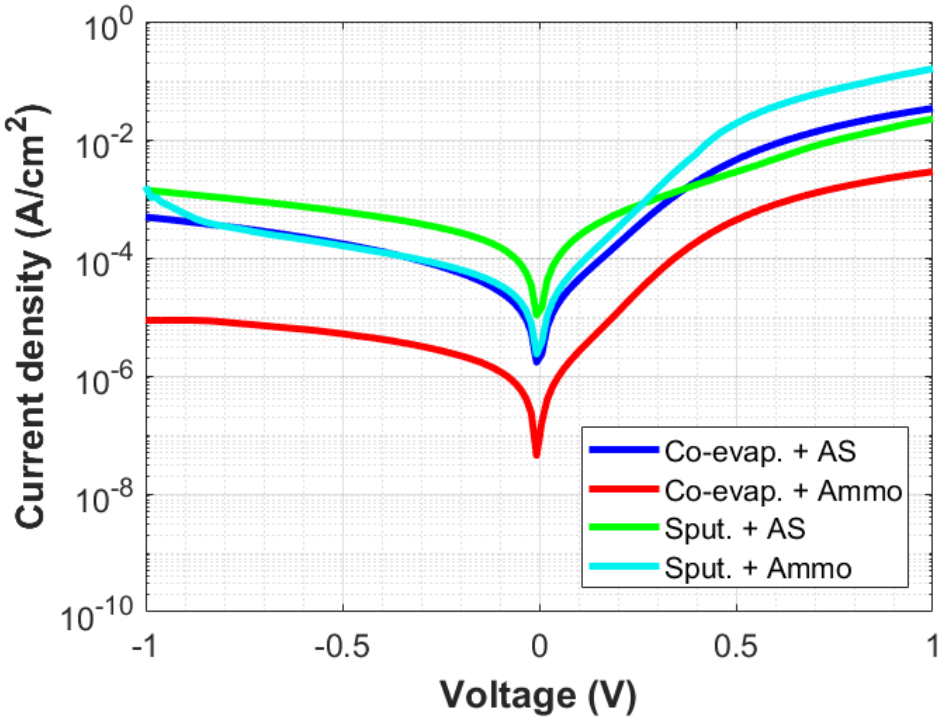

Figure 4.39: Average measured current density vs. voltage in function of the CIGS processing and surface cleaning for the whole set of hafnia samples (HF1-12). The least leaky configuration is co-evaporated CIGS cleaned with Ammonia.

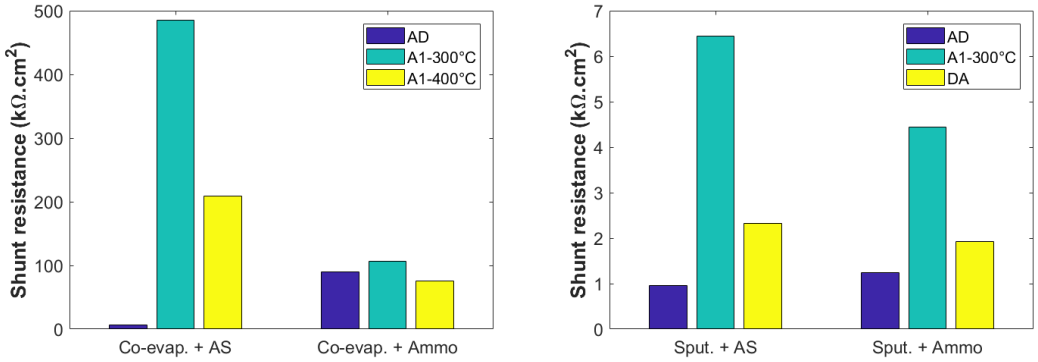

Figure 4.40: Comparison of the average shunt resistance values in function of the CIGS processing, surface cleaning and post-deposition annealing, for the whole set of hafnia samples (HF1-12). Left: A1 refers to first annealing process either at 300°C or 400°C. Right: DA refers to second annealing at 400°C applied on the same samples

4.5.2.2 2D map analysis - series resistance

In the case of hafnia samples, we observed different types of 2D maps corresponding to the different possible combinations of CIGS processing and surface cleaning, as visible on figures 4.41 and 4.43.

AS-cleaned samples - HF5-8 and HF11-12 First, the CV measurements made on sputtered and co-evaporated CIGS both pre-cleaned with AS (figure 4.41) are highly similar. One can see the high-frequency response corresponding to series resistance on the top left corner, from which extends a trail affecting the whole frequency range in the negative bias region. This second feature is more prominent for the sputtered sample (right) and presumably related to border traps, potentially merged with interface states signature as discussed below.

Still, our main interest here is the high frequency response of series resistance. The two-frequency correction provides really close estimations of R_s: $0.27\Omega.cm^2$ and $0.25\Omega.cm^2$ for respectively the co-evaporated (HF8) and sputtered (HF11) CIGS pre-treated with AS. On average and given the accuracy of the estimation, the value of R_s remains rather comparable between the two configurations: $0.48\Omega.cm^2$ for co-evaporated (HF5-8) and $0.14\Omega.cm^2$ for sputtered (HF11-12), which falls into the same range as alumina-based MIS samples. The difference might be due to the presence of a NaF precursor layer in the case of co-evaporated samples, influencing the formation of the $MoSe_2$ potential barrier at the back interface as mentioned above. Apart from the shift discussed below for field-effect passivation, there is no significant effect of 300°C single annealing on the series resistance for AS-cleaned samples as shown on figure 4.42. On the contrary, PDA treatments at 400°C lead to severe degradation of the 2D map and important increase in series resistance as depicted on figure A.5 in Appendix A.

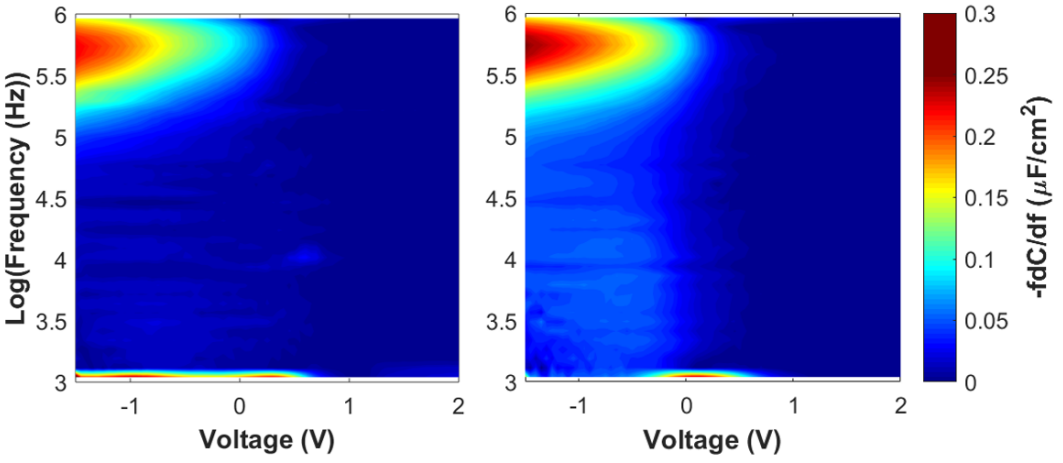

Figure 4.41: Measured capacitance derivative 2D maps. Left: co-evaporated CIGS pre-cleaned with AS (HF8) and with an estimated series resistance value of $0.27\Omega.cm^2$. Right: sputtered CIGS pre-cleaned with AS (HF11) and with an estimated series resistance value of $0.25\Omega.cm^2$.

Ammonia-cleaned samples - HF1-4 and HF9-10 There is a much larger difference between co-evaporated and sputtered absorber in the case of Ammonia pre-cleaning (figure 4.43): on the one hand, the relatively large responses observed on the 2D maps are not similarly positioned regarding bias and voltage for co-evaporated and sputtered CIGS; on the other hand, the large responses observed on these 2D maps are actually themselves rather different in terms of shape and location from the typical series resistance signatures observed on the AS-cleaned samples with hafnia or any alumina-based sample. It becomes

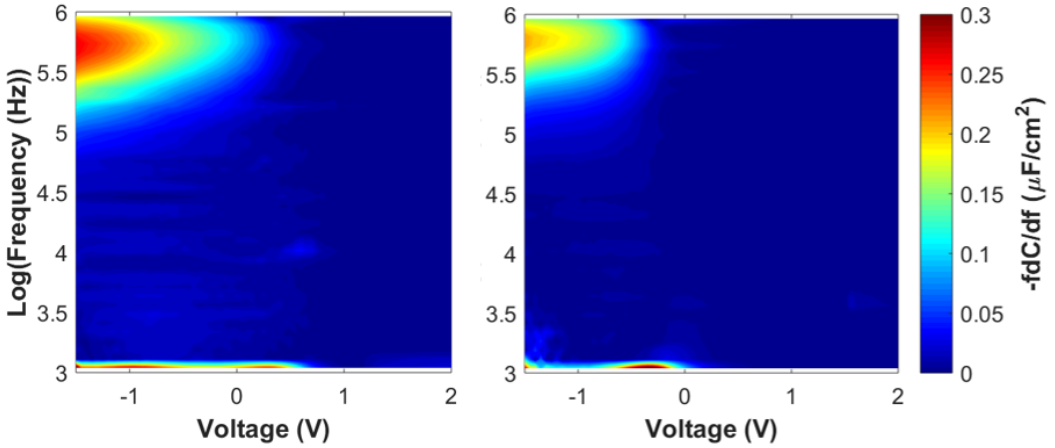

Figure 4.42: Measured capacitance derivative 2D maps before (left) and after single PDA at 300°C (right), for co-evaporated CIGS pre-cleaned with AS (HF8). Left: As-deposited estimated series resistance is $0.27\Omega.cm^2$. Right: Estimated series resistance is $0.3\Omega.cm^2$ after single annealing at 300°C.

even more obvious by looking directly at the CV data (figure 4.44). The dispersion of the CV curves is different than the previous observations about series resistance effect, which indicates that another phenomenon is likely to be present when the CIGS layer is pre-cleaned with Ammonia as compared to AS, especially in the case of hafnium oxide passivation layers. Moreover, the inspection of the CV curves and especially the decreasing trend of the capacitance in accumulation may lead to the consideration of parasitic conductivity in that bias region. This could in turn be well induced by the metallic secondary phases of Copper selenide which are not properly removed with Ammonia as compared to AS [40].

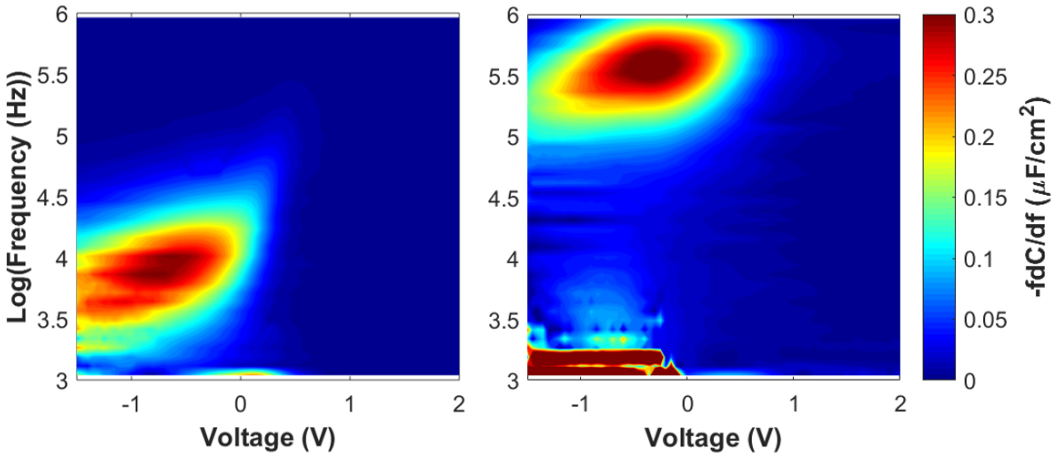

Figure 4.43: Measured capacitance derivative 2D maps. Left: co-evaporated CIGS pre-cleaned with Ammonia (HF2) and with an estimated series resistance value of $15.54\Omega.cm^2$. Left: sputtered CIGS pre-cleaned with Ammonia (HF9) and with an estimated series resistance value of $1.14\Omega.cm^2$.

We believe that two different scenarios are possible: either the large islands spotted on the 2D maps are related to series resistance and then the corresponding values of R_s widely exceed the previously observed ranges, especially for co-evaporated CIGS with an estimation of $15.54\Omega.cm^2$ well above the expectations at room temperature; or these 2D responses are related to another phenomenon, for instance the conductivity of the Cu_xSe phases appearing for Ammonia pre-treatment and potentially combined with the presupposed series resistance at the back interface. Since the same trends are observed for the other corresponding samples (HF1-3-4 and HF10), future investigations are needed regarding this matter (section 4.7).

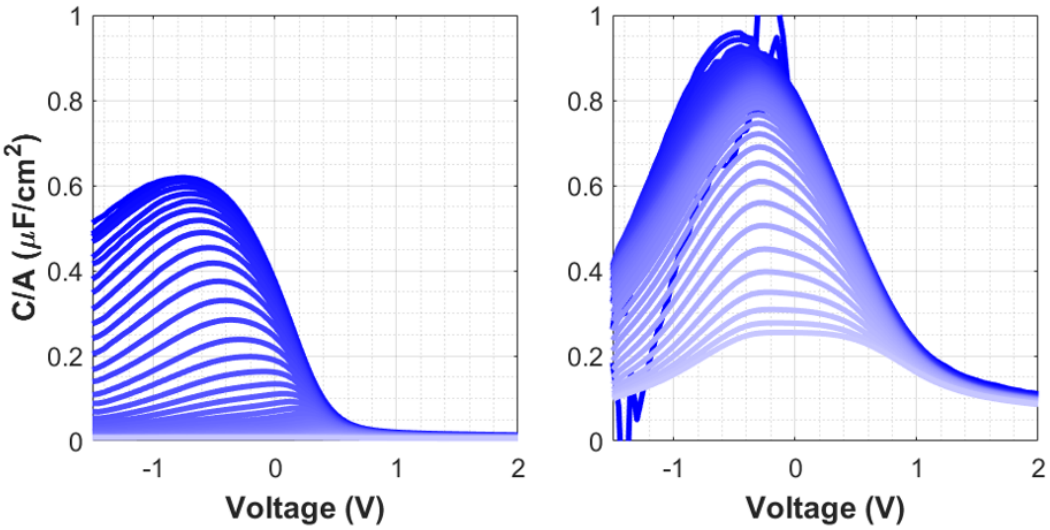

Figure 4.44: Measured CV curves from 1kHz (dark blue) to 1MHz (light blue). Left: co-evaporated CIGS pre-cleaned with Ammonia (HF2) and with an estimated series resistance value of $15.54\Omega.cm^2$. Left: sputtered CIGS pre-cleaned with Ammonia (HF9) and with an estimated series resistance value of $1.14\Omega.cm^2$.

Annealing Whether the 2D responses observed for Ammonia-cleaned samples are related to large series resistance or another phenomenon such as Cu_xSe phases, they appear to be somewhat "corrected" by single PDA treatments at either 300°C and 400°C, namely by reducing the value of R_s as visible on figure 4.45. The series resistance 2D signature is drastically diminished, from $15.54\Omega.cm^2$ to $0.61\Omega.cm^2$ for co-evaporated CIGS, but the counterpart is a much more prominent interface-trap response as discussed below for chemical passivation.

On the contrary, as shown on figures 4.42 and A.5, PDA treatments applied on AS-cleaned samples tend to either preserve or degrade the initially low values of R_s in the as-deposited configuration. This supports the hypothesis about the presence of additional side effects besides series resistance and border/interface traps, as discussed in section 4.7. Up to this point, it seems that co-evaporated CIGS pre-cleaned with AS and annealed once at 300°C is the best compromise for both series and shunt resistance in the case of hafnia-based MIS samples. The resulting outcomes for realistic solar cells need further investigations with relevant measurements on complete PV structures. The aspects of field-effect and chemical passivation are treated below.

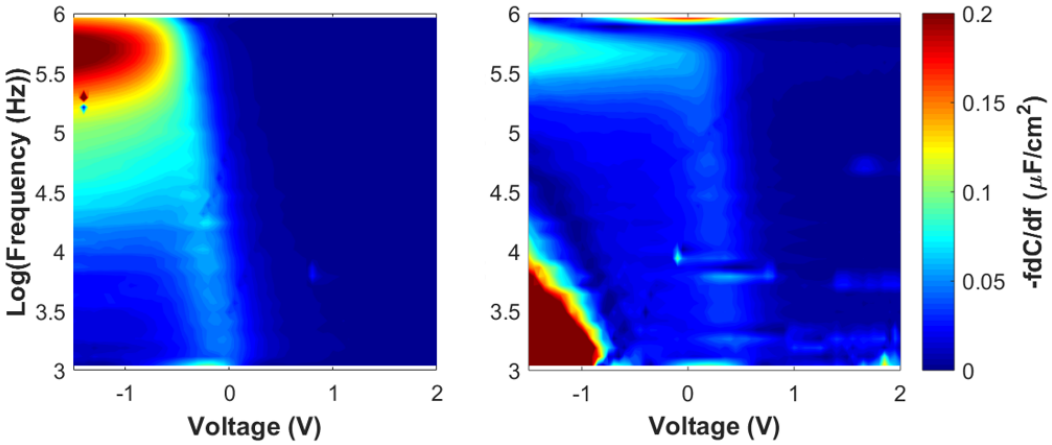

Figure 4.45: Measured capacitance derivative 2D maps after first annealing treatment at respectively 400°C and 300°C. Left: co-evaporated CIGS pre-cleaned with Ammonia (HF2), annealed at 400°C and with an estimated series resistance value of $0.61\Omega.cm^2$. Left: sputtered CIGS pre-cleaned with Ammonia (HF9), annealed at 300°C and with an estimated series resistance value of $0.1\Omega.cm^2$.

4.5.2.3 Field-effect passivation

Similarly to the MIS samples with Al_2O_3, the mean flat-band voltage of as-deposited hafnia samples is roughly comprised between $0.5V$ and $0.7V$, regardless of the CIGS surface cleaning and processing, leading to a mean density of fixed charges of negative sign and magnitude of the order of $10^{12}cm^{-2}$. More precisely, the range of Q_f values observed in all the samples (HF1-12) without any annealing process is $[-7.3; -8.7] * 10^{12}cm^{-2}$ for an average grid work-function of 4.5eV. This is visible on the left of figures 4.47 and 4.48 (AD case).

Annealing The improvements due to annealing are two-fold: on the one hand, the CV curves after the first 300°C PDA are shifted to the left (figure 4.46) meaning that positive fixed charges in the hafnium oxide layer are activated as targeted here. This in turn leads to a weakening of the negative field-effect which is further enhanced if a second annealing at 400°C is applied on the samples (DA on figure 4.46). The corresponding values of flat-band voltage and density of charges after annealing are presented on figures 4.47 and 4.48 as well; on the other hand, in the case of Ammonia-cleaned samples which, as mentioned above, exhibit a surprising behaviour in the accumulation region (normalized capacitance before annealing is higher than 1 on figure 4.46 right), the single PDA treatment at 300°C tends to "correct" this misconduct and results in a CV curve that is closer to the theoretical expectations.

Therefore, it seems that whichever phenomenon is degrading the CV behaviour of our Ammonia-cleaned hafnia samples, it may be corrected by high-temperature treatment. Similar trends are observed for other samples of the hafnia series as shown on figure A.4 in Appendix A. Eventually, the value of Q_f after annealing treatments is comprised within $[-4.8; -5.3] * 10^{12}cm^{-2}$, which is on average lower than before annealing, even though still negative.

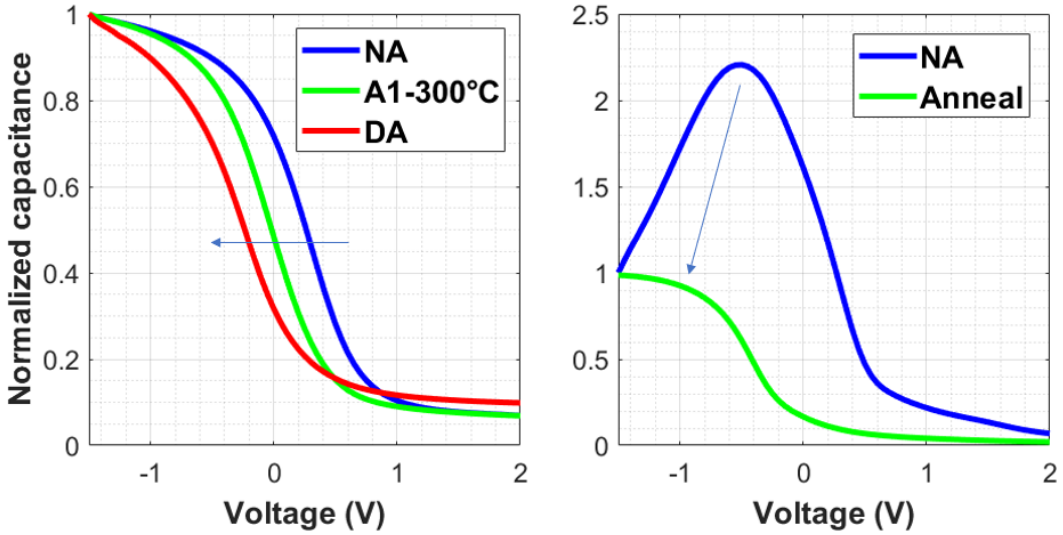

Figure 4.46: Effect of post-deposition annealing (blue arrow) on the measured normalized CV curves. Left: sputtered CIGS pre-cleaned with AS (HF10) and annealed twice, a first annealing at 300°C and a second annealing at 400°C. Right: co-evaporated CIGS pre-cleaned with Ammonia (HF2) and annealed once at 300°C.

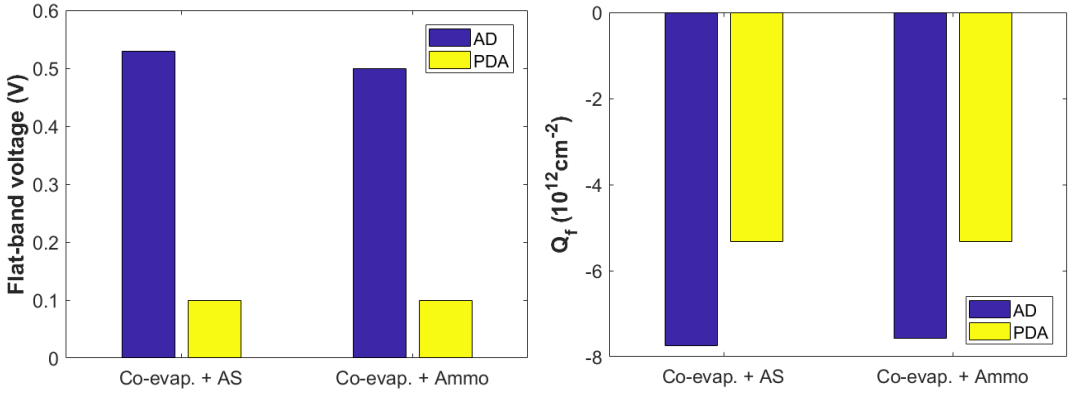

Figure 4.47: Effect of post-deposition annealing on the average values of V_{fb} and Q_f for the first series of hafnia samples (HF1-8) with co-evaporated CIGS. The work-function of the front Silver grid is taken to be 4.5eV, i.e. the mean between 4.26eV and 4.73eV. The annealing is either made at 300°C or 400°C for both types of cleaning (HF1-4 and HF5-8) with no significant difference between the two temperatures.

4.5.2.4 Chemical passivation

The analysis presented in this section follows the same reasoning based on the different types of 2D maps introduced above, without considering the effect of annealing in the first time. In particular, there is a distinction between, on the one hand, the 2D signatures appearing at high frequency, mostly for AS-cleaned samples, and considered as resulting from the effect of series resistance (figure 4.41) and, on the other hand, the larger and differently shaped responses observed in the case of Ammonia-cleaned samples (figure 4.43).

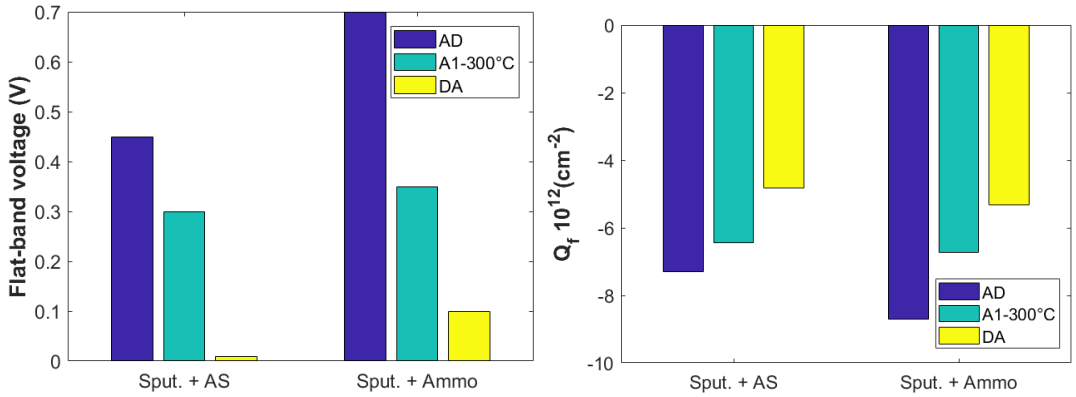

Figure 4.48: Effect of post-deposition annealing on the average values of V_{fb} and Q_f for the second series of hafnia samples (HF9-12) with sputtered CIGS. The work-function of the front Silver grid is taken to be 4.5eV, i.e. the mean between 4.26eV and 4.73eV. The first annealing made at 300°C and the second annealing (DA) at 400°C, for both types of cleaning (HF9-10 and HF11-12).

AS-cleaned samples - HF5-8 and HF11-12 In the former case, there is a slight difference between the co-evaporated and sputtered samples, namely the downward trail below the series resistance response is higher for sputtered CIGS (figure 4.41). This is even more visible by cutting the 2D map along the frequency axis as on figure 4.49 where the huge peaks located at high frequency presumably correspond to series resistance effect. Although the 2D signature is not clearly diagonal as for previous interface states simulations, the peaks observed at low frequency on the right of figure 4.49 (sputtered CIGS) may still be related to interface-trap response. Therefore, the approximate peaks roughly identified by inspecting the same frequency region for co-evaporated CIGS (left of figure 4.49) would also be related to interface states. Furthermore, the corresponding density of interface states is likely to be lower for co-evaporated CIGS when comparing the height of these peaks for sputtered CIGS. Thus, if that downward trail below series resistance response is well related to interface states, one can apply the conductance method to estimate D_{it}. The resulting mean values of D_{it} are $4.3 * 10^{11} cm^{-2} eV^{-1}$ and $5.2 * 10^{11} cm^{-2} eV^{-1}$ for respectively co-evaporated and sputtered CIGS, as reported in table 4.2 along with the results of the HLF method.

These rather low densities of interface traps are in accordance with the low magnitude of the associated 2D signatures. Besides that, D_{it} is on average lower for co-evaporated CIGS than for sputtered CIGS in the case of AS pre-treatment. Given the presence of prominent other effects such as series resistance, the accurate identification of conductance peaks related to interface states is sometimes difficult, potentially leading to less reliable estimations of D_{it}. Still, the obtained mean values fall in the expected order of magnitude. Moreover, there is a global reduction of D_{it} after single PDA at 300°C (table 4.2). On the contrary, first and second annealing treatments at 400°C lead to significant increase in D_{it} for respectively co-evaporated and sputtered CIGS. Once again, the best configuration seems to be co-evaporated CIGS pre-cleaned with AS and eventually annealed once at 300°C even though the extraction of D_{it} proves difficult in that case due to even more discrete interface-trap response.

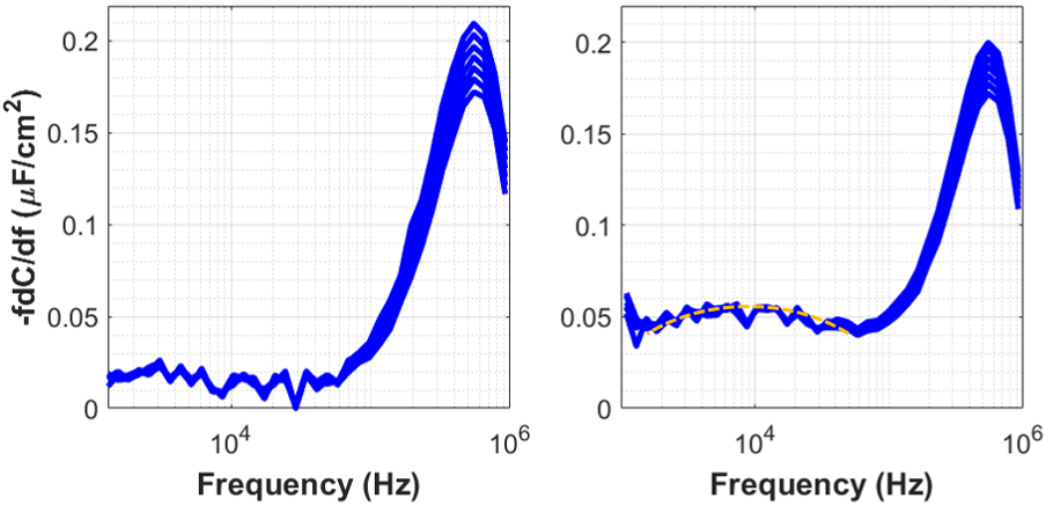

Figure 4.49: Zoom on the potential conductance peaks related to interface states observed for two samples pre-cleaned with AS, in the $[-0.9; -0.6V]$ range. Left: co-evaporated CIGS sample (HF8). It is difficult to locate a maximum in the data as discussed in the text. Right: sputtered CIGS sample (HF11) exhibiting higher interface-trap response.

Ammonia-cleaned samples - HF1-4 and HF9-10 For these samples, whether the CIGS is processed by sputtering or co-evaporation, the identification of clear conductance peaks is impossible. Furthermore, the significant degradation of the CV curves make it also difficult to obtain reliable results with the HLF technique. Therefore, for the as-deposited samples with Ammonia pre-cleaned CIGS, the value of D_{it} is not estimated. Nevertheless, as mentioned above, the PDA treatments are apparently capable of sometimes correcting this unexpected behaviour so as to obtain more typical 2D maps with the expected series resistance response and clear interface-trap 2D signature as on figure 4.45. Consequently, it becomes possible for some samples to extract the value of D_{it} after single and double annealing, as reported in table 4.2. On the whole, the estimations of D_{it} for Ammonia treatment are superior than for AS cleaning which further supports the suggestion about the latter cleaning being more advantageous in the case of hafnium oxide.

The physical origin of that new feature appearing on the 2D maps of Ammonia-cleaned samples is yet unclear. It might be related to the Cu_xSe secondary phase remaining after Ammonia treatment [40] but it is not observed on the alumina-based samples also cleaned with Ammonia. Thus, it may be related to the combination of Ammonia-cleaned CIGS surface and hafnium oxide, for instance a complex defect whose response is different from typical interface states and depends on the composition of the CIGS as discussed in [36]. This requires future investigations as discussed further in section 4.7.

4.5.3 Summary

Similarly to the Al_2O_3 series, PL measurements for hafnia-based MIS samples indicate an effective surface passivation with a global increase in PL intensity and minority carrier lifetime after oxide deposition. Besides that, the analysis of surface cleaning effect is two-fold: on the one hand, surface cleaning tends to only have a determinant effect in the case of sputtered CIGS, presumably due to the higher roughness [39] or the potential

Samples	$D_{it}[cm^{-2}eV^{-1}]$ (HLF)	$D_{it}[cm^{-2}eV^{-1}]$ (CM)
Co-evap. CIGS + AS		
AD	$8.9 * 10^{10}$	$4.3 * 10^{11}$
A1 (300°C)	$< 10^{10}$	X
A1 (400°C)	$8.3 * 10^{11}$	$8.2 * 10^{11}$
Co-evap. CIGS + Ammo		
AD	X	X
A1 (300°C)	X	X
A1 (400°C)	$9.4 * 10^{11}$	$9.4 * 10^{11}$
Sput. CIGS + AS		
AD	$4 * 10^{11}$	$5.2 * 10^{11}$
A1 (300°C)	$2.4 * 10^{11}$	$1.6 * 10^{11}$
A2 (400°C)	$2.5 * 10^{12}$	$8.3 * 10^{11}$
Sput. CIGS + Ammo		
AD	X	X
A1 (300°C)	$8.3 * 10^{11}$	$7 * 10^{11}$
A2 (400°C)	$2.7 * 10^{12}$	$6.3 * 10^{11}$

Table 4.2: Estimated average values of D_{it} for the different series of hafnia-based MIS samples (CM is conductance method). The first and second categories respectively include HF5-8 and HF1-4 with single annealing at either 300°C or 400°C. The third and fourth categories respectively include HF11-12 and HF9-10 with double annealing at 300°C first and then at 400°C. "X" indicates impossible or not reliable extraction of D_{it}.

secondary phases [40]; on the other hand, as seen above, AS cleaning provides higher PL intensity and carrier lifetimes in the case of a sputtered CIGS/Al_2O_3 interface whereas Ammonia treatment seems more advantageous for treating sputtered CIGS/HfO_2 interfaces.

The IV results suggest that, without annealing, hafnia-based MIS structures with co-evaporated CIGS pre-cleaned with Ammonia have the strongest shunt and thus lowest leakage compared to the other configurations. Nonetheless, single PDA treatments at 300°C lead to significant increase in shunt resistance for the co-evaporated CIGS treated with AS before the oxide deposition, which then takes the lead in terms of leakage for annealed structures.

Generally speaking, a clear distinction occurs between as-deposited AS-cleaned and Ammonia-cleaned samples. The former configuration results in typical CV measurements exhibiting the expected series resistance and discrete interface-trap responses regardless of the CIGS processing technique. On the contrary, a novel feature appears on the CV measurements and 2D maps of Ammonia-cleaned samples whose signature, occurring at different frequencies for sputtered and co-evaporated CIGS, make impossible the reliable extraction of D_{it}. Although its origin is yet to be discussed in section 4.57 (Cu_xSe secondary phases [40], large series resistance, complex defects [36], ...), it may apparently be weakened or even cancelled by annealing treatments, thus allowing for the quantification of chemical passivation.

With regards to field-effect passivation, the mean value of Q_f for non-annealed samples is comprised within $[-7.3; -8.7] * 10^{12} cm^{-2}$, slightly higher than for alumina. There

is once again no apparent dependence of Q_f with regards to CIGS processing and cleaning. The sign of Q_f remains negative as with alumina, with an average flat-band voltage around $0.5V$. Still, besides apparently improving the CV behaviour of the Ammonia-cleaned samples, single PDA treatments at either 300°C or 400°C also activate positive charges in the hafnia layer for both AS and Ammonia-treated configurations, leading to a leftwards shift of the CV curves. This in turn lowers the value of V_{fb} down to $0.1V$ which remains however not sufficient in this case to obtain a positive density of charges. Still, if not oriented in the desired direction, the potentially detrimental counter-effect of negative field-effect is at least mitigated. The effect of a second annealing seems to further activates positive charges in the hafnium oxide layer resulting in a minimum value of Q_f equal to $-4.8 * 10^{12} cm^{-2}$.

As summarized in table 4.2, the values of D_{it} are, when an accurate extraction is possible, on average similar to the results obtained for alumina with an order of magnitude of $10^{11} cm^{-2} eV^{-1}$ for most of the samples. For AS-cleaned samples, co-evaporated CIGS leads to the lowest density of interface traps. Single PDA treatments at 300°C result, on the one hand, to a slight decrease of D_{it} for AS-treated samples and, on the other hand, to the appearance of interface-trap response for some Ammonia-treated samples then exhibiting higher densities of interface states around $[8 - 10] * 10^{11} cm^{-2}$. Single or second annealing processes at 400°C induce significant increase in the mean values of D_{it} for each CIGS cleaning and processing.

At this point, it seems that either Al_2O_3 or HfO_2 exhibit negative densities of fixed charges resulting in misdirected field-effect passivation. On the contrary, both materials are suitable for front interface chemical passivation with densities of interface traps of the order of $10^{11} cm^{-2} eV^{-1}$. Only considering the aspect of chemical passivation, the integration of these oxide layers in complete solar cells should be discussed. In particular, it appears that Al_2O_3 is actually not completely compatible with CIGS solar cells processing. More precisely, the CBD step required to deposit the CdS layer on top of the passivation layer in our target design (figure 2.6) involves Ammonia, which is reported to be an etchant of alumina in [59]. Therefore, performing this CdS deposition step on a front-passivated Substrate/Mo/CIGS/Al_2O_3 stack might partly or totally etch the aluminum oxide layer and simultaneously the nano-openings pattern as demonstrated in [60], potentially leading to poor performances of the final solar cell.

Nevertheless, it is shown in [59] that Ammonia-based solutions selectively etch Al_2O_3 while preserving hafnium oxide compounds. This suggests that an HfO_2-based protective layer could therefore be deposited over the underlying Al_2O_3 so as to prevent the etching of both the alumina layer and the point contacts patterning by Ammonia-based solutions during CBD of CdS. This results in a more sophisticated Substrate/Mo/CIGS/Al_2O_3/HfO_2 stack for which the realization of nano-openings through the then-called Al_2O_3/HfO_2 multi-layer configuration is presently under investigation with encouraging results, hypothetically making the whole design compatible with the complete targeted solar cell from section 2.6. This is the motivation for investigating this innovative concept in the next section.

4.6 Multi-layer configuration - Al_2O_3/HfO_2

Although the problem of field-effect passivation is not likely to be solved with this design since both dielectric layers individually show negative Q_f, chemical passivation and other aspects are presumably expected to provide acceptable results. In this section, only samples with co-evaporated CIGS are investigated along with the effect of surface cleaning and single annealing at either 300°C or 400°C. The samples are designated ALHF1-8 and described in details in section 3.2.3.1. The quantitative results obtained in this section are summarized in table 4.4 along with the outcomes related to alumina and hafnia-based samples.

4.6.1 PL measurements

As expected, the increase in PL intensity observed on figure 4.50 after surface cleaning and oxide deposition suggests the effectiveness of passivation. The PL intensity is scaled up by a factor 15 to 30 in the case of Ammonia pre-treatment (ALHF1-4) whereas it is only 3 to 4 times higher for AS (ALHF5-8). Since this difference is not observed above for co-evaporated CIGS and hafnia, it may indicate that Ammonia treatment is more advantageous than AS for co-evaporated CIGS/Al_2O_3/HfO_2 stacks. However, the minority carrier lifetime increases in a similar fashion for both cleaning techniques and given the qualitative character of PL characterization, further investigations are required to verify that hypothesis about Ammonia being more advantageous than AS for ideally smooth co-evaporated CIGS [39], namely with IV and CV measurements.

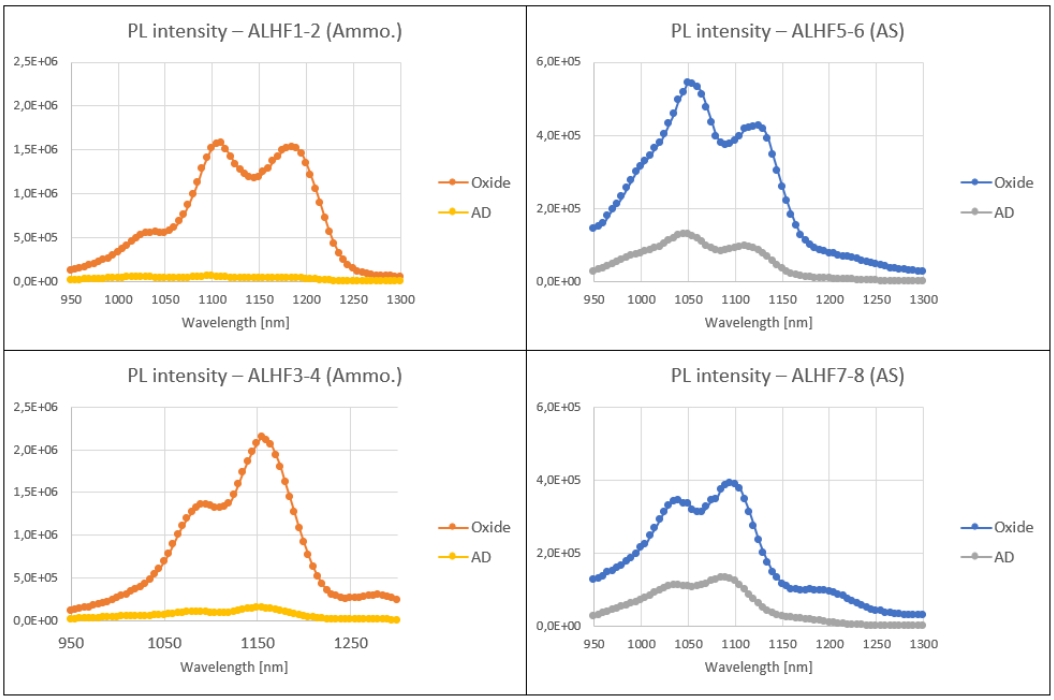

Figure 4.50: Comparison of average PL intensity before (AD) and after the deposition of 30nm Al_2O_3/20nm HfO_2 on 3-stage co-evaporated CIGS pre-cleaned with either Ammonia or AS. The ALHF1-2 and ALHF5-6 samples have similar CIGS composition with higher Cu content than the ALHF3-4 and ALHF7-8 samples (different scales from left to right).

Besides that, the shapes of the PL spectra are similar to previous observations on co-evaporated CIGS. There generally are 2 to 3 absorption peaks observed around the same wavelengths as for simple alumina or hafnia-based MIS samples, i.e. one peak close to bandgap energy transition of 1.15eV and other peaks at either higher energy (maximum bandgap due to Gallium grading) or lower energy (defects). As discussed above, the relative heights of these peaks is presumably related to the composition of the CIGS and especially the Copper content [36, 37]. Moreover, the important shifts sometimes observed on the emission spectra between repetitions of PL measurements on the same sample may be a proof of interference-related issues as reported in [55].

4.6.2 IV/CV measurements

4.6.2.1 Leakage

The mean values of shunt resistance for these samples are shown on figure 4.51, indicating lower leakage than the previous individual observations about alumina and hafnia. The nearly doubled total oxide thickness (50nm) as compared to the samples studied above might be an explanation for this reduction of parasitic currents. This is illustrated by the average values of R_{sh} that are globally superior to $1M\Omega.cm^2$ except for the case of 300°C annealed multi-layer sample pre-cleaned with Ammonia. Still, in that particular case, the shunt resistance is equal to $201k\Omega.cm^2$ which remains acceptable. For AS-treated samples, the annealing treatments result in significant increase of the shunt resistance with, as already observed above, the best PDA temperature appearing to be 300°C. The 400°C annealing applied on the Ammonia-cleaned samples slightly lowers the value R_{sh} but not sufficiently to be considered as an important degradation. One can thus conclude that, generally speaking, these samples are particularly well shunted and thus the CV data obtained on these ones are supposedly not greatly impacted by parasitic transport.

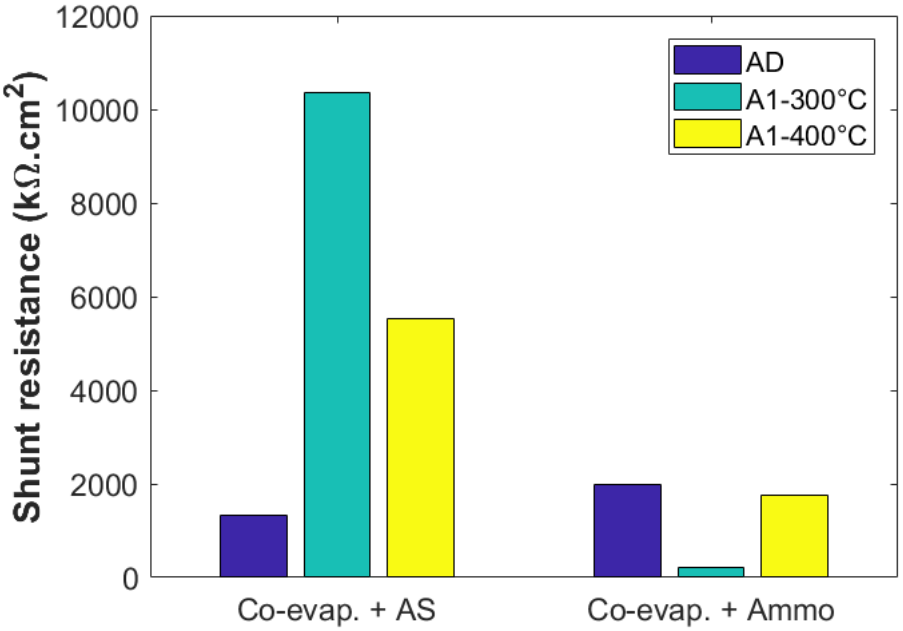

Figure 4.51: Comparison of the average shunt resistance in function of surface cleaning and annealing, for the whole set of Al_2O_3/HfO_2 multi-layer samples (ALHF1-8) with co-evaporated CIGS. A1 refers to first annealing process either at 300°C or 400°C.

4.6.2.2 2D maps analysis - series resistance

Figures 4.52 and 4.53 present the measured CV curves and 2D maps obtained on respectively AS and Ammonia-cleaned samples. Both samples exhibit two main features on their maps: first, the still unidentified large rectangular response appearing respectively at mid and high frequency in accumulation for AS and Ammonia pre-treatment; second, the diagonal signature which crosses most of the map to eventually merge into the former response is likely to be the consequence of interface traps (discussed in the Chemical passivation section below).

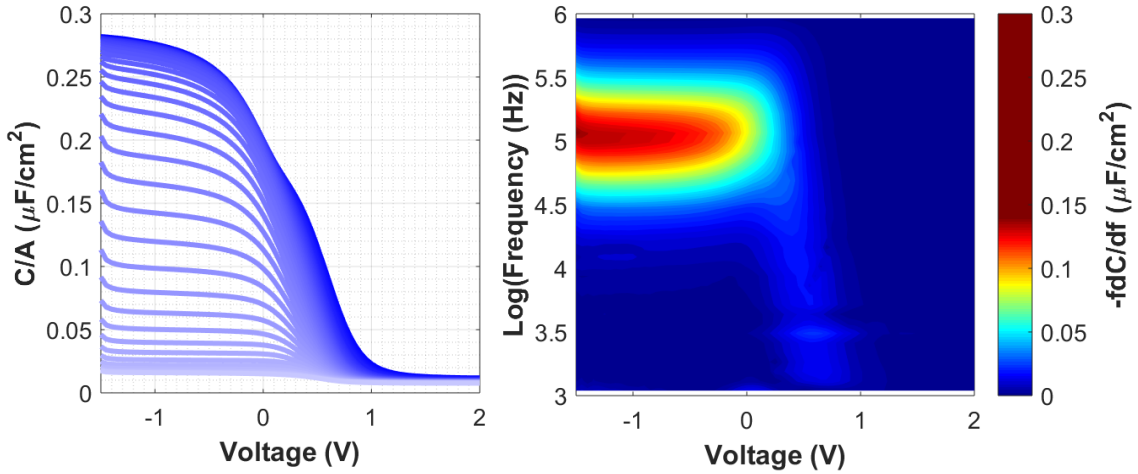

Figure 4.52: Measured CV curves and 2D maps for the ALHF4 sample, pre-cleaned with AS. Left: CV curves from 1kHz (dark blue) to 1MHz (light blue). Right: Capacitance derivative 2D map showing two main features discussed in the text, i.e. the large rectangular response on the top-left corner and the diagonal tail-like feature in the middle.

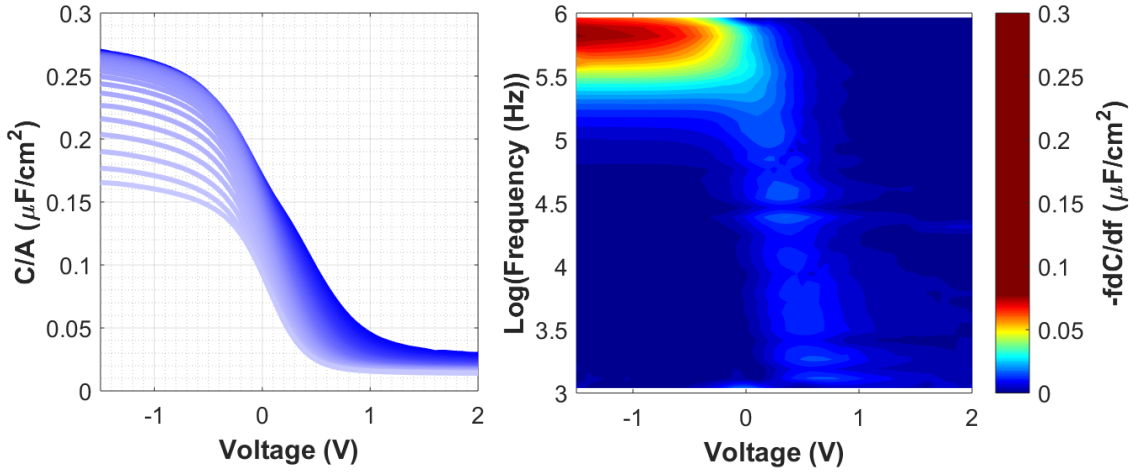

Figure 4.53: Measured CV curves and 2D maps for the ALHF1 sample, pre-cleaned with Ammonia. Left: CV curves from 1kHz (dark blue) to 1MHz (light blue). Right: Capacitance derivative 2D map showing similar features to the AS-cleaned sample.

As already discussed in details above, the physical origin of the former effect is unclear. Indeed, either the huge CV frequency dispersion observed in accumulation originates from a rather high series resistance (especially for the AS-cleaned sample), itself presumably induced by the combination of border traps and resistive potential barrier at the back interface; either it is the consequence of another phenomenon such as complex defects related to Cu [36] or metallic Cu_xSe secondary phases. The former hypothesis is discussed below in section 4.57. On the contrary, the latter suggestion is rather questionable since undesired Cu_xSe phases should be precisely removed after AS cleaning [40].

Besides that, it appears that the frequency position of this unidentified 2D signature depends on the surface cleaning and might thus as well be related to the CIGS/Oxide interface. This difference of position on the 2D map would in turn mean that, in the case of an unknown defect being the origin of this feature, its energy position is a function of the CIGS surface treatment and the defect itself is shallower in the case of Ammonia cleaning. Moreover, regardless of the cleaning, there seems to be a consistent dependence of the frequency position of that signature on the map with the variation in Copper content among the series of samples cleaned with AS, as illustrated below on figure 4.57. Finally, the vertical diagonal signature located within the $[0V; 1V]$ range and identified as the response of interface states seems to move in a similar fashion as the large rectangular response, suggesting that these two effects might actually share the same physical origin. All of this is discussed in section 4.57.

In the case where the unidentified response is actually related to series resistance, the corresponding estimated values would be quite high and in the same order of magnitude as the Ammonia-cleaned hafnia samples for which the same interrogations were expressed. In particular, the AS-cleaned samples with multi-layer configuration have an estimated average series resistance of $12.1\Omega.cm^2$ whereas the structures treated with Ammonia have $R_s = 2.46\Omega.cm^2$ on average. Besides that, the effect of PDA annealing is to slightly increase (resp. decrease) the mean value of R_s for samples cleaned with Ammonia (resp. AS) as summarized along with most of the already obtained results in table 4.4.

The cold CV measurements realized on the AS-cleaned ALHF5 sample indicate that the resistive potential barrier possibly present at the back interface has a height of 315meV (figure 4.54), by applying the same procedure as for the AL series. Not only this value of potential barrier is much higher than for alumina-based MIS samples with ideally identical back interface composition (170meV), but also the corresponding value of R_s at -75°C as estimated by comparison with the simulations is around $1400\Omega.cm^2$, which is quite above the range of values reported in [45] in the case of CIGS. Therefore, the log-linear temperature dependence observed for that 2D signature may originate from another phenomenon such as bulk [61] or interface defects (section 2.7.3.2). In this case, the obtained activation energy would be an image of the energy level associated to these hypothetical defects instead of the considered resistive potential barrier, as discussed in section 4.57.

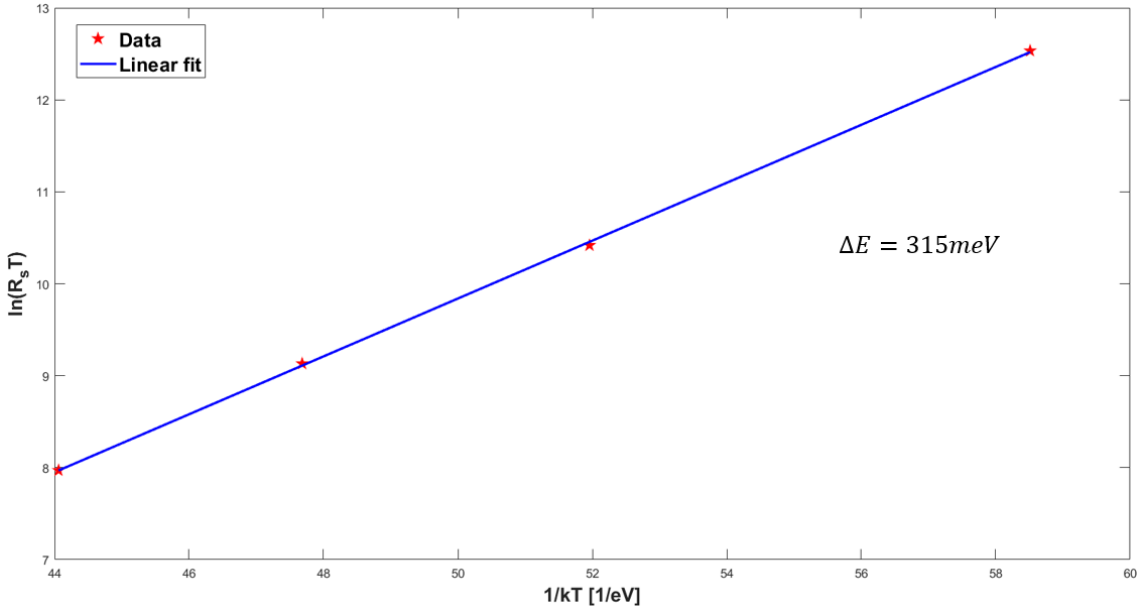

Figure 4.54: Determination of the activation energy associated to the large unidentified frequency response mainly observed in accumulation on the 2D maps of AS-cleaned samples, using CV measurements at low temperature, i.e. down to -75°C, realized on the ALHF5 sample. The extracted activation energy is estimated to be $\Delta E = 315meV$ by linear interpolation through the values of R_s estimated using MATLAB simulations.

4.6.2.3 Field-effect passivation

As expected, the value of the flat-band voltage of this multi-layer Al_2O_3/HfO stack is similar to the values obtained for MIS capacitors with single layers made either of alumina or hafnia, i.e. between $0.5V$ and $0.7V$ for as-deposited samples (figure 4.55). The stacking of these two materials with individual as-deposited negative charge density thus result in a negative field-effect whose total equivalent fixed charge density is comprised within $[-2.4; -2.8] * 10^{12} cm^{-2}$. Once again, the results obtained indicate an effective but misdirected field-effect passivation induced by the negative fixed charges intrinsically present inside both of the as-deposited oxide layers in the stack. Single PDA treatments at either 300°C or 400°C lead to the same slight leftwards shift of the CV curves, in turn resulting in moderately lower values of Q_f (figure 4.55).

Similarly to the individual observations about annealing effect on alumina and hafnia and given the rather additive character of field-effect, it is possible to softly diminish the magnitude of negative Q_f by activating positive charges presumably in both oxide layers. Nevertheless, given the inverse dependency of Coulomb's interactions with distance and the more remote location of the HfO_2 layer as compared to the Al_2O_3 layer in this configuration, the alumina layer should be more determinant in terms of field-effect passivation. This is likely to be the case for chemical passivation as well since the CIGS layer is exclusively in contact with alumina. In the target multi-layer passivated solar cell, the main role of the top hafnia layer (2nm) would then be to protect the thicker underlying alumina layer (6-10nm) from the CBD step of CdS.

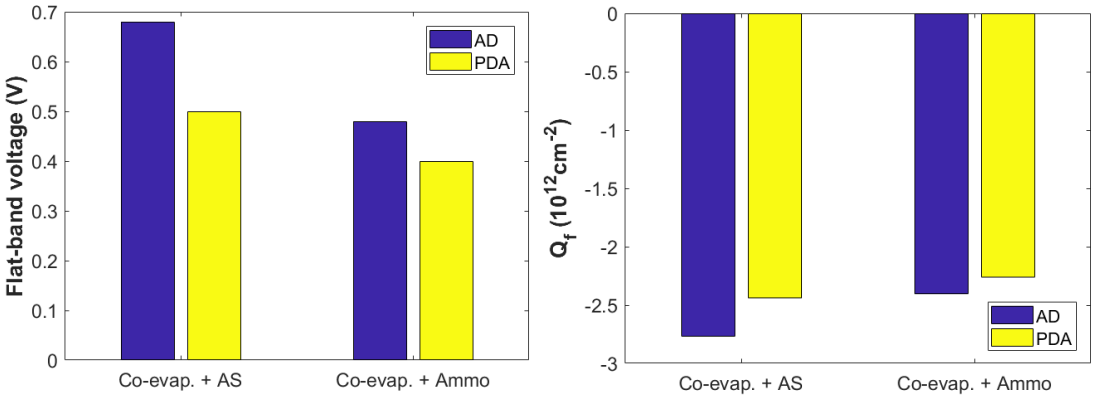

Figure 4.55: Effect of post-deposition annealing on the average values of V_{fb} and Q_f for the series of Al_2O_3/HfO_2 multi-layer samples (ALHF1-8) with sputtered CIGS. The work-function of the front Silver grid is taken to be 4.5eV, i.e. the mean between 4.26eV and 4.73eV. The PDA treatment is made at either 300°C or 400°C.

4.6.2.4 Chemical passivation

Since the expected diagonal signatures related to interface traps are clearly visible on each sample of this series, the extraction of D_{it} should be more reliable and accurate. Generally speaking, the higher prominence of this feature for the Al_2O_3/HfO_2 stacks as compared to the individual AL and HF series leads to two different hypotheses: either the effect of interface states is higher, i.e. chemical passivation is less effective, when alumina and hafnia are stacked than individually used; either the stacking of Al_2O_3 and HfO_2 mitigates the influence of side effects such as series resistance, border traps, leakage current (high shunt) or even measurement noise, thus making the response of interface traps easier to identify without necessarily increasing D_{it}.

This latter hypothesis is supported by the fact that the mean values of D_{it} presented in table 4.3 are globally similar to the previous results obtained on single-layer MIS structures with Al_2O_3 or HfO_2. Since the conductance peaks associated to interface states are more easily identified in this case, the application of the conductance method is facilitated and with greater accuracy. In particular, these peaks are located at mid frequency, i.e. around $10kHz$ (figure 4.56), which indicates relatively deep trap states with energy levels 300meV at least above the VB edge by comparing with previous simulations (section 4.2 and Appendix B). For as-deposited samples, it appears that Ammonia pre-cleaning results in slightly lower traps densities than AS treatment (table 4.3). This small difference may be explained by the higher prominence of the unidentified response for AS-cleaned samples.

The effect of annealing on the value of D_{it} is once again dependent on the annealing temperature. Indeed, table 4.3 shows that, regardless of the pre-cleaning, PDA treatments at 300°C tend to slightly decrease the average density of interface traps whereas annealing processes at 400°C induce a moderate increase of that very parameter (conductance method supposedly more accurate than HLF). This translates into a down-scaling of the diagonal interface-related signature of the 2D map. Eventually, it seems that annealing treatments at 300°C once again lead to the best results in terms of chemical passivation, as similarly observed above for alumina and hafnia-based samples.

Samples	$D_{it}[cm^{-2}eV^{-1}]$ (HLF)	$D_{it}[cm^{-2}eV^{-1}]$ (CM)
Co-evap. CIGS + AS		
AD	$3.1 * 10^{11}$	$3.9 * 10^{11}$
A1 (300°C)	$3 * 10^{11}$	$3.4 * 10^{11}$
A1 (400°C)	$1.4 * 10^{11}$	$6.4 * 10^{11}$
Co-evap. CIGS + Ammo		
AD	$1.4 * 10^{11}$	$2.2 * 10^{11}$
A1 (300°C)	$0.9 * 10^{11}$	$1.4 * 10^{11}$
A1 (400°C)	$2.9 * 10^{11}$	$5.5 * 10^{11}$

Table 4.3: Estimated average values of D_{it} for the series of multi-layer MIS samples (CM is conductance method). The first and second categories respectively include ALHF5-8 and ALHF1-4 with single annealing at either 300°C or 400°C.

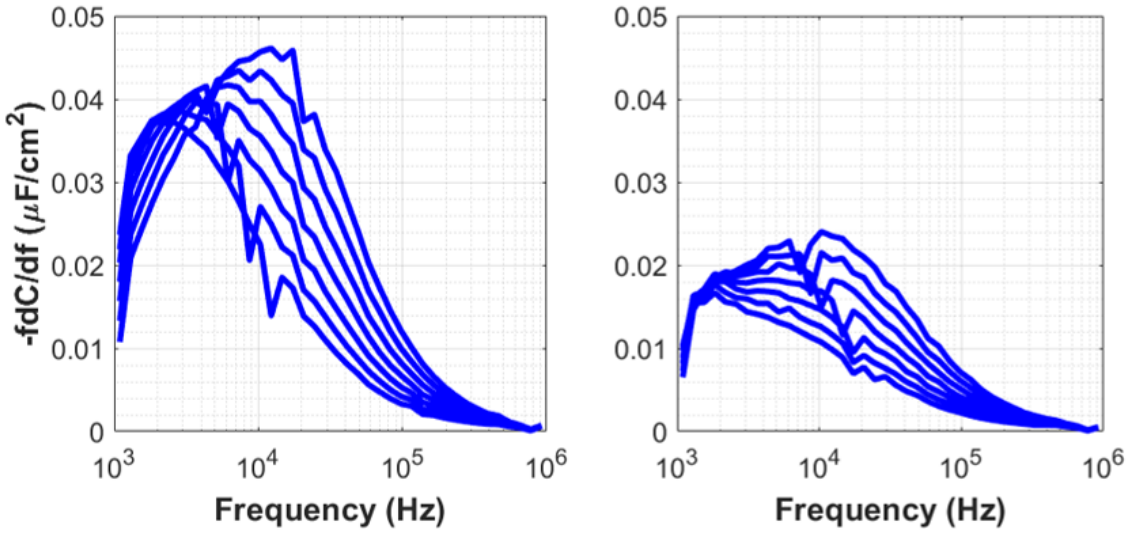

Figure 4.56: Vertical cut along the frequency axis of capacitance derivative 2D maps (ALHF2 and ALHF6) to highlight the conductance peaks related to interface states and observed in the $[0.35; 0.65V]$ range. Left: co-evaporated CIGS pre-cleaned with AS (ALHF6) exhibiting mean peak height of $0.04\mu F/cm^2$. Right: co-evaporated CIGS pre-cleaned with Ammonia (ALHF2) exhibiting mean peak height of $0.02\mu F/cm^2$.

4.6.3 Summary

The global increase in both PL intensity and carrier lifetime after surface pre-cleaning and deposition of these Al_2O_3/HfO_2 multi-layer oxide stacks on bare co-evaporated CIGS suggest effective passivation effects. This was expected given the similar trends and PL spectra observed individually for alumina and hafnia.

The leakage currents are on average lower when combining Al_2O_3 and HfO_2 than for single layers, presumably explained by the higher total thickness of the double-layer oxide stack. The mean shunt resistance for the as-deposited samples is of the order of $1M\Omega.cm^2$ which can be enhanced by either 300°C or 400°C PDA for the AS pre-cleaned configuration. This improvement of shunt due to annealing is not observed for Ammonia-treated samples. Still, R_{sh} is on the whole more than sufficient to ensure negligible degradation of CV data due to parasitic transport.

The inspection of capacitance derivative 2D maps allows to observe similar features as for single alumina and hafnia layers, i.e. interface states response, series resistance but also unidentified responses. The values of R_s presented in table 4.4 for Al_2O_3/HfO_2 stacks are then estimated by considering that these unknown 2D features are well related to series resistance. This hypothesis is discussed below in section 4.57, along with the impact of CIGS pre-cleaning and processing as compared to HfO_2. Low-temperature CV measurements realized on one sample of the multi-layer set indicate that the unidentified response has a potential barrier or activation energy of 315meV, quite higher as compared to the series resistance response in alumina-based MIS samples.

Similarly to single passivation layers made of alumina and hafnia, the stacking of Al_2O_3 and HfO_2 result in a negative equivalent density of fixed charges with an average magnitude around $2 * 10^{12} cm^{-2}$, whether the CIGS layer is pre-cleaned with AS or Ammonia. This corresponds once again to a strong but misdirected field-effect for front interface passivation. PDA treatments, regardless of the temperature (300°C or 400°C), lead to a moderate activation of positive charges in the oxide layers which in turn slightly reduces the magnitude of Q_f without inverting its sign.

The characterization of chemical passivation for these multi-layer MIS samples provide mean values of D_{it} comprised within the $[1.4 - 3.9] * 10^{11} cm^{-2} eV^{-1}$ range without any annealing treatment. The identification of the conductance peaks related to interface states is more straightforward in this case than for single alumina and hafnia layers, resulting in a more reliable extraction of that figure-of-merit. Despite being apparently more active with Ammonia than AS pre-cleaning, the effectiveness of chemical passivation seems confirmed by the rather low values of D_{it} observed for each sample of this set. Furthermore, PDA treatments at 300°C tend to slightly reduce the density of interface traps whereas 400°C annealing processes seem to increase that very quantity.

4.7 Al_2O_3 and HfO_2 - Discussion

4.7.1 Optimal design

By gathering and discussing all the results in (table 4.4 for CIGS-based MIS samples with an oxide layer made of alumina, hafnia or their superposition, it is possible to highlight the optimal combination of the different parameters investigated that result in the closest results to the targeted specifications. The aspect of series resistance and analysis of unidentified 2D features is treated below in section 4.57.

Generally speaking, the minimum values of shunt resistance are observed for MIS capacitors with sputtered CIGS of the order of $1 - 10 k\Omega.cm^2$. whereas co-evaporated CIGS layers globally result in average values of R_{sh} that are higher by 1 or 2 (resp. 3) orders of magnitude in the case of single alumina or hafnia layers (resp. multi-layer stacks). For most configurations, single annealing treatments at 300°C tend to reduce leakage currents with an increase in R_{sh} whereas 400°C single or double PDA either lead to lower enhancements or degradation as compared to 300°C annealing. The effect of CIGS surface treatment with regards to shunt depends on the CIGS processing and the oxide material.

Concerning the actual target of this study, i.e. interface passivation, the conclusion is that either alumina, hafnia or their combination lead to rather similar results with regards to both field-effect and chemical passivation. On the one hand, regardless of CIGS cleaning and processing, the equivalent density of fixed charges Q_f is negative and of the order of $10^{12} cm^{-2}$, resulting in misdirected electrical field for the targeted front passivated solar cell. The potentially detrimental effect of negative Q_f for front interface passivation can be mitigated by single and double annealing treatments at either 300°C or 400°C.

On the other hand, the density of interface traps D_{it} globally stays within the $[1 - 5] * 10^{11} cm^{-2} eV^{-1}$ range for as-deposited samples, indicating active chemical passivation. The influence of surface cleaning depends on the dielectric material and is believed to be more determinant for sputtered than co-evaporated CIGS. The effect of PDA treatments is less equivocal and consistently result in enhanced (resp. degraded) chemical passivation in the case of single 300°C annealing (resp. 400°C single and double annealing).

Finally, two configurations appear to be the most optimal: either single alumina layer with AS-treated sputtered CIGS or alumina/hafnia stack with Ammonia-cleaned co-evaporated CIGS, both annealed once at 300°C. Both showing higher PL intensity and carrier lifetimes as compared to equivalent samples, the values of Q_f and D_{it} observed for these two configurations are among the lowest, respectively corresponding to mitigated negative field-effect and effective chemical passivation.
The good performances of the former design are presumably related to the improvement of the CIGS top surface quality after AS cleaning [39, 40]. This in turn results in lower series resistance, whose estimation is discussed in the next section. Although more weakly shunted as compared to the second optimal configuration, shunt resistance is especially important for MIS samples rather than complete solar cells in which electrical current should circulate, namely through nano-openings in our targeted design.
Regarding this particular matter, the alumina/hafnia stack has the great advantage of being simultaneously compatible with the CBD processing of CdS and the patterning of point-openings [59, 60]. Even though negative field-effect is better suited to back interface passivation, the stacking of Al_2O_3 and HfO_2 as front passivation layer may provide interesting performance enhancement related to chemical passivation while providing an alternative to single alumina layers that is compatible with the full solar cell processing.

4.7.2 Analysis of 2D maps - feature identification

The analysis of capacitance derivative 2D maps in the case of hafnia-based and multi-layer MIS samples highlights the presence of two distinct features (figures 4.41, 4.43 and 4.52-4.53). On the one hand, there is a prominent response observed at mid/high frequency in the accumulation regime (top-left corner) of those 2D maps and whose origin remains unclear; on the other hand, the diagonal tail-like feature associated to the response of interface states is clearly visible on the 2D maps of most categories of samples. This very response of interface traps closely resembles to the simulations from section 4.2 and allows quite an accurate extraction of D_{it} when clearly distinguished from side effects and background noise as in the case of multi-layer stacks. However, the conductance peaks related to interface defects are much harder to identify for some samples. This in turn raises the possibility for the interface response to be actually hidden by the former unidentified feature whose physical origin seems then rather important to determine.

Configuration	$R_{sh}[k\Omega.cm^2]$	$R_s[\Omega.cm^2]$	$Q_f[cm^{-2}]$	$D_{it}[cm^{-2}eV^{-1}]$
Al_2O_3				
Co-evap-Ammo	161	0.72	$-1.9 * 10^{12}$	$3 * 10^{11}$
A1 (300°C-400°C)	772	0.47	$-1.3 * 10^{12}$	X
Sput-AS	3	0.25	$-2.1 * 10^{12}$	$1.2 * 10^{11}$
A1 (300°C)	13	0.33	$-1.4 * 10^{12}$	$0.7 * 10^{11}$
Sput-Ammo	14	0.12	$-2.3 * 10^{12}$	$2.3 * 10^{11}$
A1 (300°C)	14	0.42	$-1.5 * 10^{12}$	$0.4 * 10^{11}$
A2 (400°C)	3	0.11	$-1.3 * 10^{12}$	$4.8 * 10^{11}$
HfO_2				
Co-evap-AS	7	0.48	$-7.7 * 10^{12}$	$2.6 * 10^{11}$
A1 (300°C)	485	0.3	$-5.3 * 10^{12}$	X
A1 (400°C)	210	3.42	$-5.3 * 10^{12}$	$8.3 * 10^{11}$
Co-evap-Ammo	90	12.64	$-7.5 * 10^{12}$	X
A1 (300°C)	106	2.32	$-5.2 * 10^{12}$	X
A1 (400°C)	76	0.54	$-5.3 * 10^{12}$	$9.4 * 10^{11}$
Sput-AS	1	0.14	$-7.3 * 10^{12}$	$4.6 * 10^{11}$
A1 (300°C)	6	0.26	$-6.4 * 10^{12}$	$2 * 10^{11}$
A2 (400°C)	2	0.05	$-4.8 * 10^{12}$	$1.7 * 10^{12}$
Sput-Ammo	1	1.26	$-8.8 * 10^{12}$	X
A1 (300°C)	4	0.26	$-6.6 * 10^{12}$	$7.7 * 10^{11}$
A2 (400°C)	2	0.28	$-5.2 * 10^{12}$	$1.7 * 10^{12}$
Al_2O_3/HfO_2				
Co-evap-AS	1331	12.1	$-2.8 * 10^{12}$	$3.5 * 10^{11}$
Anneal 300°C	10360	8.23	$-2.8 * 10^{12}$	$3.2 * 10^{11}$
Anneal 400°C	5515	14.82	$-2.4 * 10^{12}$	$3.9 * 10^{11}$
Co-evap-Ammo	1981	2.45	$-2.4 * 10^{12}$	$1.8 * 10^{11}$
Anneal 300°C	201	1	$-2.3 * 10^{12}$	$1.2 * 10^{11}$
Anneal 400°C	1745	6.11	$-2.3 * 10^{12}$	$4.2 * 10^{11}$

Table 4.4: Summary of the results obtained on each series of samples with regards to IV and CV measurements, except for titania-based samples. A1 and A2 refer to single and double annealing at either 300°C or 400°C.

Originally thought as being related to series resistance and border traps, the high-magnitude responses observed mostly on the top-left corner of the 2D maps from figures 4.41, 4.43 and 4.52-4.53 may originate from a more complex phenomenon. For instance, the comparison of measured 2D maps for hafnia-based MIS configuration with sputtered CIGS pre-cleaned with either AS (figure 4.41) or Ammonia (figure 4.43) shows that the potentially present series resistance would be much higher in the case of Ammonia-cleaning ($15.54\Omega.cm^2$) than AS ($1.14\Omega.cm^2$). Since these samples should theoretically have the same back interface composition, it raises the possibility of another parasitic conductive element such as leaky Cu_xSe secondary phases that are only etched by AS cleaning [40]. However, the same cleaning comparison in the case of co-evaporated CIGS and multi-layer MIS stacks lead to the inverse ratio of series resistance, higher for AS-cleaned samples. Therefore, surface cleaning alone cannot explain these observations and the existence of another phenomenon should presumably be taken into account.

For example, figure 4.57 shows that the frequency location of the unidentified feature on the top-left corner of the measured 2D maps for AS-cleaned multi-layer samples (ALHF5-8) is consistently dependent on the CIGS composition and especially the CGI ratio. This response is not likely to be caused by the potential Cu_xSe secondary phases since these are etched by AS treatment [40]. On the contrary, if the origin of that response actually is the $MoSe_2$ potential barrier present at the back interface, figure 4.57 would indicate that the formation, composition and associated series resistance of that $MoSe_2$ interfacial layer is affected by the elemental composition of the CIGS layer. In particular, lower CGI ratios apparently induce a downward movement of the unidentified response which means, if well related to the resistive potential barrier, an increase of the associated series resistance.

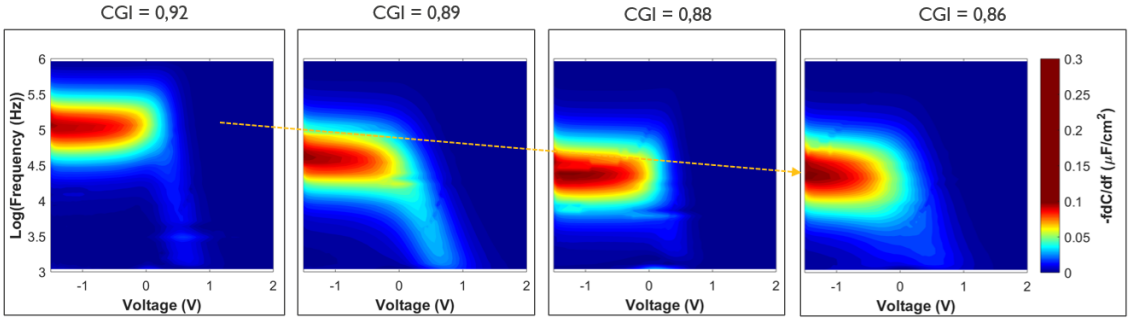

Figure 4.57: Measured capacitance derivative 2D maps for the ALHF5-8 samples (from left to right), illustrating the influence of CGI ratio on the frequency position of the unidentified 2D response.

This hypothesis seems in contradiction with the higher activation energy of 315meV obtained for the ALHF5 sample (left of figure 4.58) with CGI of 0.92 and estimated series resistance of $4.74\Omega.cm^2$, as compared to the supposed resistive potential barrier of 170meV found for the AL9 sample with similar rear interface composition (SLG/Mo/NaF/co-evaporated CIGS), lower CGI of 0.78 and estimated series resistance of $0.2\Omega.cm^2$ (right of figure 4.58). Even though possibly induced by the difference in pre-cleaning between AS-cleaned ALHF5 and Ammonia-cleaned AL9, the significant difference in activation energy tends to indicate that the features observed on the 2D maps of samples ALHF5 and AL9 are intrinsically different. In particular, given the surprisingly high values of R_s and associated potential barrier found for ALHF5, it seems more likely that AL9 is actually exhibiting the response of series resistance at high frequency whereas ALHF5 is affected by another unknown effect. Furthermore, the extracted activation energy of 315meV found for ALHF5 may rather be an image of the energy level of deep complex defects present at the interface and/or inside the bulk of the CIGS [61] and whose behaviour depends on the Copper content as in [36].

To conclude this section, it appears that the exact identification of the different features observed on the 2D maps of MIS samples may provide an interesting insight into the origin and behaviour of the corresponding entities and phenomena. The three possible effects considered here are: first, a resistive potential barrier associated to the $MoSe_2$ interfacial layer at the rear interface; second, a leaky Cu_xSe secondary phase on the top surface of the CIGS; third, complex bulk and/or interface defects related to the Copper

content of CIGS. Besides that, border traps may as well be present but the previous simulations (section 4.2 and 4.3) showed corresponding 2D responses with much lower magnitudes. Eventually, the combination of all or some of these effects might explain the observations made throughout this study, to be confirmed with future investigations (low-temperature CV, CIGS surface and bulk composition, back interface, complex defects, ...). This chapter is closed by the qualitative analysis of CIGS/TiO_2 MIS samples.

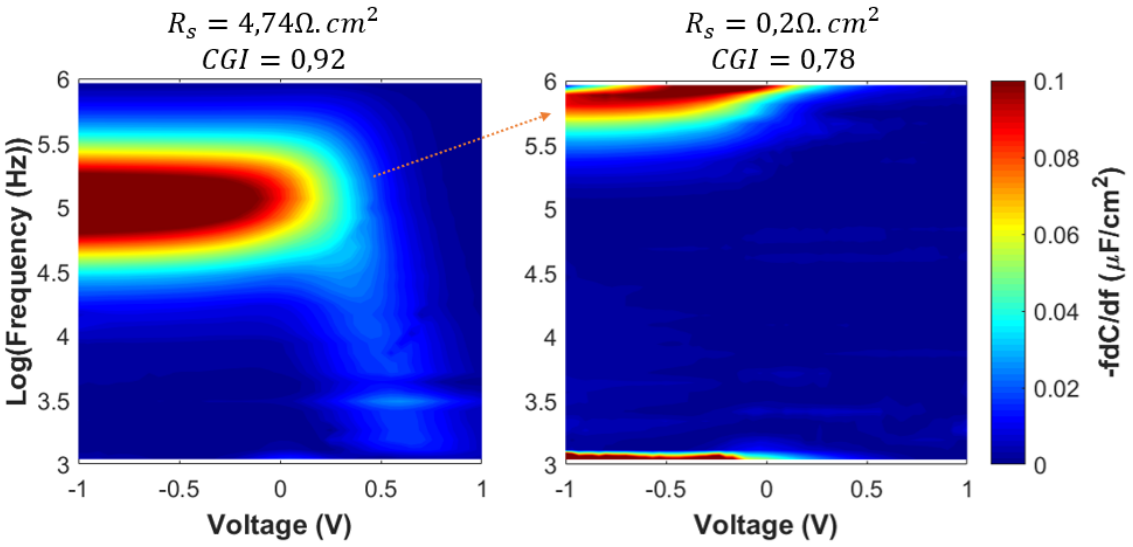

Figure 4.58: Measured capacitance derivative 2D maps for the ALHF5 (left) and AL9 (right) samples. The respective CGI ratios and estimated series resistance are indicated on top of the figures.

4.8 Titanium dioxide - TiO_2

The analysis of TiO_2-based MIS samples presented below should be set aside from the previous results about alumina and hafnia. Indeed, even though titanium dioxide is also investigated as a back passivation layer for CIGS solar cells in [28], there is a great differences to be highlighted as compared to aluminum and hafnium oxide: TiO_2 is intrinsically n-type conductive [29, 62] and has a much narrower bandgap than Al_2O_3 and HfO_2 [30]. In our case, this in turn results in a structure that rather corresponds to a poorly doped p-n junction than a typical MIS capacitor. In particular, the electronic affinity of TiO_2 is around 4eV [62] whereas it is on average equal to 4.36eV for CIGS in our case (see section 4.2). The corresponding conduction band offset, i.e. 360meV, is therefore much lower than with alumina and hafnia having wide bandgap above 6eV and electronic affinities of at least 1.4eV [23, 30]. The equilibrium band alignment of CIGS and titania thus result, on the one hand, in a relatively low the potential barrier faced by the electrons in the CB and, on the other hand, in a much higher VB offset of 1.7eV that is blocking the holes from circulating. If such a band alignment is guaranteed with the concerned semiconductor (Silicon for instance in [27]), TiO_2 can then be used as an electron selective layer.

Therefore, even though TiO_2 might well induce surface passivation effects, the CV analysis required to quantify these effects may not be applicable since the structure that is being measured is no longer behaving as a typical MIS capacitor. This is discussed further in this section. Nonetheless, these considerations have no severe implications with regards to the PL analysis presented just below. In the case of titanium oxide, two new parameters are investigated as compared to the ones already investigated above (CIGS processing and pre-cleaning, annealing treatment): the deposition temperature used to deposit the TiO_2 layers with thermal ALD (150°C or 250°C) as well as their thickness (50nm, 75nm or 100nm). The designations of the different samples are detailed in section 3.2.4.

4.8.1 PL measurements

It is worth mentioning that, for this set of samples, no PL measurements on bare absorber are available to be compared with the CIGS/Oxide stack. Still, the CIGS layer is 3-stage co-evaporated with a similar recipe and composition as the previous series of samples, allowing for comparisons where relevant.

Effect of ALD temperature The PL spectra obtained on Ammonia-cleaned and co-evaporated/sputtered CIGS in function of the TiO_2 layer deposition temperature are presented on figure 4.59, for each possible oxide thickness. There is a striking difference in PL intensity between titania layers deposited at each temperature: 250°C ALD seemingly results in very poor quality of TiO_2 layers as compared to 150°C ALD, especially for thicknesses of 75nm and 100nm and regardless of the CIGS processing. The maximum PL intensity for ALD at 150°C is much higher than the values observed for bare CIGS in the previous series of samples. On the contrary, figure A.6 in Appendix A shows that PL intensity for TiO_2 deposited at 250°C is extremely low, suggesting that surface passivation is only effective in the case of ALD 150°C TiO_2. Actually, it is also observed below that the CV data obtained on the samples with ALD 250°C TiO_2 layers are particularly difficult to analyze. Consequently, the rest of this report mainly focuses on analyzing the measurements obtained on samples with TiO_2 layers deposited at 150°C.

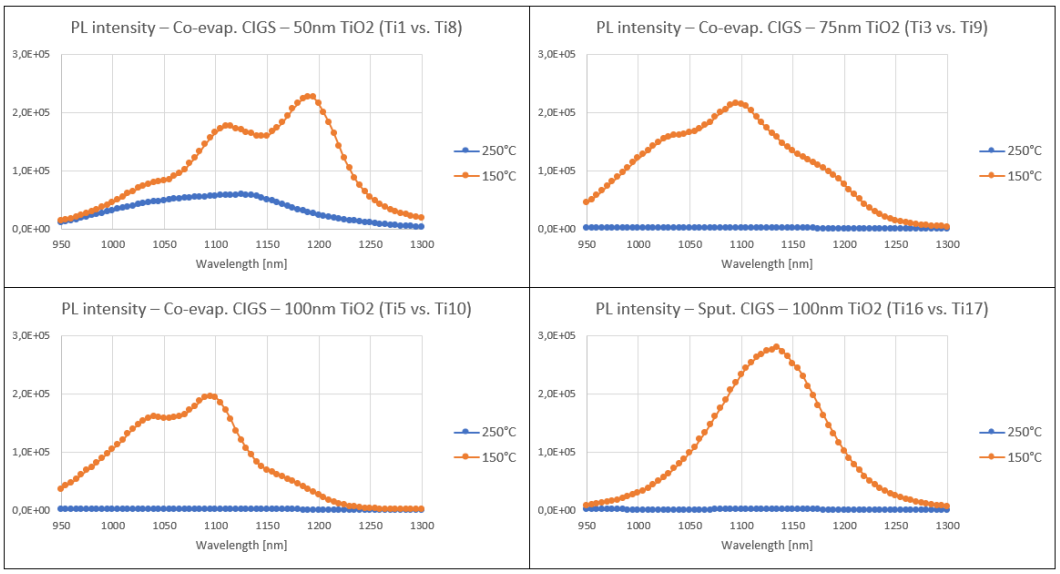

Figure 4.59: Comparison of average PL intensity in function of the ALD temperature deposition for the different oxide thicknesses and for Ammonia-cleaned CIGS only. The significant difference in magnitude between the two temperatures tend to indicate poor quality of the TiO_2 layers deposited at 250°C. The magnification of the low-magnitude PL spectra of ALD 250°C titanium oxide layers is provided on figure A.6 in Appendix A.

Effect of thickness It is depicted on figure 4.60 that, for Ammonia CIGS cleaning and ALD temperature of 150°C, the thickness of the oxide layer mostly induce horizontal shift of the different peaks observed on the PL spectra. Since the composition of the CIGS layer should be rather similar between those samples, the significant alteration of the PL spectra is presumably related to the oxide layer and its thickness. Similarly to the previous PL results, the multiple peaks are supposedly associated to band-to-band and band-to-defect transitions [36]. In particular, there appears to be one high-energy peak around 1050nm (1.18eV) which corresponds to the bandgap of the absorber layer. The other peaks located at lower energy, i.e. between 1100nm (1.13eV) and 1200nm (1.03eV), may be related to shallow defects [36] or minimum bandgap due to Gallium grading. Besides that, interference effects may provide an explanation for the important shifts in wavelength observed between the PL spectra of the different oxide thicknesses [55].

Effect of surface cleaning Figure 4.61 shows the PL spectra obtained on 150°C ALD TiO_2-based samples in function of CIGS pre-cleaning, with similar shapes to the previous results obtained for both co-evaporated CIGS (multiple peaks) and sputtered CIGS (single peak). It seems that AS and Ammonia cleaning have inverse dominance depending on the CIGS processing. This may be related to the influence of pre-cleaning on the absorber surface composition [40], and especially with regards to roughness [39]. For co-evaporated (resp. sputtered) CIGS, AS pre-treatment lead to a globally higher (resp. lower) mean PL intensity, sign of a potentially more (resp. less) effective surface passivation. Double exponential fitting of TRPL measurements result in a 25% higher minority carrier lifetime for the Ammonia-cleaned sputtered CIGS-based sample as compared to AS-treated sample, when taken at a wavelength of 1135nm (1.09eV) corresponding to the position of the single PL peak on the right of figure 4.61.

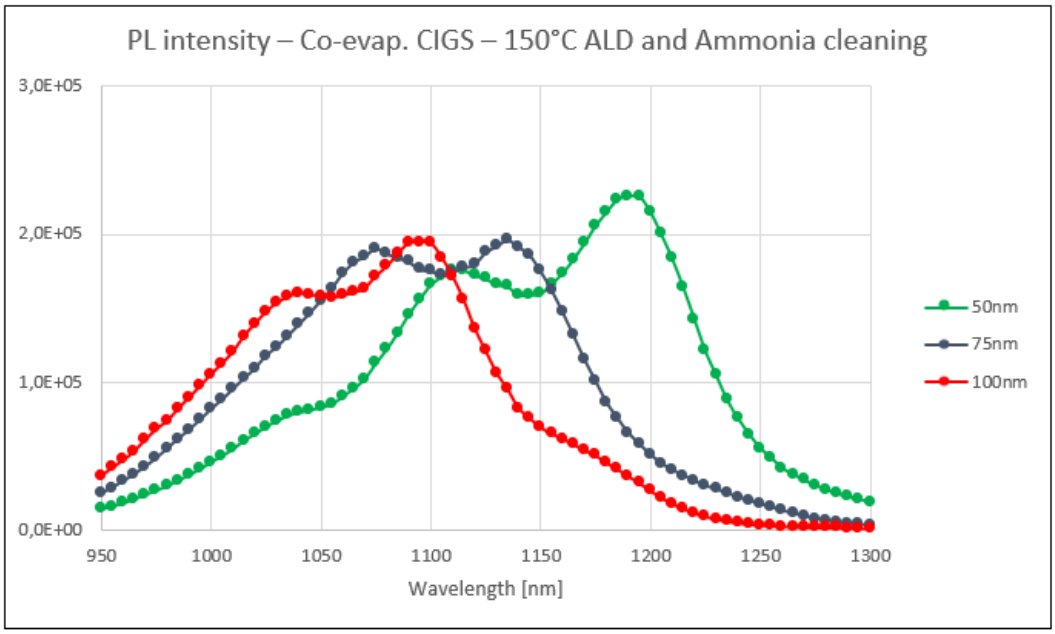

Figure 4.60: Comparison of average PL intensity in function of the titanium oxide layer thickness deposited by ALD at 150°C with Ammonia-cleaned co-evaporated CIGS (Ti1-2 and Ti5). The main difference observed concerns the relative position of the different peaks whereas their height remain globally similar for each thickness.

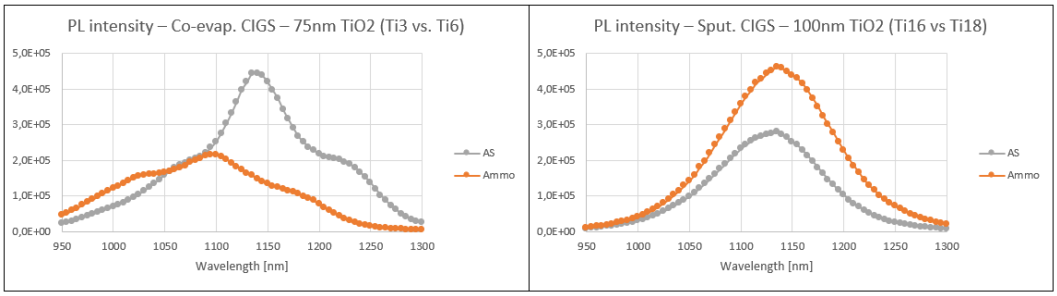

Figure 4.61: Comparison of average PL intensity in function of the CIGS layer pre-cleaning for titanium oxide layers deposited by ALD at 150°C. Left: Co-evaporated CIGS with 75nm TiO_2 (Ti3 and Ti6). Right: Sputtered CIGS with 100nm TiO_2 (Ti16 and Ti18).

4.8.2 Leakage

The clear difference between titania layers processed with ALD at 150°C and 250°C is also reflected by the significant current offset illustrated on figure 4.62. Indeed, even though the titania layers are, as mentioned above, globally more conductive than alumina and hafnia, the average current density for ALD 150°C TiO_2 is mostly below our leakage threshold of $0.01 A/cm^2$ whereas it is well above for titanium oxide layers deposited at 250°C. This in turn leads to the totally different CV behaviour observed below and for which quantifying passivation effects proves rather difficult.

The corresponding mean values of shunt resistance in $k\Omega.cm^2$ are summarized in table 4.5 in function of the combination of parameters for which IV data are available. Apart from

being globally lower than with the previously investigated dielectric materials, the available values of R_{sh} show no clear trends with regards to surface cleaning or oxide thickness, i.e. most samples with titania processed at a given temperature exhibit similar shunt resistance. Still, it appears that 50nm and 75nm-thick TiO_2 layers exhibit slightly lower leakage associated to higher shunt resistance, at least for co-evaporated CIGS pre-cleaned with Ammonia.

Besides that, for samples with ALD 150°C TiO_2, there is a significant degradation of R_{sh} following both single and double PDA treatments, resulting in average values close to the case of as-deposited ALD 250°C TiO_2. This further supports the fact that the properties of TiO_2 and especially its conductivity are highly dependent on the high-temperature treatments to which it is subjected, as expressed in [29]. Given the already really poor shunt and PL observed for as-deposited ALD 250°C titania, these samples are only briefly considered and mainly to expose the difficulty of analyzing the corresponding data. For the rest of this chapter, the CV analysis is especially focused on the samples with ALD 150°C TiO_2, namely Ti1-7, Ti16 and Ti18.

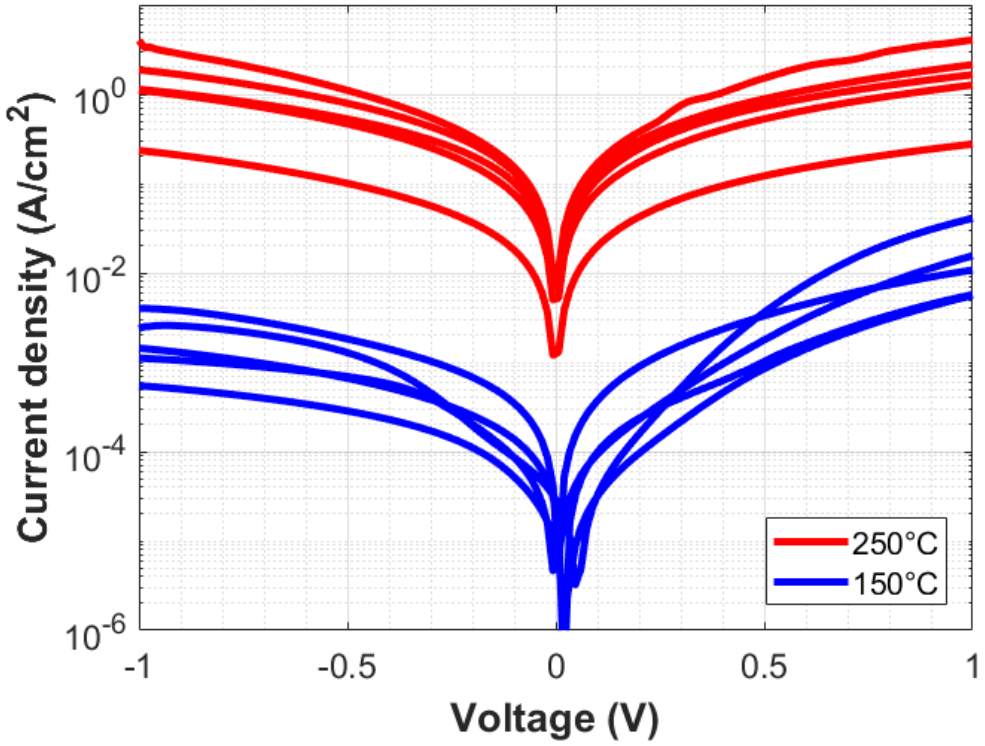

Figure 4.62: Average measured current density for the different combinations of parameters (CIGS processing and cleaning, oxide thickness) before any annealing process, with the clear difference between ALD at 150°C (blue) and 250°C (red) highlighted.

4.8.3 CV analysis

As mentioned above, the n-type intrinsic conductivity of TiO_2 [29] combined to the rather low CB offset at the interface with CIGS [62] are likely to explain the atypical CV measurements observed on figures 4.63 and 4.64 for 50nm TiO_2 on co-evaporated CIGS. In particular, as discussed throughout this whole report, the voltage sweep realized during CV measurements induce a displacement of the Fermi level which in turn modifies the energy

Thickness / ALD T°	50nm	75nm	100nm
150°C			
Co-evap. CIGS + AS	X	X	1
A1-300°C	X	X	0.2
A2-400°C	X	X	0.1
Co-evap. CIGS + Ammo	1.8	2.1	0.8
A1-300°C	X	$1.2 * 10^{-3}$	$8 * 10^{-3}$
Sput. CIGS + AS	X	X	0.2
A1-300°C	X	X	$2 * 10^{-3}$
250°C			
Co-evap. CIGS + AS	X	X	$0.6 * 10^{-3}$
Co-evap. CIGS + Ammo	$5 * 10^{-3}$	$1.2 * 10^{-3}$	$0.7 * 10^{-3}$
Sput. CIGS + AS	X	X	$0.9 * 10^{-3}$

Table 4.5: Summary of the mean values of shunt resistance in $k\Omega.cm^2$ observed for the different combination of parameters in the set of titania-based samples. Annealing treatments are only applied to 150°C ALD TiO_2 samples for the reasons expressed in the text. "X" indicates unavailable data.

bands alignment. In the case of CIGS/Oxide interfaces with wide bandgap dielectric materials such as alumina and hafnia, the offsets present at both the CB and VB edges (>1.5eV) are sufficiently large to respectively prevent the transport of electrons and holes in a relatively large range of voltages. On the contrary, the lower potential barrier (350meV) faced by the electrons in the CB of CIGS at the interface with TiO_2 is not large enough to block their circulation at every applied bias.

In accumulation, the upward band bending enlarges the CB offset between CIGS and TiO_2 which thus impedes the electrons to flow through the whole structure. Since titanium oxide layers processed by ALD at 150°C exhibit acceptable leakage current densities below $0.01A/cm^2$ without any PDA treatment, the TiO_2 layer roughly behaves like an insulator and the measured capacitance should be of the order of C_{ox}, equal to $1.4\mu F/cm^2$ in the case of 50nm TiO_2 [30]. This situation roughly corresponds to the CV measurements on the ALD 150°C TiO_2-based structure depicted on figure 4.63, for applied bias below 0.5V. On the contrary, the CV curves measured in the same region for the ALD 250°C TiO_2-based sample on figure 4.64 exhibit a totally different behaviour. The explanation for that striking difference is likely to be the significantly higher conductivity and leakage observed for ALD 250°C titania layers. Since the shunt resistance is much lower than for ALD 150°C, the conductive part of the parallel admittance dominates and the capacitance drops significantly.

As the applied bias transitions from accumulation to depletion by crossing V_{fb} (around 0.5V by inspecting figure 4.63), the band bending inverts and the potential barrier faced by electrons in CB diminishes. Consequently, an electron current flows between the CBs of CIGS and TiO_2, and the measured capacitance collapses due to the transport of charges through the oxide layer. This is the trend observed beyond 0.3V on figures 4.63 and 4.64. For sufficiently high positive bias, that CB potential barrier can even become negative and the CB electrons are then compelled to flow from the CIGS to the TiO_2.

Eventually, it appears that the intrinsic properties of TiO_2 justify the divergence in CV behaviour as compared to Al_2O_3 and HfO_2 whereas the significant difference in leakage current between titania samples deposited at either 150°C or 250°C seemingly explains the separate trends observed on figures 4.63 and 4.64. Although this reasoning seems to partially agree with the observations made 50nm-thick TiO_2 layers over Ammonia-treated co-evaporated CIGS, it is for instance not quite the case for other configurations as illustrated on figures A.8 and A.9 in Appendix A. Therefore, this preliminary development requires further investigations on the experimental, theoretical and numerical simulation aspects as discussed in chapter 5. The analysis of series resistance effect and interface passivation is qualitatively discussed in the rest of this section.

Series resistance Even though the previously investigated effect of series resistance may be present as well in titania-based samples, its characterization and estimation is much less straightforward given the unexpected CV behaviour of these structures. Indeed, with lower shunt resistances and thus weaker conductive part of the parallel admittance, the 2D feature associated to series resistance is likely to appear at lower frequencies. This is especially true in the case of 250°C ALD TiO_2 layers for which R_{sh} is in the same order of magnitude as the estimated values of series resistance for alumina and hafnia-based MIS capacitors, i.e. around $1\Omega.cm^2$.

Interface passivation The qualitative inspection of figure 4.63 suggest a flat-band voltage roughly comprised within the $[0.2V; 0.5V]$ range, i.e. at the transition between the apparent accumulation and depletion regimes. This in turn which would translate into a negative density of fixed charges Q_f similarly to alumina and hafnia and thus misdirected field-effect passivation. The identification of a clear transition between two plateaus respectively corresponding to the accumulation and depletion regimes is much less evident for other configurations as on figures 4.64 and A.8-A.9. As detailed above, the CIGS/TiO_2 stack rather behaves as a poorly doped p-n junction than as a MIS capacitor. Therefore, even though the targeted positive fixed charges may well be present in the TiO_2 layer, the characterization of field-effect passivation through CV measurements does not allow to confirm that suggestion. For the same reasons, it proves difficult to estimate the value of D_{it} based on the CV results obtained for this set of samples.

4.8.4 Summary

The main outcome of this section is the clear intricacy of quantitatively characterizing interface passivation effects of TiO_2 given the incompatibility of this material with typical MIS capacitors. In particular, the n-type native conductivity and narrow band gap of TiO_2 tend to make it a poor candidate for producing reliable MIS structures in combination with CIGS. Rather behaving as poor p-n junctions, CIGS/TiO_2 stacks are globally less shunted than alumina and hafnia-based MIS samples. This is especially true for titania layers processed by thermal ALD at 250°C ($R_{sh} \simeq 1\Omega.cm^2$) as compared to 150°C ($R_{sh} \simeq 1k\Omega.cm^2$). This in turn hinders the identification of clear trends with regards to CIGS surface cleaning and processing as well as PDA treatments.
Still, the significant increase in PL intensity observed for any configuration involving a titania layer deposited by ALD at 150°C suggests potentially effective surface passivation and thus requires future investigations.

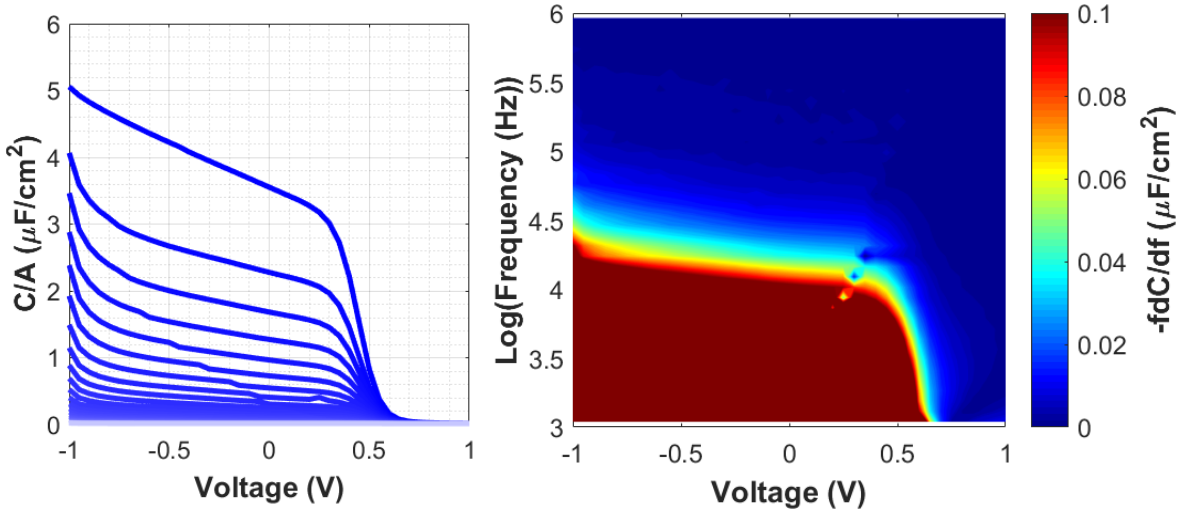

Figure 4.63: Example of CV measurements realized on the Ti1 sample with 50nm TiO_2 deposited by ALD at 150°C over Ammonia-cleaned co-evaporated CIGS. Left: Measured CV curves from 1kHz (dark blue) to 1MHz (light blue). Right: Measured capacitance derivative 2D map.

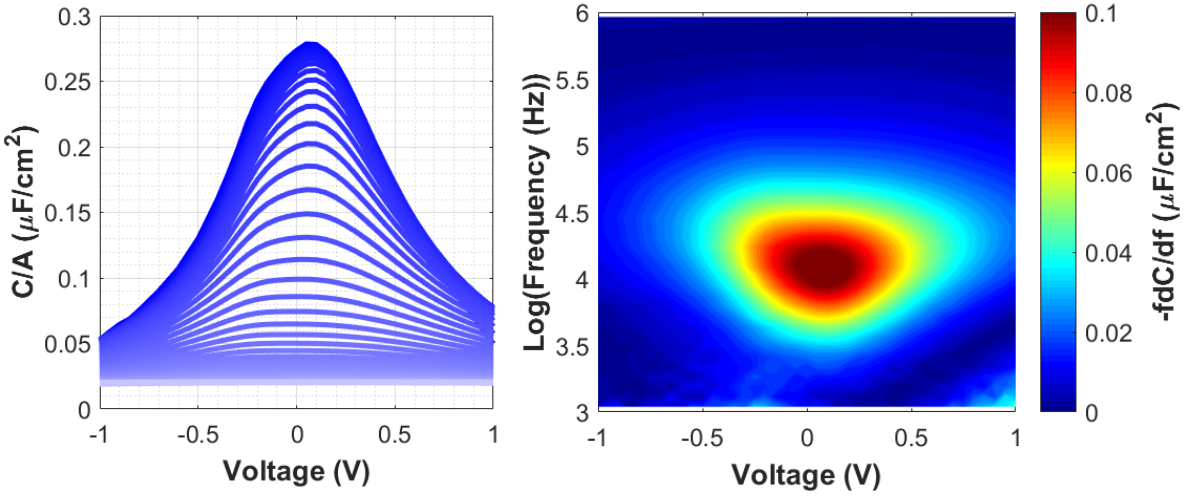

Figure 4.64: Example of CV measurements realized on the Ti8 sample with 50nm TiO_2 deposited by ALD at 250°C over Ammonia-cleaned co-evaporated CIGS. Left: Measured CV curves from 1kHz (dark blue) to 1MHz (light blue). Right: Measured capacitance derivative 2D map.

Chapter 5

Conclusion

5.1 Summary

The three first chapters of this report settle the context and objectives aimed at in this investigation of CIGS/Oxide interface characterization, with regards to both the theoretical and experimental aspects. In Chapter 1, after briefly discussing the importance of optimizing sustainable and innovative ways of producing energy, the potential of thin-film PV technologies and especially CIGS-based solar cells is expressed in parallel with one major remaining efficiency limitation. The purpose of this study is to investigate the effectiveness of a certain design that is widely used to tackle that performance issue, i.e. oxide passivation layers, in the case of the CIGS/buffer layer interface for solar cells applications. In order to fulfill the expectations of this work about characterizing passivation effects in CIGS/Oxide structures, important theoretical concepts are introduced in Chapter 2. The main outcomes of the second chapter are the technical contextualization of essential mechanisms such as defect-assisted recombination and surface passivation along with the introduction of characterization techniques mainly based on the analysis of CV measurements realized on MIS structures. Two figures-of-merit are particularly important in this study, namely the equivalent surface density of fixed charges in the oxide layer Q_f and the density of trap states at the CIGS/Oxide interface D_{it}. Chapter 3 describes in details the characteristics of the MIS samples studied throughout this work as well as the additional experimental steps involved in their entire processing (CIGS precleaning, post-deposition annealing, ...) and the types of measurements performed on them.

The fourth chapter presents the thorough characterization of CIGS/Oxide interfaces passivation based on both numerical and experimental results. In particular, SCAPS and MATLAB simulations models are firstly introduced so as to make the link between the expected theoretical trends highlighted in the second chapter and the actual observations made on realistic samples in the rest of Chapter 4. The simulated results enable to highlight the influence of the two defect densities Q_f and D_{it} on the CV curves while providing reliable points of comparison to which our experimental data can be confronted so as to assess the presence of those very defects. Meanwhile, the extraction techniques used in this work to estimate those two figures-of-merit are firstly validated through the simulations and then with actual measurements obtained on one alumina-based MIS sample. Applying our analysis to both numerical simulations and an example of real experiments not only forms a strong basis for the subsequent development but also highlights the presence of prominent supplementary effects such as series resistance and border traps.

The core of chapter 4 treats the suitability of two candidates for front interface passivation, i.e. Al_2O_3 and HfO_2. This is done through the analysis of both PL and CV measurements realized on relevant MIS structures as a way to not only characterize the CIGS/Oxide interface but also to put in evidence the influence of additional parameters such as CIGS processing, surface cleaning and post-deposition annealing. The methodology implemented here is to preliminary suggest actual passivation effects related to the oxide layer while highlighting potential trends using PL measurements, which can then be confirmed using CV measurements whose reliability is quantified by IV data. The potential passivation effects suggested by the PL intensity up-scaling for both materials is partly confirmed by the corresponding low values of D_{it} of the order of $10^{11} cm^{-2} eV^{-1}$ extracted for those samples. It is observed that as-deposited alumina layers globally exhibit slightly more effective chemical passivation as compared to hafnia. Even though both materials exhibit misdirected field-effect associated to negative values of Q_f which may potentially limit the efficiency gain related to passivation effects, the lower magnitude of Q_f in the case of alumina makes it a better candidate for front interface passivation. Moreover, the presupposed effect of series resistance firstly noticed for the alumina-based samples actually appear more prominent with hafnia, not only making the extraction of D_{it} less reliable but also suggesting the co-existence of other phenomena whose physical origins remain unclear (secondary phases, complex defects, ...) and therefore require further investigations as discussed below. The CV analysis should not be greatly affected by leakage currents in both alumina and hafnia-based samples since the values of shunt resistance are of the order of $[1 - 100] k\Omega.cm^2$. For both alumina and hafnia layers, single N_2 annealing treatments at 300°C globally enhance interface passivation by reducing both values of D_{it} and negative Q_f whereas it is more ambiguous to determine the optimal surface cleaning regarding the same aspects.

Although passivation effects seem more effective with alumina than hafnia, the integration of Al_2O_3 in front passivated solar cells seems compromised by the selective etching of alumina during processing of buffer layers involving Ammonia. Since hafnia does not present the same incompatibility with buffer layer deposition, superposing HfO_2 on top of Al_2O_3 in a multi-layer oxide passivation stack so as to protect alumina from buffer layer processing reveals interesting. Indeed, combining the active chemical passivation of Al_2O_3 at the interface with CIGS and the resistive character of HfO_2 with regards to buffer layer processing may provide an innovative solution to the front interface passivation of complete CIGS solar cells. In order to confirm the effectiveness of such a design, CIGS/Al_2O_3/HfO_2 MIS samples are analyzed similarly to both individual dielectric materials. PL and IV measurements respectively indicate active passivation and low parasitic leakage with extremely high shunt resistance ($< 1 M\Omega.cm^2$). Even though also observed for the multi-layer configuration, the unidentified features spotted for single hafnia-based samples do not make the extraction of D_{it} less reliable in this case. On the whole, both mean values of D_{it} and Q_f for the as-deposited multi-layer configuration are comprised within the individual results for alumina and hafnia, thus making a good compromise regarding most aspects discussed and confirming effective chemical passivation and mitigated negative field-effect. Ammonia cleaning and 300°C PDA combined slightly enhance surface passivation by moderately reducing D_{it} and negative Q_f. Eventually, it appears that co-evaporated CIGS/Al_2O_3/HfO_2 with Ammonia pre-cleaning and 300°C PDA is the optimal design obtained here for passivating the front interface of complete CIGS solar cells.

The last part of chapter 4 investigates the usage of TiO_2 as a dielectric material for interface passivation. Contrarily to Al_2O_3 and HfO_2, titania is intrinsically n-type conductive with a relatively narrow bandgap. This difference has important implications with regards to the CV behaviour of CIGS/TiO_2 stacks which rather behave as poor p-n junctions than typical MIS structures. This in turn makes it practically difficult to accurately quantify passivation effects associated to TiO_2 layers. Still, the qualitative analysis of both PL and IV/CV measurements enable to draw preliminary conclusions about CIGS/titania interfaces. First, the ALD temperature at which TiO_2 is processed greatly determines its properties and quality. In our case, titanium oxide layers processed by ALD at 250°C show poor PL performance and non-negligible conductivity which respectively tend to indicate ineffective surface passivation and unreliable electrical measurements (CV). On the contrary, TiO_2 layers deposited by ALD at 150°C induce PL intensity up-scaling and have acceptable levels of leakage. Since analyzing their CV data proves complex given the divergence with the expected typical curves for MIS structures, it is difficult to highlight precise trends with regards to oxide thickness, CIGS pre-cleaning and post-deposition annealing. Nevertheless, the qualitative characterization of ALD 150°C TiO_2 layers as well as their well-known electronic selectivity suggest a certain potential for front interface passivation of CIGS solar cells, requiring further investigations as discussed just below.

5.2 Further research

There obviously remains lots of aspects to be considered in order to complete this analysis of CIGS/Oxide interfaces passivation. First, further SCAPS and MATLAB simulations are likely to provide an interesting insight into the passivation behaviour of other materials than alumina, namely hafnia and titania. Second, the study of the unidentified features appearing in our measurements require additional investigations on both the theoretical and experimental aspects in order to precisely determine their physical origin as well as the effect of the CIGS composition (bulk and interface defects [36], surface roughness [39], secondary phases [40]), the rear contact (potential barrier [49, 50]), alternative annealing temperatures and environment, and surface cleaning. Finally, the interest in using TiO_2 for passivation layers in CIGS solar cells still requires to be confirmed with characterization techniques taking into account its peculiar properties as compared to alumina and hafnia.

5.3 Future prospects

Electricity generation is unfortunately not the only issue to be solved in the imminent climate crisis. Although renewable energies such as solar and wind power have now been widely accepted as promising alternatives to fossil fuels, their intrinsic volatile character remain an important bottleneck in their worldwide development. With the objective of increasing the share of renewable sources within the global energy network, the electrical energy storage capacity should increase in order to cope with the intermittence of most renewable energies. This way, electricity can be injected in the grid when required and not only when the sun is shining or when the wind is blowing. Hopefully in the future, human society will reach a cleaner and more diverse energy network mixing up both renewable and conventional sources of energy, with solar power and thin-film PV as one of the keys towards a more sustainable society.

Appendix A

Supplementary data

Aluminum oxide - Al_2O_3

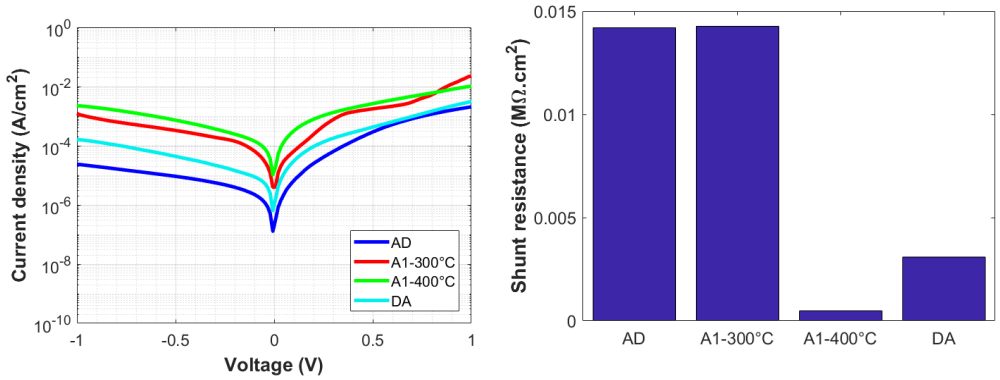

Figure A.1: Influence of different annealing treatments on the IV curves and shunt resistance, for the AL18-19 samples (co-evaporated CIGS). Left: Measured current density vs. voltage in dark environment. Right: Shunt resistance.

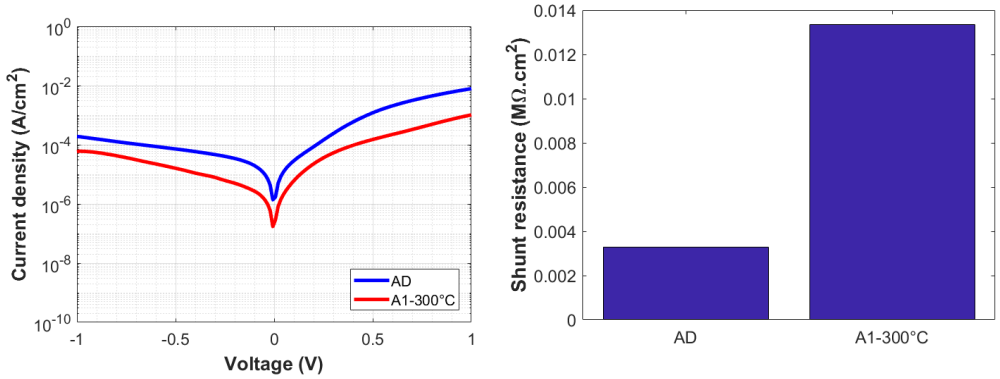

Figure A.2: Influence of different annealing treatments on the IV curves and shunt resistance, for the AL20-21 samples (co-evaporated CIGS). Left: Measured current density vs. voltage in dark environment. Right: Shunt resistance.

Hafnium oxide - HfO_2

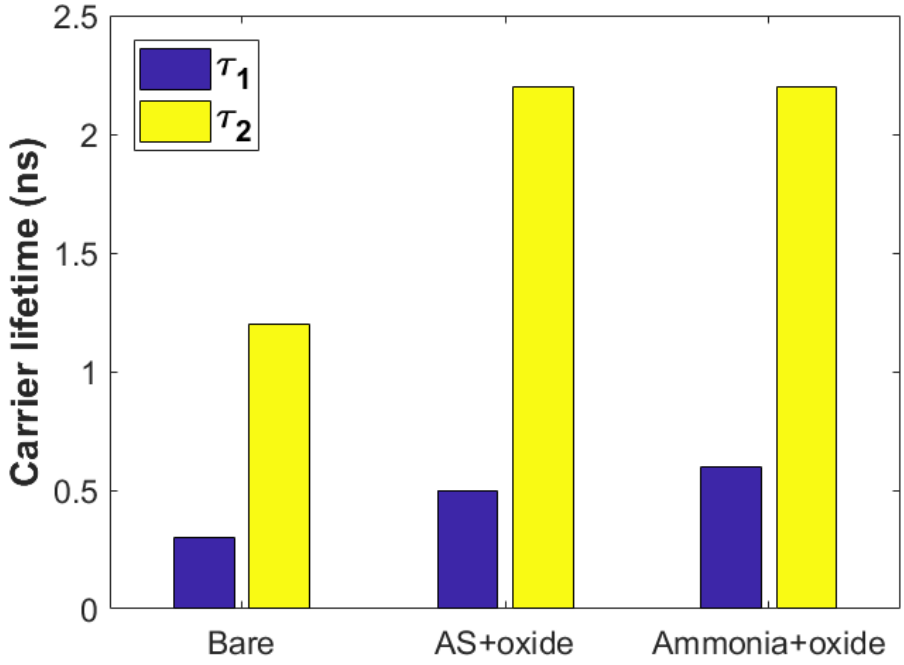

Figure A.3: Carrier lifetime at 1040nm obtained from TRPL measurements on the HF3-4-7-8 samples, with τ_1 and τ_2 respectively the short and long time constants of the double exponential fitting [40]. The two pre-cleaning treatments lead to similar improvements compared to the as-deposited results.

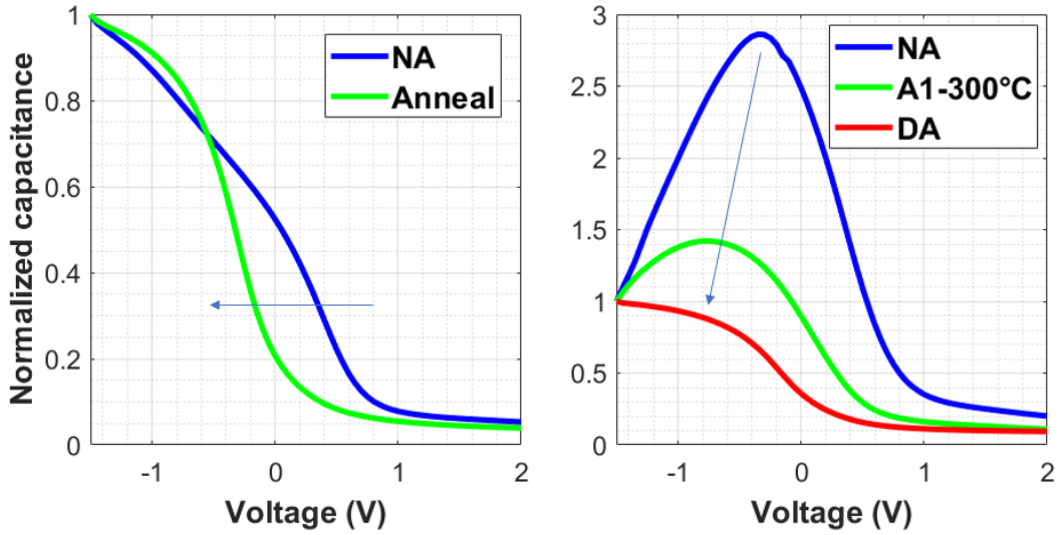

Figure A.4: Effect of post-deposition annealing on the average values of V_{fb} and Q_f for the first series of samples (HF1-8) with co-evaporated CIGS. The work-function of the front Silver grid is taken to be 4.5eV, i.e. the mean between 4.26eV and 4.73eV. The annealing is either made at 300°C or 400°C for both types of cleaning (HF1-4 and HF5-8) with no significant difference between the two temperatures.

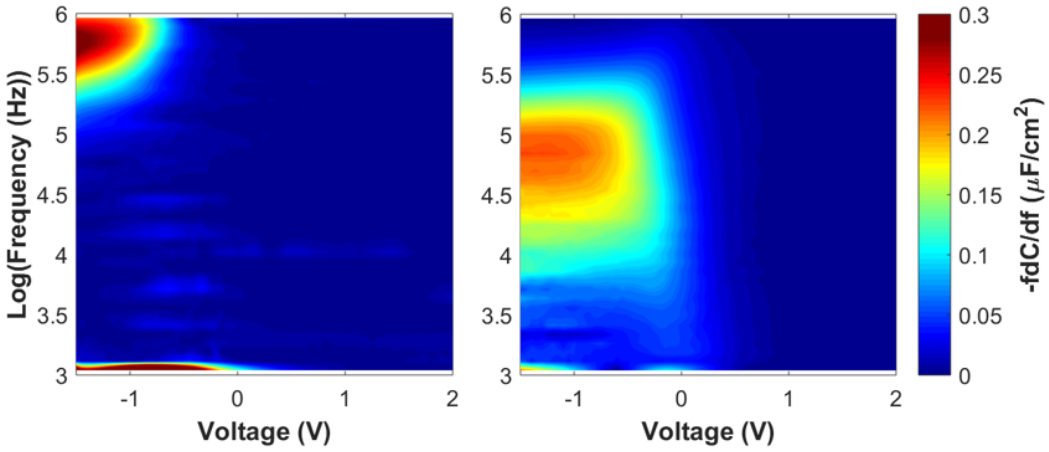

Figure A.5: Measured capacitance derivative 2D maps before (left) and after single PDA at 400°C (right), for co-evaporated CIGS pre-cleaned with AS (HF6). Left: As-deposited estimated series resistance is $0.34\Omega.cm^2$. Right: Estimated series resistance is $3.42\Omega.cm^2$ after single annealing at 400°C.

Titanium oxide - TiO_2

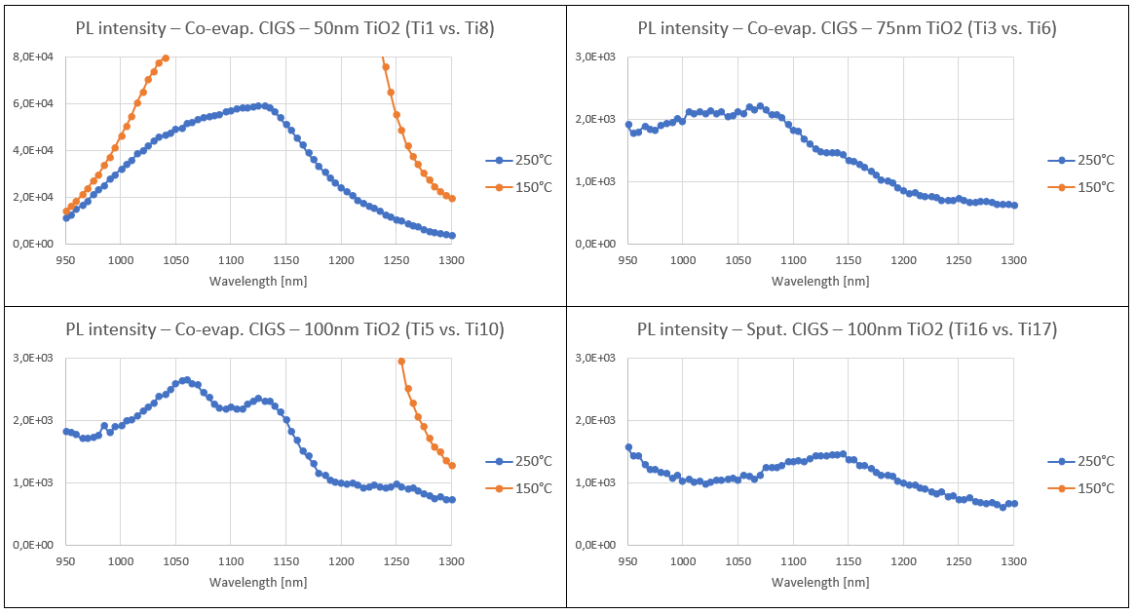

Figure A.6: Comparison of average PL intensity in function of the ALD temperature deposition for the different oxide thicknesses and for Ammonia-cleaned CIGS only. The significant difference in magnitude between the two temperatures tend to indicate poor quality of the TiO_2 layers deposited at 250°C.

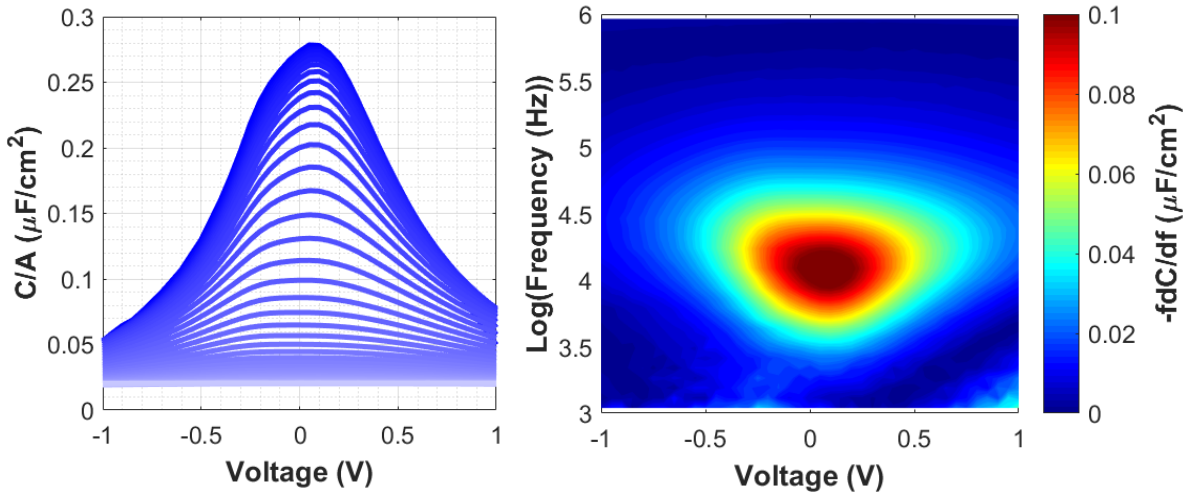

Figure A.7: Example of CV measurements realized on the Ti8 sample with 50nm TiO_2 processed by ALD at 250°C. Left: Measured CV curves from 1kHz (dark blue) to 1MHz (light blue). Right: Measured capacitance derivative 2D map.

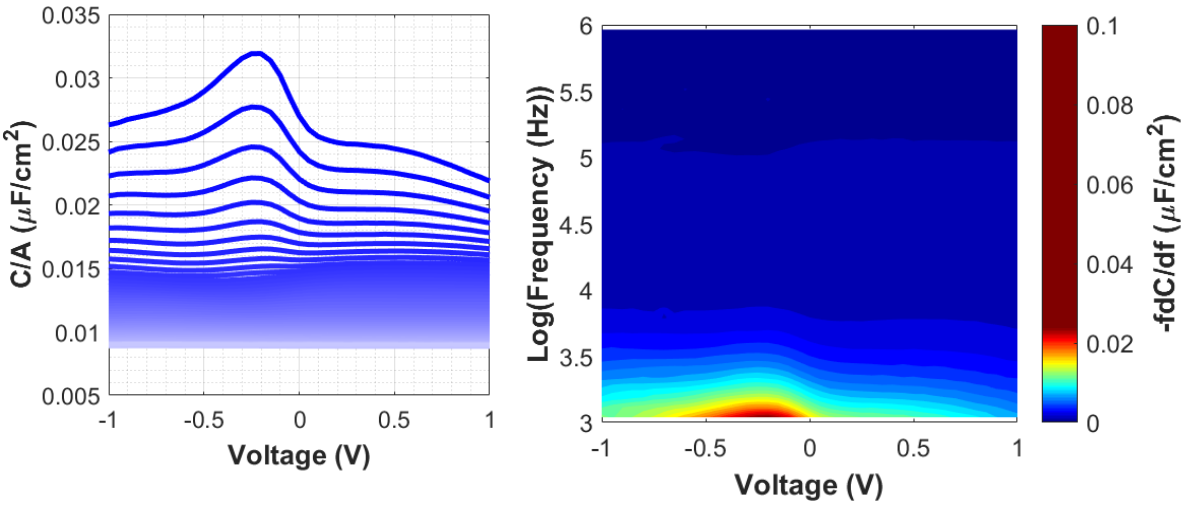

Figure A.8: Example of CV measurements realized on the Ti5 sample with 100nm TiO_2 deposited by ALD at 150°C over Ammonia-cleaned co-evaporated CIGS. Left: Measured CV curves from 1kHz (dark blue) to 1MHz (light blue). Right: Measured capacitance derivative 2D map.

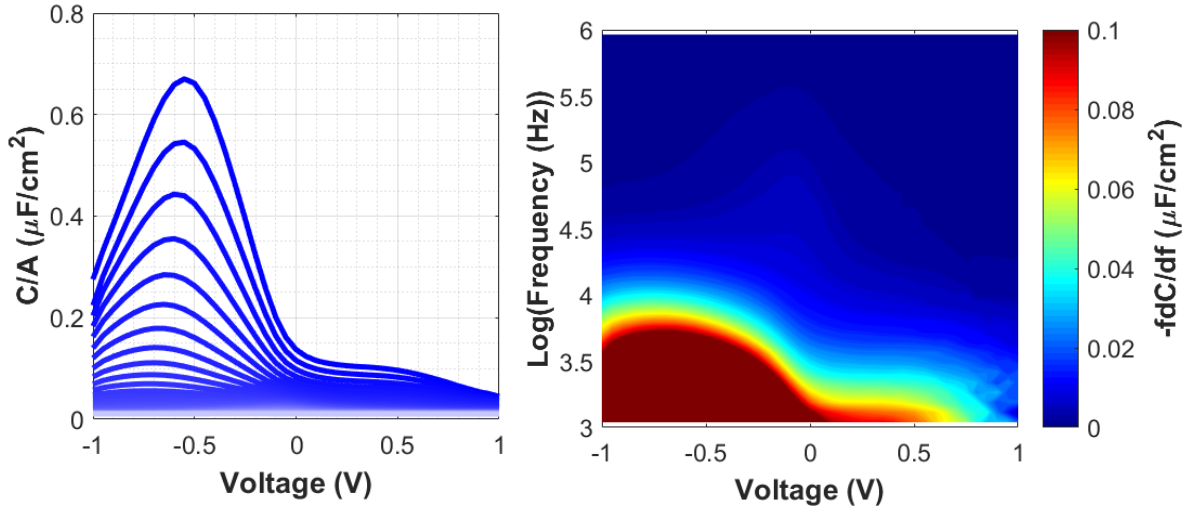

Figure A.9: Example of CV measurements realized on the Ti16 sample with 50nm TiO_2 deposited by ALD at 150°C over Ammonia-cleaned sputtered CIGS. Left: Measured CV curves from 1kHz (dark blue) to 1MHz (light blue). Right: Measured capacitance derivative 2D map.

Numerical simulations

	CIGS - 1.6μm	Oxide (Al_2O_3) - 20nm
χ (eV)	4.5	1.95
E_g (eV)	1.15	6.2
ϵ_r	13.6	6.7
N_C (cm^{-3})	$2.2 * 10^{18}$	$2.2 * 10^{18}$
N_V (cm^{-3})	$1.5 * 10^{19}$	$1.5 * 10^{19}$
$v_{th,n}$ (cm/s)	$3.9 * 10^{7}$	$3.9 * 10^{7}$
$v_{th,p}$ (cm/s)	$1.4 * 10^{7}$	$1.4 * 10^{7}$
μ_n (cm^2/Vs)	100	1
μ_p (cm^2/Vs)	12.5	1
N_A (cm^{-3})	$5 * 10^{16}$	$5 * 10^{10}$

Table A.1: SCAPS and MATLAB parameters used in the simulations from section 4.2.

Defects	CIGS	CIGS/Al_2O_3	Al_2O_3
Bulk			
ρ (cm^{-3})	10^{14} (G)		$8 * 10^{16} - 4 * 10^{17}$ (S)
E_C (eV)	0.58 (D)		[23]
E_{char} (eV)	0.1		0
Border			
ρ (cm^{-3})			$10^{18} - 10^{20}$
E_C (eV)			0.1
E_{char} (eV)			0.1-0.4
x (nm)			0-2
σ_x (nm)			1-3
Interface			
D_{it} ($cm^{-2}eV^{-1}$)		$5 * 10^{10} - 5 * 10^{12}$ (G)	
E_C (eV)		0.25-0.45 (A/D)	
E_{char} (eV)		0.1	

Table A.2: Defects introduced in the simulations (G=gaussian, S=single, A=acceptor, D=donor). E_C is energy level above VB, x and σ_x refer to position of border traps.

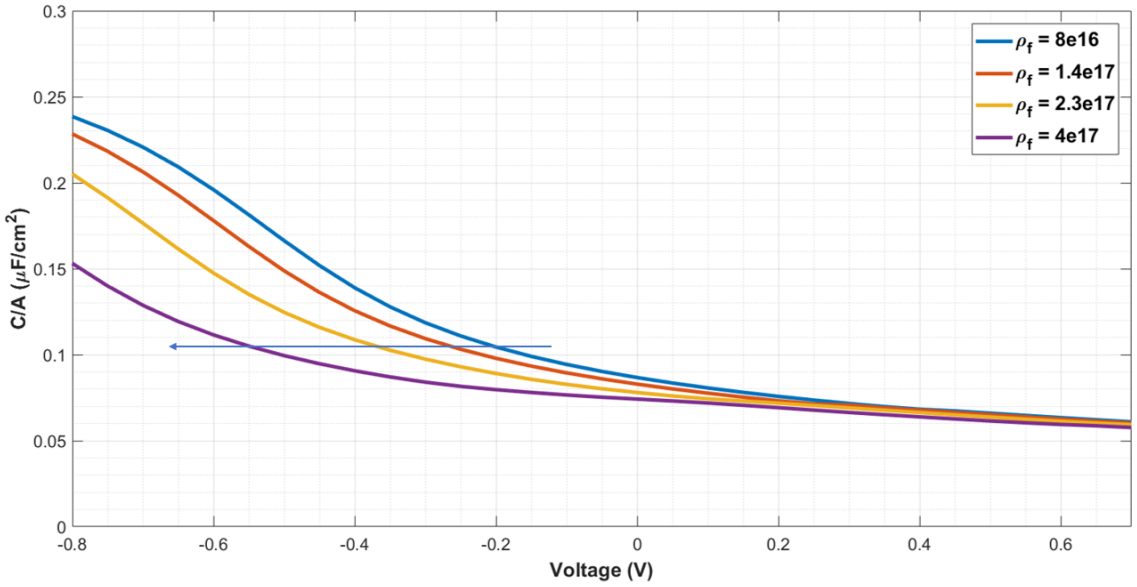

Figure A.10: Influence of the volumic density of Oxygen vacancies on the 10kHz CV curves (D_{it} set to zero) for an alumina-based MIS capacitor. The voltage shift is leftwards because the vacancies of Oxygen are of the donor type.

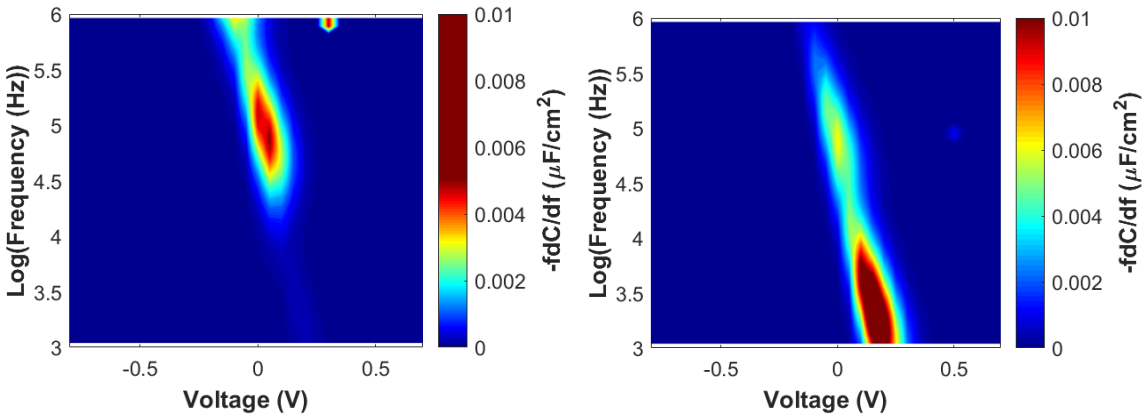

(a) Acceptor 250meV above VB

(b) Acceptor 450meV above VB

Figure A.11: SCAPS simulations of the combined effect of acceptor-type interface traps ($D_{it} = 5 * 10^{11} cm^{-2} eV^{-1}$) and oxide fixed charges ($\rho_f = 2 * 10^{17} cm^{-3}$ for each bulk defect in the oxide) on the CV results of an alumina-based MIS capacitor. Left: Central energy level $0.25eV$ above the VB edge. Right: Central energy level $0.45eV$ above the VB edge. The distribution is of the gaussian type with a variance of $0.1eV$.

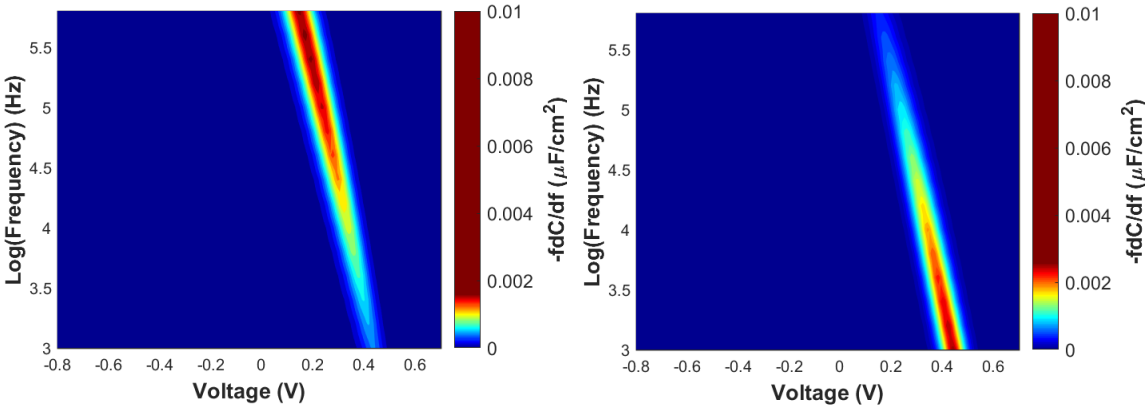

(a) Acceptor 250meV above VB

(b) Acceptor 450meV above VB

Figure A.12: MATLAB simulations of the effect of acceptor-type interface traps ($D_{it} = 5 * 10^{11} cm^{-2} eV^{-1}$) on the CV results of an alumina-based MIS capacitor. Left: Central energy level $0.25eV$ above the VB edge. Right: Central energy level $0.45eV$ above the VB edge. The distribution is of the gaussian type with a variance of $0.1eV$.

Bibliography

[1] H. Ritchie and M. Roser. CO_2 and Greenhouse Gas Emissions, December 2019 (last revised). Published for Our World in Data, available at: https://ourworldindata.org/co2-and-other-greenhouse-gas-emissions.

[2] N.G. Dhere. Toward GW/year of CIGS production within the next decade. *Solar Energy Materials & Solar Cells*, 91:1376–1382, 2017.

[3] PVthin. CIGS – Copper Indium Gallium Selenide. http://pvthin.org/technology.

[4] T.D. Lee and A.U. Ebong. A review of thin film solar cell technologies and challenges. *Renewable and Sustainable Energy Reviews*, 70:1286–1297, 2017.

[5] B. Vermang et al. Development of rear surface passivated Cu(In,Ga)Se_2 thin film solar cells with nano-sized local rear point contacts. *Solar Energy Materials & Solar Cells*, 117:502–511, 2013.

[6] J. Joel. *Characterization of Al_2O_3 as CIGS surface passivation layer in high-efficiency CIGS solar cells*. PhD thesis, Uppsala Universitet, 2014.

[7] R.V.R. Kotipalli. *Surface Passivation Effects of Aluminum oxide on Ultra-Thin CIGS Solar Cells*. PhD thesis, Université Catholique de Louvain, 2015.

[8] D. Ledinek et al. Effect of different Na supply methods on thin Cu(In,Ga)Se_2 solar cells with Al_2O_3 rear passivation layers. *Solar Energy Materials & Solar Cells*, 187:160–169, 2018.

[9] S. Choi et al. Lithographic fabrication of point contact withAl_2O_3 rear-surface-passivated and ultra-thin Cu(In,Ga)Se_2 solar cells. *Thin Solid Films*, 665:91–95, 2018.

[10] D. Ledinek et al. Effect of NaF pre-cursor on alumina and hafnia rear contact passivation layers in ultra-thin Cu(In,Ga)Se_2 solar cells. *Thin Solid Films*, 683:156–164, 2019.

[11] M. Edoff et al. Ultrathin CIGS solar cells with passivated and highly reflective back contacts. Results from the ARCIGS-M Consortium, EU PVSEC, 2019.

[12] W.-W. Hsu et al. Surface passivation of Cu(In,Ga)Se_2 using atomic layer deposited Al_2O_3. *Applied Physics Letters*, 100:023508, 2012.

[13] R.V.R. Kotipalli et al. Investigating the electronic properties of Al_2O_3/Cu(In,Ga)Se_2 interface. *AIP Advances*, 5:107101, 2015.

[14] M. Burgelman et al. SCAPS: a Solar Cell Capacitance Simulator, February 2019 (last version). SCAPS 3.3.0.7, homepage: http://scaps.elis.ugent.be/.

[15] J.-P. Colinge and C.A. Colinge. Generation/Recombination Phenomena. In *Physics of Semiconductor Devices*, chapter 3, pages 73–89. Kluwer Academic Publishers, 2002.

[16] B. Vermang et al. Approach for Al_2O_3 rear surface passivation of industrial p-type Si PERC above 19%. *Progress in Photovoltaics*, 20:269–273, 2012.

[17] T. Dullweber et al. Towards 20% efficient large-area screen-printed rear-passivated Silicon solar cells. *Progress in Photovoltaics*, 20:630–638, 2012.

[18] J.M.V. Cunha et al. Insulator Materials for Interface Passivation of Cu(In,Ga)Se_2 Thin Films. *IEEE Journal of Photovoltaics*, 8:1313–1319, 2018.

[19] S. Garud et al. Surface Passivation of CIGS Solar Cells Using Gallium Oxide. *Phys. Status Solidi A*, 215:1700826, 2018.

[20] J. Löckinger et al. The use of HfO_2 in a point contact concept for front interface passivation of Cu(In,Ga)Se_2 solar cells. *Solar Energy Materials & Solar Cells*, 195:213–219, 2019.

[21] S.M. Sze and Kwok K. Ng. Metal-Insulator-Semiconductor Capacitors. In *Physics of Semiconductor Devices*, chapter 4, pages 197–240. Wiley, 2006.

[22] R.V.R. Kotipalli et al. Passivation effects of atomic-layer-deposited aluminum oxide. *EPJ Phtovoltaics*, 4:45107, 2013.

[23] M. Choi, A. Janotti, and C.G. Van de Walle. Native point defects and dangling bonds in α-Al_2O_3. *Journal of Applied Physics*, 113:044501, 2012.

[24] A. Morato et al. Electrical characterization of ALD Al_2O_3 - HfO_2 and PECVD Al_2O_3 passivation layers for p-type CZ-Silicon PERC solar cells. 38th IEEE Photovoltaic Specialists Conference, IEEE, 2012.

[25] X. Cheng et al. Surface Passivation Properties of HfO_2 Thin Film on n-Type Crystalline Si. *IEEE Journal of Photovoltaics*, 7(2):479–485, 2017.

[26] J.A. Luceño-Sánchez, A.M. Díez-Pascual, and R. Peña Capilla. Materials for Photovoltaics: State of Art and Recent Developments. *International Journal of Molecular Sciences*, 20:976, 2019.

[27] M. Xue et al. Titanium Oxide Contact Passivation Layer for Thin Film Crystalline Silicon Solar Cells. 43rd Photovoltaic Specialists Conference (PVSC), IEEE, 2016.

[28] F. Mollica et al. Comparative study of patterned TiO_2 and Al_2O_3 layers as passivated back-contact for ultra-thin Cu(In,Ga)Se_2 solar cells. 43rd IEEE Photovoltaic Specialists Conference, IEEE, 2016.

[29] S. Na-Phattalung et al. First-principles study of native defects in anatase TiO_2. *Physical Review B*, 73:125205, 2006.

[30] J. Robertson. High dielectric constant oxides. *Eur. Phys. J. Appl. Phys.*, 28:265–291, 2004.

[31] M. Boubakeur et al. Enhancement of the efficiency of ultra-thin CIGS/Si structure for solar cell applications. *Superlattices and Microstructures*, 138:106377, 2020.

[32] M.D. Groner et al. Electrical characterization of thin Al_2O_3 films grown by atomic layer deposition on silicon and various metal substrates. *Thin Solid Films*, 413:186–197, 2002.

[33] G. Sozzi et al. Impact of front-side point contact/passivation geometry on thin-film solar cell performance. *Solar Energy Materials & Solar Cells*, 165:94–102, 2017.

[34] E.H. Nicollian and J.R. Brews. Extraction of Interface Trap Properties from the Conductance. In *MOS (Metal Oxide Semiconductor) Physics and Technology*, chapter 5, pages 212–220. Wiley, 2003.

[35] K Piskorski and H. M. Przewlocki. The methods to determine flat-band voltage VFB in semiconductor of a MOS structure. In *The 33rd International Convention MIPRO*, pages 37–42, 2010.

[36] S. Siebentritt and U. Rau. Shallow Defects in the Wide Gap Chalcopyrite $CuGaSe_2$. In *Wide Gap Chalcopyrites*, chapter 7. Springer, 2006.

[37] M. Igalson, M. Pawlowski, and D. Przado. Influence of electric field on photoluminescence of Cu(In,Ga)Se_2-based solar cells. *Opto-Electronics Review*, 19(4):435–438, 2011.

[38] J. Joel et al. On the assessment of CIGS surface passivation by photoluminescence. *Phys. Status Solidi RRL*, 9(5):288–292, 2015.

[39] J. Han et al. Comparison of thin film properties and selenization behavior of CuGaIn precursors prepared by co-evaporation and co-sputtering. *Journal of Alloys and Compounds*, 552:131–136, 2013.

[40] M. Buffière et al. Surface Cleaning and Passivation Using $(NH_4)_2S$ Treatment for Cu(In,Ga)Se_2 Solar Cells: A Safe Alternative to KCN. *Advanced Energy Materials*, 5(6):1401689, 2014.

[41] J. Frascaroli et al. Surface passivation for ultrathin Al_2O_3 layers grown at low temperature by thermal atomic layer deposition. *Phys. Status Solidi A*, 210(4):732–736, 2013.

[42] R.V.R. Kotipalli et al. Addressing the impact of rear surface passivation mechanisms on ultra-thin Cu(In,Ga)Se_2 solar cell performances using SCAPS 1-D model. *Solar Energy*, 157:603–613, 2017.

[43] G. Brammertz et al. A Combined Interface and Border Trap Model for High-Mobility Substrate Metal–Oxide–Semiconductor Devices Applied to $In_{0.53}Ga_{0.47}As$ and InP Capacitors. *IEEE Transactions on Electron Devices*, 58:3890–3897, 2011.

[44] J.X. Zheng et al. First-principles study of native point defects in hafnia and zirconia. *Physical Review B*, 75:104112, 2007.

[45] W.H. Wu et al. Two-Frequency C–V Correction Using Five-Element Circuit Model for High-k Gate Dielectric and Ultrathin Oxide. *IEEE Electron Device Letters*, 27:399–401, 2006.

[46] E.J. Kim et al. Border traps in $Al_2O_3/In_{0.53}Ga_{0.47}As$ (100) gate stacks and their passivation by hydrogen anneals. *Applied Physics Letters*, 96:012906, 2010.

[47] Y. Yuan et al. A Distributed Model for Border Traps in Al_2O_3 InGaAs MOS Devices. *IEEE Electron Device Letters*, 32:485–487, 2011.

[48] Y. Yuan et al. Effects of oxide traps, interface traps, and "border traps" on metal-oxide-semiconductor devices. *Journal of Applied Physics*, 73:50–58, 1993.

[49] K.H. Ong et al. Review on Substrate and Molybdenum Back Contact in CIGS Thin Film Solar Cell. *International Journal of Photoenergy*, 2018.

[50] Y.-C. Lin et al. Impact of Mo barrier layer on the formation of $MoSe_2$ in $Cu(In,Ga)Se_2$ solar cells. *Journal of Alloys and Compounds*, 661:168–175, 2016.

[51] O. Gunawan, T.K. Todorov, and D.B. Mitzi. Loss mechanisms in hydrazine-processed $Cu_2ZnSn(Se,S)_4$ solar cells. *Applied Physics Letters*, 97:233506, 2010.

[52] A.W. Dweydari and C.H.B. Mee. Work Function Measurements on (100) and (110) Surfaces of Silver. *Phys. Status Solidi A*, 27:223–230, 1975.

[53] C. Frisk et al. Optimizing Ga-profiles for highly efficient $Cu(In,Ga)Se_2$ thin film solar cells in simple and complex defect models. *Journal of Applied Physics D: Applied Physics*, 47(48):485104, 2014.

[54] M. Nardone et al. Baseline Models for Three Types of CIGS Cells: Effects of Buffer Layer and Na Content. 45th Photovoltaic Specialists Conference (PVSC), IEEE, 2018.

[55] J.K. Larsen et al. Interference effects in photoluminescence spectra of Cu_2ZnSnS_4 and $Cu(In,Ga)Se_2$ thin films. *Journal of Applied Physics*, 118:035307, 2015.

[56] D.G. Buldu et al. Study of Room Temperature Photoluminescence For 1-stage Co-Evaporated Ultra Thin $Cu(In,Ga)Se_2$ Solar Cells. 46th Photovoltaic Specialists Conference (PVSC), IEEE, 2019.

[57] D.G. Buldu et al. Study of Ammonium Sulfide surface treatment for ultra-thin $Cu(In,Ga)Se_2$ with different Cu/(Ga+In) ratios. *Phys. Status Solidi A*, accepted. doi:10.1002/psss.202000307.

[58] C. Dong-Sheng et al. Performance improvement of $CdS/Cu(In,Ga)Se_2$ solar cells after rapid thermal annealing. *Chin. Phys. B*, 22:018801, 2013.

[59] J. Oh et al. Etch Behavior of ALD Al_2O_3 on HfSiO and HfSiON Stacks in Acidic and Basic Etchants. *Journal of The Electrochemical Society*, 158:D217–D222, 2011.

[60] B. Chacko. *Point Contacts in Chalcopyrite Solar Cells*. PhD thesis, Helmholtz Zentrum Berlin, 2018.

[61] L. Van Puyvelde et al. Electronic defect study on low temperature processed $Cu(In,Ga)Se_2$ thin film solar cells and the influence of an Sb layer. *Journal of Physics D*, 48:175104, 2015.

[62] F.C. Marques and J.J. Jasieniak. Ionization potential and electron attenuation length of titanium dioxide deposited by atomic layer deposition determined by photoelectron spectroscopy in air. *Applied Surface Science*, 422:504–508, 2017.

UNIVERSITÉ CATHOLIQUE DE LOUVAIN
École polytechnique de Louvain
Rue Archimède, 1 bte L6.11.01, 1348 Louvain-la-Neuve, Belgique | **www.uclouvain.be/epl**